UC Berkeley

Title
Exploration of magnetic edge and dopant states in Nanographenes

Permalink
https://escholarship.org/uc/item/1533p6h4

Author
Blackwell, Raymond Edward

Publication Date
2021

Peer reviewed|Thesis/dissertation

Exploration of magnetic edge and dopant states in Nanographenes

by

Raymond E Blackwell

A dissertation submitted in partial satisfaction of the

Requirements for degree of

Doctor of Philosophy

in

Chemistry

in the

Graduate Division

of the

University of California, Berkeley

Committee in charge:

Professor Felix Fischer, Chair
Professor Stephen Leone
Professor Michael Crommie

Fall 2021

Abstract

Exploration of magnetic edge and dopant states in Nanographenes

by

Raymond Blackwell

Doctor of Philosophy in Chemistry

University of California, Berkeley

Professor Felix Fischer, chair

While the discovery of 2D graphene offered incredible promise for next generation electronics, device fabrication was severely hindered by the semi metallic nature of graphene. Graphene nanoribbons (GNRs) are quasi-1D nanostructures with similar electronic properties to the parent graphene, and the additional benefit of a widely tunable band gap. The ability to modulate the band gap in GNRs makes them particularly promising candidates for high-performance electronic devices. The band gap in these materials is intimately linked to the atomic structure of the GNR and it is essential to understand the connection between electronic structure and various parameters such a width, dopant position/concentration, and edge topology. To determine this relationship, the synthesis of atomically precise GNRs is crucial. Traditional synthetic techniques for GNR synthesis (e.g. lithographic patterning or the unzipping of carbon nanotubes) fail to meet this requirement. Instead, this thesis will focus on bottom-up synthetic techniques where a molecular precursor is sublimed onto a metallic substrate to yield the desired GNR. Moreover, the metallic substrate provides the ideal platform for electronic and atomic structure characterization using Scanned Probe Microscopy (SPM) techniques.

In this thesis, I will begin by explaining exotic magnetic phenomena that emerge from graphene nanoribbons with zigzag edge topology (Chapter 2). This chapter will discuss all-carbon GNRs and GNRs with nitrogen dopants to ascertain the effect of the dopant atom. Next, I provide information about low band gap GNRs that could be ideal candidates for next generation electronic devices (Chapter 3). Afterwards, I will consider the potential to form Nitrogen bonds with the underlying metallic substrate (Chapter 4). The final chapters in this thesis will take advantage of topological engineering to access low band gap GNRs (Chapter 5) and metallic GNRs (Chapter 6) that can be used to construct high-performance electronic devices entirely from GNRs.

Acknowledgements

They say that it takes a village to raise a child and my journey to the Ph.D. shows the accuracy in that statement. It is truly impossible to imagine reaching this point without the help of countless people.

First and foremost, I must begin by thanking my family especially my parents, Deborah, and Teddy, for always believing in me and providing me the template for success. Next, I must thank my grandparents, Clarice, Faye, Louis, and Raymond. I would not be in this position without the love from each one of you, and every day I strive to make you proud. While I am ostensibly an only child, my cousins Nikki and Jenae are effectively my sisters and have always been there for me. My aunts, Renae and Teresa spent numerous hours taking care of the three of us and making sure that we stayed on the right path and for that I will be forever grateful. My uncle, Johnny has always been a strong role model and showed me the value of hard work. My uncle, Orlando taught me the importance of perseverance and for that I am eternally grateful. Lastly, I must thank my godfather, Hubert for always being willing to drive and support me at various youth sporting events and introducing me to UNC-Chapel Hill basketball. This is just a fraction of the people that I could thank by name, but I want every member of my extended family to know that they played a role in my success.

I would not be in this position without the guidance of my high school Physics teacher, Dr. Jeff Milbourne. When I was at my lowest point during 11th grade after transferring to the North Carolina School of Science and Mathematics, he offered words of wisdom to help me understand that I belonged. He instilled a level of confidence in me that has carried me ever since. I must also give thanks to Bob Gotwals because his Research Experience in Mathematical Chemistry course sparked my initial interest in Physical Chemistry.

Next, I want to offer my gratitude to Dr. Tessa Carducci for accepting me as an undergraduate researcher in Prof. Royce Murray's lab during my sophomore year at UNC. Without that position I would not have fallen in love with research and applied to REUs programs before finally matriculating to UC-Berkeley. Moreover, at UNC, I joined the Admissions Ambassadors and met my Ambassafam: Chamara Fernando, Teddy Gonzales, Akash Shah, and Augusta Dell'Omo. Augusta has been there for me all throughout graduate school as one of the few people who can relate and has seen me at my highs and lows. I am dreaming of the next Ambassador trip and hope it can live up to Seattle and Vancouver. Also at UNC, I must mention Fedor Kossakovski for being one of the first friends that I made on campus in Chemistry 102 and quickly become my best friend. My time at UNC would have looked completely different without you between our trip to LA, our short-lived magazine Event Horizon, the course on our favorite book, and finally connecting me with the Coys Boys (Mark Taylor and Jacob Rosenberg) with whom I continue to talk and watch Spurs matches. A special shoutout to Jacob for moving to the Bay for a couple years and giving me a much-needed respite from graduate school.

Joining the Fischer group at UC-Berkeley was the best decision that I could have possibly made, and I will always appreciate Felix for his enthusiasm during our initial meeting when I was unfamiliar with his group. Felix has been a wonderful advisor and I hope to one day repay the

favor to the next generation of scientists. Dr. Danny Haberer-Germann was an incredible mentor who taught me everything that I know about STM and stayed patient as I became comfortable operating the instrument. I have seen the Fischer group grow rapidly during my time at Berkeley, but I will never forget Cameron, Wade, Stephen, and Rebecca for welcoming me into the group with open arms. Greg Veber and Ilya Piskun eventually became some of my closest friends in graduate school and I want to stay in contact long-term. Ryan, Mathew (Donnie), Michael, Ethan, and Kaitlin helped keep the Fischer group on track and I hope that tradition continues long term. I want to give a special thanks to Dr. Shenkai Wang, Junmian Zhu, and Aidan Delgado for joining me on the STM and keeping me company in the dungeon. Without you three, much of the work in this thesis would not be possible.

During my time at UC-Berkeley I have met so many incredible people, and it all started with my housemates: Josh Tworig, Michael Manoharan, and Josh Cofsky. I was able to expand my social circle from the College of Chemistry and get to know students in MCB to have some semblance of work-life separation. Josh Tworig, Michael, and Emeric Charles became my brothers, and I will forever cherish the years that we spent living together. I could not have dreamed of a better housing scenario, and it pains me to move away from the three of you. My heart is full because I know it is not a goodbye, but just a see you later, and we will continue to hang out via camping trips, concerts, etc. I cannot wait to see what the future holds for all of us. Without the three of you I would not have met Laura Craciun, who eventually became my closest friend outside of the house. Laura was able to convince me to travel to Europe for the first time and our many adventures will continue as we meet up to travel after graduation. Graduate school would have been a completely different experience had I never met Laura and it's hard to imagine enjoying nearly as much without her.

I want to give a special thanks to my childhood friends, Caleb and Jacob McCann and Jaylin Davis for putting up with the intermittent contact ever since I moved away from McLeansville. Whenever we see each other, we are always able to immediately pick up right where we left off and I am transported back to all the great times we had playing baseball together.

After leaving home, I met Taylor Rosenfeld who opened my eyes to an entirely new world of possibilities. Taylor showed me the beauty in music and introduced me to much of the music that I currently love. We have truly come full circle from listening to Phish and Umphrey's concerts to now seeing them live. I love that our friendship has survived such distances and look forward to our next backpacking trip. NCSSM also introduced me to Rebekah Wells, although we did not become friends until UNC. Rebekah is one of few people who truly understands all my idiosyncrasies and still has not managed to get rid of me. Although we are separated by an ocean, I still feel connected. One day we will continue watching Clone Wars and maybe we can do it in-person instead of virtually.

Lastly, I must thank Madame President, Liya, for recruiting me to join the Black Graduate Engineering and Science Students (BGESS) executive board. Connecting with BGESS fundamentally changed my graduate experience for the better. The BGESS community has been essential to my mental health, and I do not have the space to adequately address its impact. I love seeing how much the organization has grown over the past few years and look forward to connecting with students in the future in the same manner that BGESS alumni connect with us.

List of Figures

Chapter 1: Introduction

1.1 Graphene

First postulated in 1947[1], graphene is a 2-dimensional (2D) material made up of a honeycomb lattice of carbon atoms. Graphene is analogous to a monolayer of graphite and was long heralded as an ideal theoretical model for quantum electrodynamics[2–4] before it was first isolated almost sixty years later by Noveselov and Geim in 2004[5], ultimately resulting in the Nobel Prize in Physics in 2010. Shortly after its isolation, subsequent experiments corroborated the fact the charge carriers in graphene are massless Dirac fermions[6,7]. Further experimentation revealed that graphene hosts a myriad of exotic electronic phenomena, namely exceptionally high mobilities[6,8–10] correlated with the unique electron transport of this material[11]. Unfortunately, graphene is semimetallic and the conically shaped conduction band (CB) and valence band (VB) meet at the K and K' points in the Brillouin zone—known as the Dirac points—causing graphene to behave like a zero-band-gap semiconductor. The lack of a band gap in this material severely limits its applications for high-performance field effect transistors (FETs). FET devices require a semiconducting channel material separated from conducting electrodes by a layer of dielectric[12]. Once a potential is applied across the dielectric via a gate voltage, the semiconducting layer becomes charged, altering the conductivity and switching the device to the "on" state such that current can flow across the device (I_{on}). In the "off" state, a minimal amount of current reaches the conducting electrode (I_{off}), and FET devices are characterized by the maximum on-current and the ratio of on-current to off-current (I_{on}/I_{off}). In order to realize high-performance FETs, a band gap must be opened in graphene which can be accomplished in three different ways—applying strain to graphene[13], biasing bilayer graphene[14–17], or confining graphene into one dimension to form graphene nanoribbons (GNRs)[18–20]. The growth of GNRs will be the major focus in this thesis.

1.2 Graphene Nanoribbons

1.2.1 Introduction

While large-area graphene is a 2D array of sp[2] hybridized carbon atoms, GNRs are quasi one-dimensional (1D) nanostructures where the width of a graphene sheet is confined to a width of less than 50 nm. Initial theoretical work was limited to GNRs of two basic edge topologies—armchair and zigzag[20]—that are orthogonal to one another. Zigzag graphene nanoribbons (ZGNRs) are expected to host localized electronic states that couple ferromagnetically along the edge and antiferromagnetically across the ribbon because of the bipartite lattice in graphene[21]. If the spin degree of freedom is ignored, then ZGNRs are predicted to be metallic, but the antiferromagnetic alignment creates a band gap that is inversely dependent on width[22]. For armchair GNRs (AGNRs), the band gap is opened as a result of quantum confinement effects[20]. Furthermore, the band gap is highly sensitive to the width and AGNRs can be divided into three distinct families—3p, 3p+1, and 3p+2 where p is an integer. Within each family, AGNR also have an inverse relationship with width, but the behavior is markedly different between families. For example, the 3p+2 family is predicted to be metallic within the tight-binding framework, but

density functional theory (DFT) calculations within the local density approximation (LDA) framework confirm the presence of a narrow band gap[22]. By contrast, the $3p+1$ family displays a wide band gap in all theoretical frameworks, while the $3p+2$ family lies in the middle. Unfortunately, the Kohn-Sham eigenvalues from DFT calculations substantially underestimate the band gaps in 1D nanostructures due to enhanced electron-electron interactions[23]. To accurately calculate the quasiparticle energies in 1D systems, it is best to describe the energies in terms of the electron self-energy operator. For GNRs, the self-energy operator is evaluated in terms of the GW approximation where the first term is an expansion of the self-energy operator in terms of a dynamically screened Coulomb interaction (W) and a dressed Green's function (G)[24]. When the GW approximation is applied to GNRs, the band gaps increase dramatically and more closely resemble the band gaps that would dictate FET device performance (Figure 1.2.1).
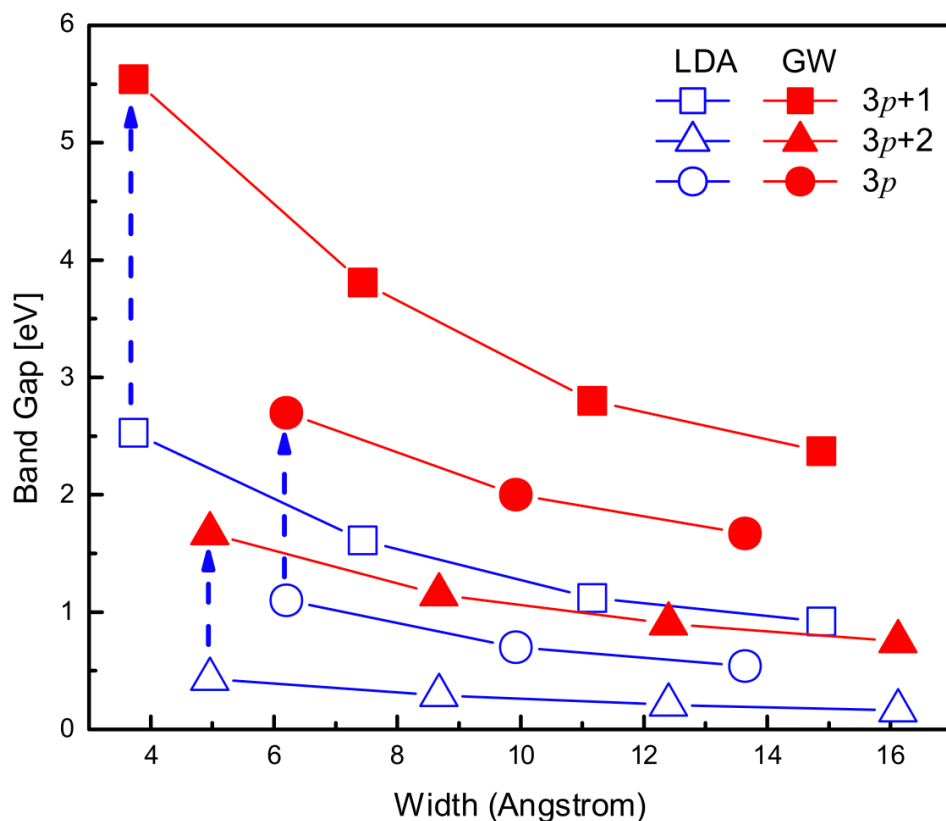
Figure 1.2.1 Quasiparticle Band Energies for AGNRs Reproduced from Ref. 23

High-performance FETs require a band gap of ~ 1eV making the $3p+2$ family of AGNRs exceptionally interesting for device applications. In particular, the 11-AGNR has been a target of our group for many years and Chapter 3 of this thesis will discuss recent attempts to access this structure. Nevertheless, one of the significant attributes of GNRs is that their electronic properties are widely tunable via factors besides width. In addition to width[25–29], the band gap can be affected by modulating the edge topology[30–38], incorporating dopant atoms along the edge or core[39–48], or adjusting the electronic topology[49,50]. This thesis will focus on each of the aforementioned topics. Edge topology will be explored in multiple chapters beginning in Chapter 2 with ZGNRs before continuing with hybrid ZGNR/AGNRs and chevron GNRs in Chapter 3. Additionally doping will

be studied across multiple sections beginning with the ZGNRs in Chapter 2 and continuing with the chevron GNRs in Chapter 3 whereas Chapter 4 will exclusively focus on core doping in AGNRs. Band gap engineering via electronic topology will be the basis for the final two chapters as I discuss strategies to make metallic GNRs. Synthesis of GNRs typically falls within two categories—top-down methods, whereby GNRs are obtained from carbon nanotubes (CNTs) or graphene sheets, and bottom-up methods where GNRs are synthesized from rationally designed precursor molecules.

1.2.2 Top-Down GNR Synthesis

A key benefit to producing GNRs through top-down methods is the low-cost and the ease with which one can produce bulk quantities of material. Graphite, a typical starting material for GNR production, is quite abundant and relatively cheap, allowing for large scale production. One top-down strategy for the formation of GNRs involves the use of electron-beam lithography and etching techniques[51]. Highly orientated pyrolytic graphite (HOPG) is first transferred onto a dielectric substrate and patterned with e-beam lithography before etching with oxygen plasma or reactive He^+ ions[52] to form GNRs of various widths. A representative image reproduced from Ref. 51 is shown below after the deposition of palladium (Pd) source-drain contacts.
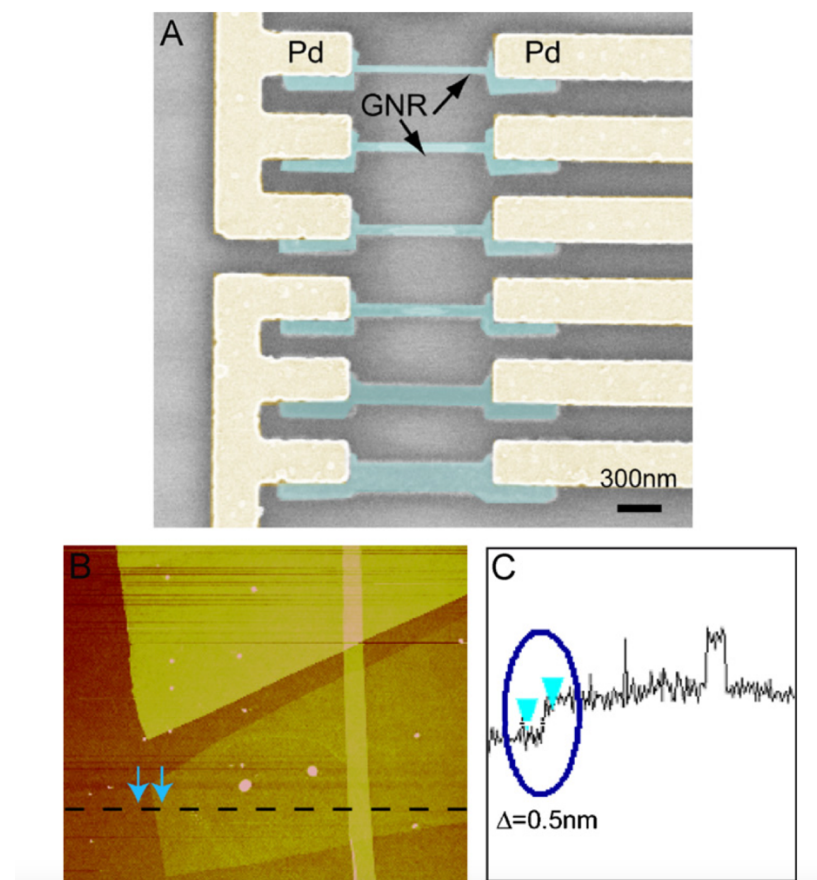
Figure 1.2.2 Top-Down Fabricated GNR Devices A) SEM picture of GNR devices fabricated on a 200 nm SiO_2 substrate. The widths of the GNRs from top to bottom are 20, 30, 40, 50, 10 and 200 nm. B) AFM image of a single layer graphene before lithographic process. C) Cross-section measurement of the AFM, which provides the thickness of the graphene. Reproduced from Ref. 51

While this method is fairly straightforward, it suffers from several major drawbacks. Firstly, the etching process tends to produce highly defective edges and the edge topologies that can be produced are fundamentally limited by the lithographic resolution. Similarly, the lithographic resolution, makes it incredibly challenging to reproducibly fabricate GNRs with widths below 10 nm.
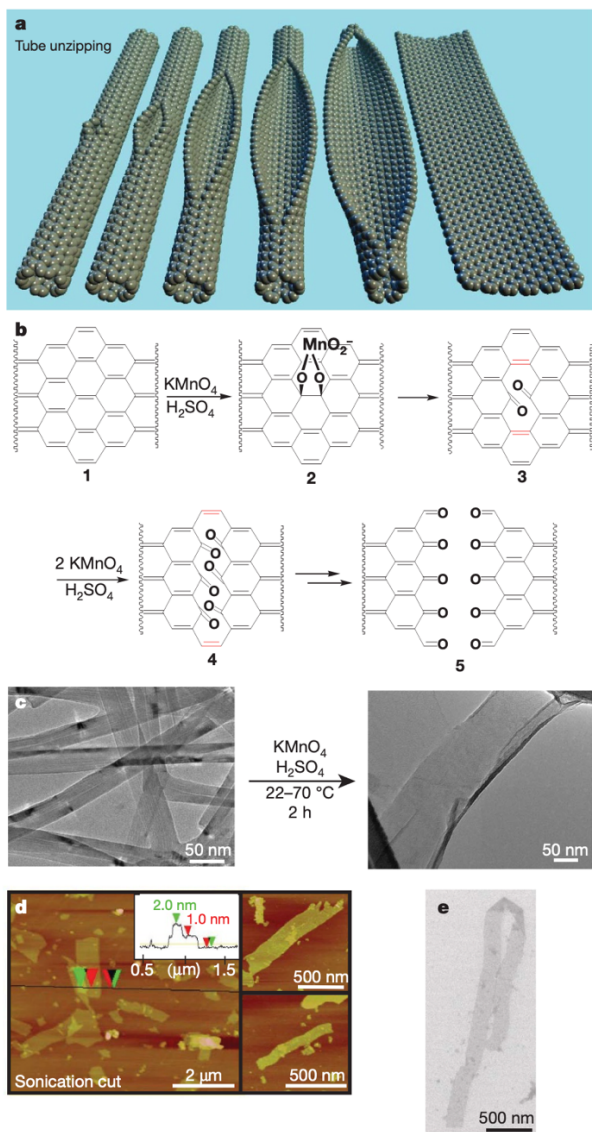
Figure 1.2.3 Nanoribbon Formation and Imaging A) Representation of the gradual unzipping of one wall of a carbon nanotube to form a nanoribbon. Oxygenated sites are not shown. B) The proposed chemical mechanism of nanotube unzipping. The manganate ester in 2 could also be protonated. C) TEM images depicting the transformation of MWCNTs (left) into oxidized nanoribbons (right). The right-hand side of the ribbon is partly folded onto itself. The dark structures are part of the carbon imaging grid. D) AFM images of partly stacked multiple short fragments of nanoribbons that were horizontally cut by tip-ultrasonic treatment of the original oxidation product to facilitate spin-casting onto the mica surface. The height data (inset) indicates that the ribbons are generally single layered. The two small images on the right show some other characteristic nanoribbons. E) SEM image of a folded, 4-mm-long single-layer nanoribbon on a silicon surface. Reproduced from Ref. 52

An alternative top-down strategy for GNR fabrication involves the unzipping of CNTs to ultimately form the desired GNR. Once again, this technique is particularly desirable because of its scalability and the widespread access to various CNTs. Moreover, this method can readily synthesize GNRs with sub-10 nm widths, which is expected to vastly improve FET device performance. There exists a diverse set of conditions to unzip CNTs including chemical oxidation via $KMnO_4$ in a concentrated solution of H_2SO_4[53] and Ar plasma etching[54]. This section will focus on chemical oxidation as this strategy has been more widely explored by the broader graphene community and is shown to produce sequential cutting. Figure 1.2.3 depicts the mechanism to create GNRs beginning with the formation of a manganate ester (Fig. 1.2.3B) followed by further oxidation to yield the dione (Figure 1.2.3C). The next permanganate attacks the double bonds highlighted in red in Figure 1.2.3C and the bond-angle strain induced by the hole acts as a self-fulfilling feedback loop enhancing the reactivity to subsequent openings. In a final step, the ketones undergo a conversion to carboxylic acids and the bond-angle strain is relieved when the CNT opens to form the GNR[53]. Unfortunately, the unzipping conditions are still quite harsh and the resulting GNRs remain highly defective. Furthermore, the innate polydispersity in CNT samples leads to the inhomogeneous GNR samples. To realize high performance FET devices, it is imperative to synthesize homogenous GNR samples that can be reproduced across multiple devices. This thesis will concentrate on GNR fabrication via surface catalyzed bottom-up methods as detailed in the following section.

1.2.3   Bottom-Up GNR Synthesis

It cannot be overstated the extent to which bottom-up synthesis has fundamentally altered GNR research. Top-down fabrication methods have proven to be extremely unreliable especially when it comes to reproducibility. The defective edge structures in these GNRs highly degrade the device performance and a method that produces smooth, pristine edges is of the utmost importance. The electronic properties of GNRs are intimately related to the atomic structure and precise control over the width, connectivity, and dopant concentration allows for unprecedented control over the band gap. This level of control is necessary for FET device applications and opens the door for all-carbon electronics. As transistors continue to downscale, we are beginning to reach the lower limit of device architectures and a replacement for silicon (Si) is highly desirable. GNRs are an intriguing candidate if structures with band gaps close to that of Si can be synthesized without much difficulty. My work relies on bottom-up synthetic procedures in ultra-high vacuum (UHV) catalyzed by metallic substrates. The first instance of bottom-up synthesis in UHV was published by Grill, *et. al* in 2007 using tetrabrominated porphyrin precursor molecules (Figure 1.2.4B) that were subsequently sublimed under UHV conditions onto an clean Au(111) substrate[55]. A schematic of the growth is displayed below in Figure 1.2.4. Once the halogenated precursor in Figure 1.2.4B has been sublimed onto Au(111), the substrate is annealed to induce dehalogenation because the C–Br bond is the weakest bond in the system (bond dissociation energy for dehalogenation in bromobenzene is 1.0 eV on Au(111)[56]). This leads to the formation of carbon centered radicals at positions previously occupied by the halogen atoms and the molecule now has sufficient energy to diffuse along the surface and covalently bond with other dehalogenated precursors to form oligomeric species.
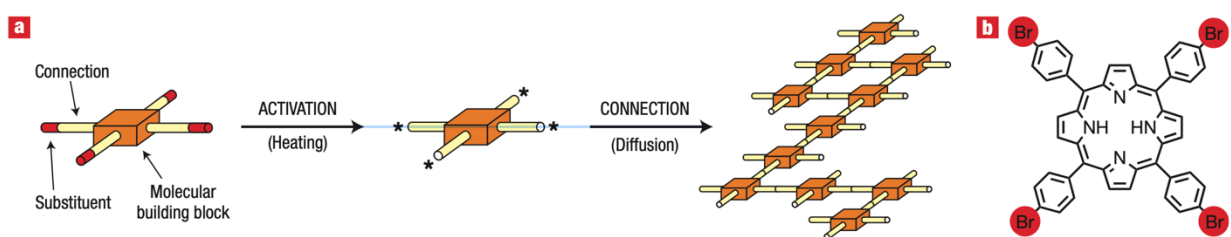
Figure 1.2.4 Nanoarchitectures of covalently bound Br4TPP molecular networks A) Concept of the formation of covalently bound networks by connecting activated molecular building blocks. B) Chemical structure of the Br_4TPP molecule (substituent Br atoms are highlighted in red). Reproduced from Ref. 55

The extension of this method to GNRs follows quite logically and the molecular precursor dictates the final structure. The beauty of this technique is that rational design of the molecular precursor allows for access to GNR architectures that are not possible with lithography. The proof-of-concept was shown by Cai, *et. al* in 2010 with dibromo-bisanthracene (DBBA), the molecule that quickly became the workhorse within the GNR community[31]. The growth of DBBA is represented below in Figure 1.2.5.
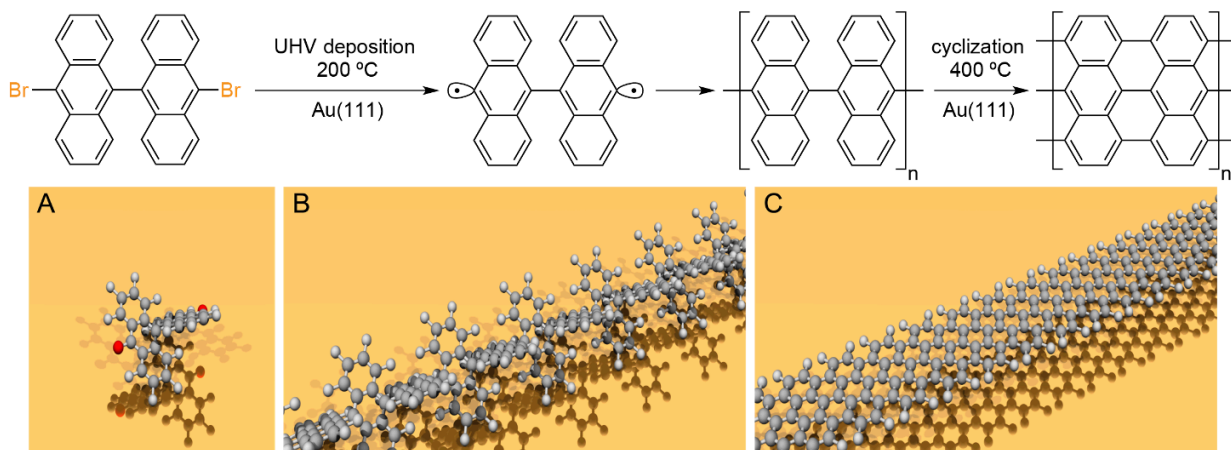
Figure 1.2.5 Schematic for 7-AGNR Growth A) Molecular model for DBBA precursor B) Molecular model of DBBA after polymerization C) Molecular model of 7-AGNR after cyclization

In an initial step, DBBA is sublimed onto a Au(111) substrate from a Knudsen cell evaporator under UHV conditions (Figure 1.2.5A). DBBA is dehalogenated after an annealing step where the substrate is held at 200 °C such that covalent C–C coupling can be achieved. Figure 1.2.6B contains topographic images of the polymer species where the apparent height is roughly 0.4 nm indicating that the polymer forms a non-planar cruciform geometry. The final step—unnecessary in the work of Grill, *et. al*—involves a final annealing step where the underlying substrate catalyzes cyclodehydrogenation yielding the fully planar GNR with an apparent height of 0.18 nm. The GNR in Figure 1.2.6C and 1.2.6E is known as the N = 7 AGNR, and it constitutes the first successful bottom-up GNR growth. The apparent width measured via Scanning Tunneling Microscopy (STM) is 1 nm, substantially smaller than the widths attained with top-down fabrication.
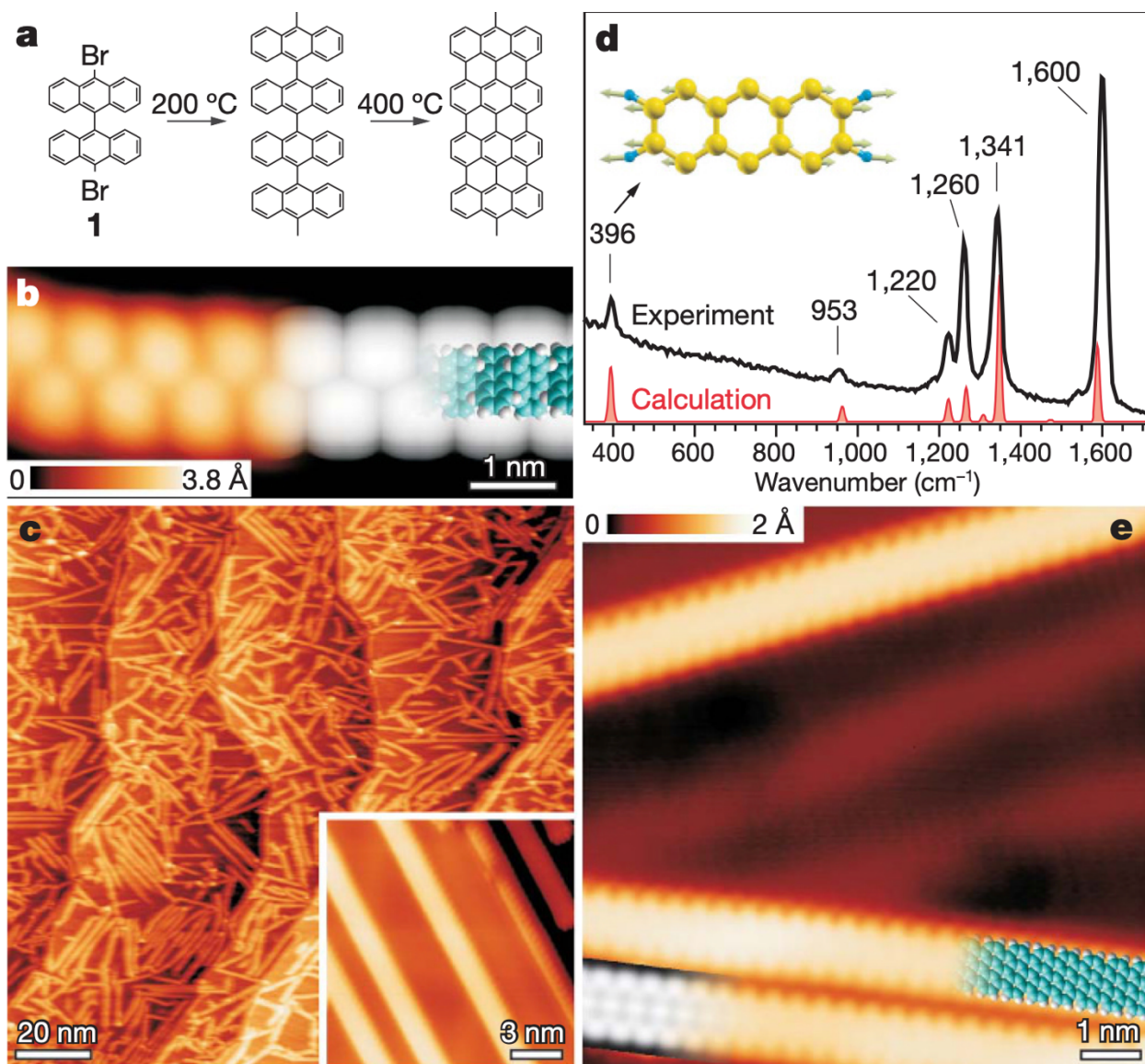
Figure 1.2.6 Straight GNRs from bianthryl monomers a, Reaction scheme from precursor 1 to straight N = 7 GNRs. **b,** STM image taken after surface-assisted C–C coupling at 200 °C but before the final cyclodehydrogenation step, showing a polyanthrylene chain (left, temperature $T = 5$ K, voltage $V_s = 1.9$ V, current $I_t = 0.08$ nA), and DFT-based simulation of the STM image (right) with partially overlaid model of the polymer (blue, carbon; white, hydrogen). **c,** Overview STM image after cyclodehydrogenation at 400 °C, showing straight N = 7 GNRs ($T = 300$ K, $V_s = 2.3$V, $I_t = 0.03$ nA). The inset shows a higher-resolution STM image taken at 35 K ($V_s = 21.5$ V, $I_t = 0.5$ nA) **d,** Raman spectrum (532 nm) of straight N = 7 GNRs. The peak at 396 cm is characteristic for the 0.74 nm width of the N = 7 ribbons. The inset shows the atomic displacements characteristic for the radial-breathing-like mode at 396 cm. **e,** High-resolution STM image with partly overlaid molecular model (blue) of the ribbon ($T = 5$ K, $V_s = 20.1$ V, $I_t = 0.2$ nA). At the bottom left is a DFT-based STM simulation of the N = 7 ribbon shown as a greyscale image. Reproduced from Ref. 31

7

This landmark paper opened the door to an entirely new field of scientific research because it finally became possible to procure atomically precise GNRs. Collaborative research between our group, the Crommie group in the UC-Berkeley Physics department, and Bokor group in the UC-Berkeley Electrical Engineering department quickly set out to characterize logic devices based on these materials[57].
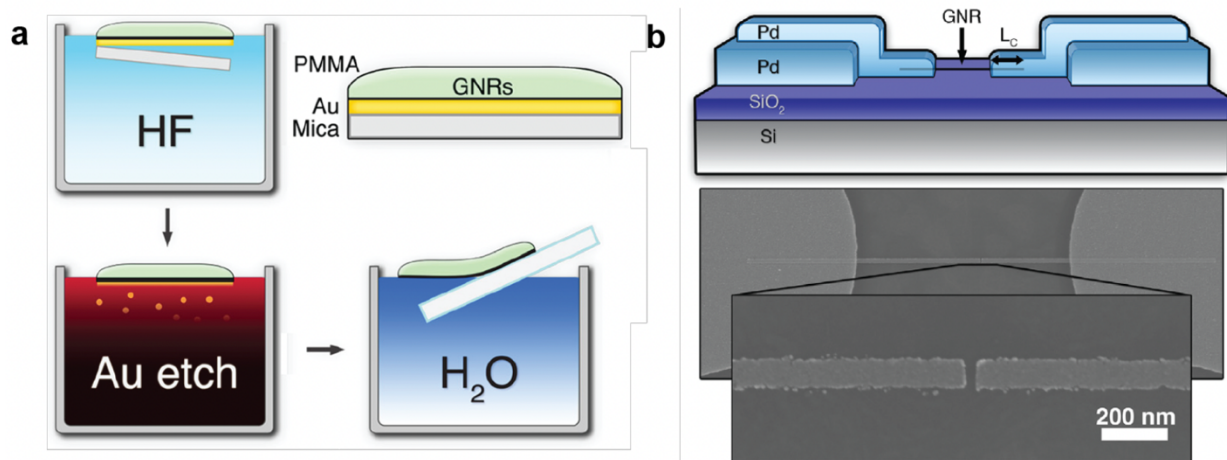
Figure 1.2.7 Fabrication of 7-AGNR FET Devices a, Schematic of wet transfer method for AGNRs **b,** Schematic of 7-AGNR FET device. Reproduce from Ref. 57

The most challenging aspect of FET device fabrication is the transfer of GNRs from the metallic growth substrate onto a dielectric. Several different procedures have been implemented for GNR transfer, but the original technique is a wet transfer process that begins with the spin-casting of poly-methyl methacrylate (PMMA) on top of GNRs. Next, the sample is baked at 180 °C for 10 min to create a PMMA/GNR/Au/mica stack. After baking, the stack is suspended in a solution of concentrated hydrofluoric acid (HF) whereby the mica is delaminated from the Au substrate. Once the mica has been delaminated the sample is rinsed with water and transferred to an Au etchant before transferring the PMMA/GNR stack to the target dielectric substrate[57]. In the final step, the film is once again baked to remove any residual water and the PMMA layer is stripped with acetone. The device architecture is shown in Figure 1.2.7b and it is vital that GNRs have sufficient length to bridge the gap between the Pd electrodes. The gap is limited by lithography and ideal GNRs are greater than 30 nm long. If the GNR does not lie across the gap indicated by L_c in Figure 1.27B, then there is no conductance. Fortunately, when L_c is on the same order as the GNR length, it is possible to observe gate modulated conductance. The devices in Figure 1.2.8 have an I_{off}/I_{on} ratio of 10^3, but this value is limited by the measurement. The I_{on} is greater than 1 nA, but the I_{off} is equally large because of substantial leakage caused by charge carriers tunneling across the barrier. In these devices, there is a large Schottky barrier at the GNR-metal interface because the 7-AGNRs have an especially wide band gap (> 3.5 eV). To further improve device performance, it became immediately obvious that the GNRs with narrower band gaps must be synthesized. Bottom-up synthesis is uniquely situated to address this issue and I allocate much of this thesis towards the strategies to determine the optimal GNRs for device applications.
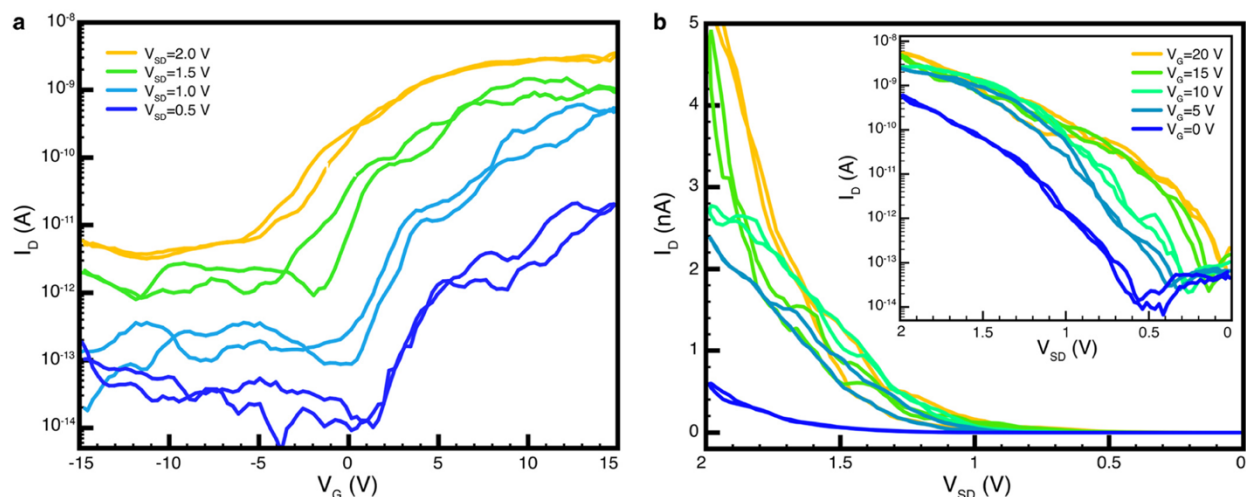
Figure 1.2.8 Electrical characterization of a typical device post passivation, under vacuum, at 77 K a, Drain-current response with respect to gate voltage, I_D-V_G, at different source drain bias, V_{SD}, and **b,** drain-current response with respect to drain voltage, I_D-V_D, of same device at different gate bias, V_G, inset: The same data presented in logarithmic scale. Reproduced from Ref. 57
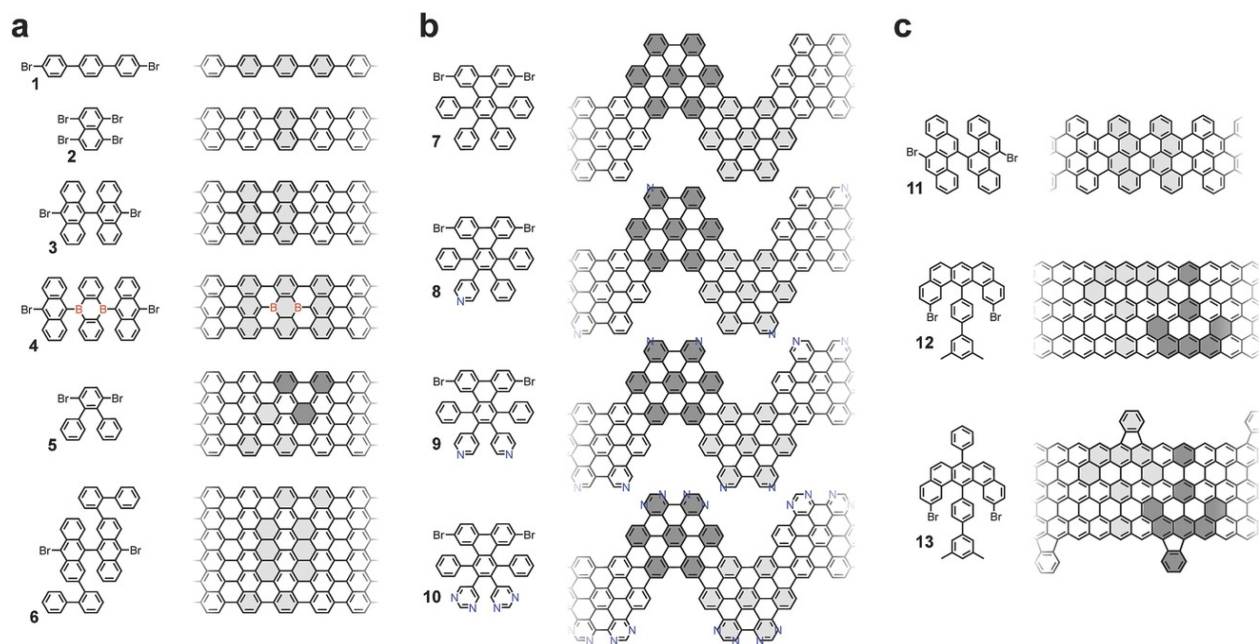
Figure 1.2.9 Catalogue of molecular precursors for the on-surface synthesis of atomically precise graphene nanoribbons a, Armchair GNRs **b,** Chevron GNRs **c,** Zigzag GNRs Reproduced from Ref. 58

In the years following the advent of bottom-up synthesized GNRs, the field exploded and numerous GNRs that were previously inaccessible have begun to be explored. A review article published by Talirz, *et. al*[58] serves as a useful starting point to understand the depth of GNR research. AGNRs represent the most studied family on account of their chemically inert edge topology and the theoretical work outlining the band gap trends. Our group modified the DBBA precursor utilized for 7-AGNR with biphenyl wings to increase the width by six carbon atoms

resulting in the 13-AGNR[27]. In short order various groups designed molecular precursors for the 9-AGNRs[26] and 5-AGNRs[25] so that at least one member of each AGNR family had been synthesized. Although many wider AGNRs (e.g. 6-AGNRs[59], 12-AGNRs[59], 14-AGNRs[60], 15-AGNRs[59], and 21-AGNRs[60]) have been synthesized via lateral fusion techniques, I will not go into much detail on this strategy in my thesis because it involves a high temperature annealing step to fuse smaller GNRs into larger structures. Attempts to synthesize wider GNRs within the $3p+2$ family have produced mixed results. The 11-AGNR has remained a target of our research group and I will present strategies toward this structure in Chapter 3. Recently, Yamaguchi, *et. al* reported the synthesis of 17-AGNRs[29] and measured a band-gap of 0.20 eV (theoretical quasiparticle gap: 0.63 eV). Unfortunately, the 17-AGNRs are less than 10 nm long and far too short to bridge the gap between source and drain electrodes in FET devices. One strategy that has proven successful to affect the length of AGNRs is to use iodine to halogenate the molecule precursor instead of bromine[61]. The BDE for iodobenzene is 0.7 eV on Au(111) compared to the 1.0 eV for bromobenzene[62]. The lower BDE manifests itself in the dehalogenation temperature, which Ref. 59 shows begins at 80 °C. If the dehalogenation step is the rate-limiting step for the formation of aryl-aryl bonds, then it is expected that a lower dehalogenation temperature will produce longer GNRs. Ref. 59 clearly shows that the average length for 9-AGNRs is increased using an iodinated precursor, the same effect is not observed in chevron GNRs. The length distribution is unaffected by the halogen identity implying that the polymerization in chevron GNRs is diffusion limited[63].The formative work of Cai, *et. al* introduced the chevron family of GNRs[31] in panel b of Figure 1.2.9 and the zigzag family of GNRs was finally accessed in 2016 by Ruffieux, *et. al*[33]. A myriad of other GNR edge topologies have been realized, but these families will be heavily discussed in the next chapters.
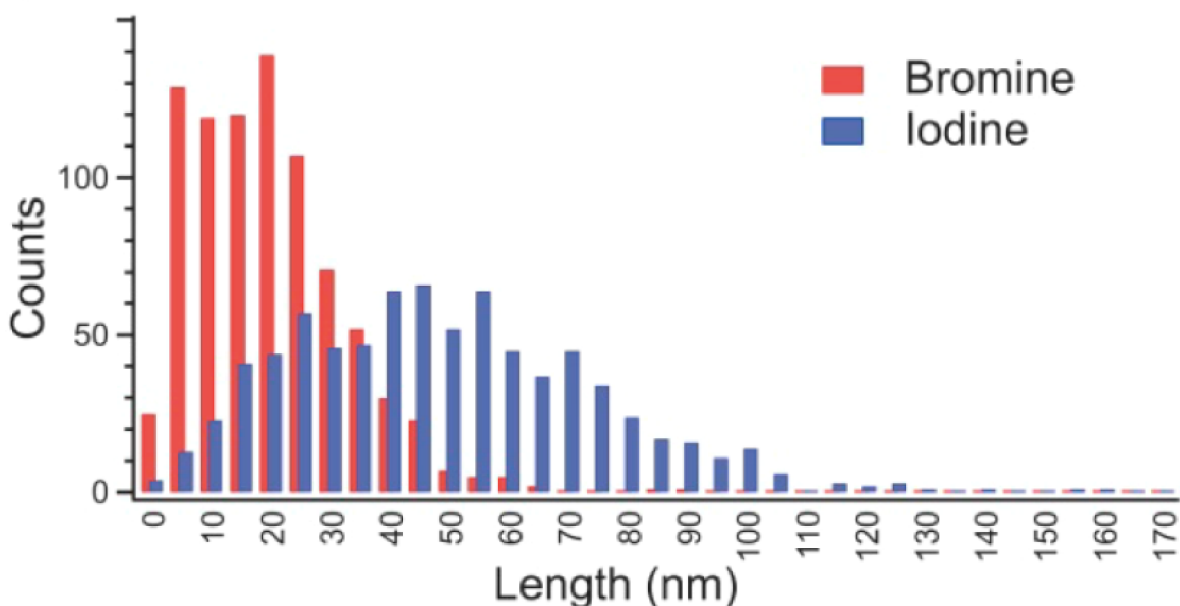
Figure 1.2.10 Length Distribution of 9-AGNR Reproduced from Ref. 61
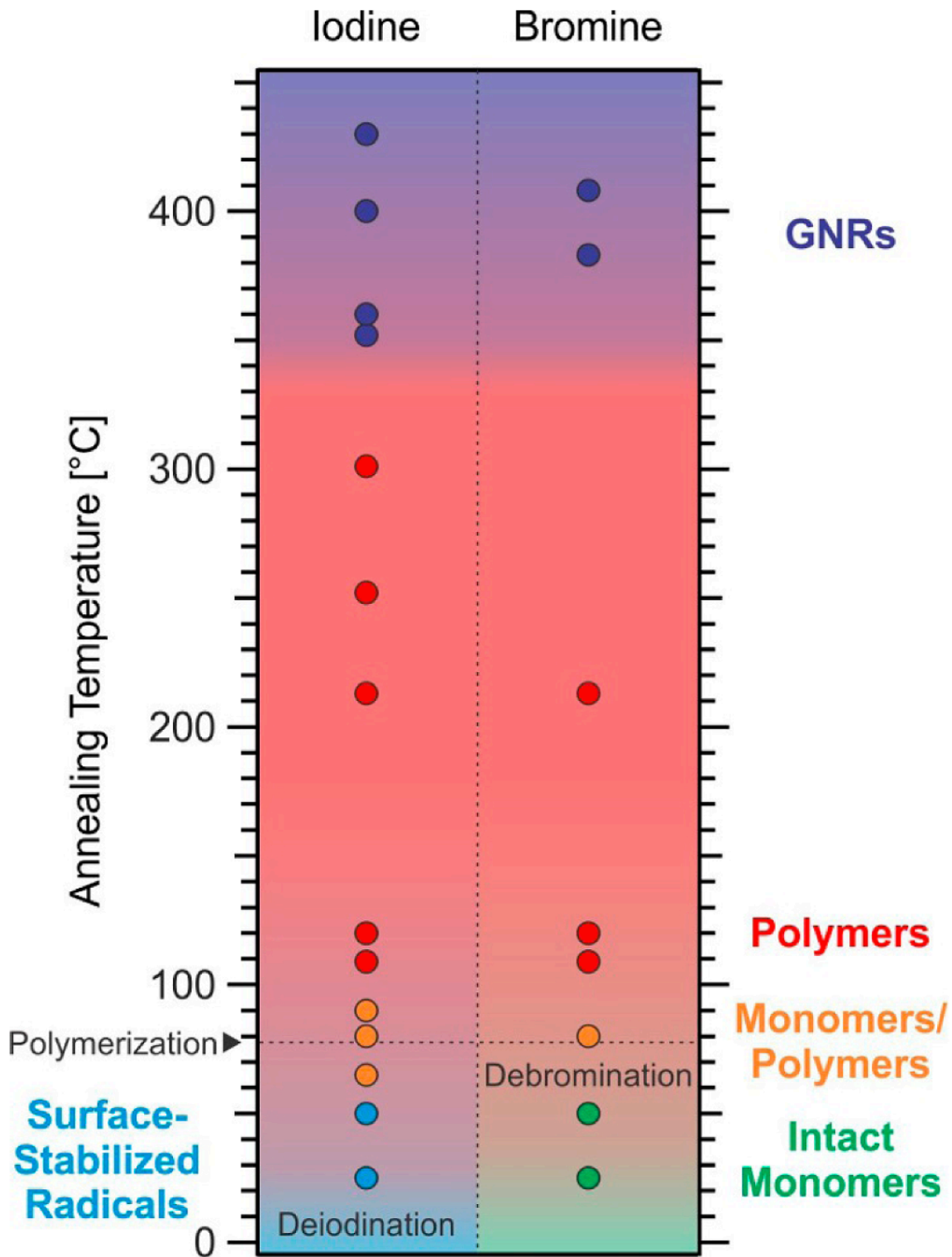
Figure 1.2.11 Phase Diagram for chevron GNR synthesis Reproduced from Ref. 63

One remaining challenge in bottom-up synthesis is the construction of GNR heterojunctions. For GNR heterojunctions, it is common to deposit multiple precursors that are compatible with one another to create the desired GNR. However, this method is inadequate because the polymerization is random, and the final structures are not reproducible. Figure 1.2.12 displays several examples of GNR heterojunctions that have arisen from collaborative efforts between our own research group and the Crommie lab in the Physics department[64–67]. Each panel depicts the uncontrollable nature of these polymerizations, highlighting the need for a novel synthetic approach because exclusively relying on surface-catalyzed reactions cannot circumvent this problem. In Chapter 5, I will show that it is possible to create controlled heterojunctions with a single rationally designed precursor. Alternatively, it is possible to use Matrix Assisted Direct-Transfer techniques (MAD) to design and synthesize exotic GNR heterostructures.
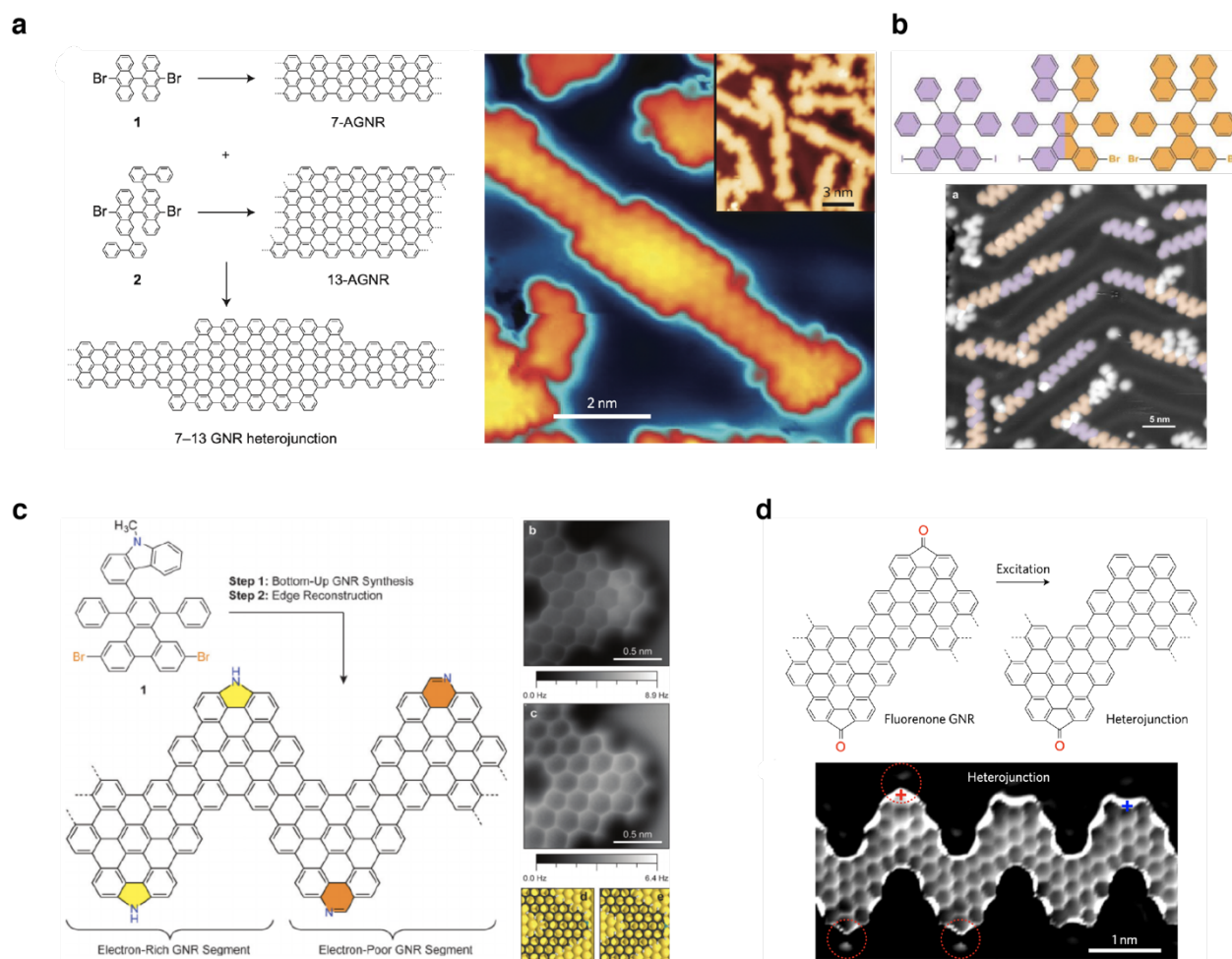
Figure 1.2.12 GNR Heterojunctions a, 7/13-AGNR from Ref. 62 **b,** Chevron GNR Heterojunction from Ref. 63 **c,** surface-catalyzed rearrangement in N-doped Chevron GNR from Ref. 64 **d,** Fluorenone GNR from Ref. 65

1.2.4   Matrix Assisted Direct-Transfer (MAD Transfer)

The newest addition to the toolkit for bottom-up synthesis in GNRs comes in the form of the MAD transfer technique. Strategies that exclusively use noble metal surfaces will never be

ideal for polymerizations involving multiple precursors. UHV synthesis offers no path towards sequence control, therefore any co-polymerization will be completely random. Furthermore, UHV synthesis only allows minimal control over the ultimate GNR length. On the other hand, a solution-based approach can provide substantially more control by taking advantage of modern step-growth and living polymerization techniques[68,69]. At first glance, these two approaches seem incongruent especially considering the difficulty that arises when trying to characterize solution synthesized GNRs with Scanned Probe Microscopy (SPM). Our groundbreaking work by McCurdy, *et. al* combined these two approaches and opened the door for entirely new avenues of GNR synthesis[70]. The first step is to take advantage of solution polymerization techniques to produce sequence-controlled co-polymer GNR precursors comprising narrow and well-defined length distributions. Dispersions of the polymer precursor were prepared in molten pyrene—chosen due to its low enthalpy of sublimation and because it undergoes a solid/gas phase transition in UHV—and ground into a fine powder. Next a fiberglass stamp was pressed into the powder and transferred into UHV before the stamp was applied to a clean Au(111) substrate. Annealing the substrate to 420 °C for 30 min removes all pyrene and leaves only the desired GNRs on the Au(111) substrate. A schematic for this process can be seen in Figure 1.3.13. While this work focused on a known scaffold—chevron GNRs—this technique can easily be extended to realize unconventional architectures.
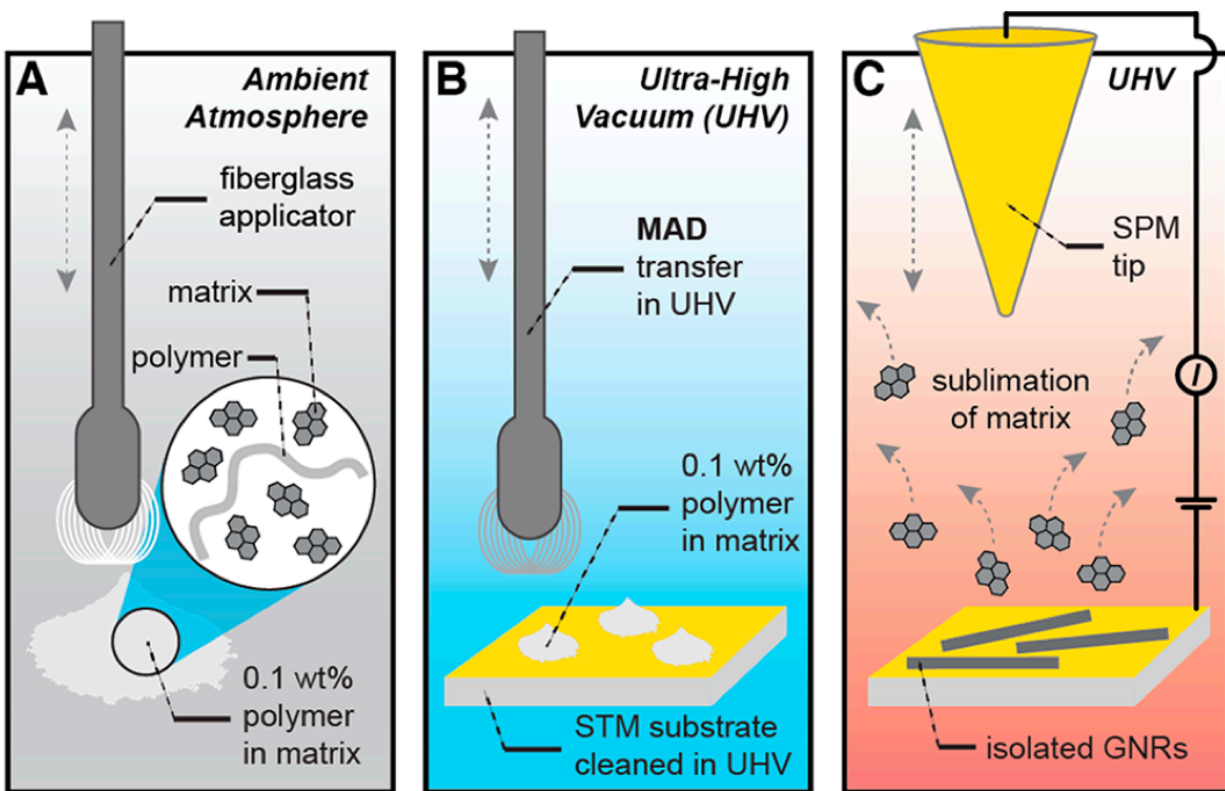
Figure 1.2.13 MAD Transfer Process a, Loading of fiberglass applicator with polymer sample dispersed in an inert matrix under ambient conditions **b,** MAD transfer of polymer dispersion onto STM substrate in ultrahigh vacuum (UHV) **c,** annealing induces traceless sublimation of bulk matrix followed by cyclodehydrogenation leaving spatially isolated GNRs behind.

1.3 Principles of Scanned Probe Microscopy Techniques

1.3.1 Introduction

The field of Scanned Probe Microscopy (SPM) was birthed with the invention of the Scanning Tunneling Microscope (STM) by IBM scientists Binning, Rohrer, Berberm and Weibel[71,72]. For this discovery, Binning and Rohrer were awarded the Nobel Prize in Physics in 1986. The fundamental design of an STM is as follows—a sharp, metallic tip is mounted onto piezoelectric motors allowing movement in the (x,y,z) directions. The quantum mechanical phenomena known as tunneling underpins measurements within an STM. If the tip is brought close enough to a conducting substrate, then it is possible for electrons to tunnel through the vacuum gap separating the tip and sample. The tunneling current has an exponential relationship with the tip-sample distance giving SPM methods unparalleled resolution. The physical quantity measured by an STM is the tunneling current and the major scanning modes are constant-current and constant-height. In constant-current measurements, a tunneling current setpoint is defined and the tip-sample distance is adjusted to keep this current constant as the tip raster scans in the (x,y) plane. The resulting scan gives the apparent height profile for the sample of interest. Most of the STM images shown in this thesis were taken in constant-current mode. Nevertheless, it is also possible to carry out constant-height measurements where the tip-sample distance is fixed and the tunneling current adjusted as the tip raster scans in the (x,y) plane. Another common measurement mode is known as Scanning Tunneling Spectroscopy (STS). In this mode, the differential conductance (dI/dV) is used to acquire information about the local density of states (LDOS) The following section will outline the quantum mechanics that serve as the basis for all STM experiments.

1.3.2 Quantum Theory of Tunneling

To use STS and observe electronic states, it is necessary to prove that differential conductance (dI/dV) is proportional to local density of states (LDOS) in the sample of interest. While this can be demonstrated a number of different ways, I will use the Bardeen and Tersoff-Hammann theories of quantum tunneling[73,74] and obtain the result

1-1

$$\frac{dI}{dV} \propto LDOS(E; x, y, z)$$

I will begin with the transition rate of a single-electron state in the tip-sample junction using Fermi's golden rule

1-2

$$W_{i \to f} = \frac{2\pi}{\hbar} \left| \langle \psi_f | H' | \psi_i \rangle \right|^2 \delta(E_f - E_i)$$

In this expression the electron is initially in the STM tip, ψ_i, and the final state, ψ_f, is in the sample implying that the electron is tunneling from tip-to-sample. $\delta(E_f - E_i)$ is the Dirac delta function and the tunneling matrix element can be defined as

1-3

$$M_{s,t} \equiv |\langle \psi_f | H' | \psi_i \rangle|$$

In the elastic tunneling regime ($E_s = E_t$), the energies of the tip and sample are aligned to the Fermi energy, E_F, and **1-1** can be rewritten as

1-4

$$W_{t \to s} = \frac{2\pi}{\hbar} |M_{s,t}|^2 \delta(E_F - E)$$

The total tunneling rate must include all states that participate in the tunneling between tip and sample. With proper choice of STM tip material and prudent tip conditioning, then it is sufficient to assume that the tip DOS is uniform at all energies. This is equivalent to integrating over a constant tip DOS, ρ_t. Additionally, we can approximate the sample states as a series of discrete delta functions and sum over all states:

1-5

$$W_{t \to s} = \frac{2\pi}{\hbar} \sum_s \int_{-\infty}^{\infty} |M_{s,t}|^2 \delta(E_F - E) \rho_t dE$$

If the electron is to successfully tunnel from the tip to the sample, then it must be tunneling from a filled state within the STM tip to an empty state within the sample. Therefore **1-5** must be modified to account for the electron-hole populations using the Fermi-Dirac distribution:

1-6

$$f(E) = \left(\frac{1}{e^{E-E_F/kT} + 1} \right)$$

Combing **1-5** and **1-6** gives:

1-7

$$W_{t \to s} = \frac{2\pi}{\hbar} \rho_t \sum_s \int_{-\infty}^{\infty} |M_{s,t}|^2 \delta(E_F - E)[1 - f(E)]f(E)dE$$

$$= \frac{2\pi}{\hbar} \rho_t \sum_s \int_{-\infty}^{\infty} |M_{s,t}|^2 \delta(E_F - E) \left[1 - \left(\frac{1}{e^{E-E_F/kT} + 1} \right) \right] \left(\frac{1}{e^{E-E_F/kT} + 1} \right) dE$$

A non-zero bias, V, must be applied to the tip-sample junction to offset the Fermi levels and permit tunneling. In this derivation the bias is applied to the sample, such that the sample states are shifted

away from E_F by the quantity eV, the charge of an electron times the applied voltage V, and **1-7** is now

1-8

$$W_{t \to s} = \frac{2\pi}{\hbar} \rho_t \sum_s \int_{-\infty}^{\infty} |M_{s,t}|^2 \delta(E - eV - E_F)[1 - f(E - eV)]f(E)dE$$

The corresponding equation when the electron tunneling from the sample to the tip is immediately obvious as one can think about inverting the applied bias.

1-9

$$W_{s \to t} = \frac{2\pi}{\hbar} \rho_t \sum_s \int_{-\infty}^{\infty} |M_{t,s}|^2 \delta(E - eV - E_F)[1 - f(E)]f(E - eV)dE$$

The total tunneling current is equal to the sum of **1-8** and **1-9**

1-10

$$I = -e(W_{s \to t} - W_{t \to s}) = \frac{2\pi}{\hbar} \rho_t \sum_s \int_{-\infty}^{\infty} |M_{s,t}|^2 \delta(E - eV - E_F)[f(E) - f(E - eV)]dE$$

All the STM measurements presented in this thesis occur at 4 K and at these temperatures the Fermi-Dirac distribution behaves as a step function so **1-10** can be further simplified to:

1-11

$$I = \frac{2\pi}{\hbar} \rho_t \sum_s \int_0^{eV} |M_{t,s}|^2 \delta(E - eV - E_F)dE$$

Thus, it is imperative to evaluate the tunneling matrix elements $M_{t,s}$, if one wants to understand STM experiments. Bardeen accomplished this by treating the sample Hamiltonian as a perturbation to the tunneling process. Here the assumption is an elastic tunneling process and zero tip bias such that:

1-12

$$M_{s,t} = \int \psi_s^* H' \psi_t dr = \int \psi_s^* \left(E_s - \frac{p^2}{2m} \right) \psi_t dr = \int \psi_s^* \left(E_s - \frac{\hbar^2}{2m} \nabla^2 \right) \psi_t dr$$

$$= \frac{\hbar^2}{2m} \int \psi_t \nabla^2 \psi_s^* - \psi_s^* \nabla^2 \psi_t dr$$

Using the Tersoff-Hamman approximation,[73] which assumes a spherically symmetric tip state where ϕ is the work function of the STM tip

1-13

$$\psi_t = \frac{e^{-\kappa r}}{4\pi r}, \kappa = \frac{\sqrt{2m\phi}}{\hbar}$$

Combining **1-12** and **1-13**:

1-14

$$M_{s,t} = Ce^{(-\kappa z)}\psi_s(z = 0)$$

1-14 can now be plugged into **1-11** to acquire the final equation for STM tunneling current:

1-15

$$I(V) \propto e^{(-2\kappa z)}\sum_s \int_0^{eV} |\psi_s(z = 0)|^2 \delta(E - eV - E_F)dE$$

As one can see from **1-15**, when the STM is operated in constant-current mode with the feedback loop turned on, the topographic map as the tip is raster scanned across the surface is a 2-dimensional map of the total DOS integrated from E_F to eV (with e representing the elementary charge of an electron and V representing the applied bias). If the derivative of **1-15** is taken with respect to the voltage, then the equation becomes

1-16

$$\left(\frac{dI}{dV}\right)_{V'} \propto \sum_s |\psi_s(z = 0)|^2 \delta(E - eV - E_F)dE = LDOS(E_F + eV)$$

In this section I have shown how the differential conductance measurements taken in STS give information about the sample LDOS. This thesis will heavily feature two different types of STS measurements—point spectroscopy and spatial maps. For point spectroscopy the dI/dV vs. V signal is measured, providing the energy dependent LDOS for the sample. Spatial maps of the dI/dV signal at a sample bias V give a 2-D picture of the spatial distribution of the sample DOS at the given energy.

1.3.3   Non-contact Atomic Force Microscopy

Shortly after the invention of the STM, Binning, Quate and Geber invented another instrument that quickly ingratiated itself to surface scientists—the atomic force microscope (AFM)[75]. The AFM builds off the principles established in STM but can be used with a wider variety of samples. In an AFM, a sharp conducting tip is mounted onto a cantilever that is raster scanned across the substrate of interest. The AFM tip is capable of measuring force gradients between the cantilever and substrate. While there are many operating modes for the AFM, this section (and later work in this thesis) will focus on non-contact AFM (nc-AFM)[76]. In nc-AFM, the cantilever is driven at its eigenfrequency, f, and the amplitude of the oscillation is kept constant. The frequency shift required to keep the tip oscillating at a constant amplitude is then fed back to the cantilever. Forces between the tip and sample cause a change in $f = f_0 + \Delta f$ and the

eigenfrequency for a harmonic oscillator can represented as follows where k^* is the effective spring constant and m^* is the effective mass.

1-17

$$f = \frac{\sqrt{k^* m^*}}{2\pi}$$

Assuming that the second derivative for the tip-sample potential, $k_{ts} = \frac{\partial^2 V_{ts}}{\partial z^2}$, is constant over the range of the oscillating cantilever, then the effective spring constant can be written as

1-18

$$k^* = k + k_{ts}$$

In the limit where $k_{ts} \ll k$, then the square root in **1-17** can be expanded as a Taylor series yielding:

1-19

$$\Delta f = \frac{k_{ts}}{2k} f_0$$

If the potential between the tip and sample follows a Lennard-Jones potential, then the frequency shift gives direct information about the force gradient between the tip and sample because the force gradient is equal to the second derivative of the potential with respect to distance. The final section in this introduction will explain the mechanism that produces atomic resolution in STM and nc-AFM measurements.
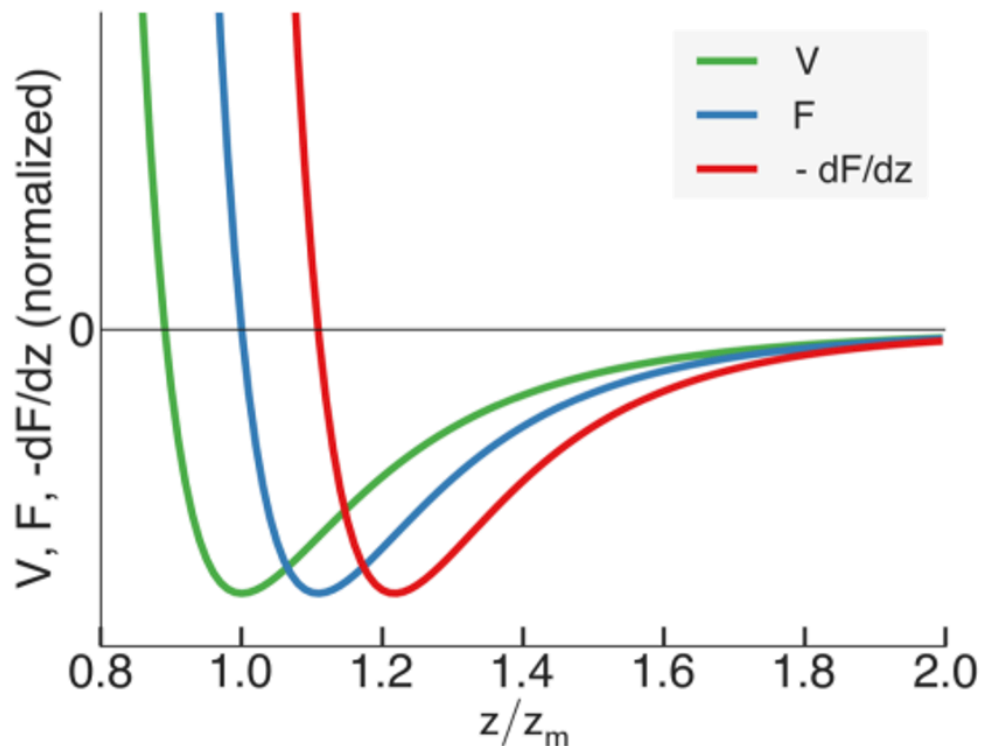
Figure 1.3.1 Graphical Representation of Tip-Sample Interactions

1.3.4   Mechanism of High-Resolution SPM Imaging

One of the most striking features of SPM techniques is the ability to obtain topographic images that clearly show covalent bonds (Figure 1.2.12C-D)[67,77]. These high-resolution images can be observed in STM, and nc-AFM spotlighted throughout this thesis. For this reason, a brief explanation of the mechanism will be given here. First, it is important to point out that the tip must be functionalized to acquire these high-resolution measurements. This section will focus on functionalization with carbon monoxide (CO) molecules with well-defined p_z orbitals. In nc-AFM, the mechanism is straightforward. The minima in Figure 1.3.1 occurs when the attractive and repulsive forces between the tip and sample perfectly cancel out. As the tip-sample distance is decreased past this point, the repulsive forces dominate the tip-sample interaction. In nc-AFM, these repulsive forces occur because of the Pauli repulsion. Since electrons are fermions, they cannot occupy the same physical space. To avoid this forbidden overlap, the wavefunction for the CO molecule on the tip must tilt away from the wavefunctions protruding from the substrate. This underlines the importance of using a CO molecule because the well-defined shape of the p_z orbital leads to this enhanced resolution. This regime was inaccessible until the invention of Q-plus cantilevers that were sufficiently stiff to prevent the cantilever from snapping into contact with the sample when the tip-sample distance reached the repulsive regime[78]. A similar mechanism can be used to explain the atomic resolution in bond-resolved STM (BRSTM).
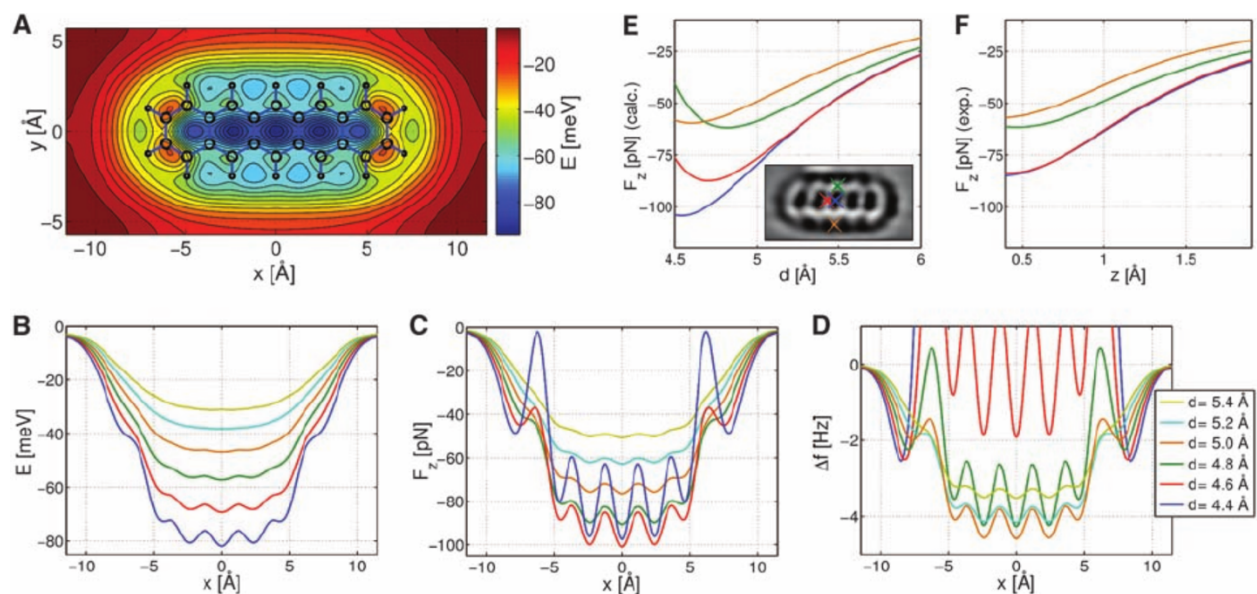
Figure 1.3.2 Calculated Energy Maps a, for a CO-pentacene distance of $d = 4.5$ Å. Calculated line profiles of the energy **b,** the vertical force **c**, and Df, **d,** above the long molecular axis for different molecular distances. Calculated, **e,** and measured, **f,** force-distance curves above different molecular sites: central hollow site (blue), C–C bond of central ring on long molecular axis (red), C atom of central ring on short molecular axis (green), and H atom on short axis (orange). The inset in, **e,** shows a measured Df map with the different molecular sites indicated. Reproduced from Ref. 77

Chapter 2: Emergent Magnetic Order in Zigzag Graphene Nanoribbons

Parts of this chapter have been published in: <u>"Spin Splitting of Dopant Edge State in Magnetic Zigzag Graphene Nanoribbons"</u> Blackwell, R. E.; Zhao, F.; Brooks, E.; Zhu, J.; Piskun, I.; Wang, S.; Delgado, A.; Lee, Y.L.; Louie, S.G.; Fischer, F.R. *Nature* in press. **2021**

2.1   Introduction

Graphene nanostructures terminated by zigzag edges host spin-ordered electronic states that give rise to quantum magnetism[21,79]. These intrinsic magnetic edge states emerge from the zigzag edge structure of graphene itself and create opportunities for the exploration of carbon-based spintronics and qubits[80–82], paving the way for the realization of high-speed, low-power operation spin-logic devices for data storage and information processing[83–86]. The edge states of zigzag graphene nanoribbons (ZGNRs) have been predicted to exhibit a parallel (ferromagnetic) alignment of spins on either edge of the ribbon while the spins on opposing edges are antiferromagnetically coupled (antiparallel alignment)[21,79]. This unusual electronic structure can give rise to field- or strain-driven half-metallicity in ZGNRs[79,87]. A strong hybridization of the electronic states of ZGNRs with those of the underlying support, along with the susceptibility of zigzag edges to undergo passivation through atom-abstraction or radical-recombination reactions represents a veritable challenge to their exploration[88]. To electronically characterize the ZGNR, it is necessary to reduce the ZGNR-substrate interaction by edge modification.

In this chapter I will present two different methods to reduce the ZGNR-substrate interaction via edge modification. The first strategy builds off the work in Ref. 33 by Roman Fasel and colleagues where a ZGNR is synthesized via the U-shaped monomer shown in Fig 2.2.4. The addition of a single phenyl ring to the U-shaped monomer (Fig 2.X) decouples the resulting ZGNR allowing electronic characterization on the growth substrate. After reproducing the synthesis, we attempted to fabricate ZGNR/AGNR T-junction heterostructures via a novel linker molecule. Additionally, I will discuss experiments to homopolymerize the linker molecule and form nanoporous graphene with zigzag edges and armchair edges.

The second half of this chapter will be devoted to the synthesis of ZGNRs with substitutional nitrogen dopants. The first section will focus on ZGNRs with every sixth C–H group along the zigzag edge replaced by a single N-atom. Here we provide the first direct evidence for magnetism in ZGNRs by measuring the exchange field induced by the spin-polarized ferromagnetically ordered edges of ZGNRs. The second section will explore the synthesis of ZGNRs with every third C–H group replaced by a single N-atom.

2.2 Bottom-Up Synthesis of all-carbon ZGNRs

2.2.1 Introduction

While extensive research has been conducted on graphene nanoribbons with armchair edges (AGNRs), related work on zigzag graphene nanoribbons has proven to be more challenging. Zigzag graphene nanoribbons (ZGNRs)—quasi one-dimensional semiconducting strips of graphene featuring two parallel zigzag edges along the main axis of the ribbon—have been predicted to host intrinsic electronic edge states that are ferromagnetically ordered along the edges of the ribbon and antiferromagnetically coupled across its width since the seminal works of Mitsutaka Fujita in 1996[21]. This antiferromagnetic spin configuration is a consequence of the honeycomb lattice of graphene and follows from a well-established theorem for electrons on a bipartite lattice[89]. These initial calculations were carried out within the tight-binding framework and predicted that ZGNRs would always be metallic, but calculations later done by Young-Woo Son *et al.* based on the *ab initio* pseudopotential density functional method within the local spin density approximation (LSDA) showed ZGNRs are semiconducting with a band gap that is inversely proportional to the width[79]. In all bands, states of opposite spin are degenerate without the presence of an external electric field. Upon application of transverse electric fields, the valence and conduction bands of one spin state close their gap while those associated with the other spin state widen their gap (Figure 2.2.1). As a result, ZGNRs have the potential to exhibit metallic behavior for one spin and insulating behavior for the other giving ZGNRs the property of half-metallicity, a crucial component for the realization of spin-based electronic devices.
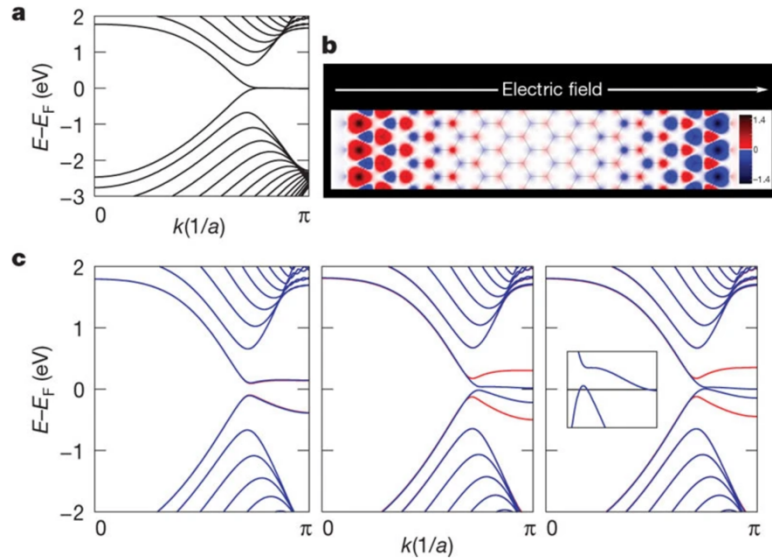
Figure 2.2.1 Electronic Structure of ZGNRs In all figures, the Fermi energy (E_F) is set to zero. **a,** The spin-unpolarized band structure of a 16-ZGNR. **b,** The spatial distribution of the charge difference between α-spin and β-spin ($\rho_\alpha(r) - \rho_\beta(r)$) for the ground state when there is no external field. The magnetization per edge atom for each spin on each sublattice is $0.43\mu_B$ with opposite orientation, where μ_B is the Bohr magneton. The graph is the electron density integrated in the z direction, and the scale bar is in units of $10^{-2}|e|$ Å^{-2}. **c,** From left to right, the spin-resolved band structures of a 16-ZGNR with $E_{ext}=0.0$, 0.05 and 0.1 V Å^{-1}, respectively. The red and blue lines denote bands of α-spin and β-spin states, respectively. Inset, the band structure with $E_{ext}=0.1$ V Å^{-1} in the range $|E-E_F|<50$ meV and $0.7\pi \leq ka \leq \pi$ (the horizontal line is E_F). Reproduced from Ref. 79

The first example of bottom-up synthesis of a ZGNR was reported in 2016 by Ruffieux *et al*[33]. ZGNRs that were 6 carbon atoms wide (6-ZGNRs) were readily synthesized by this precursor, but spectroscopic characterization on the growth substrate was not possible due to the strong ZGNR-substrate interaction. Subsequent depositions of NaCl were necessary to allow for the lateral manipulation of 6-ZGNRs onto NaCl islands to sufficiently reduce the ZGNR-substrate interaction and confirm the edge-localized states (Fig. 2.2.2).
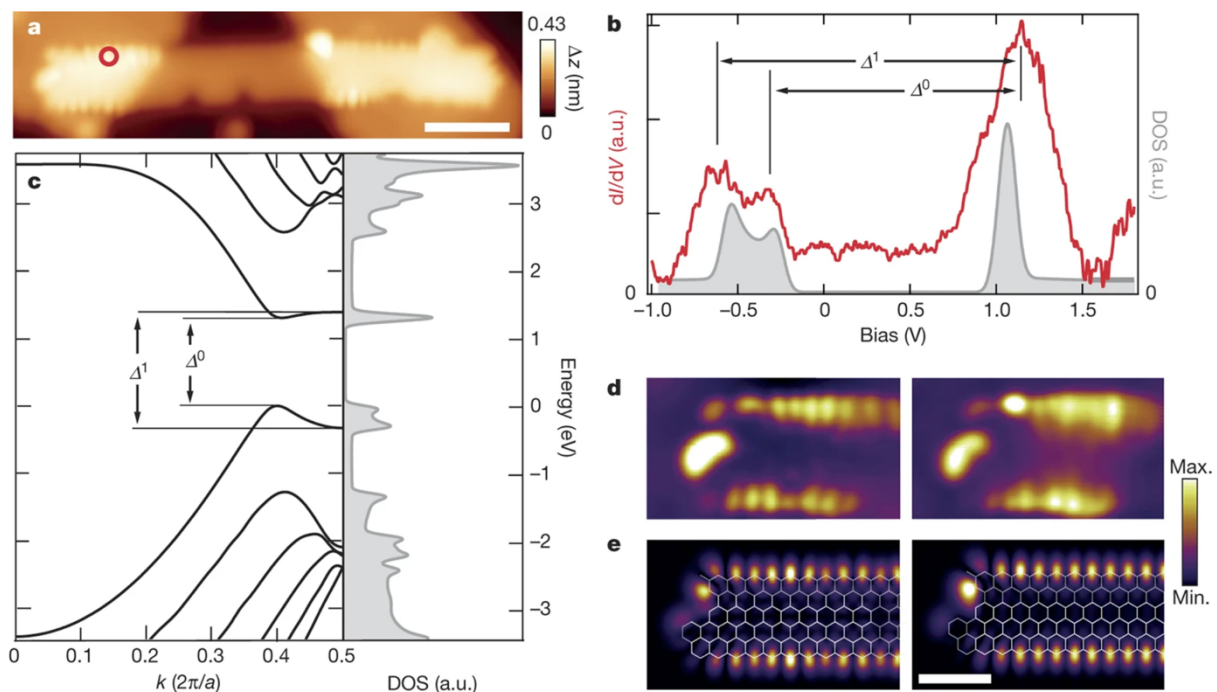
Figure 2.2.2 Electronic Structure Characterization of 6-ZGNRs a, STM topography image ($V_s = -0.25$ V, $I_t = 100$ pA) of a 6-ZGNR bridging between two NaCl monolayer islands, achieved through STM manipulation. Scale bar, 2 nm. **b,** Differential conductance (dI/dV) spectrum (red) taken at the zigzag edge marked by the red circle in b and the quasiparticle density of states (DOS; grey). **c,** Quasiparticle band structure (energy versus wave vector k) (left, black; b is the lattice parameter) and DOS (right, grey) calculated for an infinitely long 6-ZGNR. **d,** Differential-conductance maps of filled (left) and empty (right) edge states taken at a sample bias of -0.3 V and 1.0 V, respectively. **e,** DFT-based local DOS at a 4-Å tip–sample distance, showing the spatial distribution of filled (left, with overlaid structural model) and empty (right, with overlaid structural model) edge states. Scale bar for b and e, 1 nm. a.u., arbitrary units. Reproduced from Ref. 33

Another strategy for reducing the ZGNR-substrate interaction relies on the introduction of an additional phenyl ring to U-monomer used to synthesize the 6-ZGNR (Figure 2.2.3a). Ruffieux *et al* synthesized this precursor as well and showed that the resulting GNR can be characterized on the growth substrate[33]. Although the external phenyl group undergoes a ring closure that does not form periodic fluoranthene units, the precursor synthesis is significantly shortened (5 total steps vs. 14 total steps for the 6-ZGNR precursor) making the phenyl-substituted 6-ZGNR an ideal candidate to test the synthesis of AGNR/ZGNR networks.
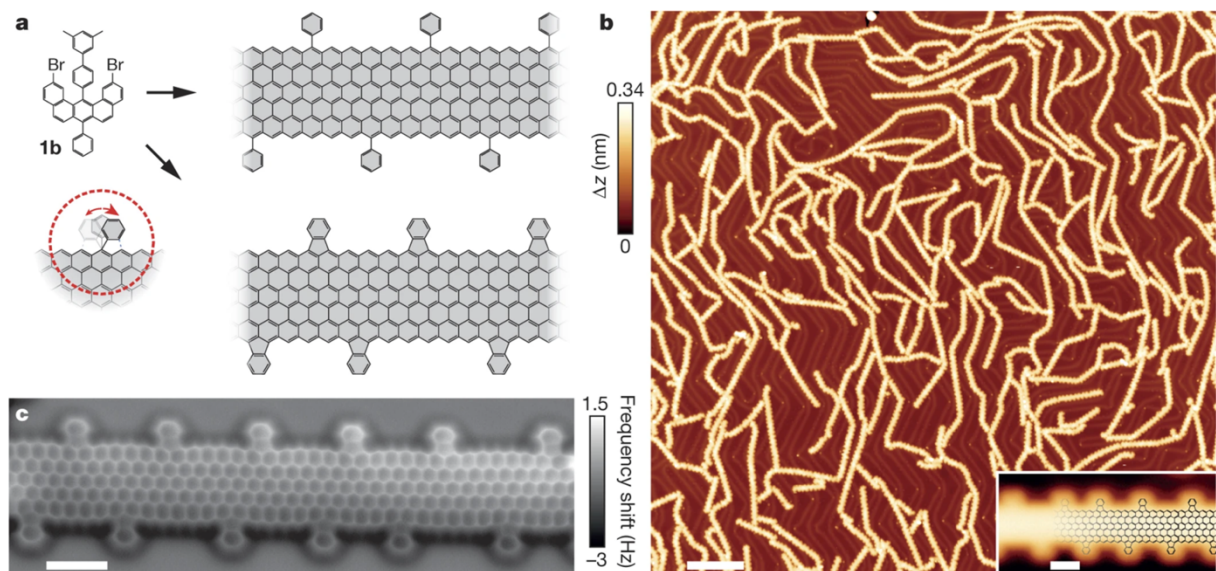
Figure 2.2.3 Synthesis of edge-modified 6-ZGNRs a, Monomer 1b (top left) with an additional phenyl group at the R_3 position of the monomer 1a, which is designed to afford an edge-modified 6-ZGNR upon polymerization and subsequent cyclization. The highlighted scheme (dashed red circle) illustrates the two possible rotation possibilities (bottom left, red arrow) upon activation of the external phenyl ring. Right, possible cyclodehydrogenation products assuming no activation of the external phenyl groups (top) and formation of fluoranthene subunits based on an additional dehydrogenative ring closure at the external phenyl groups (bottom). **b,** Overview STM image ($V_s = -1.5$ V, $I_t = 150$ pA) of edge-modified 6-ZGNRs fabricated on a Au(111) surface. Scale bar, 20 nm. Inset, high-resolution STM image ($V_s = 0.15$ V, $I_t = 2$ pA). Scale bar, 1 nm. **c,** Constant-height nc-AFM frequency-shift image of edge-modified 6-ZGNR ($A_{osc} = 0.7$ Å, $V_{ac} = 25$ mV). Scale bar, 1 nm. Reproduced from Ref. 33

2.2.2 Bottom-Up Synthesis of ZGNR Networks

To date, there has been no published studies on the bottom-up synthesis of atomically defined zigzag/armchair heterojunctions. These structures are of particular interest because they have the possibility of hosting exotic topological states that would be particularly useful for quantum computing. The first step in attempting to realize these structures is the design of a novel precursor molecule capable of copolymerization with the 6-ZGNR scaffold and an AGNR scaffold. The junction molecule (2-1 in Figure 2.2.4) used for these experiments contains a U-shaped core similar to the 6-ZGNR scaffold and an additional anthracene functionality that is compatible with 7-AGNR scaffold creating the possibility to form an AGNR/ZGNR T-junction (Figure 2.2.4). Additionally, the junction molecule has the potential to self-polymerize and yield nanoporous graphene containing pores with both zigzag and armchair edges (Figure 2.2.5).
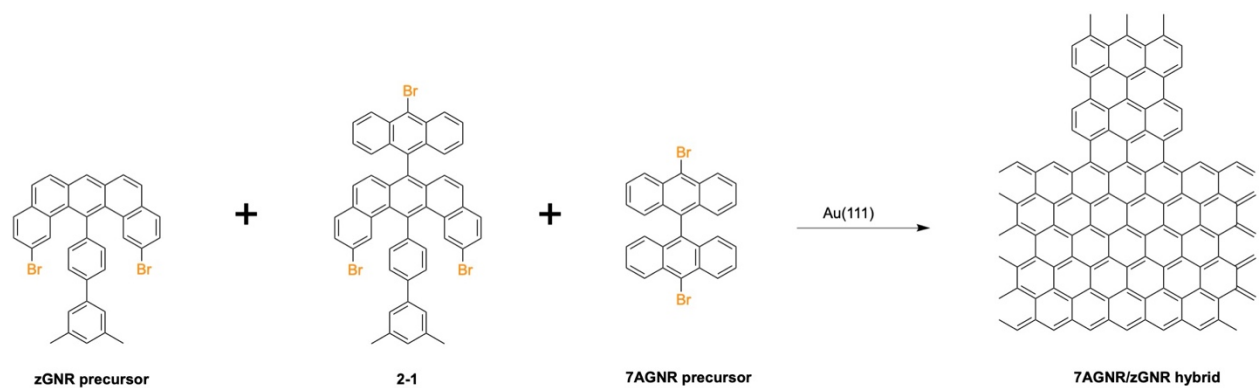
Figure 2.2.4 Schematic of aGNR/zGNR Hybrid
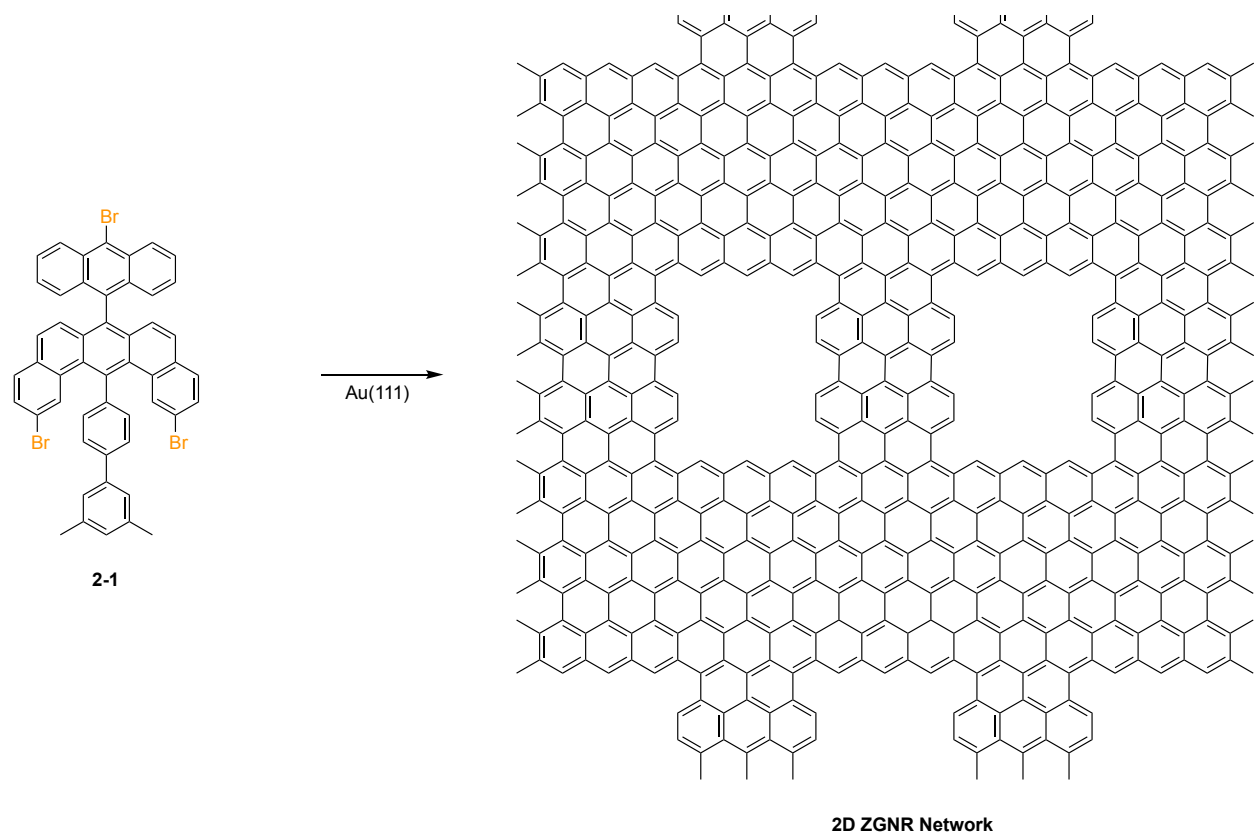
Figure 2.2.5 Schematic of 2D ZGNR Growth

Initial attempts at the self-polymerization of **2-1** to form a nanoporous graphene network were conducted on Au(111). **2-1** was sublimed under UHV conditions from a Knudsen cell evaporator onto an Au(111) substrate that was held at 25° C. Figure 2.2.6b shows a STM topographic image taken of the molecule immediately after deposition. The monomer self-assembles nicely into extended linear structures. Subsequent annealing of the substrate to 375° C should induce polymerization and cyclodehydrogenation, but the image in Figure 2.2.6c shows no

evidence of controllable polymerization. There are no distinguishable structures on the surface implying that we have only made amorphous carbon.
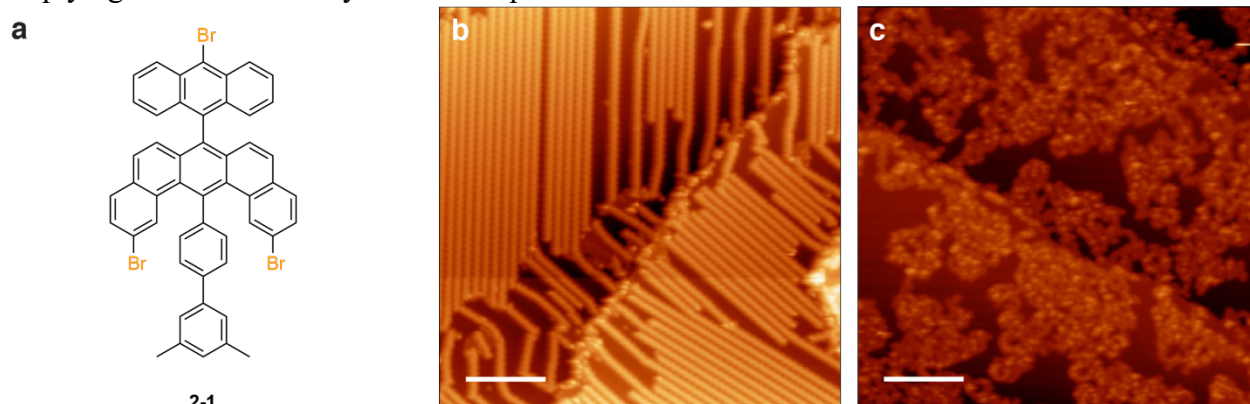
Figure 2.2.6 Surface-Assisted Homopolymerization of aGNR/zGNR Linker a, T-Junction molecule **b,** STM topographic image of **4-1** after deposition on Au(111) substrate held at 24 °C **c,** STM topographic image of **4-1** following an anneal to 375 °C (scale bars: 10 nm, V_s = 50 mV, I_t = 20 pA)

After unsuccessful attempts at the homopolymerization of **2-1**, the feasibility for AGNR/ZGNR heterostructures was explored. The phenyl-substituted precursor from Ref. 33 was co-deposited under UHV conditions along with **2-1** onto a Au(111) substrate that was held at 25° C. A STM topographic image after deposition of both monomers is shown in Figure 2.2.7b and there are clearly two distinct regions of self-assembled monomers. One region strongly resembles the linear structures from Figure 2.2.6b while the other region can be assigned to the phenyl-substituted 6-ZGNR. The substrate was then annealed to 300° C and the STM topographic image is displayed in Figure 2.2.6c. The surface predominately consists of similar structures to the phenyl-substituted 6-ZGNR, but there are regions that may indicate the incorporation of the linker molecule. Instead of a single lobe that corresponds to the extra phenyl ring, there is a slightly elongated segment that could be attributed to an anthracene along the zigzag edge. Higher resolution images (e.g., bond-resolved STM or nc-AFM) were not conducted making any conclusions on these structures purely speculative. Future experiments on this system must include higher resolution imaging to accurately assess the deposition.
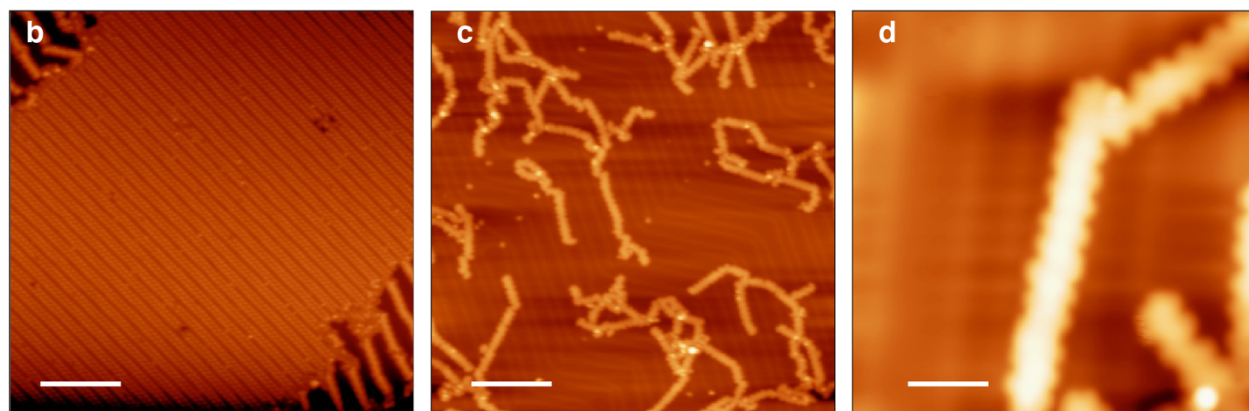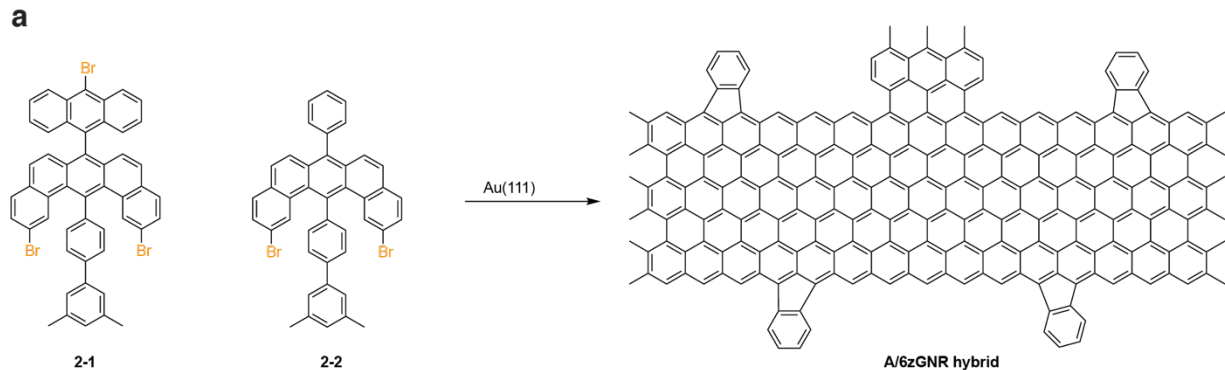
Figure 2.2.7 Phenylated Zigzag GNR and T-Junction Molecule Co-Polymerization a, Schematic displaying growth of phenylated zGNR and T-Junction **b,** STM topographic image of **2-1** and **2-2** following deposition at 24 °C (scale bar: 10 nm) **c,** STM topographic image after subsequent annealing to 300 °C (scale bar: 10 nm, V_s = 50 mV, I_t = 20 pA) D) Zoom-in image of zGNR displayed in **d,** (scale bar: 4 nm, V_s = 50 mV, I_t = 20 pA)

2.3   Controllable Edge Modification in ZGNRs via Nitrogen Doping

2.3.1   Introduction

Our strategy for engineering chemically robust ZGNR edge states relies on the introduction of a superlattice of isoelectronic substitutional dopant atoms along both edges of a ZGNR. Replacement of every sixth C–H group along the zigzag edge of a 6-ZGNR (a zigzag GNR featuring six lines of carbon atoms across the width of the ribbon) by a N-atom leads to the structure of N-6-ZGNRs depicted in Figure 2.3.1a. Each trigonal planar N-atom contributes the same number of electrons (one electron in a half-filled p_z-orbital) to the extended π-system of the N-6-ZGNR as the trigonal planar C–H groups they replace. While the magnetic spin-polarized edge states remain largely unaffected by the subtle modulation of frontier bands imposed by a superlattice of N-dopant atoms, *ab initio* quantum mechanical calculations show that the

substitutional doping in N-6-ZGNRs leads to a lowering of the total energy of formation (E_f) by $\Delta E_f = -0.124$ eV per unit cell when compared to the parent 6-ZGNRs.
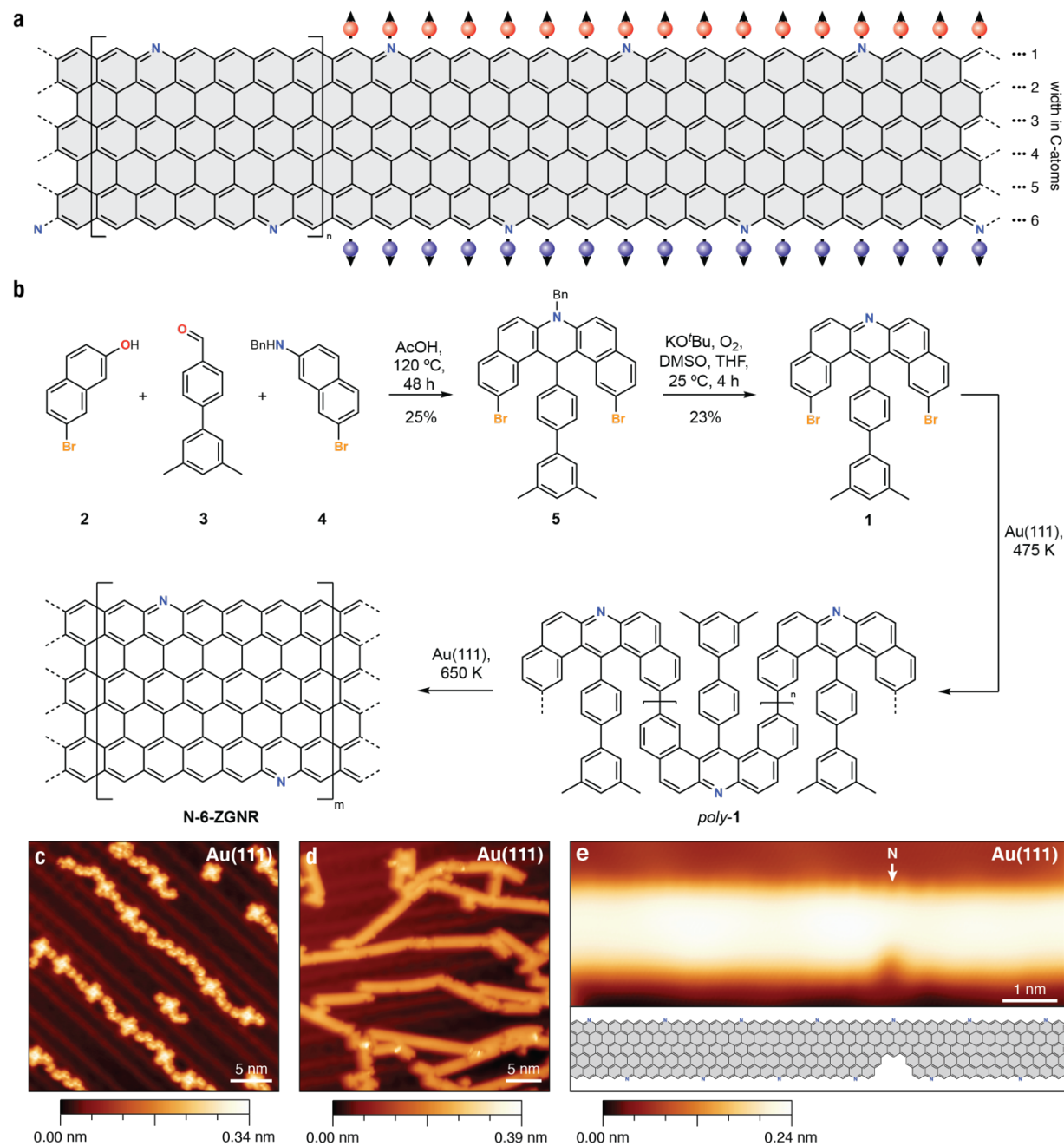
Figure 2.3.1 Bottom-up Synthesis of N-doped N-6-ZGNR a, Schematic representation of spin-ordered edge states in N-6-ZGNRs. **b,** Schematic representation of the bottom-up synthesis and on-surface growth of N-6-ZGNRs from molecular precursor **1**. **c,** STM topographic image of molecular precursor **1** as deposited on Au(111) ($V_s = 50$ mV, $I_t = 20$ pA). **d,** STM topographic image of fully cyclized N-6-ZGNRs following annealing to 650 K ($V_s = 50$ mV, $I_t = 20$ pA). **e,** STM topographic image of a fully cyclized N-6-ZGNR featuring a characteristic single point defect resulting from the cleavage of an m-xylene group ($V_s = 50$ mV, $I_t = 20$ pA). Arrow marks the position of a N-atom. Inset, chemical structure of the N-6-ZGNR segment imaged in (e). All STM images recorded at $T = 4$ K.

2.3.2 Stabilization of ZGNR Edges Through Substitutional Doping with N-Atoms

For any molecule the total energy of formation E_f is the energy required to break all covalent bonds in the molecule into the constituent isolated atoms and stripping all the electrons from the corresponding atomic nuclei. Conversely this corresponds to the energy released upon assembling any molecular structure from the constituent isolated atomic nuclei and electrons. E_f can be directly estimated using *ab initio* quantum mechanical calculations with reference to a chosen standard state of the atoms (often the most stable molecular species of the element). A comparison of the energy of formation ΔE_f between two molecular species requires the application of an imaginary reaction that converts reactants E_f(reactants) into products E_f(product) along with the associated release of energy ΔE_f.

$$\Delta E_f = \sum v E_f \text{ (products)} - \sum v E_f \text{ (reactants)} \qquad \text{(Equation 2-1)}$$

Below we show that the introduction of a superlattice of isoelectronic substitutional dopant atoms (1/6 of C_{sp2}–H groups replaced by N_{sp2} groups) along the edges of ZGNRs leads to an overall lowering of the energy of formation ΔE_f. Following the imaginary reaction

$$6\text{-ZGNR} + 2\,N \rightarrow N\text{-}6\text{-ZGNR} + 2\,C + 2\,H \qquad \text{(Equation 2-2)}$$

and substituting in Equation 2-1 we can determine the difference in the energy of formation ΔE_f.

$$\Delta E_f = \left(E_f(\text{N-6-ZGNR}) + 2\mu\!\left(C_{\text{graphene}}\right) + 2\mu\!\left(H_{\text{dihydrogen}}\right) \right) \\ - \left(E_f(\text{6-ZGNR}) + 2\mu\!\left(N_{\text{dinitrogen}}\right) \right) \qquad \text{(Equation 2-3)}$$

Using the same DFT functionals (LDA), cutoffs, and other parameters, we calculated the energy of formation at E_f at $T = 0$ K for the unit cell ($C_{70}N_2H_{10}$) of a nitrogen doped N-6-ZGNR ($E_f(\text{N-6-ZGNR})$) and the identical size unit cell ($C_{72}H_{12}$) of the analogous carbon 6-ZGNRs $E_f(\text{6-ZGNR})$. $\mu\!\left(C_{\text{graphite}}\right)$, $\mu\!\left(H_{\text{dihydrogen}}\right)$, and $\mu\!\left(N_{\text{dinitrogen}}\right)$ are the calculated chemical potential energies for carbon, hydrogen, and nitrogen atoms in the lowest energy conformation of the element, respectively.

Substituting in Equation S3 gives:

$$\Delta E_f = (-852.07689658 \text{ Ry} - 22.90528962 \text{ Ry} - 2.27558494 \text{ Ry}) \\ - (-837.46377334 \text{ Ry} - 39.78491647 \text{ Ry}) =$$

$$\Delta E_f = -0.00908134 \text{ Ry} = -0.124 \text{eV}$$

The introduction of a superlattice of substitutional N-atom dopants along the edges of 6-ZGNRs leads to an overall lowering of the energy of formation ΔE_f of N-6-ZGNRs by –0.124 eV per unit cell when compared to the structure of the all carbon 6-ZGNR.

2.3.3 Surface-Assisted Synthesis of N-ZGNRs

Guided by this idea we designed a molecular precursor for N-6-ZGNRs, the dibenzoacridine **1** (Fig. 2.3.1b). N-6-ZGNRs were grown on Au(111)/mica films by sublimation of **1** in UHV onto a

clean Au(111) surface held at 297 K. Figure 2.3.1c shows a constant-current scanning tunnelling microscopy (STM) topographic image of a sub-monolayer coverage of **1** on Au(111) at $T = 4$ K. Molecule-decorated surfaces were subsequently annealed at 475 K to induce the homolytic cleavage of C–Br bonds followed by a radical step-growth polymerization to give *poly*-**1**. Further annealing at 650 K induces a thermal cyclodehydrogenation that leads to the fully fused N-6-ZGNR backbone (Fig. 2.3.1d). STM topographic images reveal extended GNRs featuring atomically smooth zigzag edges with an apparent height and width of 0.23 nm ± 0.03 nm and 1.95 nm ± 0.05 nm, respectively, consistent with the formation of the fully conjugated N-6-ZGNR backbone (Fig. 2.3.2). To infer the position of the N-atoms along the edges of N-6-ZGNRs, we relied on the presence of a characteristic edge-defect, previously observed for all-carbon 6-ZGNRs. The excision defect depicted in Figure 1e emerges from the homolytic cleavage of a *m*-xylene group in *poly*-**1** during the thermal cyclodehydrogenation step and results in an indentation along the zigzag edge of the GNR (see inset in Fig. 2.3.1e). Based on the chemical structure of the molecular building block **1** we can unambiguously assign the position of a N-dopant atom at the opposing zigzag edge across from the defect site.
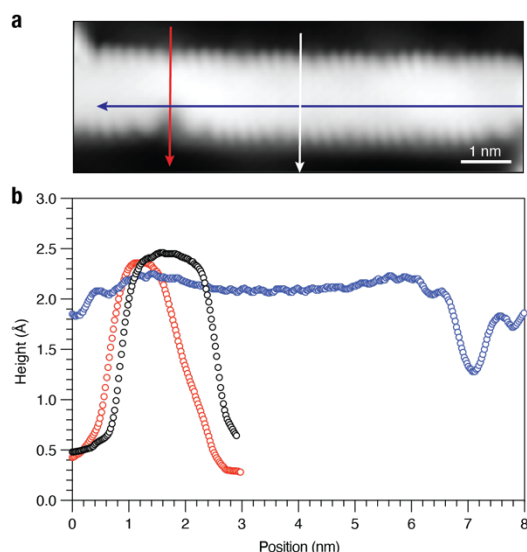
Figure 2.3.2 Height profiles of N-6-ZGNRs on Au(111) a, STM topographic image of N-6-ZGNR on Au(111) ($V_s = 50$ mV, $I_t = 20$ pA; CO-functionalized tip). **b,** Height profile recorded along the arrows marked in (a).

Topographic (Fig. 2a) and bond-resolved STM (BRSTM) images (Fig. 2.3.3b) using CO-functionalized STM tips were recorded on a fully cyclized segment of N-6-ZGNR featuring the same *m*-xylene deletion defect described above. While the topographic STM image (Fig. 2.3.3a) resolves the zigzag edge structure of N-6-ZGNRs and hints at a superlattice associated with the position of substitutional N-dopants, the BRSTM image (Fig. 2.3.3b) shows an alternating pattern of five bright lobes protruding from the edge of the N-6-ZGNRs (arrows in Fig. 2.3.3b) flanked on either side by indentations of darker contrast. Most notably the pattern on one zigzag edge is offset by ½ period from the opposite edge and is superimposable with the position of N-atoms derived from the analysis of *m*-xylene deletion defects. The enhanced signal in zero-bias dI/dV imaging suggests a strong hybridization of the Au(111) surface state with the spin-polarized edge states of the ribbon. dI/dV point spectra recorded along the edges of as grown N-6-ZGNRs show

only a broad featureless local density of states (LDOS) that cannot be assigned to the van Hove singularities of the valence band (VB) and conduction band (CB) edge (Fig. 2.3.9a).
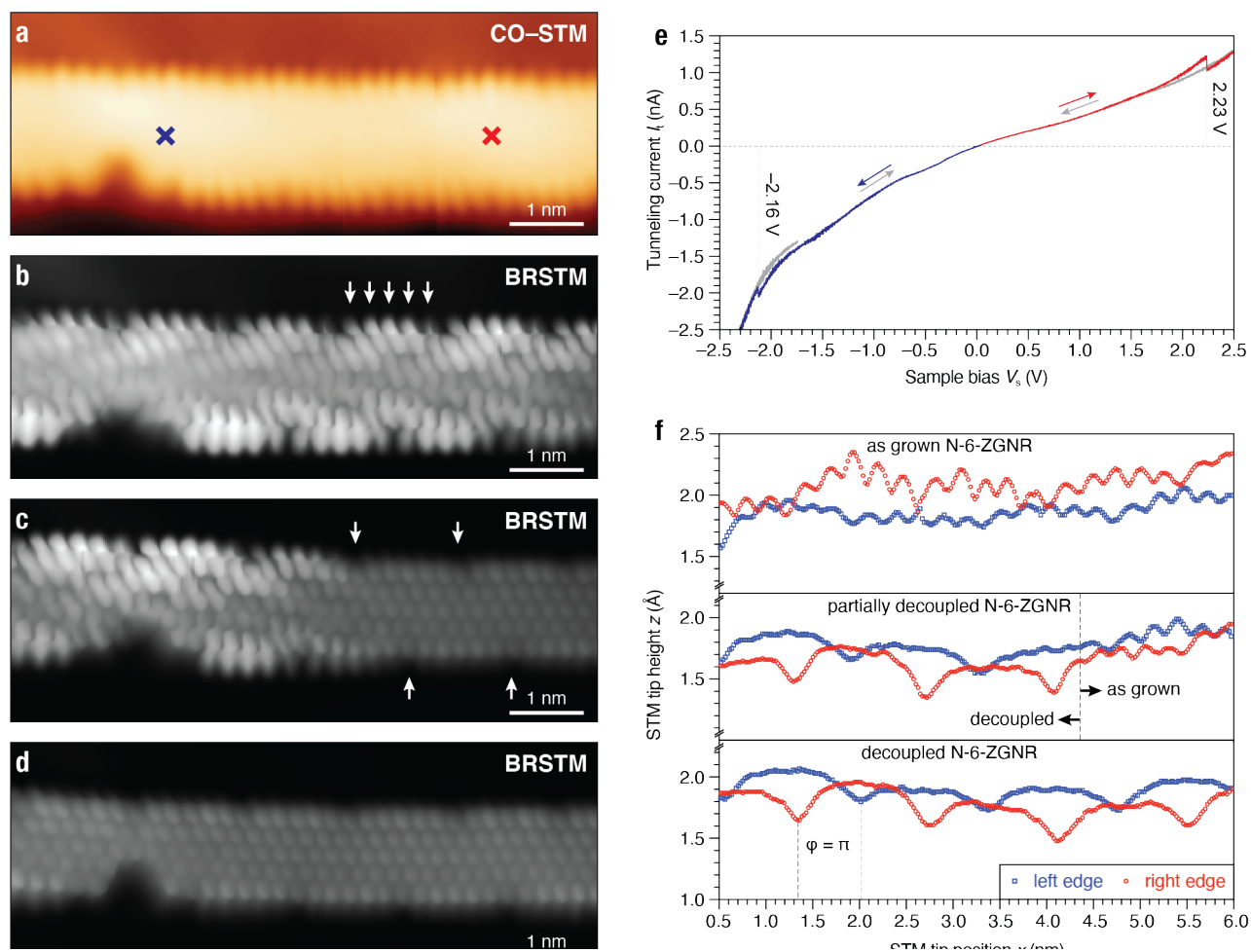
Figure 2.3.3 Tip-induced decoupling of magnetic edge states in N-6-ZGNRs from Au surface a, Topographic image of a fully cyclized N-6-ZGNR segment recorded with CO-functionalized STM tip. **b,** Constant-height BRSTM image of the N-6-ZGNR segment from **(a)**. Arrows mark the position of the five lobes associated with the C–H groups along the edges of the N-6-ZGNR. (V_s = 0 mV, modulation voltage V_{ac} = 11 mV, modulation frequency f = 455 Hz). **c,** Constant-height BRSTM image of N-6-ZGNR segment following tip-induced decoupling using a positive voltage sweep from V_s = 0.0 V to V_s = +2.5 V at the position marked by a red cross in **(a)** (V_s = 0 mV, V_{ac} = 11 mV, f = 455 Hz). Arrows mark the position of selected N-atoms along the edge of the N-6-ZGNR. **d,** BRSTM image of N-6-ZGNR segment following tip-induced decoupling using a negative voltage sweep from V_s = 0.0 V to V_s = –2.5 V at the position marked by a blue cross in **(a)** following decoupling in **(c)** (V_s = 0 mV, V_{ac} = 11 mV, f = 455 Hz). **e,** I_t/V_s plot showing the positive (red) and negative (blue) voltage sweeps used during the decoupling procedure. Return sweeps (gray) show the irreversible shift in the tunneling current I_t. **f,** STM height profiles showing the corrugation recorded along the left edge (blue squares) and the right edge (red circles) of (top) a representative as grown N-6-ZGNR, (middle) a partially decoupled N-6-ZGNR, and (bottom) a fully decoupled N-6-ZGNR (V_s = 50 mV, I_t = 20 pA; CO-functionalized tip). All STM experiments performed at T = 4 K.

To overcome this robust electronic coupling and to experimentally access the magnetic edge states of ZGNRs, we developed a SPM tip-induced decoupling protocol that disrupts the strong hybridization of the N-6-ZGNRs with the Au(111) surface state. When placing the STM tip ~ 4 Å above the center of a N-6-ZGNR (red cross in Fig. 2.3.3a) and sweeping the bias voltage from V_s = 0.00 V to V_s = +2.50 V, a discontinuous drop (ΔI_t^+ = 0.16 nA) in the tunnelling current can be observed at a bias of V_s^+ = +2.23 ± 0.05 V (Fig. 2.3.2e, Fig. 2.3.4). The abrupt decrease in the tunnelling current suggests an electronic decoupling of the GNR from the underlying Au(111) substrate. Subsequent bias sweeps from V_s = 0.00 V to +2.50 V near the position of the red cross yield no further change in the tunnelling current.
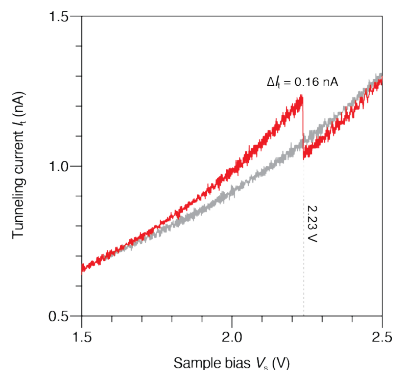
Figure 2.3.4 Tip induced decoupling of N-6-ZGNRs I_t/V_s plot showing in red the positive voltage sweep (V_s = +1.50 V to V_s = +2.50 V) used during the decoupling procedure. The respective return sweep (V_s = +2.50 V to V_s = +1.50 V) is depicted in gray and shows the irreversible shift in the tunneling current I_t.

STM imaging of the same N-6-ZGNR segment following tip-induced decoupling reveals a local change in the constant-height dI/dV map (Fig 2.3.5).
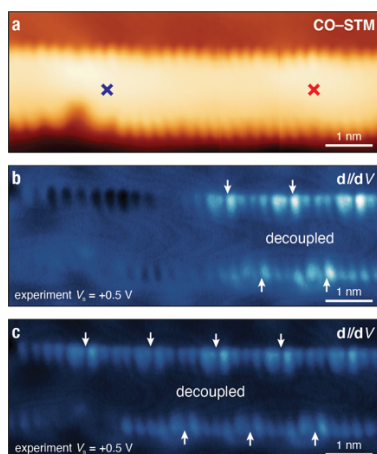
Figure 2.3.5 Tip-induced decoupling of magnetic edge states in N-6-ZGNRs a, Topographic image of a fully cyclized N-6-ZGNR segment recorded with CO-functionalized STM tip. **b,** Constant-current dI/dV map recorded at a voltage bias of V_s = +0.5 V of N-6-ZGNR segment following tip-induced decoupling using a positive voltage sweep from V_s = 0.0 V to V_s = +2.5 V at the position marked by a red cross in **(a)** (V_{ac} = 11 mV, I_t = 200 pA, f = 455 Hz, CO functionalized tip). **c,** Constant-current dI/dV map recorded at a voltage bias of V_s = +0.5 V of N-6-ZGNR segment following tip-induced decoupling using a negative voltage sweep from V_s = 0.0 V to V_s = –2.5 V at the position marked by a blue cross in **(a)** (V_{ac} = 11 mV, I_t = 200 pA, f = 455 Hz, CO functionalized tip). Arrows mark the position of selected N-atoms along the edge of the N-6-ZGNR.

In the BRSTM image (Fig. 2.3.3), the immediate area of the ribbon in the vicinity of the STM tip during the decoupling step (1–2 nm surrounding the position of the red cross) is clearly resolved and shows the distinctive structure of the N-6-ZGNR backbone as well as the characteristic pattern of N-atoms along both zigzag edges (arrows in Fig. 2.3.3c; N-atoms appear with a darker contrast when compared to the C–H groups). The same irreversible decoupling event can be observed by applying a negative bias. Sweeping the bias voltage from $V_s = 0.00$ V to $V_s = -2.50$ V at the position marked by a blue cross in Figure 2.3.3a, reveals a comparable drop in the tunnelling current at V_s^- $= -2.16 \pm 0.05$ V ($\Delta I_t^- = 0.15$ nA). The resulting BRSTM image (Fig. 2.3.3d) shows the bond-resolved structure of the N-6-ZGNR backbone along the entire length of the ribbon. Neighboring ribbons that are not covalently fused with the N-6-ZGNR subjected to the decoupling protocol remain unaffected by this process (Extended Data Fig. 2.3.6).
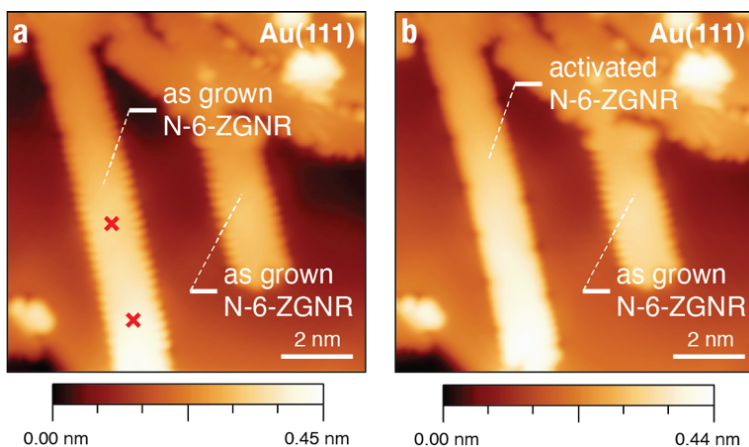
Figure 2.3.6 STM Images of partially decoupled N-6-ZGNRs a, STM topographic image of as-grown N-6-ZGNRs with CO-modified tip. **b,** STM topographic image of N-6-ZGNR after decoupling the GNR on the left. ($V_s = 50$ mV, $I_t = 20$ pA)

The mechanism of this electronic decoupling can be rationalized through a tip induced mechanical relaxation of the adsorption geometry of N-6-ZGNRs on the Au(111) surface. STM height profiles recorded along opposing zigzag edges of as grown N-6-ZGNRs (Fig. 2.3.3f, top) are characterized by irregular π-bonding interaction patterns between the Au(111) surface layer and C- and N-atoms lining the edges of the ribbon (Fig. 2.3.7). Local application of our STM tip-induced decoupling protocol reversibly breaks C–Au and N–Au π-bonds allowing the backbone of N-6-ZGNRs to adopt a strain-free lower energy adsorption geometry that is epitaxial with respect to the Au(111) surface (Fig. 2.3.7). STM line profiles (Fig. 2.3.3f, middle and bottom) of decoupled N-6-ZGNRs show that this global minimum adsorption geometry is characterized by a height modulation ($\Delta z \sim 0.3$ Å) along the edges of the ribbon that places each N-atom closest to the Au(111) surface. The corrugation of opposing zigzag edges in decoupled N-6-ZGNRs is offset by ½ period ($\varphi = \pi$) to fall in registry with the atomic spacing of the Au(111) surface layer (lattice constant difference N-6-ZGNRs and Au(111) < 1.8%, see Fig. 2.37).
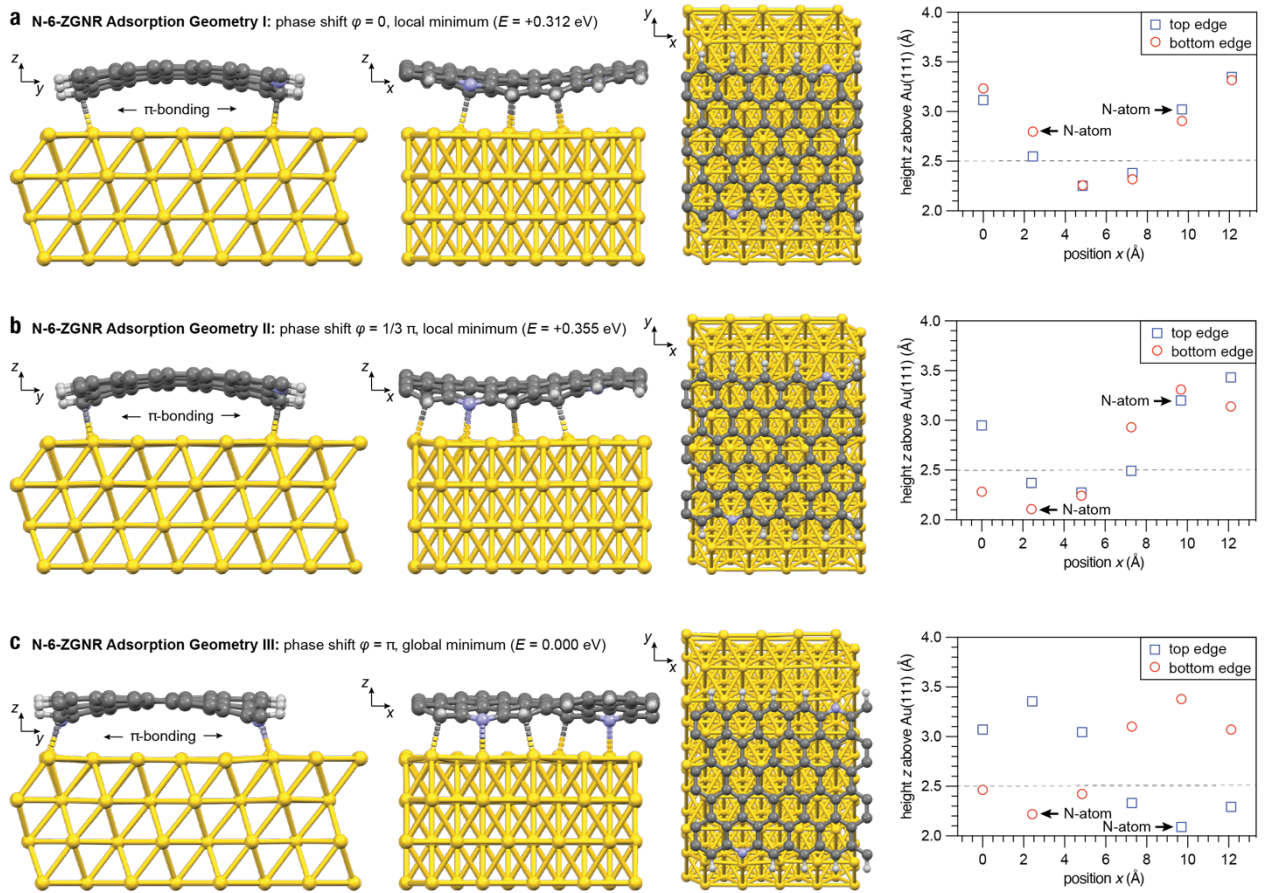
Figure 2.3.7 Calculated adsorption geometries of N-6-ZGNRs on Au(111) a, Local minimum Adsorption Geometry I (E = +0.312 eV). Four C-atoms per unit cell interact through π-bonding (< 2.5 Å) with the Au(111) surface. The corrugation on opposing zigzag edges is in phase (φ = 0). **b,** Local minimum Adsorption Geometry II (E = +0.355 eV). Five C-atoms and one N-atom per unit cell interact through π-bonding (< 2.5 Å) with the Au(111) surface. The corrugation on opposing zigzag edges is phase shifted by φ = 1/3π. **c,** Global minimum Adsorption Geometry III (E = +0.000 eV). Four C-atoms and two N-atoms per unit cell interact through π-bonding (< 2.5 Å) with the Au(111) surface. The corrugation on opposing zigzag edges is phase shifted by φ = π. All calculations performed with ultrasoft pseudopotentials and 40 Ry cut-offs.

2.3.4 Electronic Structure of N-ZGNRs

The local electronic structure of surface-decoupled N-6-ZGNRs was characterized by dI/dV point spectroscopy. A typical dI/dV point spectrum recorded along the edge of a N-6-ZGNRs (> 3 nm from either end of the ribbon; see inset in Fig. 2.3.9a) shows two prominent electronic states. A sharp peak centered at V_s = –0.30 ± 0.02 V and a broader feature centered at V_s = +0.50 ± 0.05 V can be assigned to the N-6-ZGNR VB and CB edge, respectively. Substitution of C–H groups with the more electronegative N-atoms not only leads to an overall thermodynamic stabilization of N-6-ZGNRs but a significant reduction of the band gap ΔE_{exp} = 0.80 ± 0.05 eV when compared to a pristine all-carbon 6-ZGNRs (ΔE_{exp} = 1.5 eV) (Fig. 2.3.8).
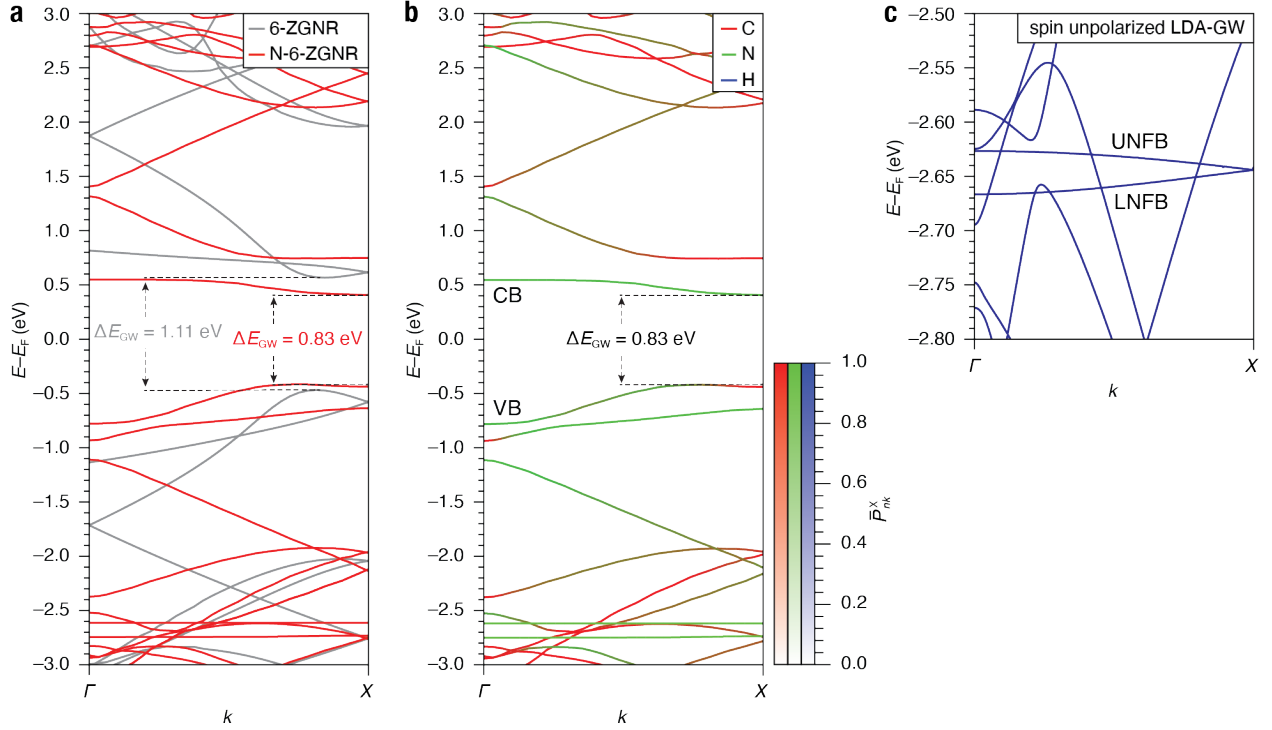
Figure 2.3.8 Electronic Structure of 6-ZGNR and N-6-ZGNRs a, LDSA-GW band structure of freestanding 6-ZGNR (gray) and N-6-ZGNR (red) calculated using the same dimension unit cell. **b,** LDSA-GW band structure of a freestanding N-6-ZGNR. The color code shows contributions from C-atoms, N-atoms, and H-atoms to the normalized atomic wavefunction of each state. The number of $p_z + \sigma$ orbitals for C, N, and H atoms are 280, 8, and 10 per unit cell, respectively. The wavefunction projection of the state in the nth band and at wavevector k to the C, N, and H atoms is described by by P_{nk}^C, P_{nk}^N, and P_{nk}^H, respectively. We define the quantities $\bar{P}_{nk}^C$, $\bar{P}_{nk}^B$, and $\bar{P}_{nk}^N$ as the wavefunction projection on the C, N, and H atoms per atom in the unit cell: $\bar{P}_{nk}^C = \frac{P_{nk}^C}{280}$, $\bar{P}_{nk}^N = \frac{P_{nk}^N}{8}$, $\bar{P}_{nk}^H = \frac{P_{nk}^H}{10}$. **c,** Spin unpolarized LDA-GW band structure of a freestanding N-6-ZGNR. In the spin unpolarized calculation the UNFB and LNFB form a narrow metallic band with a width smaller than 50 meV.

dI/dV imaging of the spatial distribution of the N-6-ZGNR LDOS at energies close to the CB edge (Fig. 2.3.9b) shows the largest contrast along the zigzag edge C–H groups immediately flanking the position of N-atom dopants while the intensity decreases toward the center of the N-6-ZGNR backbone. dI/dV maps recorded at an imaging bias of –0.30 V reveal the LDOS associated with the VB state (Fig. 2.3.9b) evenly distributed over the C–H groups lining the zigzag edges. Both dI/dV maps of the CB and VB edge states show slightly weaker contrast at the position of the N-atom dopants, a prominent feature that creates the illusion of isolated pentacene-like fragments lining the edges of the N-6-ZGNR. Rather than invoking a localization of the extended CB and VB edge states, the difference in contrast between C–H groups and N-atoms is a consequence of the subtle modulation of the extended edge state by the dopant superlattice along with the difference in height associated with the preferred adsorption geometry of decoupled N-6-ZGNRs.
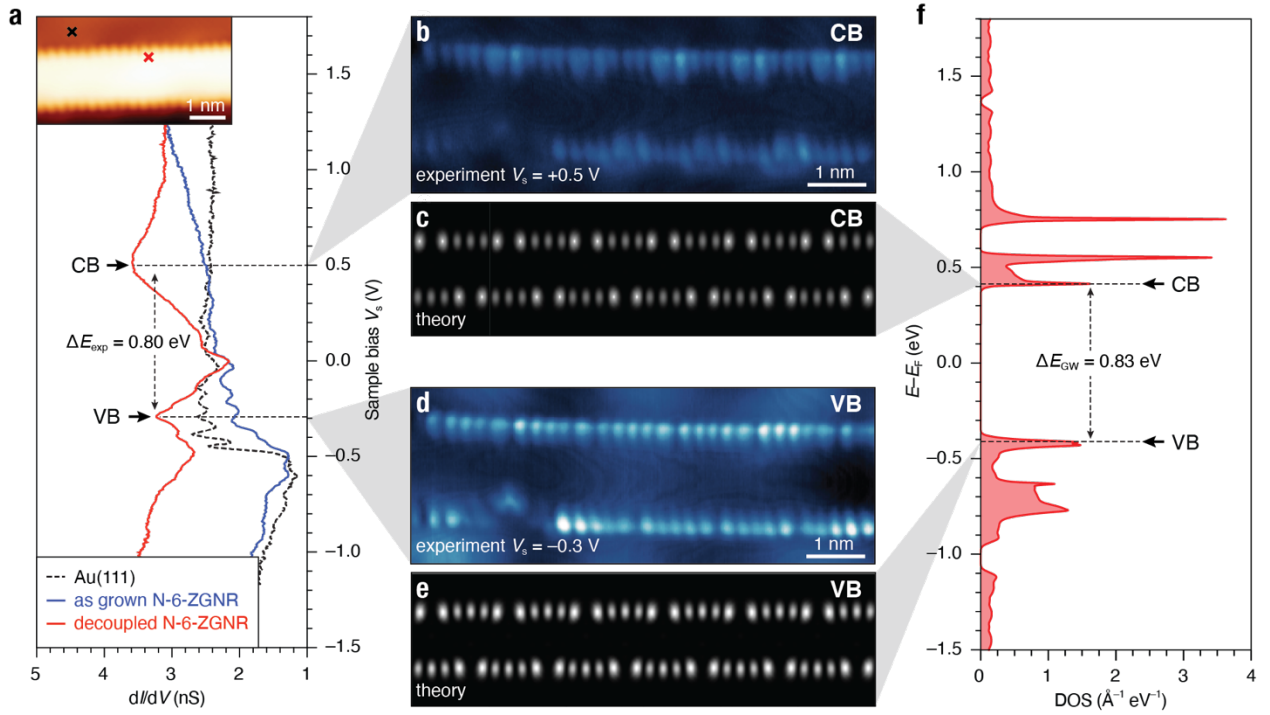
Figure 2.3.9 Electronic structure of N-6-ZGNR a, dI/dV point spectroscopy of as grown (blue) and decoupled (red) N-6-ZGNR/Au(111) at the position marked in the inset (red cross, imaging: V_s = 50 mV, I_t = 20 pA, CO functionalized tip); Au(111) reference spectrum (black) (spectroscopy: V_{ac} = 11 mV, f = 455 Hz). **b,** Constant-current dI/dV map recorded at a voltage bias of V_s = +0.5 V (V_{ac} = 11 mV, I_t = 200 pA, f = 455 Hz, CO functionalized tip). **c,** Calculated GW LDOS at the conduction band (CB) edge. **d,** Constant-current dI/dV map recorded at a voltage bias of V_s = –0.3 V (V_{ac} = 11 mV, I_t = 170 pA, f = 455 Hz, CO functionalized tip). **e,** Calculated GW LDOS at the valence band (VB) edge. **f,** Calculated GW DOS for a N-6-ZGNR (spectrum broadened by 4 meV Gaussian). All STM experiments were performed at T = 4 K. Theoretical LDOS are sampled at a height of 4 Å above the atomic plane of the N-6-ZGNR.

Experimental results are in excellent agreement with theoretical calculations based on *ab initio* density functional theory (DFT) within the local spin density approximation (LSDA)[90], and *ab initio* GW calculations, which includes the important self-energy corrections to the quasiparticle excitations measured in STS experiments. First-principles results provide quantitative evidence that the SPM tip-induced decoupling has resulted in a full recovery of the intrinsic magnetic edge states (both in energy and wavefunction) of N-6-ZGNRs. Figures 2.3.9c,e show the calculated LDOS maps at a distance of 4 Å above the plane of the freestanding N-6-ZGNR at energies corresponding to the CB and VB edges. The characteristic pattern and relative contrast of protrusions lining the zigzag edges of N-6-ZGNRs seen in the experimental dI/dV maps of CB and VB states (Figs. 2.3.9b,d) are faithfully reproduced in the corresponding GW LDOS maps (Figs. 2.3.9c,e). The GW band structure and the corresponding density of states (DOS) are depicted in Figures 2.3.10 and 2.3.9f, respectively. The quasiparticle bandgap ΔE_{GW} = 0.83 eV is consistent with the experimental gap ΔE_{exp} = 0.80 ± 0.05 eV derived from STS. The agreement between experimental dI/dV maps and the theoretically predicted LDOS, in conjunction with the quantitative match between the measured and calculated quasiparticle bandgap, strongly

corroborates the electronic decoupling of N-6-ZGNRs from the underlying metallic Au(111) substrate.
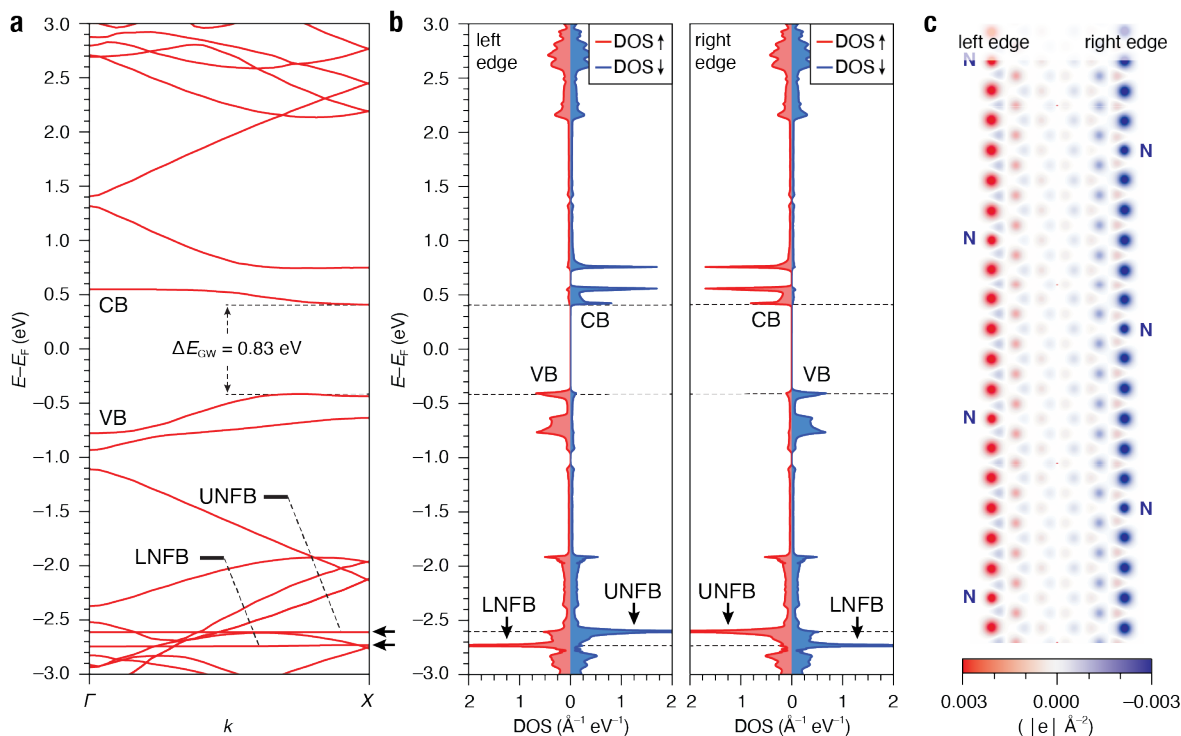
Figure 2.3.10 Band structure and spatial distribution of spin-ordered edge states in N-6-ZGNRs a, GW band structure of a freestanding N-6-ZGNR. Upper (UNFB) and lower (LNFB) nitrogen flat bands are highlighted by arrows. **b,** GW LDOS of up (red) and down (blue) spin integrated over the left half and right half of a N-6-ZGNR as shown in (C). **c,** Spatial distribution of the areal spin density distribution difference between up and down spin $(\rho_\uparrow(r) - \rho_\downarrow(r))$. The areal density is the density integrated in the direction out of the GNR atomic plane.

2.3.5 Theoretical Electronic Structure of N-ZGNRs

Ab initio calculations on N-6-ZGNR show that an antiferromagnetic alignment of spins (across the ribbon width) between ferromagnetically-ordered edge states (e.g., as shown in Fig. 2.3.10c — left edge ↑↑, right edge ↓↓; the absolute spin orientation direction is arbitrary due to negligibly small spin-orbit interactions) is favored as the ground state over a spatially spin-unpolarized configuration. The spin-polarization energy is 16 meV per edge atom, indicating large magnetic interaction energies. The antiferromagnetic spin configuration in the ground state is consistent with Lieb's theorem[89] for interacting electrons on a bipartite lattice. The GW LDOS of up (↑) and down (↓) spin integrated over the left and right half of a N-6-ZGNR (Fig. 2.3.10b) shows the expected spatial distribution of the two spin species at the bottom CBs and top VBs. Besides the obvious polarization of the frontier bands, calculations predict two low-lying highly spatially localized spin-polarized states at $E–E_F = –2.60$ eV and $E–E_F = –2.72$ eV, respectively. These highly localized flat-band states are formed by the lone-pair orbitals of trigonal planar N-atoms lining the edges of N-6-ZGNRs. The two bands (which are degenerate in spin-unpolarized calculations, Fig. 2.3.8) split into an upper nitrogen flat band (UNFB; –2.60 eV) and a lower nitrogen flat band (LNFB; –

2.72 eV) due to the exchange interaction of the lone-pair electron with the spin-polarized π-electrons, which have a net spin population of opposite sign along the two edges. The exchange field generated by the ferromagnetic ordering on either N-6-ZGNR edge (corresponding to an effective Zeeman field of $B_{calc.} \sim 1000$ T) favors a local spin orientation that is parallel to the local exchange field. The LNFB and UNFB with spatial spin polarization in the same (left edge $\uparrow$, right edge $\downarrow$) and opposite (left edge $\downarrow$, right edge $\uparrow$) direction as the magnetic ordering of the N-6-ZGNR edges are lowered and raised in energy, respectively, leading to a splitting of the flat N-lone-pair bands.
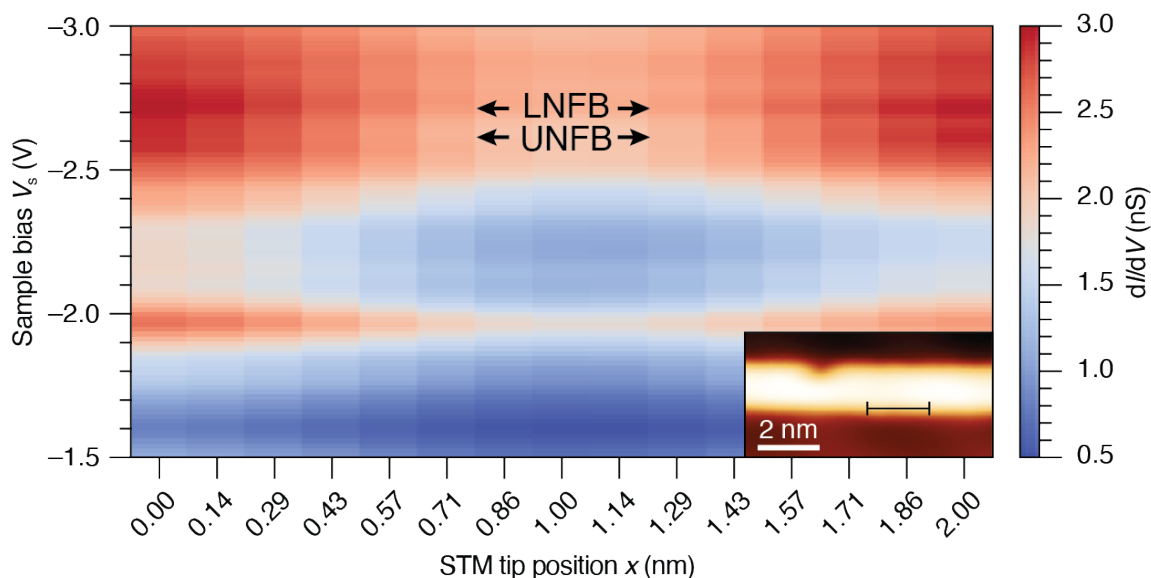
Figure 2.3.11 dI/dV point spectroscopy of spin split low-lying nitrogen dopant flat band states Waterfall plot of dI/dV point spectra collected along a line marked in the inset long the edge of a N-6-ZGNR ($V_{ac} = 11$ mV, $f = 455$ Hz). When the STM tip is located immediately above the position of a nitrogen dopant atom ($x = 0.28$ nm, and $x = 1.72$ nm) the dI/dV point spectra show two characteristic peaks centered at $V_s = -2.60 \pm 0.02$ V and $V_s = -2.70 \pm 0.02$ V, corresponding to the UNFB and LNFB states, respectively.

To validate the theoretical predictions, we recorded dI/dV point spectra along the edge of a fully decoupled N-6-ZGNR at a bias from $V_s = -1.50$ V to $V_s = -3.00$ V (Fig. 2.3.11). Only when the STM tip is located immediately above the position of a N-atom (Fig. 2.3.12), the dI/dV point spectra show two characteristic peaks centered at $V_s = -2.60 \pm 0.02$ V and $V_s = -2.70 \pm 0.02$ V, corresponding to the UNFB and LNFB states, respectively. dI/dV imaging of the spatial distribution of the LDOS at energies close to the UNFB and LNFB reveals a featureless ZGNR backbone that shows enhanced contrast at the edge of the ribbon at the precise position of the N-dopant atoms (Figs. 2.3.12b,d). The distinctive patterns in the dI/dV maps faithfully reproduce the calculated UNFB and LNFB LDOS maps (Figs. 2.3.12c,e) further corroborating the assignment of UNFB and LNFB to the spin split N-lone-pair bands.
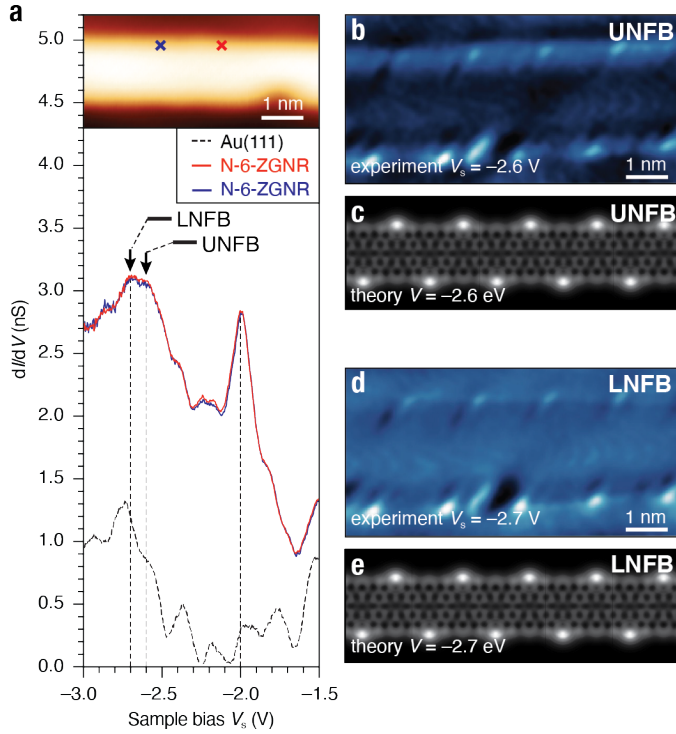
Figure 2.3.12 Spin splitting of nitrogen flat band states (NFB) of sp^2 lone-pair orbitals in N-6-ZGNRs
a, dI/dV point spectroscopy of decoupled N-6-ZGNR/Au(111) at the position of two N-atoms marked in the inset (red and blue cross, imaging: V_s = 300 mV, I_t = 20 pA); Au(111) reference spectrum (black) (spectroscopy: V_{ac} = 11 mV, f = 455 Hz). **b,** Constant-current dI/dV map of UNFB recorded at a voltage bias of V_s = –2.6 V (V_{ac} = 11 mV, I_t = 2 nA, f = 455 Hz). **c** Calculated GW LDOS integrated in a bias range ΔV = 200 mV around the UNFB. **d,** Constant-current dI/dV map of LNFB recorded at a voltage bias of V_s = –2.7 V (V_{ac} = 11 mV, I_t = 2 nA, f = 455 Hz). **e,** Calculated GW LDOS integrated in a bias range ΔV = 200 mV around the LNFB.

While the longitudinal modulation imposed by a substitutional N-dopant superlattice represents a universal strategy to thermodynamically stabilize and decouple the exotic magnetic edge states in ZGNRs, the isoelectronic substitution of a sixth of the C–H groups along the zigzag edge with N-atoms does not deteriorate the spin polarization and the edge magnetism in ZGNRs. Calculated spatial distribution of electron spin polarization in the ground state (Fig. 2.3.10c) reveals that the magnetization on one N-atom in N-6-ZGNRs amounts to ~80% of the expected magnetization of a C-atom along the edge of a pristine 6-ZGNR, indicating almost unaltered magnetic edge states. The experimentally observed large exchange splitting $\Delta E_{(STS)}$ = 100 ± 30 meV of the low-lying N-lone-pair dopant flat bands by the ferromagnetically ordered spins along the edge of N-6-ZGNRs implies that the two electrons occupying the N-lone-pair experience an effective local exchange field B_{eff} = 850 ± 250 T, consistent with the theoretical prediction. Therefore, the isoelectronic substitution of C–H groups with N-atom dopants does not disrupt the intrinsic magnetization emerging from the spin-polarized edge states in ZGNRs.

The results here provide a general strategy to stabilize the chemically reactive edges of zigzag nanographene without sacrificing the emergent spin degree of freedom and provide direct experimental evidence for the antiferromagnetic coupling of the ferromagnetically ordered edge

states on opposite edges of ZGNRs. This approach creates a path for the development of atomically precise graphene-based high-speed low-power spin-logic devices for data storage and information processing.

2.3.6   Surface-Assisted synthesis of 2N-ZGNRs

Looking at the precursor **1** that resulted in a successful N-6-ZGNR synthesis, the most logical follow-up experiment would double the density of nitrogen dopants by placing an additional nitrogen opposite the acridinic nitrogen in the original precursor. Here the replacement of every third C–H group along the zigzag edge of a 6-ZGNR by a N-atom would lead to the 2N-6-ZGNR structure depicted in Figure 2.3.13. Once again, each trigonal planar N-atom contributes the same number of electrons (one electron in a half-filled p_z-orbital) to the extended π-system of the 2N-6-ZGNR as the trigonal planar C–H groups they replace. Theoretical calculations based on *ab initio* DFT within the LSDA framework predict a similar band structure to that of the N-6-ZGNR (Figure 2.3.13). The magnitude of the band gap is roughly the same for the N-6-ZGNR and the presence of a UNFB and LNFB are still expected to appear. The second nitrogen additionally serves to lower the overall Fermi energy level and leads to an even further thermodynamic stabilization when compared to the 6-ZGNR. Moreover, the lower overall Fermi energy level is expected to decrease the overall reactivity of the zigzag edge as it pertains to oxidative degradation.
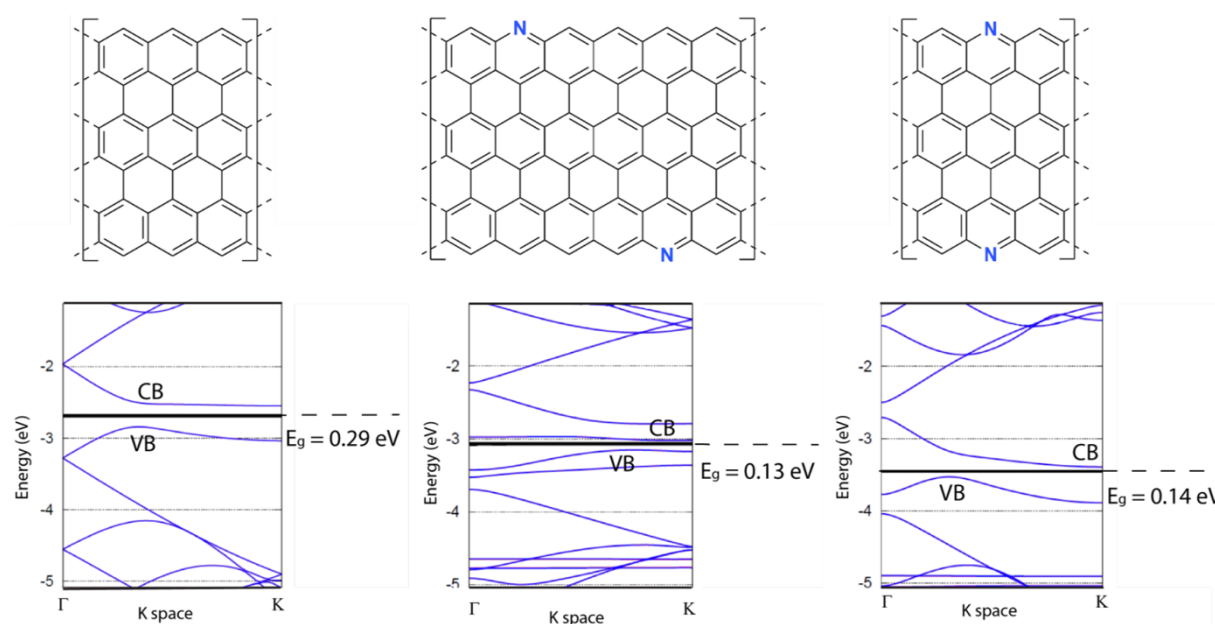
Figure 2.3.13 Theoretical Electronic Structure of ZGNRs

Initial attempts at synthesizing the 2N-6-ZGNR followed the sublimation of precursor **2** from a Knudsen cell evaporator under UHV conditions onto an Au(111) substrate held at 25 °C. STM topographic images of the precursor after deposition show a similar structure to precursor **1** which successfully formed the N-6-ZGNR. Unfortunately, after annealing the substrate to 350 °C to induce polymerization and cyclodehydrogenation, there is no evidence of 2N-6-ZGNR formation. In fact, there is no evidence of polymerization as there appear to be no extended linear

structures on the surface. Careful analysis of the bond dissociation energies (BDEs) associated with the lutidine wing that contributes the additional nitrogen helps elucidate the reason for the this failed growth attempt. The BDE for an Ar–Br bond (80 kcal/mol) is extremely similar to the BDE for a C–H bond in 2-methylpyridine (88 kcal/mol)[91]. This suggests C-H bonds in 2-methylpyridine are also cleaving during the polymerization step which significantly increases the likelihood of deleterious side reactions that would lead to the branching shown in Figure 2.3.14B. To circumvent this problem, an iodinated version of **2** was used because the BDE of an Ar–I bond (~ 65 kcal/mol) should allow sufficient separation for polymerization. Figure 2.3.14c shows the Au(111) surface following the deposition of the iodinated precursor and networks of iodine are clearly visible on the surface as expected. Slowly annealing the substrate to 350 °C yields mostly bundled, short GNRs, but there is evidence of ~ 10 nm long 2N-6-ZGNRs. Higher resolution imaging is needed to confirm the 2N-6-ZGNR before attempting to do any electronic structure characterization.
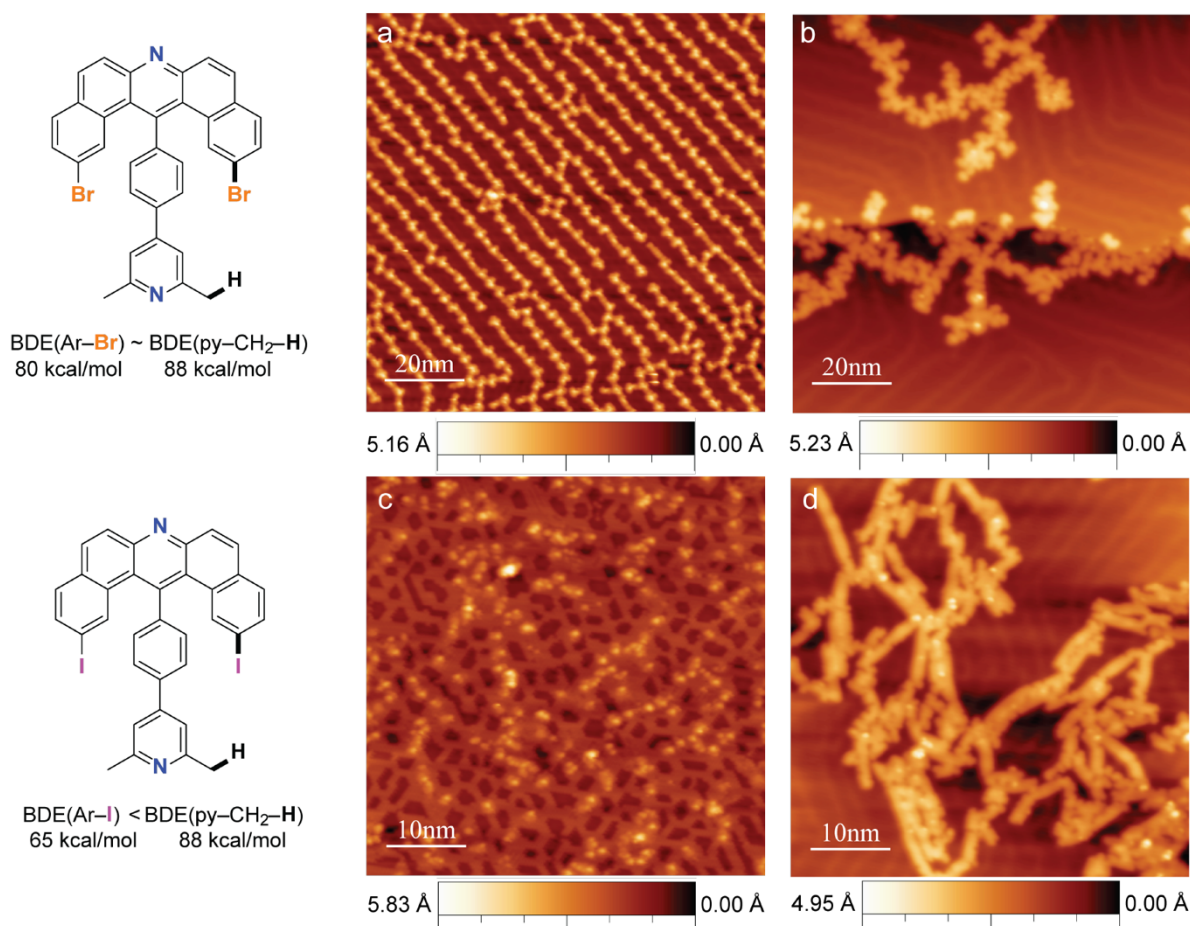
Figure 2.3.14 Bottom-up Synthesis of 2N-6-ZGNR a, STM topographic image of Brominated 2N-6-ZGNR on Au(111) after deposition at 24 °C (V_s = 50 mV, I_t = 20 pA) **b,** STM topographic image of sample from panel a) after annealing to 350 °C (V_s = 50 mV, I_t = 20 pA) **c,** STM topographic image of iodinated 2N-6-ZGNR on Au(111) after deposition at 24 °C (V_s = 50 mV, I_t = 20 pA) **d,** STM topographic image of sample from panel c) after annealing to 350 °C (V_s = 50 mV, I_t = 20 pA)

2.4 Summary and Future Outlook

In this chapter I have discussed the synthesis of edge-modified ZGNRs that reduce the ZGNR-substrate interaction enough to permit characterization on the growth substrate. I report the first attempts at synthesizing atomically defined AGNR/ZGNR heterojunctions, as well as the first attempts at growing nanoporous graphene with pores containing both armchair and zigzag edges. Future work on this project should use Ag(111) to synthesize the nanoporous graphene as there is literature precedent suggesting Ag(111) is the ideal substrate to template 2D network growth. Furthermore, triple deposition experiments should be conducted with the linker molecule, DBBA, and the phenyl-substituted U-monomer to unambiguously determine the efficacy of the linker molecule.

The second half of this chapter focuses on the synthesis of ZGNRs with a superlattice of substitutional nitrogen dopants. Herein, I describe the measurement of a Zeeman-like spin splitting in low-lying nitrogen lone pair flat bands in an N-6-ZGNR. The splitting is induced by the spin-polarized ferromagnetic edge states of ZGNRs and provides the first direct confirmation of their expected magnetic ordering. Additionally, I present attempts to synthesize a 2N-6-ZGNR with similar properties to the N-6-ZGNR. The 2N-6-ZGNR requires an iodinated precursor to polymerize, and future experiments should focus on finding the growth conditions that optimize the GNR length for electronic structure characterization.

Chapter 3: Band Gap Engineering of Low Band Gap Graphene Nanoribbons

Parts of this chapter have been published in: "Orbitally Matched Edge-Doping in Graphene Nanoribbons" Durr, R.A.; Haberer, D.; Lee, Y.L.; Blackwell, R.E.; Kalayjyian, A.M.; Marangoni, T.; Ihm, J.; Louie, S.G; Fischer, F.R. *J. Am. Chem. Soc.* **140**, (2018)

3.1   Introduction

This chapter will discuss various strategies to reduce the band gap in GNRs for applications in high-performance FET devices. GNRs represent a particularly interesting platform for high-performance FET devices because they have a band gap that is highly tunable. For example, it is possible to synthesize metallic GNRs, as well as GNRs with band gaps upwards of 4 eV. This wide range for the same material allows for the possibility of creating all-carbon FET devices and work towards the synthesis of metallic GNRs will be discussed in depth in a later Chapter. At present, all GNR FET devices suffer from a parasitic contact resistance stemming from the large Schottky barrier between the metallic leads and the semiconducting GNR. Transport through the Schottky barrier is dominated by tunneling as evidenced by the lack of temperature dependence when measuring the current-voltage characteristics in vacuum. To increase the current and begin the realization of high-performance FETs, it is necessary to improve transmission through the Schottky barrier. One potential method to address this problem is to synthesize GNRs with a band gap approaching that of Si (~1.1 eV) and study the intrinsic transport behavior in GNRs. Band gap engineering can be readily achieved via controlled modification of critical parameters like width, edge topology, and dopant position/density. In this chapter one section will be dedicated to each of the aforementioned parameters.

The first section in this chapter will address the synthesis of AGNRs in the low band gap $3p+2$ family. GNRs in this family have been notoriously difficult to synthesize even though they offer the greatest potential for FET applications. In this section I will report the first bottom-up synthesis of an 11-atom wide GNR, a long sought-after structure within our own research group. Moreover, I will discuss electronic characterization and MAD transfer (Section1.2.4) of the 11-AGNR to synthesize GNRs that are of sufficient length for FET applications.

The second section of this chapter will be devoted to band gap engineering via edge topology. Here I will address the design and synthesis of a GNR with armchair and zigzag edges from two molecular precursors that differ only by the position of methyl groups. The different precursors give insight into the design principles for bottom-up GNR growth on metallic substrate.

The final section of this chapter will focus on edge dopant atoms in chevron GNRs. The electronic structure of chevron GNRs with oxygen, nitrogen, and sulfur dopant atoms will be compared to the pristine all-carbon chevron GNRs to determine the effect of various dopant atoms on the band structure.

3.2   Synthesis of 3*p*+2 Armchair GNRs

3.2.1   Introduction

One crucial factor that limits the performance of FET devices currently fabricated from surface-synthesized GNRs is the high contact resistance resulting from the large Schottky barrier between the metallic contacts and the semiconducting GNRs[92]. A Schottky barrier arises in metal-semiconductor junctions as a consequence of a misalignment between the Fermi level of the metal and the band edge in the semiconductor. In GNR FETs, this misalignment is a result of the relatively wide quasiparticle bandgaps in GNRs that have been used to date (3.7 eV for 7-AGNRs[93], 2.10 eV for 9-AGNRs[23], 2.35 eV for 5-AGNRs[23]). For that reason, it is imperative to synthesize narrow band gap GNRs (< 1.5 eV) to reduce the effect of the Schottky barrier. An additional challenge stems from the fact that the bottom-up synthesized GNRs are grown on metallic substrates and must be transferred to dielectric substrates to build FET devices. GNRs must be stable under the somewhat harsh conditions used in the wet transfer process, severely limiting the possible GNRs due to the high reactivity of zigzag edges. Moreover, the ideal length for GNRs used in FET devices is upwards of 20 nm because GNRs must bridge the channel between the source and drain electrodes.

Therefore, armchair GNRs in the 3*p*+2 family offer the most promise for high-performance FET devices. To date, the 5-AGNR has been synthesized from halogenated perylene precursors, although its quasiparticle band gap is ~1.75 eV making it a less than desirable candidate for FET applications. As mentioned previously, the band gap of AGNRs within the same family has an inverse relationship with width making the 8-AGNR, 11-AGNR, and 17-AGNR particularly desirable structures. Synthesis of the 8-AGNR and 11-AGNR has remained elusive, but there is a single study showing the synthesis of a 17-AGNR (predicted quasiparticle band gap 0.63 eV)[29]. However, the length of the 17-AGNRs is far too short for device fabrication. In the following section I will discuss progress in bottom-up synthesis of 11-AGNRs for high-performance FETs.

3.2.2   Bottom-Up Synthesis of 11-AGNR on Ag(100)

At the time of this writing there have been no publications reporting the synthesis of 11-AGNRs. This GNR has been highly sought after in the Fischer group with multiple generations attempting to find a precursor that would ultimately lead to the desired structure. In my research, the first attempt at synthesizing the 11-AGNR was conducted using 13,13'-dibromo-6,6'-bianthrylpentacene (**3-1** in Figure 3.2.1). When **3-1** is sublimed under UHV conditions onto a Au(111) substrate and subsequently annealed, there is no evidence of polymerization. Instead, the molecule cyclizes at a temperature below the debromination temperature to yield peripentacene. Therefore, I attempted to deposit **3-1** on a more reactive substrate to induce polymerization by lowering the dehalogenation temperature while keeping the cyclodehydrogenation roughly constant. It is well-established that the <100> family of planes have a larger number of dangling bonds leading to a higher reactivity when compared to those in the <111> family. For this reason, **3-1** was sublimed under UHV conditions onto a Ag(100) substrate that was held at 25 °C (Figure 3.2.1B). Figure 3.2.1C shows that the Ag(100) surface after annealing to 350 °C contains

predominately peripentacene, but there are extended linear structures that are not seen on Au(111). However, careful analysis shows an apparent width of ~1 nm which is too small for the 11-AGNR. The apparent width instead corresponds to chiral(5,1) GNRs implying that polymerization occurs at the 3,3' and 9,9' positions after a radical migration. A similar polymerization occurs to yield chiral(3,1) GNRs when DBBA is deposited on Cu(111) because of the highly reactive Cu surface. Further attempts to polymerize **3-1** on Cu(111) did not result in any discernible structures.
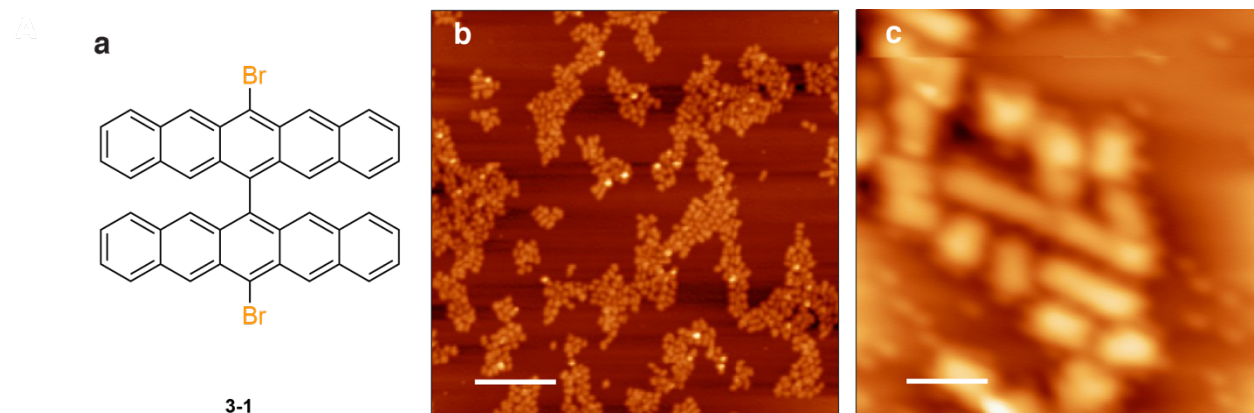
Figure 3.2.1 Bottom-Up Synthesis of Chiral(5,1) GNRs a) Chemical Structure of DBP monomer **b)** STM topographic image of monomer **3-1** after annealing to 350 °C (V_s = 50 mV, I_t = 20 pA, scale bar: 10 nm) **c)** Zoom-in image of region from panel **b** (V_s = 50 mV, I_t = 20 pA, scale bar: 2 nm)

3.2.3   Bottom-Up Synthesis of 11-AGNR on Au(111)

Following the unsuccessful attempts to synthesize an 11-AGNR via **3-1**, a new precursor was designed based on the perylene scaffold in Ref. 25 that leads to 5-AGNRs. Previous research in our group showed that the incorporation of biphenyl moieties at the 2 and 2' positions in bisanthracene scaffold for 7-AGNRs increases the width of the resulting GNR by six carbon atoms. Based on these results, a biphenyl substituted iodinated perylene (**3-2** in Figure 3.2.2) was used for the synthesis of 11-AGNRs. In particular, the iodinated precursor was chosen because of studies showing that long and pristine 5-AGNRs can be obtained via diiodoperylene because of the lower dehalogenation temperature for iodine compared to bromine. **3-2** was sublimed from a Knudsen cell evaporator under UHV conditions onto an Au(111) substrate held at 25 °C (Figure 3.2.2B). Subsequent annealing to 350 °C begets extended linear structures with an apparent width of 1.5 nm, consistent with the expected width for an 11-AGNR. High-resolution bond resolved STM (BRSTM) topographic images confirm the successful synthesis of 11-AGNRs and reveal a "mouse bite" defect present in many of the GNRs (Figure 3.2.2D). This defect corresponds to the excision of a biphenyl and likely stems from the overlap of two biphenyl units during polymerization. A similar defect is seen in the 9-AGNRs and N-6-ZGNRs following the excision of a single phenyl although the electronic structure is unaffected.
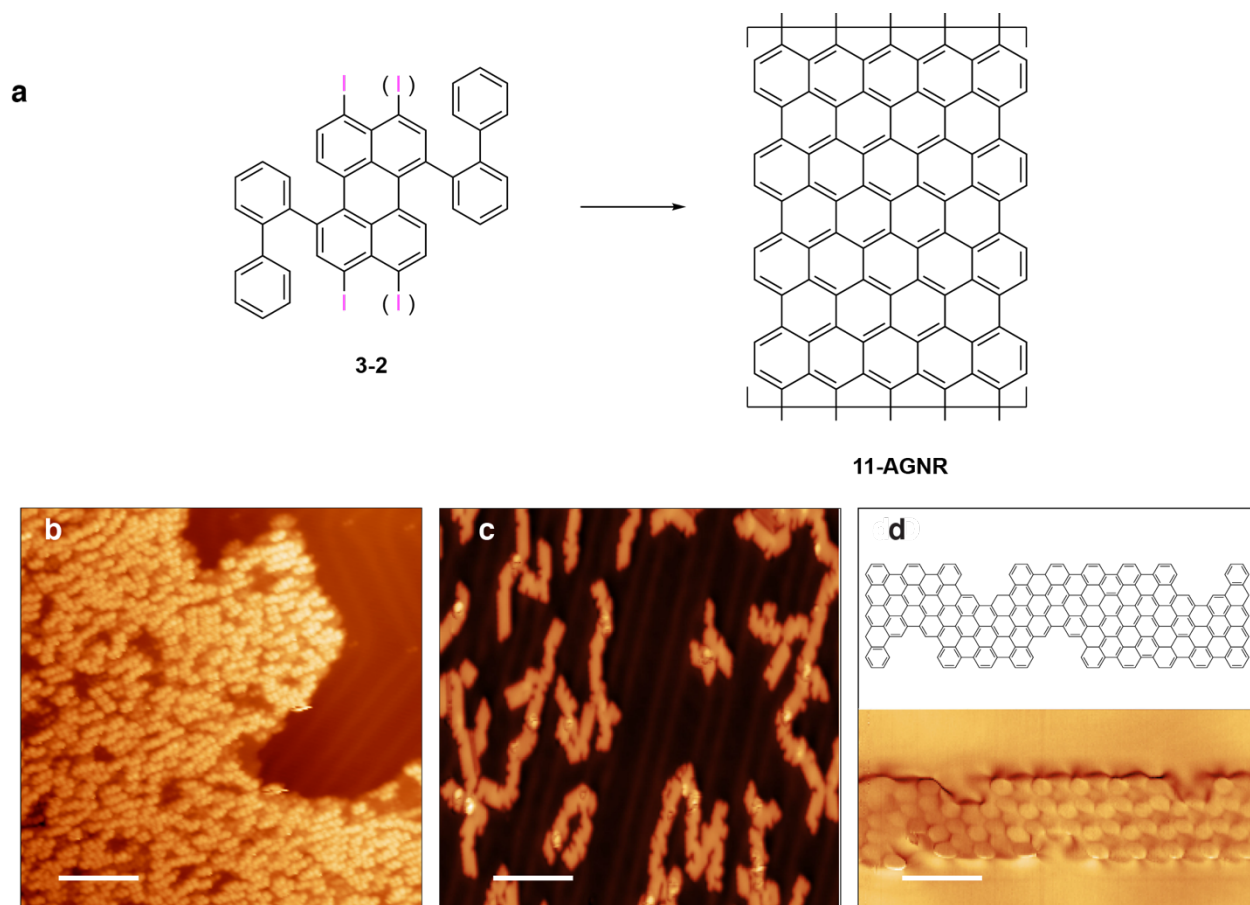
Figure 3.2.2 Bottom-Up Synthesis of 11-AGNR a, Chemical structure of diiodo-biphenyl substituted perylene precursor **b,** STM Topographic Image of **3-2** after deposition onto Au(111) substrate held at 25 °C (V_s = 50 mV, I_t = 20 pA, scale bar: 10 nm) **c,** STM Topographic image of panel **B** after annealing to 350 °C (V_s = 50 mV, I_t = 20 pA, scale bar: 10 nm) **d,** BRSTM image of an 11-AGNR showing the characteristic biphenyl excision (V_s = 10 mV, I_t = 200 pA, scale bar: 2 nm)

3.2.4 Electronic Structure Characterization of 11-AGNRs

dI/dV point spectroscopy with a metallic PtIr tip was used to characterize the local electronic structure. Figure 3.2.3A shows typical point spectra recorded along the edge of an 11-AGNR and several peaks are clearly visible depending on the position of the tip. One broad peak is centered at V = 0.50 eV, another sharper peak is centered at V = -0.07 eV, and finally there is sharp peak centered at V = –0.440 eV. The peak at 0.50 eV can be attributed to the CB edge, but this is much less clear for the VB edge because the peaks overlap with the Au(111) Shockley surface state. After attaching a CO-molecule to the STM tip, dI/dV images were taken to elucidate the spatial distribution of 11-AGNR LDOS at energies near peaks mentioned previously. dI/dV maps taken at 0.50 eV show increased LDOS contrast along the edge of the 11-AGNR, as expected for the CB state. Maps recorded at –0.07 eV and –0.4 eV show similar contrast complicating the assignment for the VB edge. The calculated quasiparticle band gap for the 11-AGNR is ~1.2 eV, therefore the VB is most likely –0.07 eV resulting in a band gap of 0.57 eV. An accurate assessment of the band gap would require decoupling the 11-AGNR from the underlying Au(111) substrate.

a

b

V = -450 mV   V = -70 mV   V = 500 mV
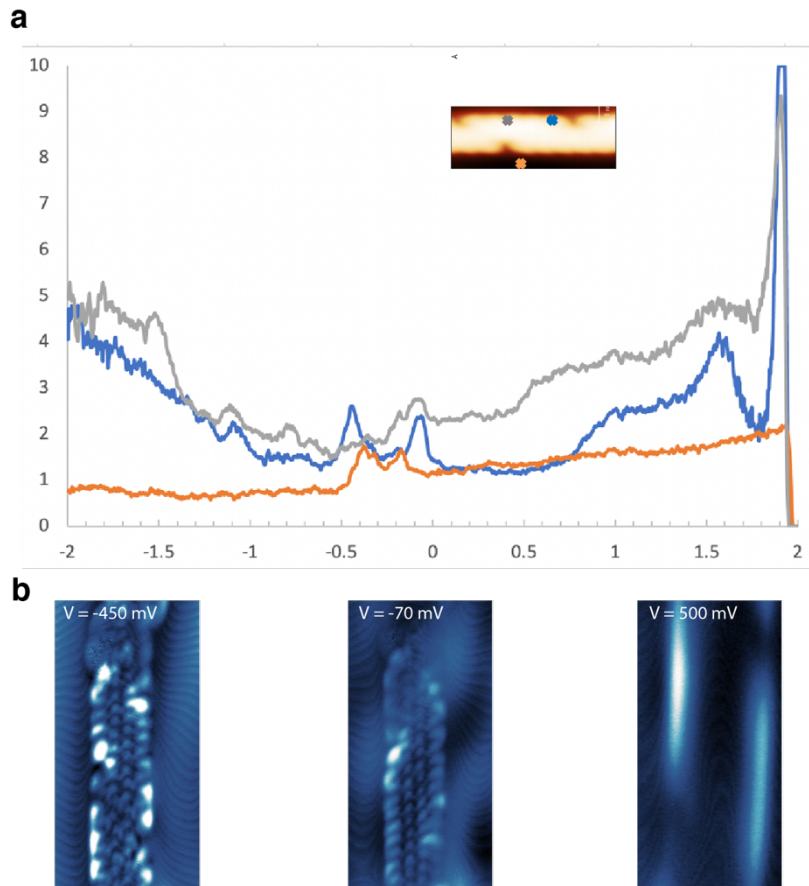
Figure 3.2.3 Electronic Structure Characterization of 11-AGNRs a, dI/dV point spectroscopy of 11-AGNRs a **b,** dI/dV map at –440 meV **c,** dI/dV map at –70 meV **d,** dI/dV map at 500 meV

One potential strategy is dragging the 11-AGNR onto insulating NaCl islands as this will sufficiently decouple molecules and allows for the study of the inherent electronic structure[94]. This is particularly important because FETs are fabricated on dielectric substrates and the band gap measured on metallic substrates is severely underestimated when compared to the quasiparticle band gap of a freestanding GNR. Therefore, experimental data on NaCl will be substantially closer to the band gap in actual devices. Another method involves the sublimination of Si onto Au(111) which can intercalate underneath the GNR and form a semiconducting AuSi[93]. While this technique has been shown to eliminate the Au(111) Shockley surface state, the experimental band gap is still significantly lower than the quasiparticle gap. Moreover, while the 11-AGNRs synthesized in this section are of adequate length for electronic structure characterization, they are not suitable for high-performance FET devices and an alternative method that produces 11-AGNRs that are ~ 20 nm long is required.

3.3 Synthesis of Hybrid Zigzag/Armchair GNRs

3.3.1 Introduction

Graphene nanoribbons (GNRs) have emerged as promising candidates for electronic devices beyond silicon due to the connection between geometric structure and the subsequent electronic and magnetic properties. As a result of this intimate link, it is imperative to find methods for the synthesis of the atomically precise GNRs. Traditional methods such as lithography, chemical processing, and the unzipping of carbon nanotubes fail to produce the desired uniformity. On the other hand, bottom-up methods—particularly, growth on coinage metal surfaces under ultrahigh vacuum (UHV) conditions—allow for the synthesis of previously inaccessible geometries with the desired atomic precision.

A critical component of these bottom-up methods is the halogenated molecular precursor as this ultimately determines the final GNR structure. Typically changes to the molecular precursor have led to different GNR structures with the exception of changes to the halogen atom. There has been minimal research on using multiple precursors to achieve the same GNR structure to produce design principles for GNR growth. Moreover, while GNRs with armchair, zigzag, chevron, cove, and chiral edges have been synthesized from a single molecular precursor, GNRs with hybrid edge structures—e.g., armchair/zigzag edge topologies—have to date relied on random and uncontrollable lateral fusion. In this work, we report the bottom-up surface assisted synthesis of a GNR with a periodic arrangement of four armchair segments followed by four zigzag segments (herein referred to as 4,4-GNR) from two distinct molecular precursors. The two precursors differ in the placement of methyl groups along the GNR backbone (Figure 3.3.1). This work addresses both aforementioned gaps in GNR research and provides a novel set of design principles for growth on the surface.
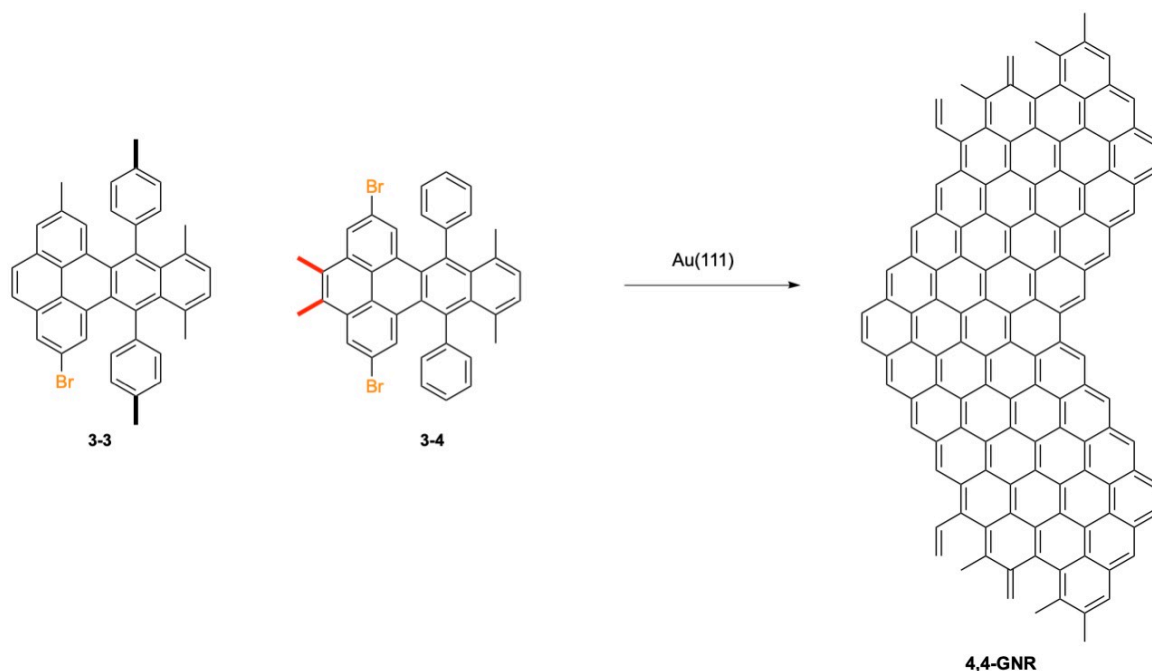
Figure 3.3.1 Schematic representation of 4,4-GNR

3.3.2 Bottom-Up Synthesis of Hybrid Zigzag/Armchair GNRs

First, precursor **3-3** in Figure 3.3.2 was deposited from a Knudsen cell evaporator at a crucible temperature of 185 °C onto a Au(111) surface held at room temperature. Topographic scanning tunneling microscopy (STM) images of as deposited precursor molecules are shown in Figure 3.3.2B and reveal that the monomer prefers to assemble into amorphous islands like the precursor chevron GNRs. Subsequent annealing to 350 °C at a ramp rate of 3 °C min^{-1} yields linear, fully cyclized structures (Figure 3.3.2C) as seen by large-area STM images. A zoomed-in image of the sample shown in Figure 3.3.2C is shown in Figure 3.3.2D and it is apparent that the seemingly pristine GNRs in Figure 3.3.2C are relatively defective with several misconnected monomer units along the backbone (Figure 3.3.2D white oval). While there are some segments of the 4,4-GNR that show the correct connectivity, we were unable to find a defect-free GNR without any the misconnections. The most probable explanation for the prevalence of these misconnections is the sterically accessible methyl group on the periphery of the molecule. This methyl group can readily undergo side reactions that result in the transfer of a hydrogen atom to growing chain end (aryl radical, red species in Figure 3.3.2E) on the surface before the aryl radical can form the correct C–C bond between adjacent monomers. At this stage there are two radicals on the monomer—one at the halogen site and one on the methyl group—that can potentially react with nearby monomers to form C–C bonds.
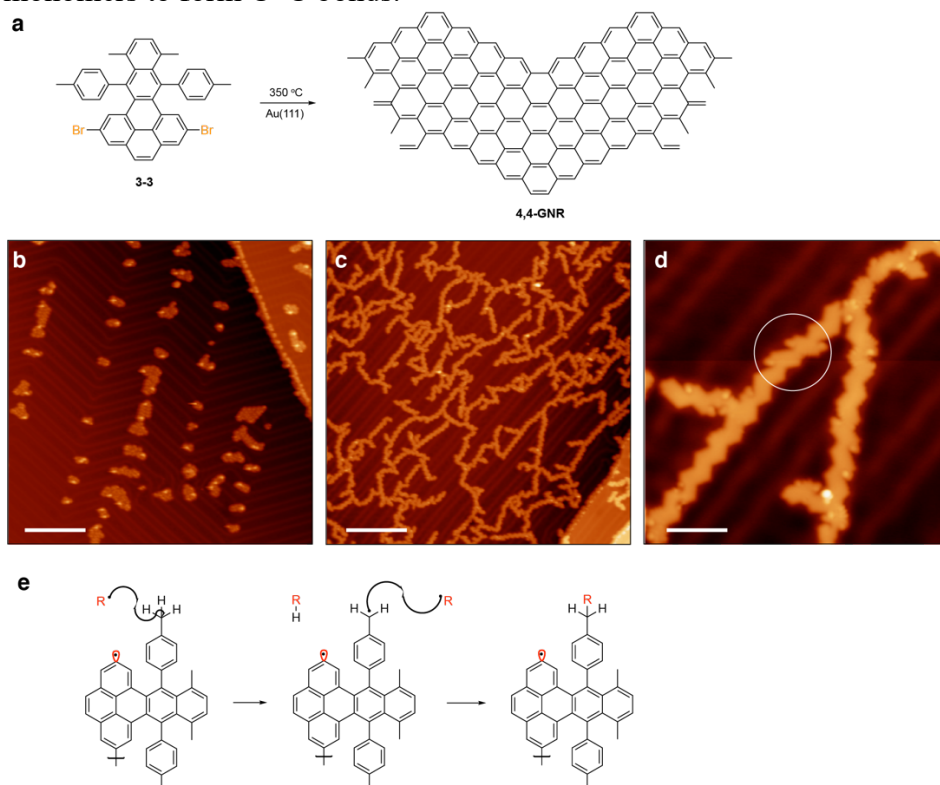
Figure 3.3.2 Bottom-Up Synthesis of 4,4-GNR a, Schematic representation of 4,4 GNR from **3-3 b,** STM topographic image of **3-3** as-deposited (V_s = 50 mV, I_t = 20 pA, scale bar: 10 nm) **c,** STM topographic image of **3-3** after annealing to 350 °C (V_s = 50 mV, I_t = 20 pA, scale bar: 10 nm) **d,** STM topographic image displaying defective GNR backbone(V_s = 50 mV, I_t = 20 pA, scale bar: 4 nm) **e,** H-atom transfer mechanism for misconnection in panel **d**

To circumvent this issue, the peripheral methyl groups (Figure 3.3.1, bold black bonds) in the second precursor were placed in a new, sterically less accessible position (Figure 3.3.1, bold red bonds), yielding the same 4,4-GNR backbone but without the same potential for deleterious side reactions. Precursor **3-3** was similarly deposited onto a Au(111) substrate from a Knudsen cell evaporator at a crucible temperature of 175 °C. An STM topographic image of **3-3** as deposited is shown in Figure 3.3.3B, which indicates that the precursor adsorbs to the surface in a more ordered and linear structure than precursor 1. The Au(111) substrate was again annealed to 350 °C at a ramp rate of 3 °C min^{-1} and STM topographic images display linear, fully cyclized polymeric structures (Figure 3.3.3C) that look similar to those in Figure 3.3.2. Focusing on the STM topographic images in Figure 3.3.3D it is clear that the 4,4-GNRs formed via monomer **3-2** show none of these previously observed misconnections. A further zoomed in image (Figure 3.3.3E) displays a pristine 4,4-GNR backbone that cannot be seen in the GNRs produced from precursor **3-3**. Bond-resolved STM (BRSTM) images were acquired using a CO-functionalized STM tip by recording the out-of-phase component of constant-height dI/dV maps at zero tip-sample bias (Figure 3.3.3F). The BRSTM images confirm that the 4,4-GNR has the correct connectivity.
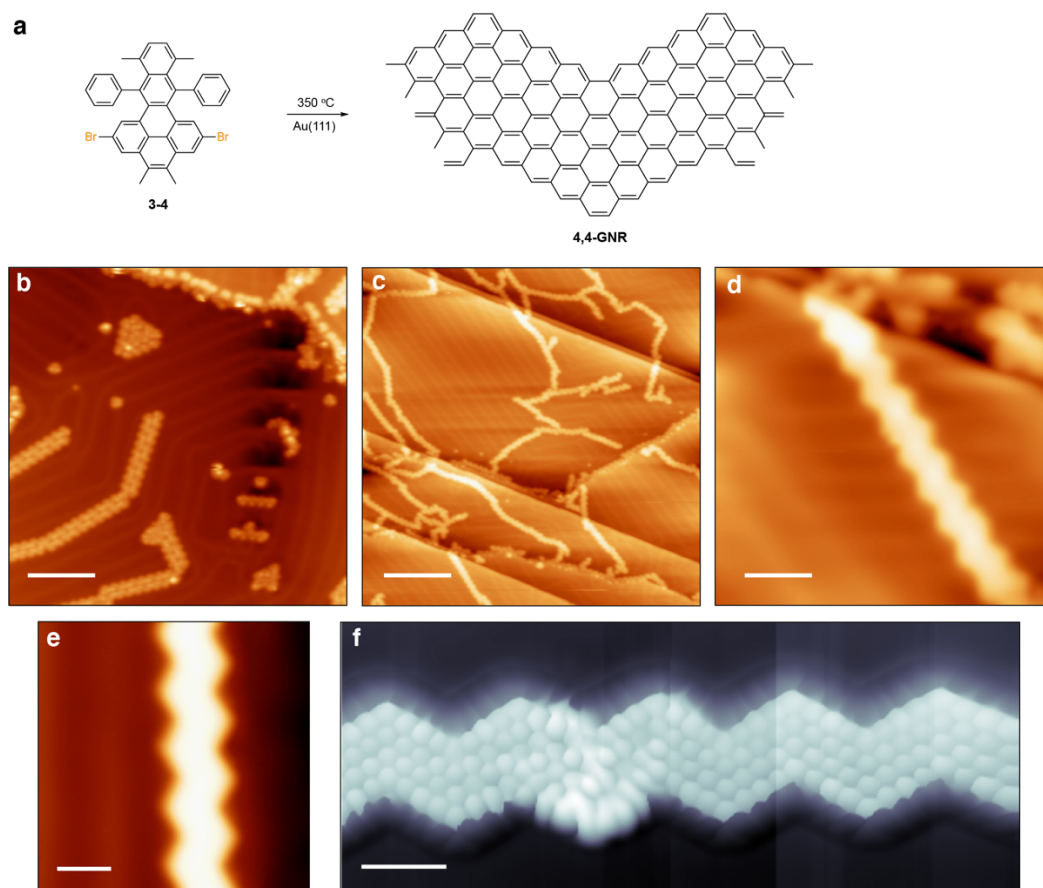
Figure 3.3.3 Bottom-Up Synthesis of 4,4 GNR from Monomer 3-4 a, Schematic representation of 4,4-GNR formation from **3-4 b,** STM topographic image of **3-4** as deposited ($V_s = 50$ mV, $I_t = 20$ pA, scale bar: 10 nm) **c,** STM topographic image of **3-4** after annealing to 350 °C ($V_s = 50$ mV, $I_t = 20$ pA, scale bar: 10 nm) **d,** Zoom-in STM topographic image of pristine 4,4-GNR ($V_s = 50$ mV, $I_t = 20$ pA, scale bar: 3 nm) **e,** Zoom-in STM topographic image showing pristine 4,4-GNR backbone ($V_s = 50$ mV, $I_t = 20$ pA, scale bar: 1.5 nm) **f,** BRSTM Image showing correct 4,4-GNR structure

3.3.3 Electronic Structure of Hybrid Zigzag/Armchair GNRs

The local electronic structure of the 4,4-GNR was characterized using dI/dV point spectroscopy taken on the apex of one pristine edge of the GNR (Figure 3.3.4A, inset). All point spectra were recorded with a CO-functionalized STM tip and compared to a Au(111) background spectrum. The Shockley state of the Au(111) surface at approximately –500 mV serves as reference. Figure 3.3.4A shows two distinct peaks that are not present in the Au(111) background at –700 mV and 1.1 V. Investigating the two distinct peaks further through dI/dV mapping reveals the two peaks display an enhanced local density of states (LDOS) localized on the zigzag edges. This matches nicely with the LDOS calculated within the local density approximation (LDA) framework for the VB–1 and CB+1, respectively. However, a relatively clear slope in the positive bias regime (~0.5–1V) leading toward the CB+1 peak can be observed in the point spectra. dI/dV maps taken at 800 mV show that the LDOS becomes localized within the bay region opposite each apex of the GNR backbone. The map taken at this voltage is in excellent agreement with the calculated LDOS for the CB and thus this shallow sloped feature is representative of the CB onset. Unfortunately, no features in either the STS or dI/dV mapping revealed the presence of the VB. This is most likely due to two major factors: (1) the VB is located close to the Au surface state (Figure 3.3.4A, red region) and this overlap conceals any presence of the state, and (2) similar to the CB the VB has a low DOS and thus could easily be overwhelmed by the nearby surface state. This surface state screening has been previously reported for hybrid zigzag armchair GNRs formed via lateral fusion. Therefore, the experimental gap on Au(111) could not be determined but it should be <1.3 eV, which agrees with the calculated DFT-LDA gap.
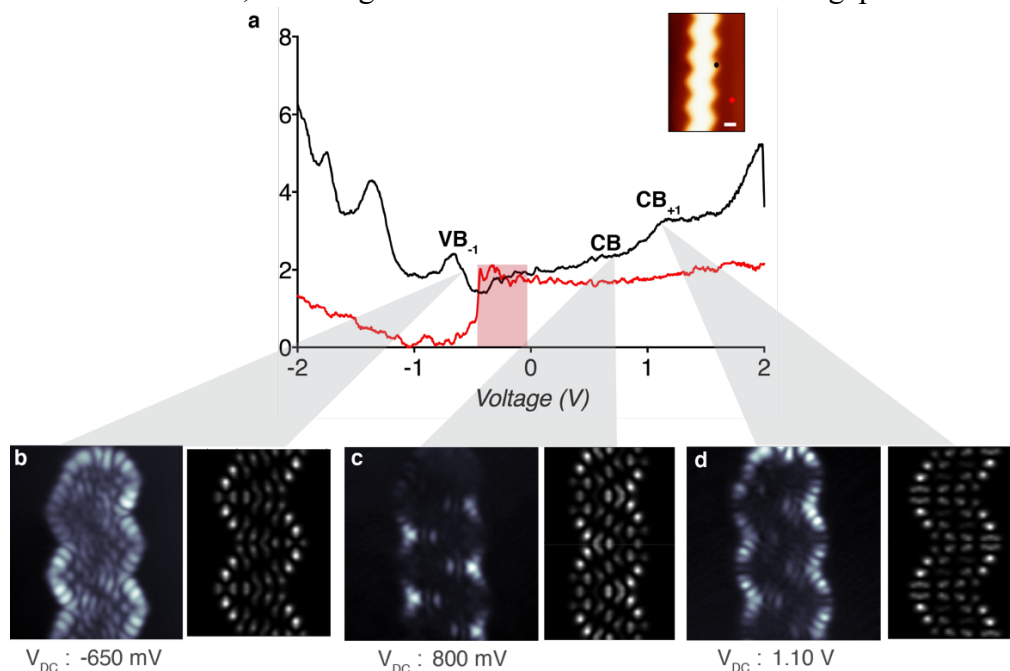
Figure 3.3.4 Electronic Structure Characterization of 4,4-GNR a, STS spectrum recorded near the apex of the GNR edge (black line) and the Au(111) background (red line). The inset shows the positions at which the spectrum was acquired. Region around the Au(111) surface state where VB is expected (shaded red region) **b,** dI/dV map with associated DFT calculated LDOS for the VB–1 (map acquired at –650 mV). **C,** dI/dV map with associated DFT calculated LDOS for the CB (map acquired at 800 mV). **d,** dI/dV map with associated DFT calculated LDOS for the CB+1 (map acquired at 1.10 V).

Herein, novel zigzag/armchair 4,4-GNRs with low band gaps from discrete molecular precursors (no inter-ribbon fusion required) have been synthesized. Additionally, it has been demonstrated that methyl groups utilized to incorporate zigzag edges can greatly affect GNR growth and that placement of the methyl groups in steric accessible positions, especially near the polymerization site, yield more defective ribbons due to H-atom transfer side reactions. This is one of the only studies to provide insight into molecular design parameters as a function of GNR growth.

3.4   Synthesis of Chevron GNRs

3.4.1   Introduction

Lateral quantum confinement of graphene has exposed a wealth of truly exotic physical and electronic properties in carbon-based nanomaterials. Graphene nanoribbons (GNRs) in particular have emerged as a privileged motif for applications in advanced electronics as they combine some of the most desirable intrinsic properties of graphene with the emergence of a highly tunable band gap. Minute variations in the width, the crystallographic symmetry, or the edge structure of GNRs can be translated into major shifts in the electronic band structure[79,95–97]. Deterministic bottom-up synthetic approaches based on judiciously designed molecular precursors have demonstrated an unprecedented atomic control over width[25,27,98,99], edge-topology[20,30,31,33], and the placement of dopants[40,45,65,100–102] that is indispensable for the rational tuning of the electronic structure of GNRs[69]. The development, the fundamental exploration, and the mastery of these molecular engineering tools are critical steps toward the integration of functional GNRs into advanced electronic devices[19,92,93,103–105].

A common strategy used to fine-tune the electronic structure of GNRs is the substitution of C-atoms along the edges or along the backbone of GNRs with Boron or Nitrogen heteroatom dopants. Substitutional backbone-doping with B-atoms demonstrated for $N = 7$ armchair GNRs (AGNRs) introduces deep-lying dopant states by forcing the empty p-orbital on B-atoms into conjugation with the extended π-system of the GNR[40,101]. However, this backbone-doping strategy is limited to heteroatoms that can adopt the trigonal planar geometry required for the incorporation along the GNR backbone. A second approach used to alter the electronic structure of GNRs relies on replacing C–H groups along the ribbon edge. Nitrogen dopant atoms, for example, have been incorporated as part of pyridine or pyrimidine groups along the edges of chevron GNRs (cGNRs)[45,100,102]. In these structures the lone-pairs of the N-atoms come to rest in the plane of the ribbon, perpendicular to the extended π-system of the GNR backbone. Substitutional edge dopants alter the electronic structure of the GNR merely through inductive effects. This is reflected in the observation of a rigid shift of valence and conduction band edges with respect to the Fermi energy of the metal substrate, without any significant changes in the size of the band gap. Previous efforts aimed at incorporating edge-dopants in conjugation with the extended π-system of GNRs have led to defects and uncontrolled edge-reconstruction, yielding samples featuring heterogenous doping patterns along the length of the ribbon[39,44,65]. Orbitally matched edge-doping merges both the inductive and the orbital overlap effects by placing heteroatom lone-pairs in conjugation with the extended π-system. This strategy not only provides a rational tool to control the relative energy of the band edge states but also exerts control over the absolute size of the band gap.

The bottom-up synthesis of a series of atomically precise nitrogen-, oxygen-, and sulfur-doped cGNRs is reported. The placement of trigonal planar heteroatom dopants at defined positions along the convex protrusion lining the edges of cGNRs ensures the overlap of the heteroatom lone-pairs with the extended π-system. N-, O-, and S-dopant atoms were selected in this series for their varying degrees of electronegativity. Samples of edge-doped cGNRs were prepared in ultra-high vacuum (UHV) on a Au(111) surface. Scanning tunneling microscopy (STM) as well as non-contact atomic force microscopy (nc-AFM) confirms the precise dopant incorporation along the GNR edges. Scanning tunneling spectroscopy (STS) reveals a narrowing of the band gap by ~0.2–0.3 eV per dopant atom per monomer unit when compared to unsubstituted cGNRs. A correlation of the electronic band structures of N-, O-, and S-doped cGNRs establishes rational and predictable structure-function relationships that are corroborated by density functional theory (DFT) calculations.

3.4.2   Surface-Assisted Synthesis of Doped Chevron GNRs

N-, O-, and S-doped cGNRs were fabricated by thermal deposition of a sub-monolayer of the respective molecular building blocks **1a**–**c** on a Au(111) surface held at 120 °C in UHV.[12,14] STM images recorded on the intermediate polymer chains emerging from the step-growth polymerization of **1a**–**c** show characteristic protrusions along the edges commensurate with the expected position of the fused heterocyclic wings (Figure 3.4.1). The irregular edge-pattern observed in the topographical images is consistent with a random *co*-polymerization of both the R_a and S_a enantiomers on the metal surface.
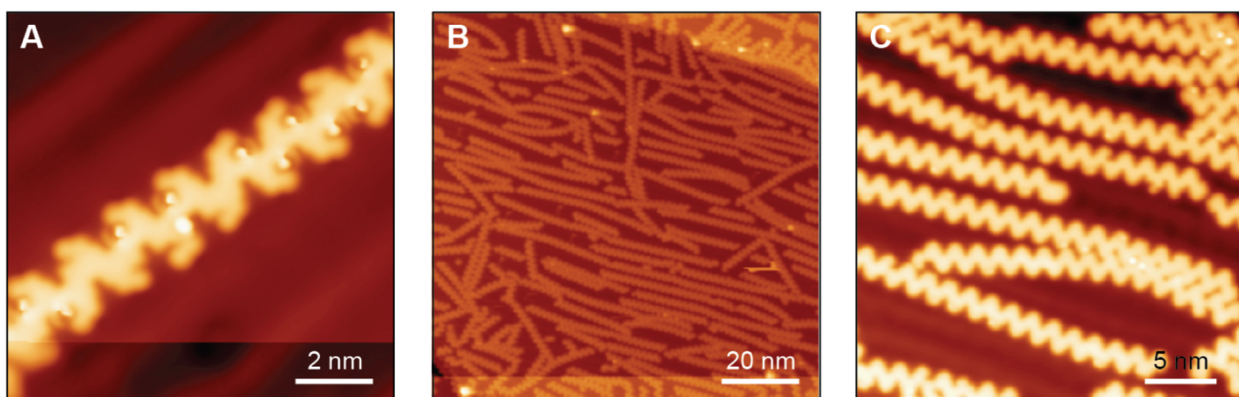
Figure 3.4.1 Bottom-Up Synthesis of O-Doped Chevron GNR a, STM topographical image of O-doped cGNR polymer intermediate. Uncyclized wings protruding from polymer backbone appear as brighter protrusions. This polymer intermediate is representative of the intermediate structures also observed for the S-doped and N-doped precursor polymers; other examples of precursor polymer intermediates from this series of GNRs can be found in the literature **b,** Representative large area STM topographical image of O-doped cGNR and **c,** magnified image of O-doped cGNR illustrating the virtually quantitative yield of fully cyclodehydrogenated GNRs. ($V_s = 50$mV, $I_t = 20$ pA)

Gradual annealing (5 C min^{-1}) first induces the complete cyclodehydrogenation of the triphenylene cGNR backbone until at 400–450 °C the heterocyclic wings fuse to form the extended graphitic backbone of cGNRs. Low temperature (4.5 K) STM images of N-, O-, and S-doped cGNRs show an apparent height of 0.16 nm and the characteristic periodicity of 1.7 nm (Figure

3.4.3A-C)[31]. Statistical analysis on different samples of doped cGNR reveals an average length clustering around 10–15 nm, with some cGNRs exceeding 40 nm (Figure 3.4.2).
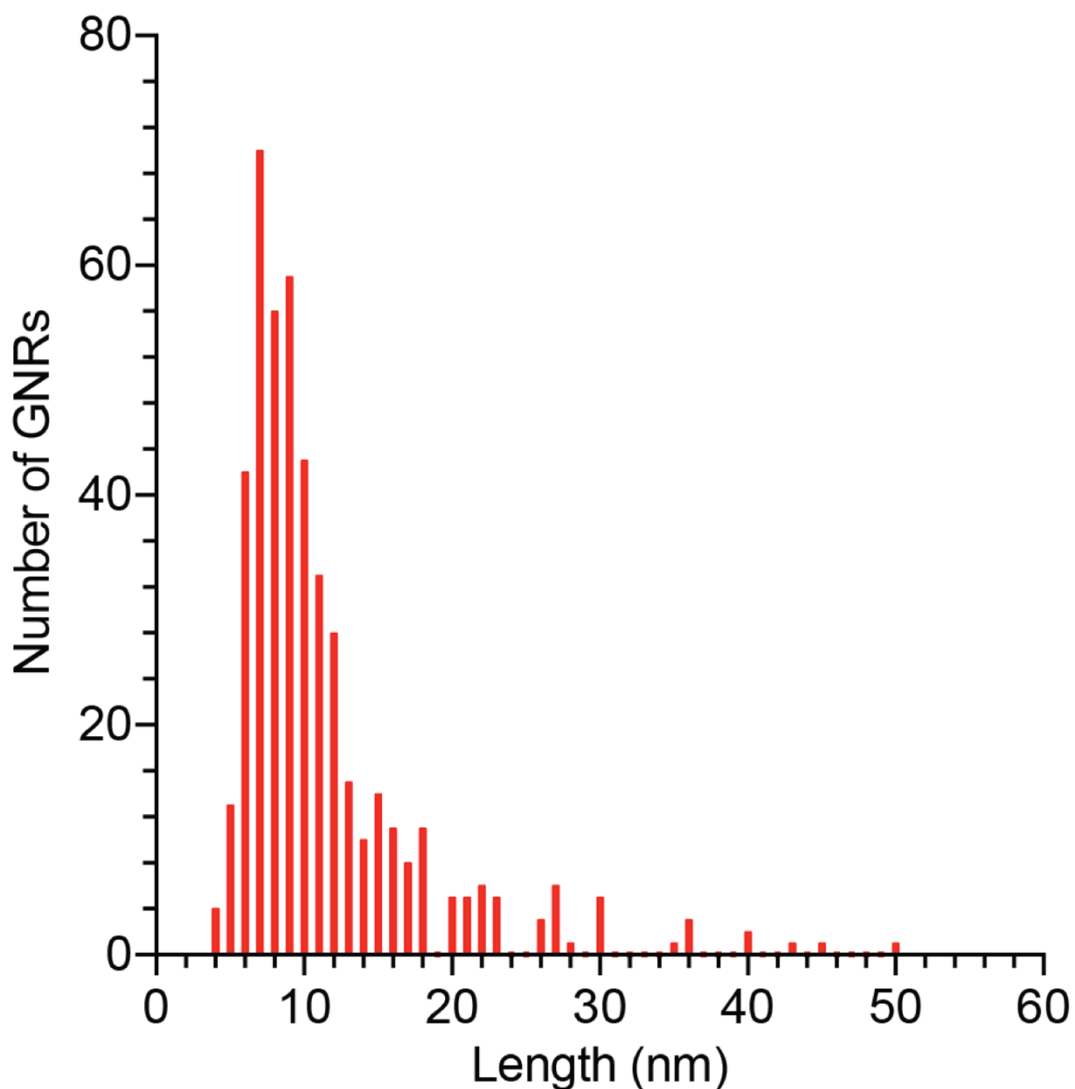
Figure 3.4.2 Statistical Analysis of GNR Length Distribution

While these observed parameters are consistent with the reported structures of the parent unfunctionalized cGNRs, significant differences in the apparent width of N-, O-, and S-doped cGNRs, 2.3 ± 0.1, 2.2 ± 0.1, and 2.4 ± 0.1 nm respectively[106,107] were observed. Since variances in the apparent width of edge-doped cGNRs could be attributed to changes in the local electronic structure or result from the cleavage of the dopant heteroatom itself during the thermal annealing process, nc-AFM imaging with CO-modified tips[77] was performed. nc-AFM images of N-, O-, and S-doped cGNRs unambiguously confirm the position of dopant heteroatoms at the apex of each of the convex protrusion along the cGNR edges (Figure 3.4.3D–F). An evaluation of large area nc-AFM scans of doped cGNRs and the corresponding STM images indicates that N- and O-doped cGNRs retain >99% of the expected dopant atoms along the edges. Samples of S-doped cGNR, instead, suffer from sporadic defects resulting from the random excision of S-atoms during the cyclodehydrogenation step.

Contrast in the nc-AFM images attributed to the position of N- and S-atoms appear brighter than the position of O-dopants in corresponding images of O-doped cGNRs (Figure 3.4.3E). This superficial difference has in the past been attributed to the enhanced interaction between the terminal oxygen of the CO-modified tip and O-atoms in molecular adsorbates[108]. Since nc-AFM imaging revealed no significant changes to the absolute width of N-, O-, and S-doped cGNRs, we conclude that the variations in apparent cGNR width observed by STM originate mainly from the modifications of the local electronic structure of the cGNRs by the dopant atoms.
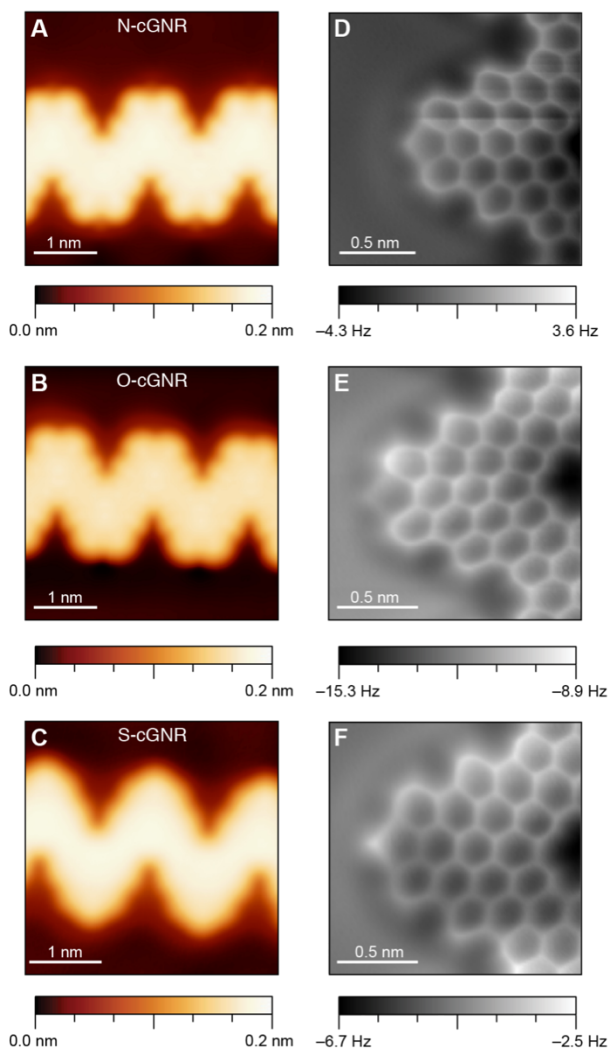
Figure 3.4.3 STM and nc-AFM Topographic Images (**a**, **d**) N-doped cGNRs (V_s = 10 mV, I_t = 40 pA), (**B**, **E**) O-doped cGNRs (V_s = –1.1 V, I_t = 500 pA), (C, F) S-doped cGNRs (V_s = –0.75 V, I_t = 300 pA).

3.4.3 Electronic Structure of Doped Chevron GNRs

Scanning tunneling spectroscopy (STS) on various samples of N-, O-, and S-doped cGNRs was performed. Representative dI/dV point spectra acquired along the convex edge of cGNR close to the position of the heteroatom dopant are depicted in Figure 3.4.4. The experimental band edge energies and band gaps for N-, O-, and S-doped cGNR are summarized in Figure 3.4.5.
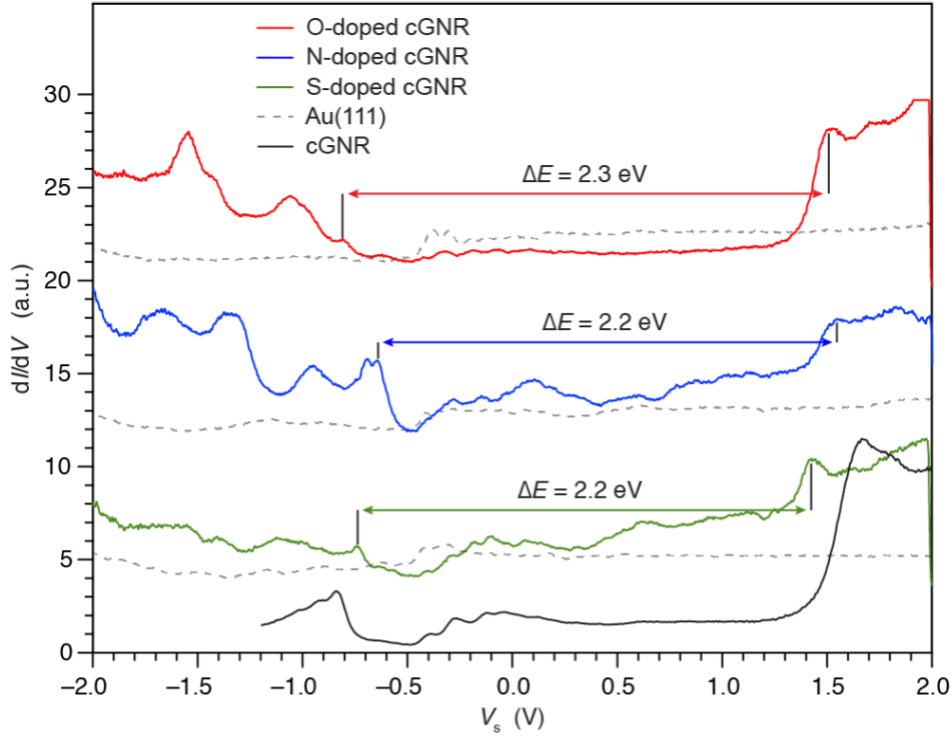
Figure 3.4.4 Electronic Structure Characterization of doped Chevron GNRs STM dI/dV point spectra of O-cGNR (red), N-cGNR (blue) S-cGNR (green), and representative Au(111) backgrounds (gray). Spectra were recorded at a position in the vicinity of the dopant atom along the GNR edge. Spectra are offset vertically (O-cGNR set point: $V_s = -1.1$ V, $I_t = 50$ pA; S-cGNR set point: $V_s = 0.05$ V, $I_t = 20$ pA; N-cGNR set point: $V_s = 0.05$ V, $I_t = 20$ pA).

	VB$^\Phi$ Edge	CB$^\Psi$ Edge	Band Gap
cGNR, exp.	−0.80	1.70	2.45 ± 0.05
cGNR, calc.	−3.36	−1.51	1.85
N-cGNR, exp.	−0.65 ± 0.02	1.55 ± 0.02	2.20 ± 0.05
N-cGNR, calc.	−2.91	−1.43	1.48
O-cGNR, exp.	−0.80 ± 0.02	1.50 ± 0.02	2.30 ± 0.05
O-cGNR, calc.	−3.19	−1.64	1.55
S-cGNR, exp.	−0.74 ± 0.02	1.46 ± 0.02	2.20 ± 0.05
S-cGNR, calc.	−3.08	−1.60	1.48

Figure 3.4.5 Tabulated Values for Band Gaps in Doped Chevron GNRs

For this discussion, we operationally define the band gap as the peak-to-peak distance in the STS, and the band edge positions are similarly defined as the corresponding peak positions in the STS. The corresponding data for unfunctionalized cGNRs is provided as a reference[67]. When compared to pristine cGNRs, the introduction of O-dopant atoms leads to a significant shift of the conduction band (CB) edge to lower energies while the valence band (VB) edge remains essentially unperturbed. This is reflected in a reduction (~0.2 eV) of the band gap of O-doped cGNRs to 2.3 eV. The incorporation of S-dopant atoms in S-cGNR not only induces a significant shift of the CB edge to lower energies when compared to unsubstituted cGNRs and O-cGNR, but also increases the energy of the VB by 0.1 eV when compared to the O-cGNR, leading to an overall reduction of the band gap to 2.2 eV. N-doping in N-cGNRs yields the largest observed increase in the VB energy within our doping series. The corresponding shift of the CB edge state is comparable to the O-doped cGNRs, leading to an overall reduction of the band gap of 2.2 eV, ~0.3 eV smaller than the unsubstituted cGNRs. The relative energy of VB edge states follows the trend cGNR $\leq$ O-cGNR < S-cGNR < N-cGNR. The corresponding sequence for the CB band edge states is S-cGNR < O-cGNR < N-cGNR < cGNR.
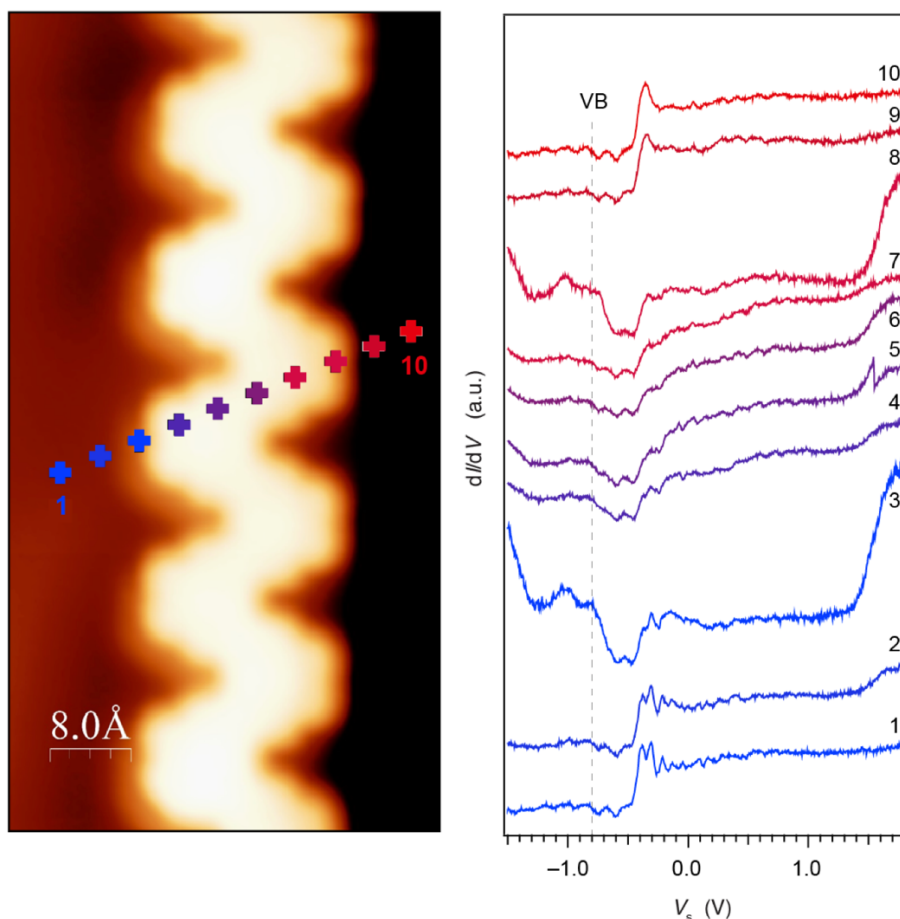
Figure 3.4.6 Spatial Dependence of dI/dV Point Spectroscopy STM topographic image (left) and corresponding dI/dV point spectra (right) of O-doped cGNR recorded at various positions above the GNR. Spectra recorded at positions marked on the GNR (left), with the first spectrum shown in blue, moving across the ribbon to the tenth spectrum shown in red. Spectra are offset vertically (set point: V_s = 0.05 V, I_t = 20 pA

We used dI/dV mapping to further explore the spatial distribution of VB and CB edge states in N— O-, and S-doped cGNRs (Figures 3.4.6 and 3.4.7A-C). A common feature of all doped cGNRs is a confinement of the spatial distribution of the local density of states (LDOS) at the energy associated with the VB and the CB edge states to the geometric real-space edges of the ribbons[99]. In the VB edge-state dI/dV map of N- and S-doped cGNRs, bright protrusions corresponding to the position of the dopant heteroatoms can be observed. The analogous maps for O-doped cGNRs show a node at the expected position of the O-atom. dI/dV maps of the CB edge states for N-, O-, and S-doped cGNRs are predominantly localized along the concave edges of the cGNRs and show a node at the position of the dopant heteroatom.
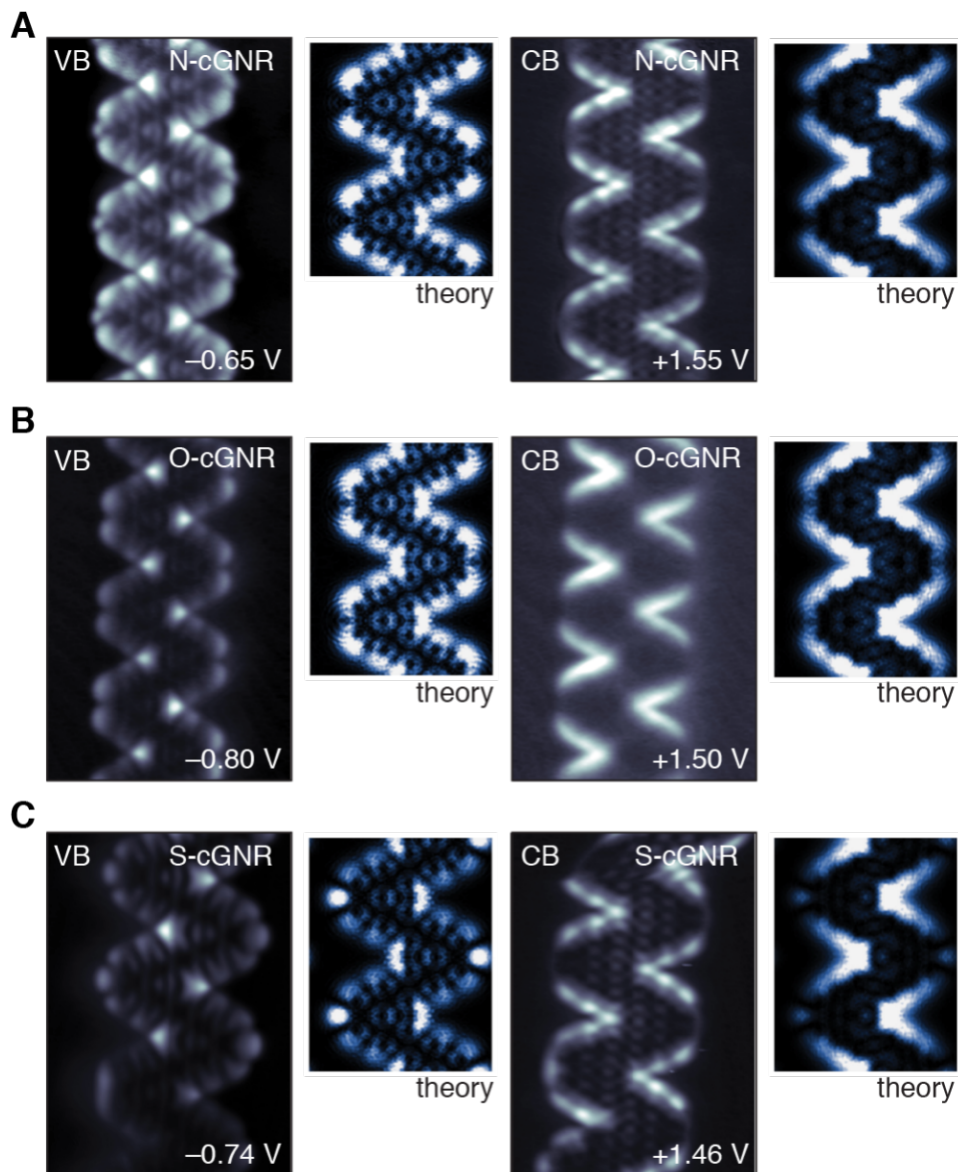
Figure 3.4.7 dI/dV Spatial Maps for Doped Chevron GNRs Experimental dI/dV spatial maps and calculated position dependence of the LDOS (or charge-density distribution) map of states with energy fixed at the valence band (VB) and the conduction band (CB) edges for (**a**) N-cGNRs (VB, I_t = 1.25 nA; CB, I_t = 10 nA). **b,** O-cGNRs (VB, I_t = 300 pA; CB, I_t = 300 pA), and **c,** S-cGNRs (VB, I_t = 1.5 nA; CB, I_t = 15 nA). Calculated lateral spatial distribution of LDOS at fixed energy is evaluated at a height of 4 Å above the doped cGNR plane.

3.4.4   Theoretical Electronic Structure of Doped Chevron GNRs

DFT calculations were performed by the Louie group within the local density approximation (LDA) to gain additional insight into the electronic structure of N-, O-, and S-doped cGNRs[109]. The introduction of dopant atoms at the apex of the convex edges of cGNRs significantly changes both the positions of band edge states and the energy band gaps. The DFT-LDA band gap of the heteroatom-doped cGNR series ranges from 1.4–1.6 eV, a decrease of ~0.3–0.4 eV when compared the unsubstituted cGNR (Figure 3.4.5). While calculations at the LDA level of theory for an isolated ribbon do not accurately account for the electron correlation effect to the self-energy of electron states nor the electron screening from the Au(111) substrate, previous studies show that the relative positions of band edge states and trends in the magnitude of the band gap can be faithfully reproduced[24,66]. This arises from a cancellation of errors: the enhancement of the band gap due to the self-energy correction is counteracted by the large metallic substrate screening, making the DFT Kohn Sham gaps close to experiment by neglecting both. Thus, considering the three systems consistently within the same DFT-LDA framework, the reduction of the band gap in edge-doped cGNRs may be attributed to an extension of the π-conjugated network to include the p-orbital associated with the heteroatom dopant. While the calculated density of states (DOS) of each isolated ribbon can only be referenced to the vacuum energy, we can still compare the relative movements of the positions of the VB and CB edges (Figure 3.4.8) with different dopants.
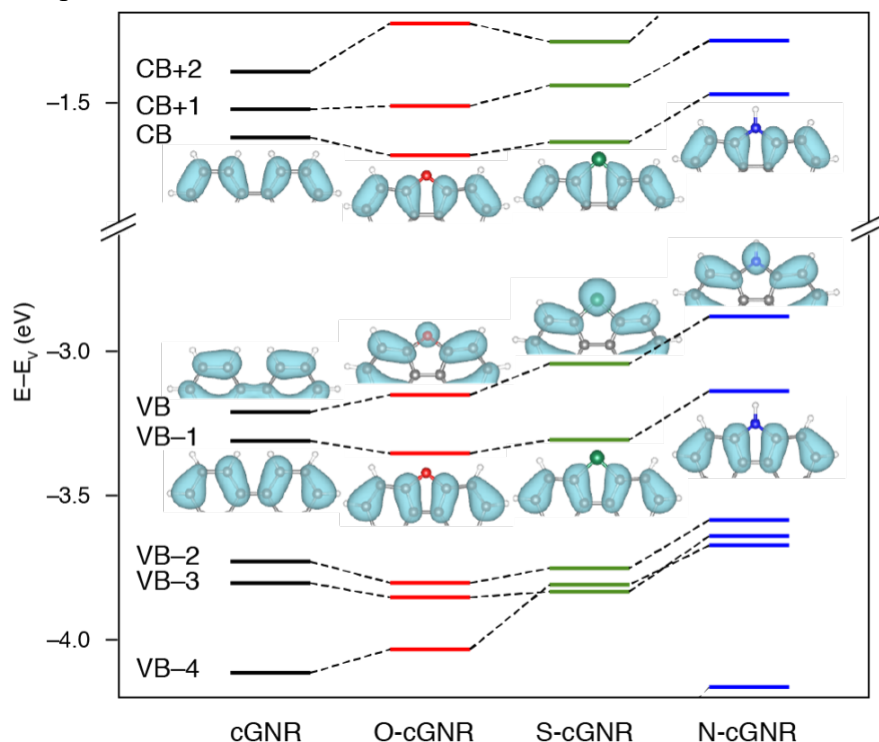
Figure 3.4.8 Theoretical Electronic Structure for Doped Chevron GNRs Calculated energy levels at the Γ point of unsubstituted cGNR (black), O-cGNR (red), S-cGNR (green), and N-cGNR (blue) near the band gap. Energy is referenced to the vacuum energy E_v. The wave functions of each cGNR at the CB, VB, and VB–1 along the GNR edges are shown as insets. Color coding for the atoms: C (black), O (red), S (green), N (blue). Hydrogen atoms, and solvent molecules are omitted for clarity.

The position of the theoretically predicted energy of the VB edge states (as defined by the peak in the density of states) in heteroatom-doped cGNRs mirrors the experimental trend determined by STS (cGNR < O-cGNR < S-cGNR < N-cGNR). The relative positions calculated for the CB edge states however deviate from the experimentally observed trend (O-cGNR < S-cGNR ≤ cGNR < N-cGNR). Most striking is the apparent inversion of the order between O-cGNR and S-cGNRs. In an effort to account for the experimental differences in the electronic structure of doped cGNRs, we investigated possible effects induced by the interaction of the ribbon with the underlying Au(111) substrate by calculating the interaction between 9*H*-carbazole (**4**), dibenzofuran (**5**), and dibenzothiophene (**6**) (small-molecule models for the functional groups lining the edges of N-cGNR, O-cGNR, and S-cGNR, respectively) and a four-layer Au(111) substrate (Figure 3.4.9).
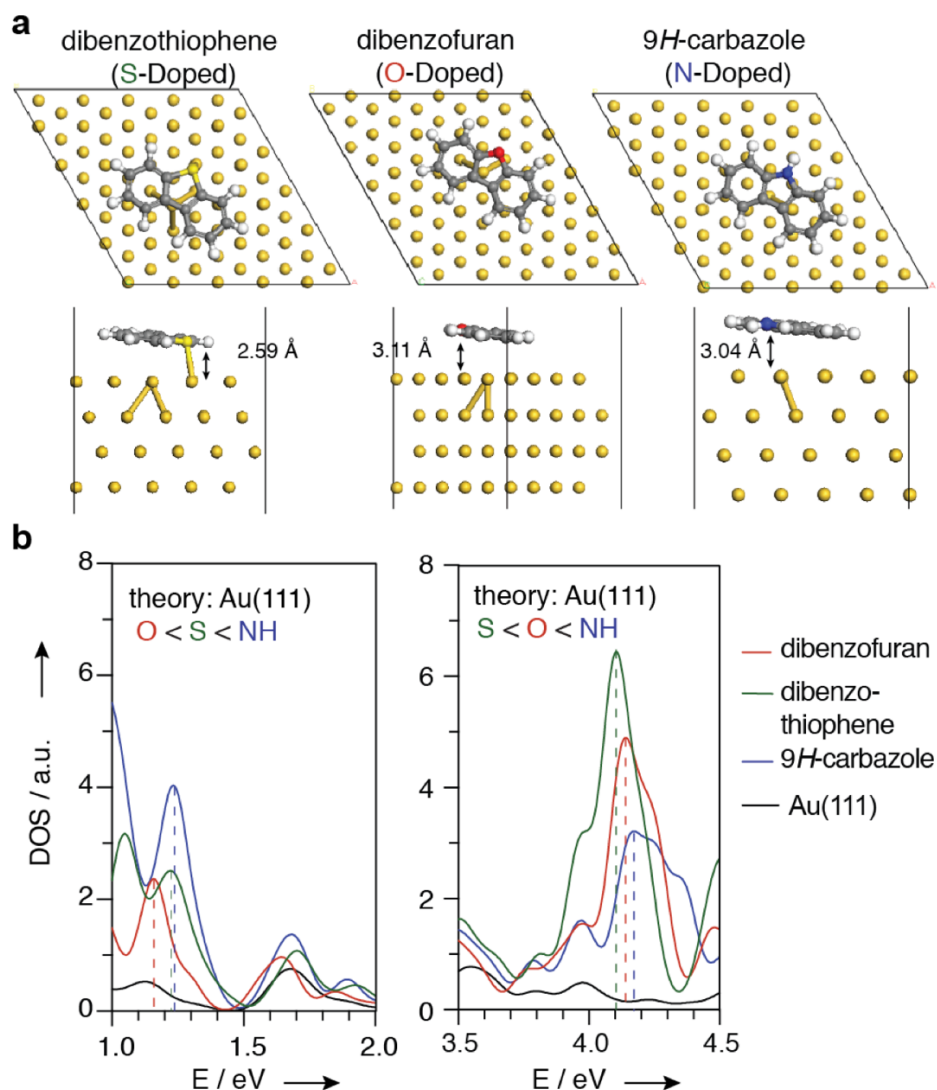
Figure 3.4.9 Representative Small Molecule Calculations for Doped Chevron Electronic Structure a, Schematic representation of structure of dibenzothiophene (left), dibenzofuran (middle), and 9*H*-carbazole (right) molecules on four-layer Au(111) substrate (upper panels; Color coding: C (gray), N (blue), O (red), S (green), H (white)); calculated heteroatom dopant height above the Au(111) surface (lower panels). **B,** Total density of states (DOS) from DFT-LDA calculations of dibenzofuran (red), dibenzothiophene (green), 9*H*-carbazole (red), on Au(111) surface (with the DOS of Au(111) surface only shown in black)

Analysis of the relaxed atomic structures of small-molecule model systems on the Au(111) substrate shows a strong interaction between the dibenzothiophene group and the underlying substrate that is absent in the dibenzofuran and 9*H*-carbazole model and is directly reflected in the shorter S–Au distance (2.59 Å) between the substrate and the dibenzothiophene when compared to the corresponding structure of dibenzofuran or 9*H*-carbazole (O–Au 3.04 Å and N–Au 3.11 Å, respectively). Calculations show that a significant electron transfer from the Au substrate to the dibenzothiophene lowers the energy of the LUMO, leading to an inversion ($6_{LUMO} < 5_{LUMO} < 4_{LUMO}$ on Au) of the trend observed in the gas phase ($5_{LUMO} \leq 6_{LUMO} < 4_{LUMO}$ gas phase, Figure 3.4.10). The calculated trend observed for the small-molecule model systems on Au(111) mirrors the experimentally observed changes in the relative alignment of the CBs in N-cGNRs, O-cGNRs, and S-cGNRs.
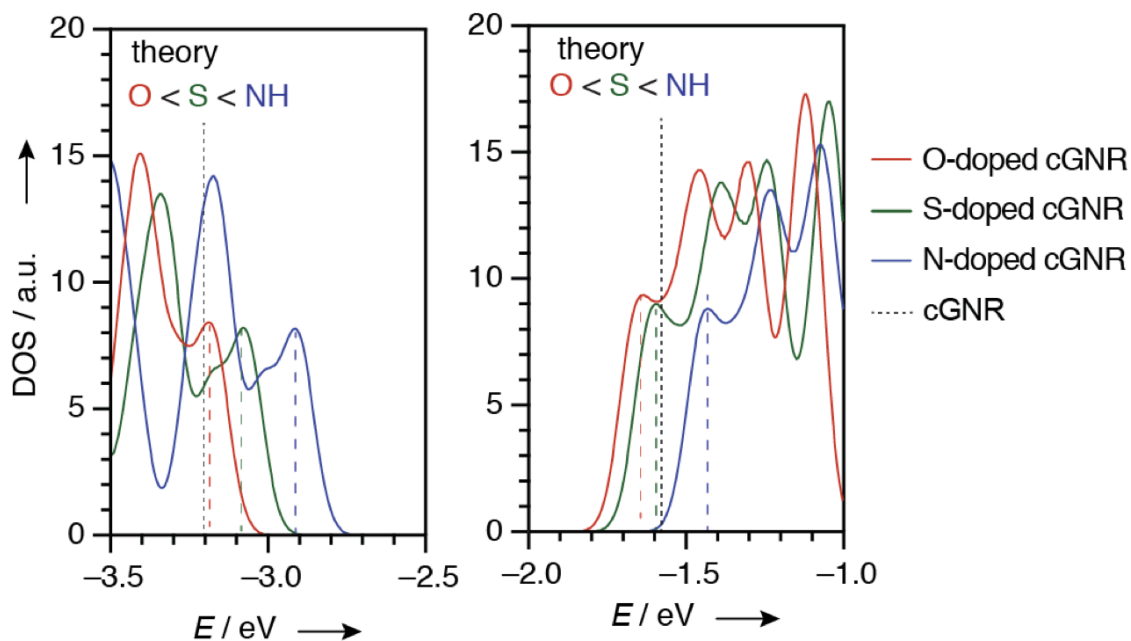
Figure 3.4.10 Theoretical Electronic Structure for Doped Chevron GNRs and Substrate Density of states from DFT-LDA calculations of free-standing O-doped cGNR (red), S-doped cGNR (green), and N-doped cGNR (blue); dashed lines indicate valence and conduction band positions. Origin of energy scale is set at the vacuum level.

After accounting for the subtle changes induced by the underlying substrate, the experimentally observed trends in the band shift of cGNRs upon introducing N-, O-, and S-dopant atoms along the edges can be rationalized. Two distinctive effects dominate changes in the band structure of edge-doped cGNRs: electron transfer between the GNR and the dopant atom and the expanded delocalization of the wave function to include the lone-pair p-orbitals at the site of the heteroatom. Löwdin charge analysis[109] suggests that each O- and S-dopant atom withdraws 0.17 and 0.12 electrons from the cGNR backbone. N-atoms instead act as donors and contribute 0.11 electrons to the cGNR. This electron transfer generates a local potential gradient near cGNR edges, resulting in a downward shift of the overall band energies for O-cGNRs and S-cGNRs and an upward shift for N-cGNRs when compared to the parent unsubstituted ribbons. While our analysis does not account for higher-order many-body effects[24], the relative energy level shifts should not change significantly as the electrostatic potential change due to the electron movement is expected to be much stronger than any induced changes in the self-energy correction. The observed band

shift is supported by wave function analysis at the point (Figure 3.4.8). The wave functions of doped cGNRs at CB, VB–1, VB–2, and VB–3 (VB–4 for S-cGNR) have the same character as unsubstituted cGNR, and their energy levels undergo a rigid shift to lower energies for O-cGNRs, a slightly smaller shift to lower energies for S-cGNR, and a shift to higher energies for N-cGNR. The wave functions of doped cGNRs at CB+2, CB+1, VB, and VB–4 (VB–3 for S-cGNR) show an overlap between the p-orbital lone-pair of the dopant atom and the extended π-system. The conjugation with the lone-pair leads to a reduction in the band gap (lowering the empty states and raising the occupied states relative to the midgap energy), leading to an upward shift of the occupied energy levels exceeding the potential gradient imparted by the electron transfer for the case of O- and S-doping. The alignment of electronic states near the Fermi level in orbitally matched edge-doped cGNRs is thus dictated by both the partial electron transfer between the dopant atoms and the cGNR (O- and S-dopants act as acceptors while N-dopants are donors), and the effective conjugation of the extended π-system with the lone-pairs on the dopant atoms.

We herein report a deterministic strategy to tune the electronic band structure of bottom-up synthesized GNRs by introducing orbitally matched edge-dopant heteroatoms. Trigonal planar N– O-, and S-dopant atoms incorporated along the convex protrusion lining the edges of cGNRs not only induce a characteristic shift in the energy of CB and VB edge states but lead to a significant reduction of the band gap of ~0.3 eV for the fully doped case of one dopant atom per monomer. STS and DFT calculations reveal that the complex shifts in the electronic structure can be attributed to an inductive effect, a partial charge transfer between the cGNR backbone and the dopant atoms that correlates with the electronegativity of the dopant element, and an expansion of the effective conjugation length facilitated by the overlap of a p-orbital lone-pair on the trigonal planar dopant atoms with the extended π-system of the cGNR. The modular and versatile doping strategy not only broadens the scope of accessible dopant atoms but also effectively blends the respective advantages of substitutional edge-doping and backbone-doping in a single step critical to the integration of functional GNRs into advanced electronic devices.

3.5   Summary and Future Outlook

In this chapter strategies for engineering the band gap in a variety of GNRs have been discussed. The first synthesis of the 11-AGNR, part of the low band gap $3p+2$ family that is especially intriguing for FET devices has been reported. The 11-AGNRs that are discussed here are not the requisite length for device fabrication. Future work on this project should take advantage of Matrix Assisted Deposition (MAD) techniques to form long polymers that will ultimately yield 11-AGNRs upon cyclodehydrogenation. One such polymer is shown below as it incorporates the oligoterphenyl used to synthesize the 9-AGNR and the precursor molecule for 13-AGNR in Ref. 29. **3-5** can be synthesized in solution via AA-BB polymerization which is not possible with surface-assisted methods. Annealing **3-5** to cyclodehydrogenation temperature should yield 11-AGNRs that can be used for future device fabrication.

3-5
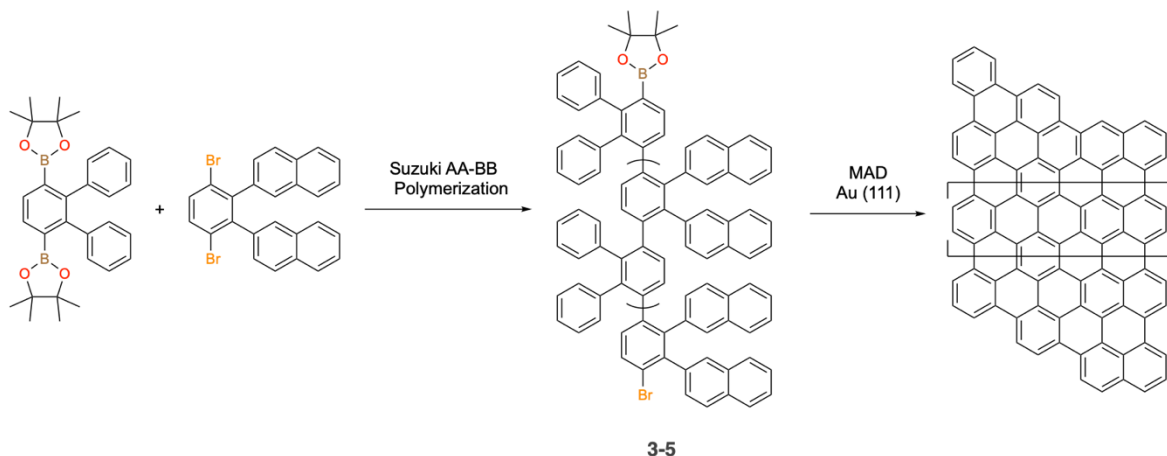
Additionally in this chapter, the first synthesis of GNRs with hybrid armchair/zigzag edge topology has been reported. In this section, design principles were introduced that show the placement of methyl groups in the precursor molecule is a critical parameter for the final structure. When the methyl groups are placed along the axis of polymerization, it can lead to deleterious side reactions and undesired final products.

Finally, the effect of edge doping in chevron GNRs is discussed. Here we show that to reduce the band gap via edge doping, the lone-pair in the dopant atom must overlap with the extended π-system of the chevron GNR. This overlap effectively widens the GNR and leads to a reduction in the band gap.

Chapter 4: Alternant Surface Catalyzed Bond Formation in Carbon Nanostructures

4.1 Introduction

Beginning with the pioneering work of Saw-Wai Hla, *et. al* in 2000, noble metal surfaces have been used as catalysts for elementary organic reactions[110]. In that work, iodobenzene molecules were dehalogenated with an STM tip and laterally manipulated on Cu(111) to form biphenyl and simulate the Ullmann coupling reaction. While a true Ulmann reaction uses Cu, Ni, or Pd as a catalyst, surface couplings can occur on metal surfaces including but not limited to Au, Ag, Cu, etc. These "Ullmann-like" couplings are particularly useful for the bottom-up synthesis of graphene nanoribbons, porophyrins[55,111] and other carbon nanostructures from halogenated precursors[112]. Nevertheless, surface catalyzed reactions over the last two decades have not been limited to the Ullmann coupling. The proliferation of STMs has allowed the study of organic reactions with unprecedented precision. The STM tip can act as a nanocatalyst to induce intramolecular couplings via dehalogenation[113], dehydrogentation[114], or desulfurization[115] reactions on inert surfaces like NaCl without the need for further lateral manipulation. Reaction intermediates can be characterized with atomic resolution for the first time providing valuable insight towards the understanding of organic mechanisms. Additionally, a myriad of thermally induced organic reactions are now accessible on noble metal surfaces including a variety of homocouplings[116], cross-couplings[117], and cyclizations[118]. However, all of these reactions are limited to formation of C–C bonds. There have been no studies into alternant bond formation and this chapters aim to fill that gap.

In this first section of this chapter, I will discuss attempts to introduce nitrogen heteroatoms in the chevron GNR scaffold. In order to fully cyclize the resulting GNR, it is necessary to form both C–N and N–N bonds, which have not been reported anywhere in literature. I will show the initial progress towards alternant bond formation within a well-established GNR framework and potential strategies for future growths.

The second half of this chapter will be devoted to nitrogen heteroatom dopants in the 7-AGNR scaffold. I will show multiple generations of precursor molecules that would in principle produce a nitrogen doped 7-AGNR. Although the attempts to synthesize a nitrogen doped 7-AGNR were unsuccessful, I was able to characterize the first C–N bond formation.

4.2 Core Heteroatom Doping in Chevron GNRs

4.2.1 Introduction

Since the seminal publication of Cai, *et. al* in 2010 launching the field of bottom-up GNR synthesis, the chevron GNR has remained one of the most studied scaffolds[31]. The precursor molecule contains a triphenylene core that results in a chevron-type GNR with alternating widths of 6-AGNRs and 9-AGNRs where the growth direction is templated by the Au(111) herringbone reconstruction. Moreover, X-ray photoelectron spectroscopy (XPS) analysis of GNRs after transfer through air show that chevron GNRs are inert under ambient conditions making them a particularly interesting candidate for device fabrication. However, all-carbon chevron GNRs have a wide quasiparticle band gap (> 3 eV) severely limiting potential applications. While the band gap can be reduced by increasing the width of GNR, the effect is not sufficient.
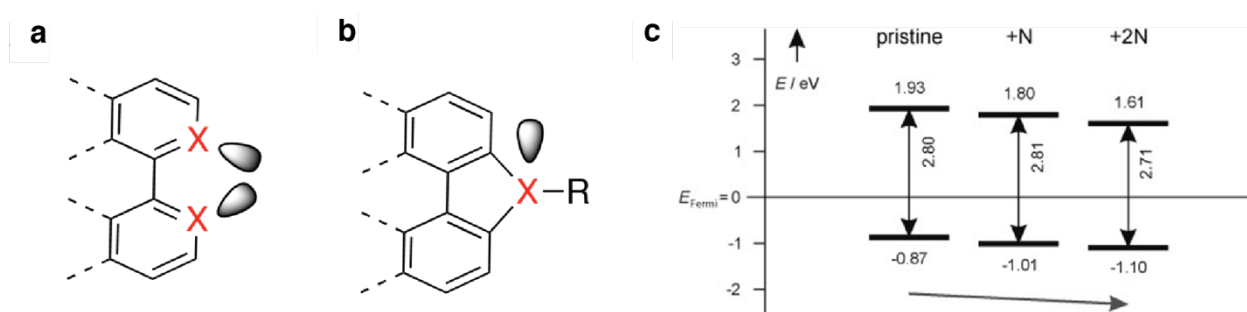
Figure 4.2.1 Schematic of Heteroatom Doping in Chevron GNRs a, Substitutional edge doping in Chevron GNRs where heteroatom lone pair is ***not*** conjugated with the extended π-system **b,** Substitutional edge doping in Chevron GNRs where heteroatom lone pair ***is*** conjugated with extended π-system **c,** Electronic structure when the edge doping is similar to **c**

An alternative approach to affecting the band gap involves the incorporation of substitutional heteroatom dopants within the GNR. The introduction of heteroatom dopants leads to new states within the band structure and can reduce the band gap without a subsequent lateral extension. To realize this effect, it is imperative that the orbitals from the dopant atom overlap with the extended π-system. For example, Bronner, *et. al* showed in 2013 that nitrogen edge dopants in the positions marked with an X in Figure 4.2.1a lead to rigid bandgap shift to lower energies[100]. This rigid bandgap shifts occurs because the nitrogen lone pair lies in a sp^2 orbital that is perpendicular to the extended π-system. As a result, the lone pair acts as an additional potential along the side of the GNR and then bandgap remains the same. The bandgap continues to shift to lower energies as the number of nitrogen atoms is increased, which is to be expected as the potential along the edge increases (Figure 4.2.1c). As shown in the previous chapter, edge dopant atoms that significantly overlap with the extended π-system (Figure 4.2.1b) can reduce the band gap in chevron GNRs by up to 0.3 eV. One strategy to further reduce the band gap is to move the heteroatoms more into the core of GNR. Dopant atoms within the core will contribute new electronic states that lie close to the Fermi level and lead to a substantially lower band gap.

4.2.2   Nitrogen Dopants in Chevron GNRs

As previously mentioned, the chevron GNR results from a precursor molecule featuring a triphenylene core that is particularly susceptible to a modular synthetic approach. Numerous studies have been published showing the edge modification of chevron GNRs aside from the work of Bronner, *et. al* and my own work[41,100]. Prior research in our own group showed the formation of nitrogen-edge doped chevron GNR heterostructures via thermal rearrangement of the precursor molecule and subsequent studies focused on the length-dependent heterojunction evolution within the ribbon. Other work involves the addition of carbonyl groups along the chevron edge and the incorporation of thiopene moieties. The common themes of these works are the following: 1) all the dopant atoms lie on the chevron edge and more importantly, 2) all carbon-heteroatom bonds were installed prior to the sublimation of the precursor molecule. As such, it is not clear if carbon-heteroatom bonds can be formed via thermal catalyzed surface reactions. The structure shown below in Figure 4.2.2 can address both issues simultaneously. Firstly, the four nitrogen dopant atoms are placed more towards the core of the GNR when compared to the precursor used by Bronner, *et. al* (Figure 4.2.2). More interestingly, the nitrogen dopant atoms now lie along the bay positions of the chevron GNR, and the formation of a fully planar structure necessitates the formation of C-N and N-N bonds.
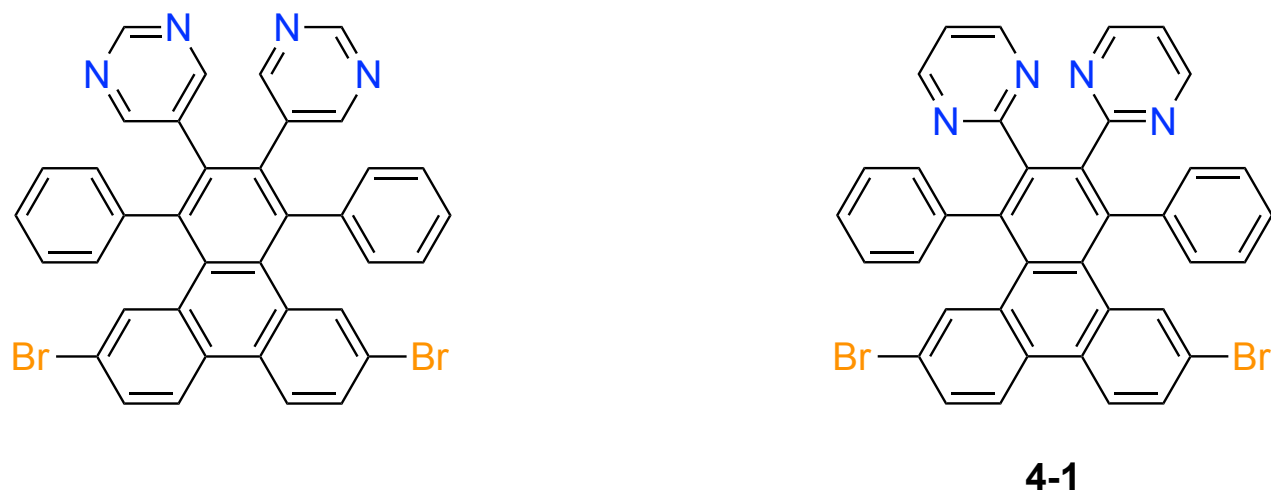
Figure 4.2.2 Nitrogen Doped Chevron GNR Precursors

Following the successful synthesis of **4-1**, shown in Figure 4.2.2, the precursor molecule was sublimed from a Knudsen cell evaporator onto a Au(111) surface held at 25 °C. The sublimation temperature was approximately 200 °C, consistent with previous depositions of chevron-type GNRs. Figure 4.2.3b shows **4-1** immediately after deposition. Unlike the unfunctionalized all-carbon chevron GNR precursor, which self-assembles into amorphous islands, **4-1** self-assembles into linear chains and it is possible to distinguish individual monomer units. Figure 4.2.3c shows the sample after annealing to 200 °C and isolated polymeric structures are clearly observed. This result stands in stark contrast to images obtained after annealing the all-carbon chevron to 200 °C where the chevron polymer can be found islands on the surface. Interestingly, the image in Figure 4.2.3c appears to have closed down quite significantly even at

the annealing temperature of 200 °C. Each of the isolated polymers contains a few bright lobes/protrusions that can be attributed to an incomplete cyclodehydrogenation as expected at 200 °C, but the core appears to have mostly cyclized. Attempts at getting high-resolution images were unsuccessful. Further annealing to 400 °C seems to produce regular planar structures, although they appear to be non-linear (Figure 4.2.3d). Bond-resolved STM (BRSTM) images displayed in Figure 4.2.3e confirms that the structure has not undergone complete cyclization, complicating subsequent analysis of the BRSTM images due to the lack of planarity. Based on these results, it is readily apparent that deleterious side reactions occur during the annealing phase between 200 °C and 400 °C. Varying the annealing rates to 400 °C and varying the annealing times at 200 °C yielded no discernible effect on the resulting structure. Attempts to anneal at intermediate temperatures similarly did not affect the final structure. While the results of this study were inconclusive, later work in this chapter (Section 4.4.2) implies that the N–N bond formation served as the most likely barrier to successful GNR formation. Future work on this scaffold should include only the formation of C–N bonds through the design of a novel precursor molecule.
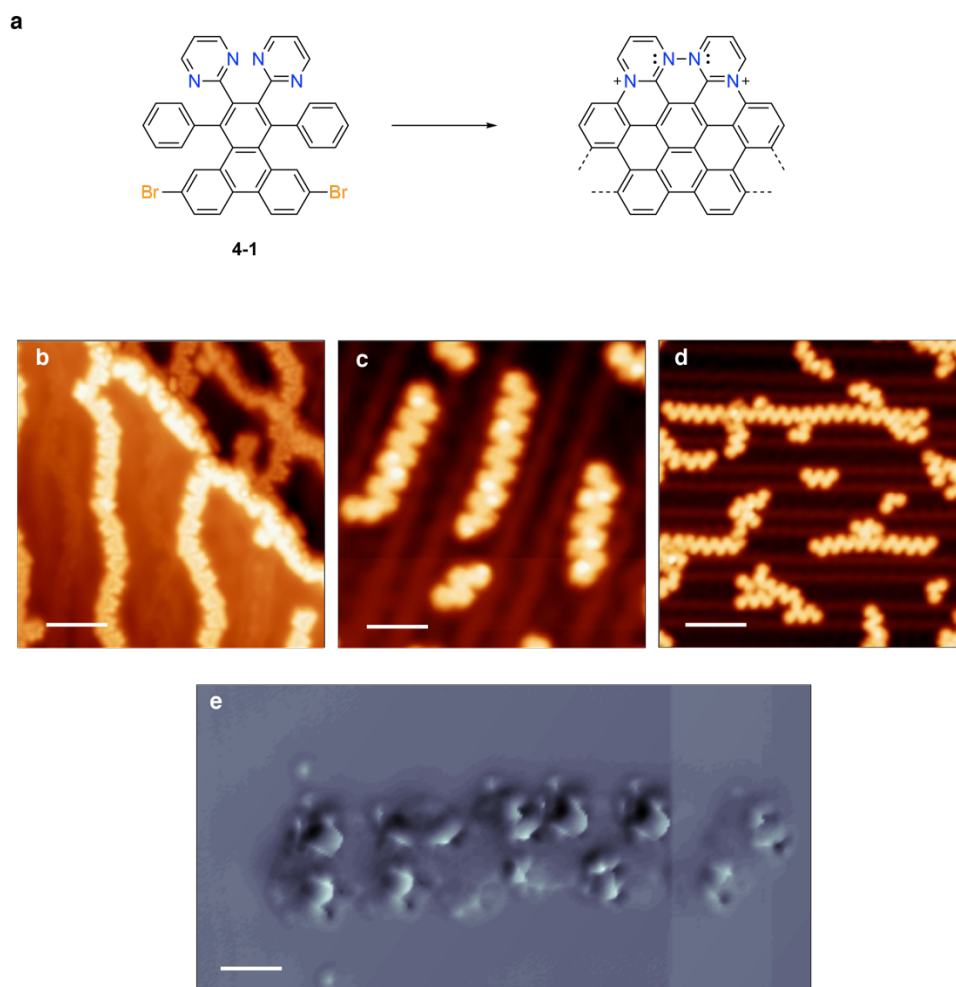
Figure 4.2.3 Bottom-Up Synthesis of 4N-Chevron GNR a, Schematic of 4N-Chevron GNR synthesis **b,** Topographic STM image of **4-2** after deposition ($V_s = 50$ mV, $I_t = 20$ pA, scale bar: 5 nm) **c,** Topographic STM image of panel A after anneal to 200 °C ($V_s = 50$ mV, $I_t = 20$ pA, scale bar: 5 nm) **d,** Topographic STM image of panel A after annealing to 400 °C ($V_s = 50$ mV, $I_t = 20$ pA, scale bar: 8 nm) **e,** Bond Resolved STM of GNRs from panel D ($V_s = 20$ mV, $I_t = 60$ pA $V_{ac} = 11$ mV, $f = 455$ Hz)

67

4.3 Core Heteroatom Doping in Armchair GNRs

4.3.1 Introduction

Armchair GNRs (AGNRs) represent the most robust and well-studied scaffold of GNRs, dating back to the theoretical work of Son, *et. al* in 2006 and Yang, *et. al* in 2007[22,23]. These publications established the fact that AGNRs can be divided into three distinct families based on their width ($3p$, $3p+1$, and $3p+2$ where p is an integer) where the band gap within each family is inversely proportional to the GNRs width. The first GNRs to be successfully synthesized via bottom-up fabrication were the 7-AGNR and 13-AGNR from the $3p+2$ family[27,31]. Although this family represents the AGNRs with the widest band gaps (> 2.5 eV), the relatively straightforward synthesis of 7-AGNR and 13-AGNR precursors allow ample opportunities to explore the effects of doping. Our own research group published the first study of edge doping in AGNRs, wherein sulfur atoms replaced alternating CH_2 groups along the edge of a 13-AGNR[39]. Unlike edge doping in chevron GNRs, the lone pairs on the trigonal planar S atoms have p orbital character and lie in conjugation with the extended π-system of the 13-AGNR. According to density functional theory (DFT) calculations within the local density approximation (LDA) framework, the overall band gap reduction was 0.2 eV, consistent with the results shown when edge doping chevron GNRs.
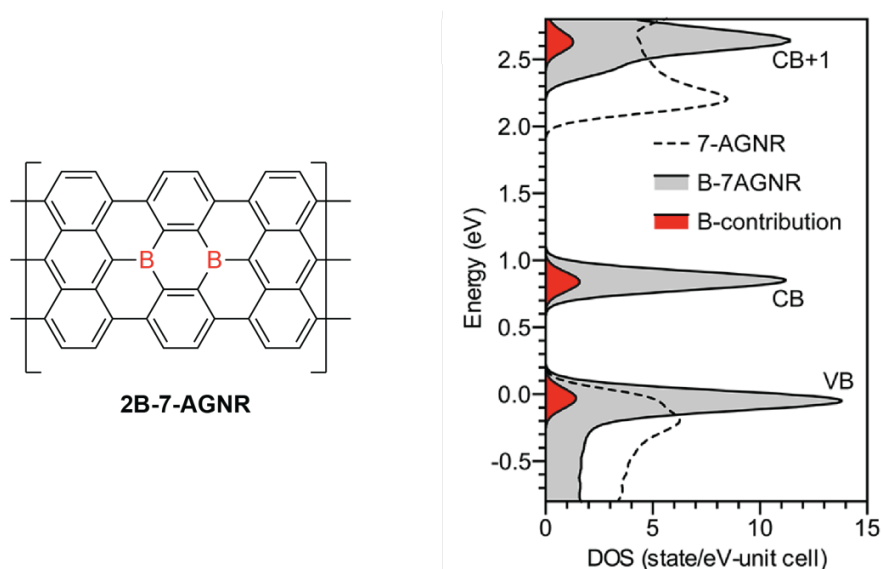
Figure 4.3.1 Electronic Structure of 2B-7-AGNR

On the other hand, the introduction of heteroatom dopants into the core of AGNRs has been shown to significantly alter the electronic structure because the orbitals contributed by dopant atoms are fully conjugated with the extended π-system and therefore introduce either filled or empty orbitals within band gap. Cloke, *et. al* and Kawai, *et. al* independently reported the replacement of carbon atoms along the backbone of a 7-AGNR with boron atoms (Figure 4.3.1)[40,101]. The boron atoms in the core contain an empty p-orbital in full conjugation with the extended π-system. Scanning tunneling spectroscopy (STS) results from both studies, along with

DFT calculations within the GW approximation confirm the B-doping introduces a low-lying acceptor state within the band gap. Later experiments by Pedramrazi, *et. al*, Carbonell-Sanroma, *et. al*, and Senkovsiky, *et. al* show that the dopant-derived states hybridize strongly with the underlying Au substrate preventing the exploration of the most interesting features of B-7AGNRs[119–121]. Nevertheless, all the C–B bonds are pre-formed, and the surface only catalyzes C–C bonds. One potential strategy to address both issues is to replace the boron atoms with nitrogen atoms, which should contribute filled orbitals instead of empty orbitals and more importantly should interact less strongly with the underlying Au (111) substrate and offer potential pathways towards alternant bond formation. Three potential N-7-AGNR structures are shown below with the corresponding electronic structures (Figure 4.3.2). All three structures would ultimately result in metallic GNRs.
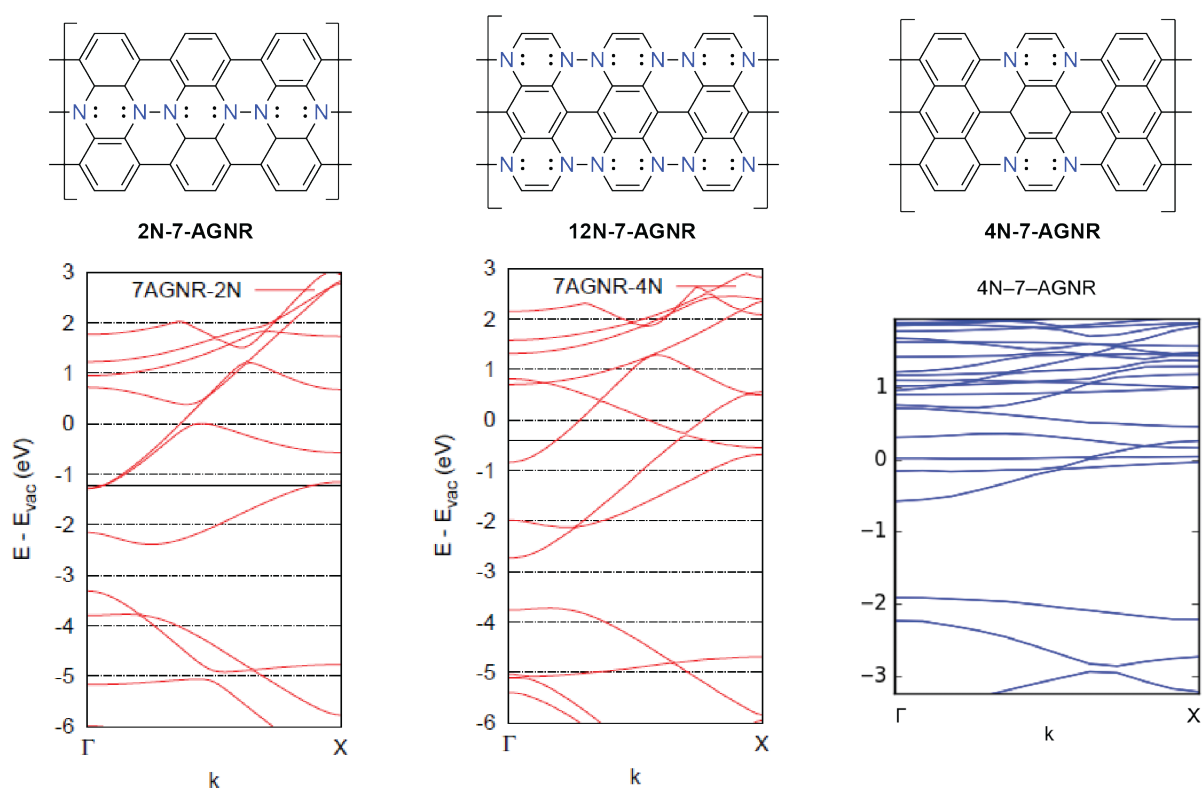
Figure 4.3.2 Electronic Structure of N-doped AGNRs

The first proposed structure has a similar dopant concentration to the 2B-7-AGNR that has been reported in literature. This structure would require the formation of N–N bonds on the surface, which has never been reported. The Fermi level is represented by a solid black line and two bands slightly overlap with the Fermi level insinuating that the 2N-7-AGNR may exhibit weak metallicity. In the 12N-7-AGNR, the metallicity is immediately obvious from the electronic structure calculations at the DFT-LDA level as three bands clearly cross the Fermi level (represented by a solid black line). Similarly, this GNR builds off the themes of the previous section as the successful synthesis would require the formation of N–N bonds. The metallic character in 4N-7-AGNR is more subtle because the band structure contains a wide gap, but the

increased nitrogen content pushes the Fermi level into the conduction band, thus inducing metallicity. In this figure, the y-axis represents the total energy with respect to the Fermi level. Once more, this precursor necessitates alternative bond formation, albeit C–N bonds, to produce the desired structure.

4.3.2   Synthesis of 2N-7-AGNR

The synthesis of the 2N-7-AGNR shown in Figure 4.3.2 would result from precursor **4-2** shown in Figure 4.3.3. The results of the sublimination of **4-2** from a Knudsen cell evaporator onto an Au(111) substrate held at 25 °C are displayed in Figure 4.3.3b. The monomer self-assembles into a complex 2D array that can be found consistently on the Au(111) surface. Subsequent annealing to 400 °C to induce polymerization and cyclodehydrogenation yields the images shown in Figure 4.3.3c. At first glance, the cyclodehydrogenation looks successful and the surface contains many extended linear structures. Zoom-in images in Figure 4.3.3d show that regrettably as opposed to the expected 2N-7-AGNR structures, these images appear to contain a GNR with a regularly spaced sawtooth-type edge structure. High resolution BRSTM images were not taken because it is clear from the topographic STM scans that the desired GNR has not been formed. Instead, the images in Figure 4.3.3d implies that **4-2** polymerizes to the planar **4-3** and each **4-2** cannot rotate as necessary to undergo the correct cyclization for a 2N-7-AGNR.

4-2
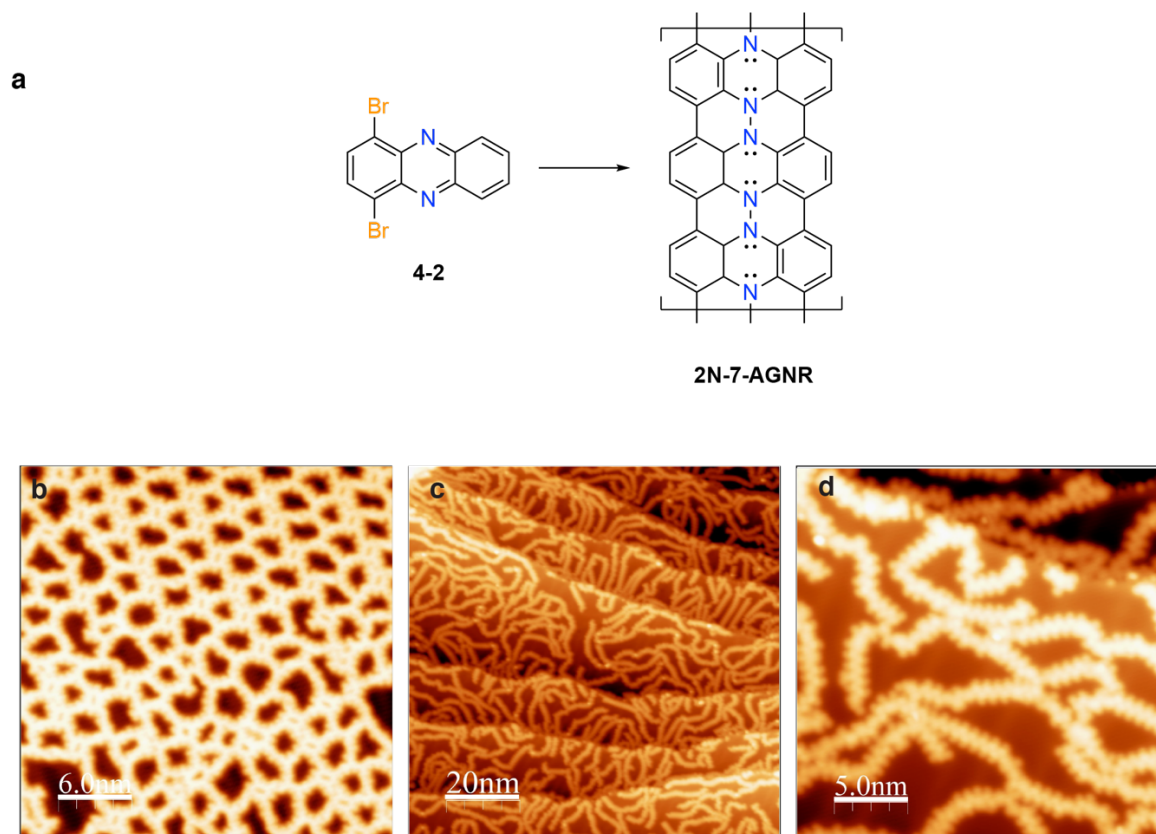
2N-7-AGNR

Figure 4.3.3 Bottom-Up Synthesis of 2N-7-AGNR a, Schematic of 2N-7-AGNR **b,** STM Topographic image of **4-2** after deposition (V_s = 50 mV, I_t = 20 pA) **c,** STM Topographic image of panel B after annealing to 400 °C (V_s = 50 mV, I_t = 20 pA) **d,** Zoom-In STM Topographic image of panel **c** (V_s = 50 mV, I_t = 20 pA)

4-3
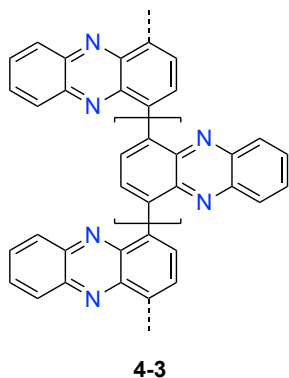
Figure 4.3.4 Hypothesized 2N-7-AGNR Polymer Structure

Following the unsuccessful depositions of **4-2**, a tetrabrominated precursor (**4-4** in Figure 4.3.5) was synthesized to try to force the correct polymerization. **4-4** was sublimed onto an Au(111) substrate held at room temperature and Figure 4.3.5b shows the precursor immediately after deposition. As expected, the self-assembly displays a similar 2D pack to precursor **4-2**. Woefully, attempts to anneal **4-4** to 400 °C in order induce polymerization and cyclodehydrogenation yielded similar sawtooth edge structures (Figure 4.3.5c and Figure 4.3.5d). Future attempts to synthesize the 2N-7-AGNR will require a novel precursor molecule that avoids the polymerization shows in Figure 4.3.4.
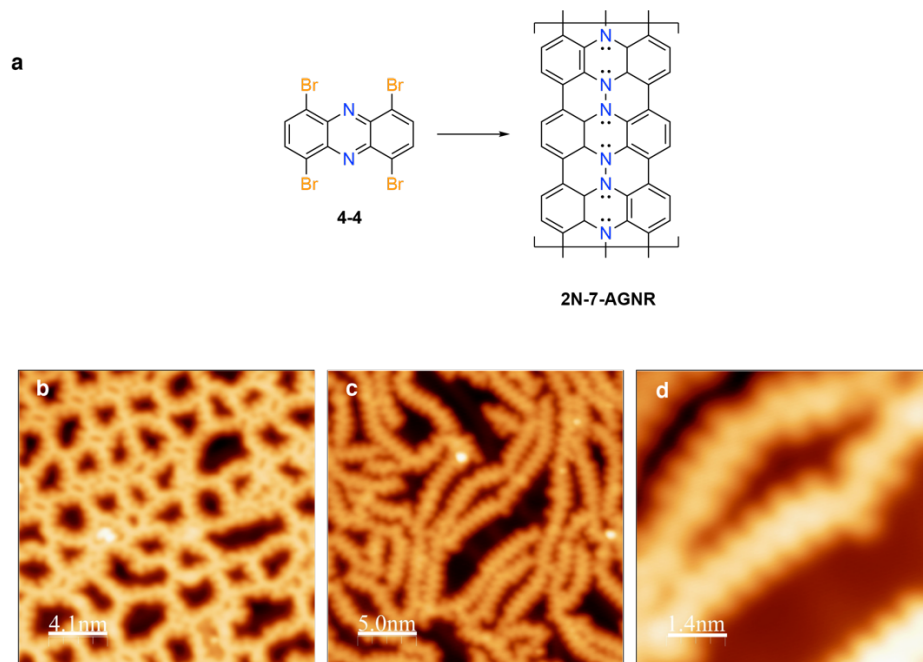
Figure 4.3.5 Bottom-Up Synthesis of 2N-7-AGNR via Gen-2 Precursor a, Schematic of 2N-7-AGNR Synthesis (V_s = 50 mV, I_t = 20 pA) **b,** STM Topographic image of **4-4** immediately after deposition (V_s = 50 mV, I_t = 20 pA) **c,** STM Topographic image of panel B after annealing to 400 °C **d,** Zoom-in STM Topographic image of panel **c** (V_s = 50 mV, I_t = 20 pA)

4.3.3   Synthesis of 12N-7-AGNR

The heavily nitrogen doped AGNR in Figure 4.3.2 (12N-7-AGNR) would stem from precursor molecule **4-5** in Figure 4.3.6. This molecule contains 28.5% nitrogen (8 nitrogen atoms out of 28 total atoms) and the expected band structure is metallic with four bands crossing the Fermi level. Additionally, **4-5** is structurally similar to the dibromobisanthracene (DBBA) molecule used to synthesize the 7-AGNR. Owing to this similarity, it is expected that a successful deposition of **4-5** offers the best platform to study the feasibility of N–N bond formation. Attempts to deposit **4-5** proved to be incredibly challenging due to difficulty isolating sufficient amounts of the molecule. Figure 4.3.6B shows an Au(111) substrate following the sublimation of **4-5** from a Knudsen cell evaporator. While it is possible to see self-assembled structures that resemble DBBA (Figure 4.3.6C), as expected, the surface is also coated with foreign substances. After further annealing to 200 °C to induce polymerization, the Au(111) surface was completely clean, and the herringbone reconstruction was clearly visible. Attempts to obtain a clean deposition of only **4-5** or to increase the amount of **4-5** on the surface was not possible before subliming all the molecule. Deposition attempts of **4-5** that had adhered to the walls of borosilicate test tube vials only served to produce dirty Au(111) substrates. Any future experiments on this system would require the synthesis of greater amounts of **4-5.**
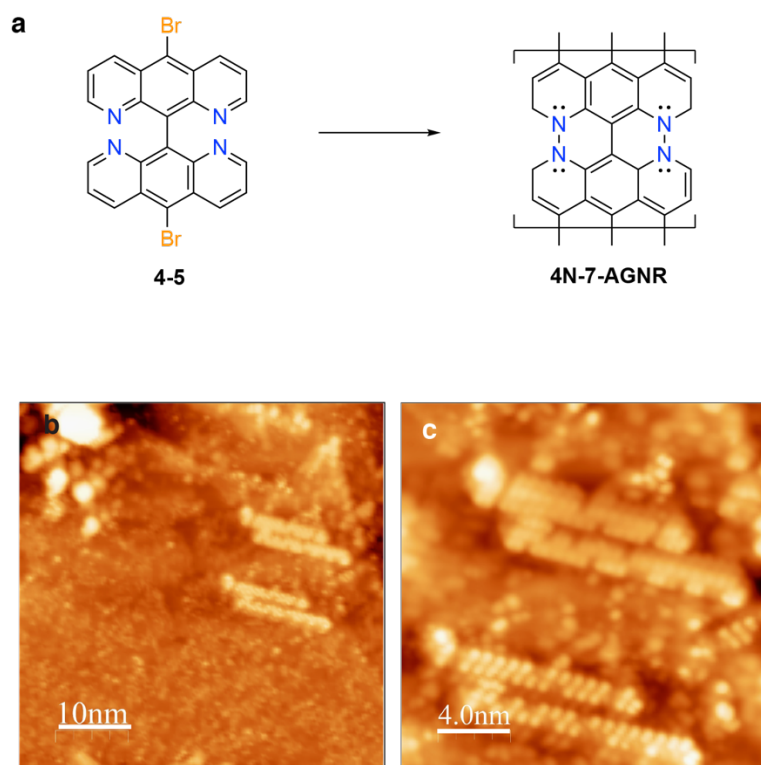
Figure 4.3.6 Bottom-Up Synthesis of 4N-7-AGNR a, Schematic of 4N-7-AGNR Synthesis **b,** STM Topographic Image of **4-5** immediately after deposition (V_s = 50 mV, I_t = 20 pA) **c,** Zoom-In STM Topographic Image of panel B (V_s = 50 mV, I_t = 20 pA)

4.4 Covalent C–N Bond Formation Through a Surface-Catalyzed Thermal Cyclodehydrogenation

4.4.1 Introduction

Oxidative cyclodehydrogenation reactions have found extensive use in the synthesis of extended polycyclic aromatic hydrocarbons (PAH). Solution-based *Scholl* and *Kovacic* reactions among many others, which rely on Lewis acid/oxidant combinations, have widely been used to induce the intramolecular cyclodehydrogenation of carefully designed *oligo*-arene precursors into extended PAHs. The emergence of bond-resolved SPM characterization techniques along with an expanded understanding of surface catalyzed reaction mechanisms[122] has even provided access to PAH structures featuring high energy ground states[123–125], open shell electron configurations[126], and highly reactive unsaturated spin systems[114]. One of the most common approaches relies on a thermally induced 6π electrocyclization of an *oligo*-arene precursors that is either preceded or followed by the transfer of two hydrogen atoms to the underlying metal surface[127]. The thermal activation barrier for this process varies with the underlying substrate and to a lesser extent with the structure of the molecular precursor but generally requires annealing temperatures ranging between 300–450 °C[128,129]. While this approach has been broadly applied to the formation of covalent C–C bonds on Au, Ag, and Cu surfaces the analogous reaction establishing covalent C–heteroatom bonds has never been observed. While a wide variety of heteroatoms (e.g. N, S, O, B) have been used to replace C–H groups along the edges of PAHs[41,100,130,131], the electronically much more interesting substitution of trigonal planar carbon atoms at the center of extended π-system remains rare. Access to these backbone-substituted PAHs has exclusively relied on the pre-assembly of all carbon–heteroatom bonds present in the product at the *oligo*-arene precursor stage[40,46,139–141,101,132–138].

The first example of a surface catalyzed cyclodehydrogenation that leads to the formation of covalent C–N bonds in an extended PAH is reported. The thermally induced intramolecular cyclodehydrogenation of pyrazino[2,3-g]quinoxalines **4-6a**–**c** (Scheme 1) on Au(111) or Ag(111) surfaces proceeds at unusually low temperatures and leads to the formation of four covalent C–N bonds in the tetraazateranthene **4-7**.

4-6a R = H
4-6b R = Br
4-6c R = I

4-7
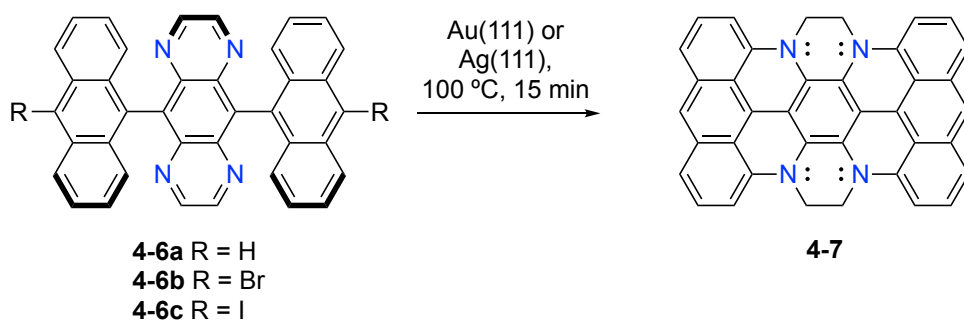
Figure 4.4.1 Scheme of Tetraazateranthene Synthesis

4.4.2 Synthesis of N-Doped Teranthene
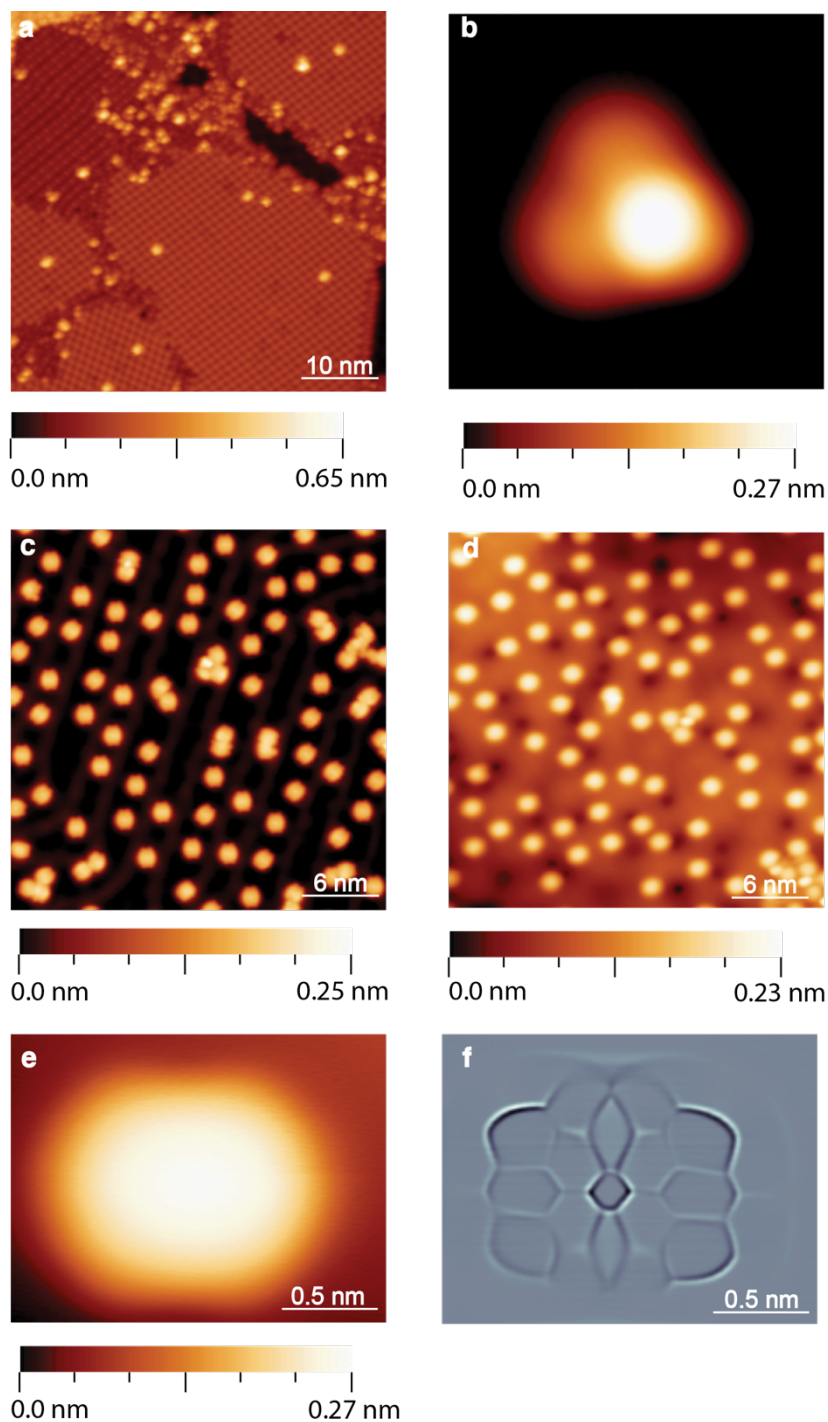
Figure 4.4.2 Bottom-Up Synthesis of Tetraazaanthene STM topographic image of **(a)** self-assembled islands and **(b)** an isolated molecule of **4-6a** on a Au(111) surface. STM topographic image of **(c)** a Au(111) and **(d)** a Ag(111) surface after annealing to 100 °C showing the clean transformation of **4-6a** to **4-7**. **(e)** STM topographic and (F) bond resolved STM (BRSTM) image of fully cyclized tetraazateranthene **4-7** on Au(111). **((a)–(e):** $V_s = 50$ mV $I_t = 20$ pA; **(f)** $V_s = 0$ mV, f_V: 455 Hz, $V_s = 10$ mV)

Pyrazino[2,3-g]quinoxalines **4-6a**–**c** were deposited from a Knudsen cell evaporator in ultra-high vacuum (UHV) onto Au(111) and Ag(111) surfaces held at 24 °C. Figure 4.4.2a shows a representative STM topographic image (5 K) of self-assembled multilayer islands of **4-6a** on a Au(111) crystal surface. Isolated molecules of **4-6a** adsorb preferentially in a conformation that places the anthracenyl groups at either end of the molecule nearly coplanar to the underlying surface (Figure 4.4.3). One side of the central pyrazino[2,3-g]quinoxaline ring protrudes high above the plane of the molecule and appears as a characteristic bright feature in in the topographic image in Figure 4.4.2b. Annealing of molecule decorated surfaces at temperatures as low as 75–100 °C for 15 min induces a thermal cyclodehydrogenation of all *peri*-positions to form tetraazateranthene **4-7** (Figure 4.4.2c,d). STM images on Au(111) or Ag(111) reveal a sub-monolayer coverage of the surface with discrete rectangular structures measuring 0.95 ± 0.05 nm, 1.20 ± 0.15 nm, and 0.19 ± 0.02 nm in width, length, and height, respectively (Figure 4.4.2E). Bond-resolved STM (BRSTM) imaging, where in the STM tip is functionalized with a carbon monoxide (CO) molecule to conduct imaging in the Pauli repulsive regime[142,143], confirms the tentative structural assignment and shows the fully fused core along with the four covalent C–N bonds of tetraazateranthene **4-7** (Figure 4.4.2f). Large area scans on Au(111) and Ag(111) highlight the remarkable selectivity and the high yield of this transformation (Figure 4.4.2c,d). Even in the presence of the thermally labile C–Br or C–I bonds in **4-6b** and **4-6c** the cyclodehydrogenation to form **4-7** proceeds at temperatures < 100 °C, precluding the expected radical step-growth polymerization on the surface (Figure 4.4.4).
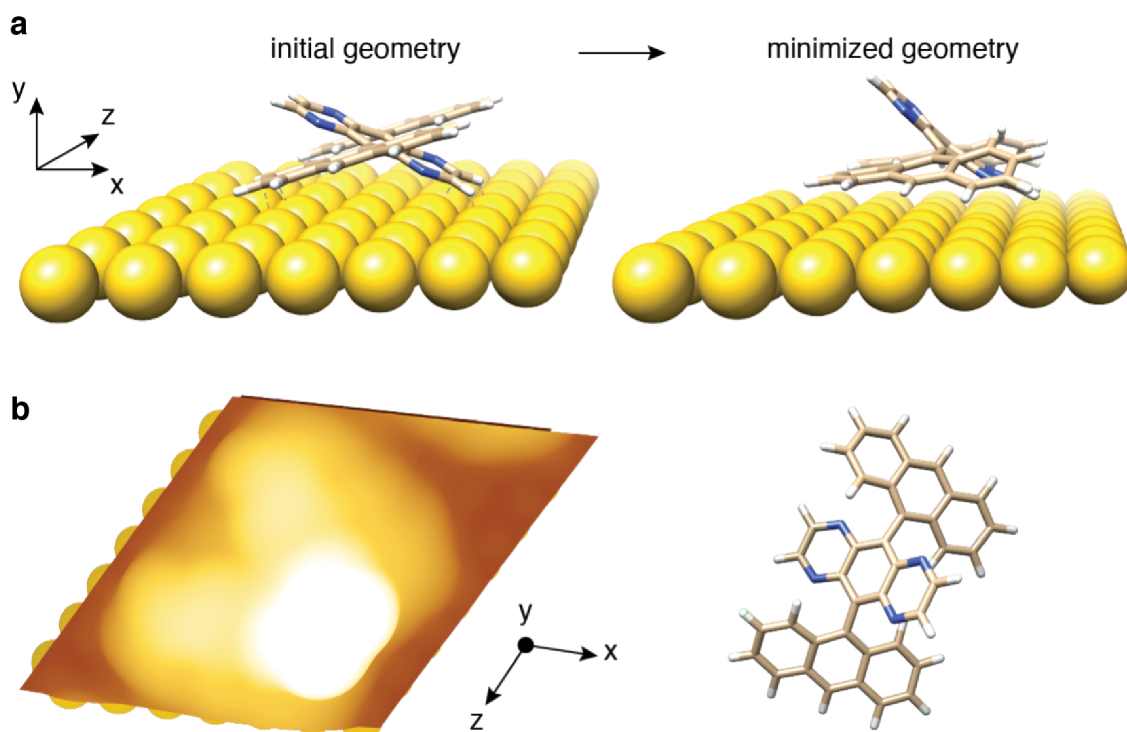
Figure 4.4.3 Optimization of Adsorption Geometry of 4-6a (a) Comparison of starting geometry (left) and final geometry (right) for **4-6**. Starting geometry is placed 3.5 Å from the surface, central torsion angle between anthracene and pyrazino[2,3-*g*]quinoxaline moieties is 40°, four Au layers are used in calculation. **(b)** Simulated STM image of **4-6**
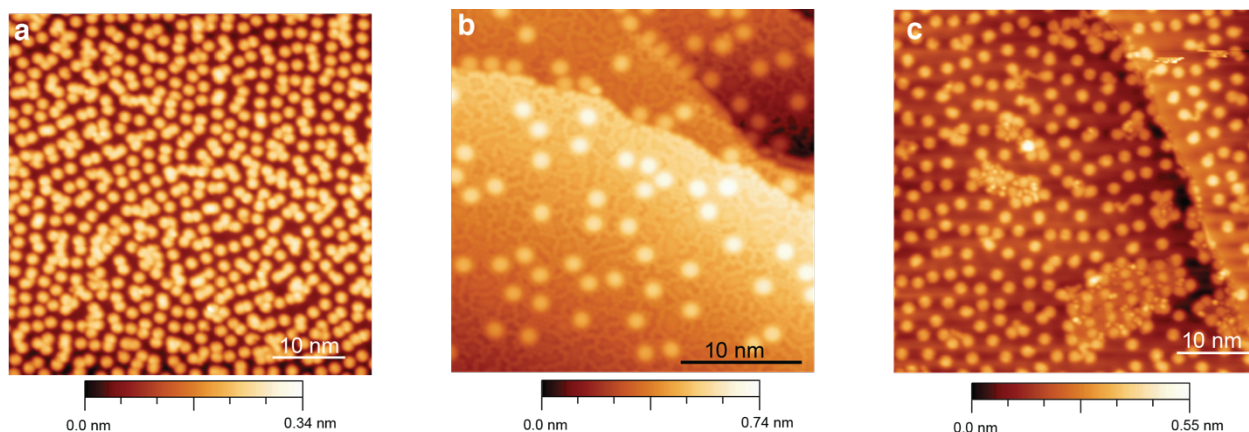
Figure 4.4.4 STM Topographic Images of 4-6b,c on Au(111) and Ag(111) a, SPM topographic image of a high-coverage deposition of **4-6b** on a Au(111) surface followed by annealing to 250 °C. The predominant molecular species on the surface is the cyclized product **4-7**. The few fused species observed on the surface can be attributed to random C–H bond dissociation processes that lead the formation of dimers and trimers. No structures that extend via the halogenated positions can be identified on the surface observed. **b,** SPM topographic image of a high-coverage deposition of **4-6b** on a Ag(111) surface followed by annealing to 100 °C. The predominant molecular species on the surface is the cyclized product **4-7** The closely packed spherical structure below the layer of molecules is atomic bromine adsorbed to the Ag(111) surface. **c,** SPM topographic image of a high-coverage deposition of **4-6c** on a Au(111) surface followed by annealing to 100 °C. The predominant molecular species on the surface is the cyclized product 1. The closely packed spherical structure below the layer of molecules is atomic iodine adsorbed to the Au(111) surface. **((a)–(c)):** $V_s = 50$ mV, $I_t = 20$ pA)

4.4.3   Electronic Structure of Tetraazateranthene

Differential conductance (dI/dV) point spectra collected above the nitrogen atoms along the armchair edge of tetraazateranthene **4-7** (inset Figure 4.4.5) reveals two characteristic features associated with an occupied and an unoccupied state at a sample bias of –0.6 V and +1.6 V, respectively (Figure 4.4.5). dI/dV maps recorded at the corresponding energies show the spatial distribution of the local density of states (LDOS) across the surface of the adsorbed molecule. In an effort to assign the peaks in the differential conductance spectra to molecular frontier orbitals density functional theory (DFT) calculations with local density approximation (LDA)[109] were performed, as well as a GW calculation which incorporates the electron self-energy in a many-electron Green function approach[24,144]. The peak at –0.6 V closely resembles the projection of the HOMO–2 orbital of tetraazateranthene, while the broader feature at +1.6 V is best represented by a superposition of the LUMO and the LUMO+1 orbitals. While the degeneracy between LUMO and LUMO+1 is not immediately apparent from calculations within the LDA framework alone, quasiparticle calculations using the GW correction confirm that LUMO and LUMO+1 of **4-7** are separated by $\Delta E < 50$ meV. An analysis of wavefunction symmetry of the frontier orbitals of tetraazaanthene **4-7** calculated in the gas phase (Figure 4.4.6) suggests strong hybridization of HOMO and HOMO–1 states with the underlying Au(111) or Ag(111) substrate. The resulting significant broadening prevents an unambiguous assignment of the HOMO and HOMO–1 feature in the dI/dV spectrum.
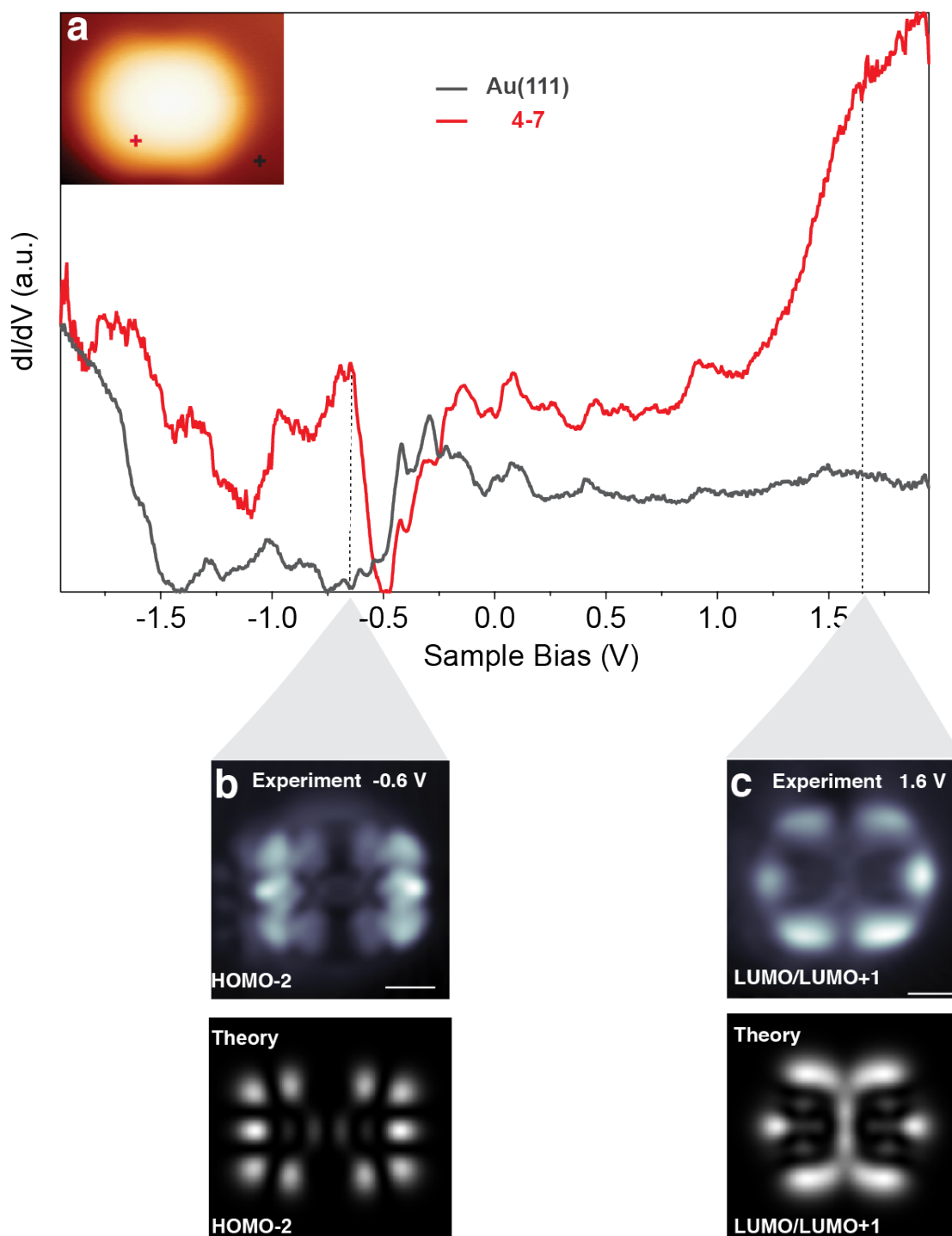
Figure 4.4.5 Electronic Structure of Tetraazaanthene (a) STM dI/dV point spectrum of **4-7** on Au(111). Experimental dI/dV spatial maps and calculated position dependence of the LDOS map of states with energy fixed at **(b)** $V_s = -0.6$ V ($I_t = 0.60$ nA) and **(c)** $V_s = +1.6$ V ($I_t = 0.75$ nA). Calculated lateral spatial distribution of LDOS at fixed energy is evaluated at a height of 4 Å above the plane.
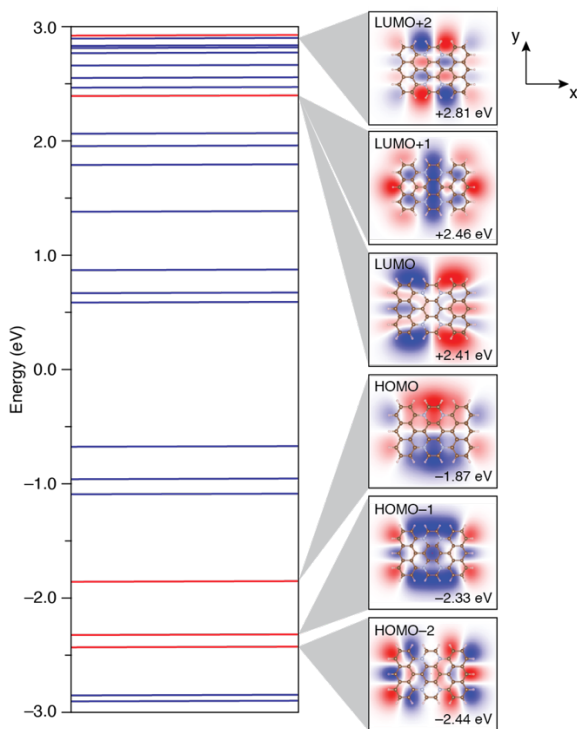
Figure 4.4.6 Gas Phase DFT and GW Energy Levels and Wavefunctions of 4-7 Red/blue color in the wavefunction plot show the plus/minus sign of the wavefunction. The energy levels marked below the wavefunction plots are GW energy levels, and they are up to a reasonable arbitrary constant shift.

4.4.4 Mechanistic Analysis of C-N Bond Formation

Further insight into the mechanism of the surface-assisted cyclodehydrogenation of **4-6a** including the formation of four C–N bonds was obtained from *ab initio* calculations using the all-electron FHI-aims code[145]. The reaction-energy landscape including all transient intermediates and transition states was determined using density functional theory (DFT) at PBE+VdW+ZORA level for four discrete cyclization sequences. While the calculated rate determining transition states range between $\Delta E^{\ddagger} = 0.6$–3.5 eV above the starting materials (**4-6a** physisorbed on Au(111)), in the following discussion we will focus only on the most plausible mechanism involving the lowest overall activation barrier (Figure 4.4.7).

An initial step involving the concerted formation of two C–N bonds between the physisorbed side of the pyrazino[2,3-g]quinoxaline and the two anthracene units represents the rate determining transition state and is associated with an activation barrier of $\Delta E^{\ddagger} = +0.6$ eV. The transition state structure **TS1** is characterized by an allylic diradical that undergoes a rapid suprafacial [1,2] hydrogen shift (red H atoms in **TS1**) to give the stabilized benzylic radical intermediate **Int1**. The subsequent transfer of the two hydrogen atoms closest to the substrate (black H atoms in **Int1**) to the Au(111) surface is virtually barrierless ($\Delta E^{\ddagger} = +0.3$ eV) and leads to the partially cyclodehydrogentated intermediate **Int2** featuring two out of the four C–N bonds in the tetraazateranthene **4-7**. The cyclization of the remaining pyrazino[2,3-g]quinoxaline wing protruding from the surface proceeds through a single transition state, albeit with a higher activation barrier ($\Delta E^{\ddagger} = +1.1$ eV). The two remaining C–N bonds are formed through an approach of the pyrazino[2,3-g]quinoxaline wing from above the plane of the anthracenes placing the red hydrogen atoms in the allyl diradical-like transition state **TS3** in a position pointing directly

78

towards the underlying Au(111) surface. Direct transfer of these hydrogen atoms to the surface yields the fully cyclized tetrateranthene **4-7**.
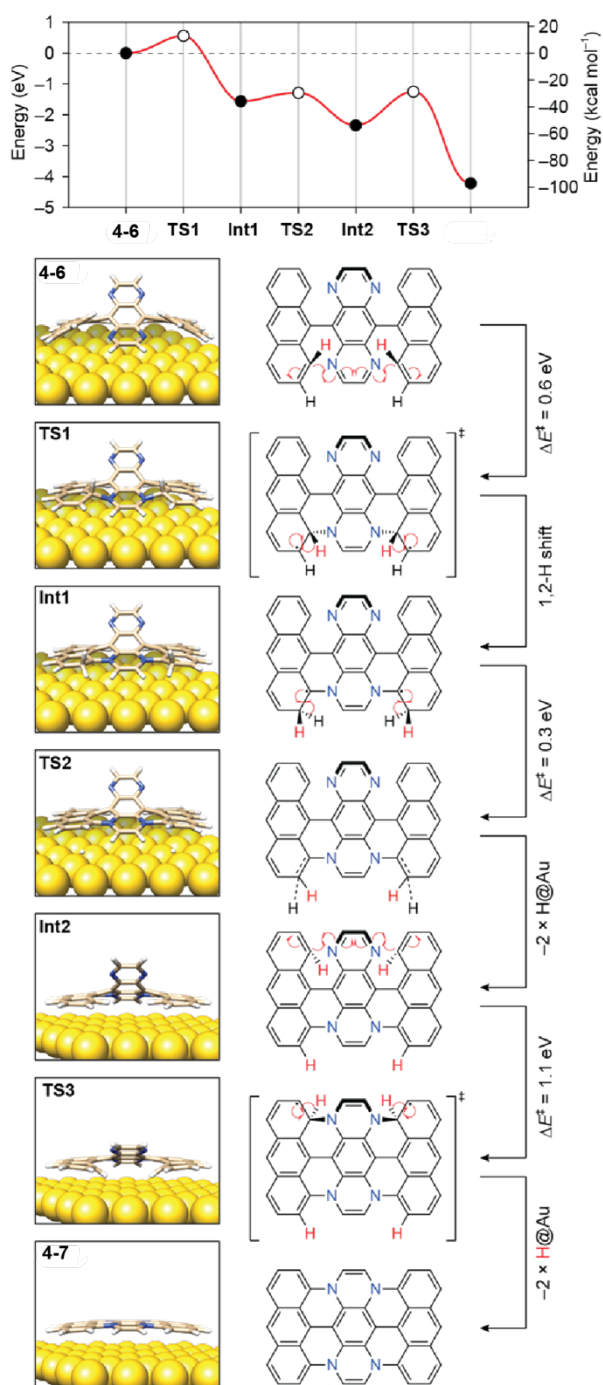
Figure 4.4.7 Calculated energy diagram for the stepwise cyclodehydrogenation of 4-6a to 4-7 The graph shows the *ab-initio* energy landscape for intermediates and transition states along the reaction pathway from **4-6a** to **4-7**. Calculated activation energies are shown next to the reaction arrows.

In summary, the experimental demonstration and detailed mechanistic investigation of an intramolecular cyclodehydrogenation that leads to the formation of four covalent C–N bond on

Au(111) and Ag(111) surfaces was reported. SPM imaging reveals that molecular precursors **4-6a**–**c** adsorb in a chair-like conformation on metal substrates and undergo a clean conversion to tetraazateranthene **4-7** under mild conditions. Bond resolved STM and differential conductance spectroscopy unambiguously confirm the structural assignment. Mechanistic analysis based on *ab-initio* DFT calculations reveals the most likely stepwise mechanism featuring a rate determining barrier of only $\Delta E^{\ddagger} = 0.6$ eV, consistent with the experimentally observed reaction conditions ($T = 75$–100 °C, 15 min). This work expands our mechanistic understanding of oxidative C–N bond formation reactions on metal surfaces and provides a useful tool for the incorporation of substitutional heteroatom dopants into the extended π-backbone of bottom-up synthesized nanographene.

4.5 Summary and Outlook

In this chapter different strategies towards to the formation of carbon-heteroatom bonds via surface catalyzed reactions have been reported. The first half of this chapter focuses on attempts at C–N and N–N bond formation within the chevron GNR scaffold. While it is not clear from the data presented in this chapter if C–N bond formation can readily occur, it does appear obvious that N–N bond formation cannot occur within this system. Future work on this project should focus exclusively on C-N bond formation to determine the efficacy of this route. An alternative monomer is necessary to continue exploration along this route.

The second half of this chapter is devoted to the core heteroatom doping in the AGNR scaffold. Once again, it is not possible to say definitively whether the formation of N–N bonds is feasible. In this case, there was not enough molecule to conduct all the necessary experiments. Nonetheless, this chapter the first surface catalyzed formation of C–N bonds is reported. The C–N bond formation occurs at a much lower temperature when compared to C–C bond formation and prevents the formation of the polymer and subsequent GNRs. Future work in this project should focus on N–N bond formation and the design of a precursor molecule with a suitable synthesis.

Chapter 5: Topological Band Engineering in Graphene Nanoribbons

5.1 Introduction

Research on topologically induced states in carbon nanomaterials has peaked in the last five years following the 2016 Nobel Prize in Physics shared by Thouless, Duncan, Haldane, and Kosterlitz for theoretical discoveries of topological phase transitions and topological phases of matter. In particular, the low spin-orbit coupling in carbon is hypothesized to lead to long spin coherence times offering a new platform to realize robust spintronic devices[146]. Spintronic-based logic devices take advantage of the spin degree of freedom in electrons to reduce power consumption and standby leakage, which is of vital importance as logic devices continue scaling down. For this reason, there is an obvious need to develop defect-free materials that allow for the manipulation of spin on timescales that can be useful for device applications as any defect can be detrimental towards device performance. Armchair graphene nanoribbons (AGNRs) stand out as a promising material because of the ability to create atomically well-defined heterojunctions that can host exotic topologically-protected states at the interface[49]. Furthermore, AGNRs are known to be chemically robust compared to the highly reactive zigzag edge. The challenge is synthesizing controlled heterojunctions on metallic substrates from a single molecular precursor since on-surface sequence control is currently not possible. Topological phases can also be expected in cove-edge (Figure 1.2.9c) graphene nanoribbons which can be thought of as zigzag graphene nanoribbons with missing benzene rings[147].

The first section in this chapter will build on the innovating work of Rizzo, *et. al* that showed topologically induced bands in a 7/9-AGNR superlattice[49]. In this section, I will show progress towards the growth 9/7/9-AGNR oligomeric structures where two topological protected states are expected to form at the junction between the 7-AGNR and 9-AGNR segments creating a double quantum dot. Additionally, I will discuss the effect that the length of the wide band gap 7-AGNR segment has on the *J*-coupling between the topologically protected states.

The second section in this chapter will be focused on attempts to synthesize a 5/7-AGNR superlattice that should show similar topologically induced bands to the 7/9-AGNR superlattice. The 5/7-AGNR superlattice offers the unique ability to extend the smaller band gap segment (in this case the 5-AGNR) and I provide a method to achieve this.

The final section in this chapter is devoted to initial work on realizing metallicity in asymmetric cove-edge GNRs. Here, I will also examine alternative cove-edge GNR structures that take advantage of the newly developed Matrix Assisted Deposition (MAD) technique and could facilitate the design of more exotic GNRs.

5.2 Bottom-Up Synthesis of 9/7/9-AGNR Double Quantum Dot

5.2.1 Introduction

Mathematically, topology is defined as the study of geometric properties and spatial relations unaffected by continuous change of shape or size. Objects are grouped together in a topological class if they can be interconverted without any discontinuities. The classic example used to illustrate topological classes is the following—donuts and coffee mugs are members of the same topological class and therefore are identical because they each have one hole. On the other hand, perfect spheres (e.g., a baseball) belong to a different topological class because you must create a hole to convert a baseball into a donut. In condensed matter physics, a deeper comprehension of the topology of the electronic ground state has been critical in furthering our understanding of other properties of matter[148–150]. For example, it is well-established that bringing two insulators from different topological classes together it is possible to realize localized boundary states within the band gap[151–153]. In 2017, Cao, *et. al* married this concept with the emerging field of bottom-up GNR synthesis by deriving a relationship between the atomic structure and band topology of GNR systems[154]. This pioneering work connects the unit cell termination and ribbon width to topological invariants establishing the topological classes of various GNRs. The topological phases of GNRs are characterized by an integer (0 or 1), known as the Z_2 invariant. This Z_2 invariant comes from the Zak phase, which consists of two parts (intercell and intracell). When the system has mirror and/or inversion symmetries, only the intercell part contributes to the total Zak phase and it is quantized to values of 0 or π. The topological phase is determined by the sum of the intercell Zak phase for all bands and this quantity is related to Z_2 by the following relation, where γ^n represents the integral of the Berry connection

$$(-1)^{Z_2} = e^{i \sum_n \gamma^n}$$

Therefore, it is expected that topologically protected states will emerge at the interface of topologically distinct classes and the table below (Figure 5.1.1) describes the Z_2 invariants for various terminations.

Termination type	Zigzag (N = Odd)	Zigzag' (N = Odd)	Zigzag (N = Even)	Bearded (N = Even)
Unit cell shape				
Bulk Symmetry	Inversion/mirror	Inversion/mirror	Mirror	Inversion
Z_2	$\dfrac{1 + (-1)^{\left\lfloor \frac{N}{3} \right\rfloor + \left\lfloor \frac{N+1}{2} \right\rfloor}}{2}$	$\dfrac{1 - (-1)^{\left\lfloor \frac{N}{3} \right\rfloor + \left\lfloor \frac{N+1}{2} \right\rfloor}}{2}$		$\dfrac{1 - (-1)^{\left\lfloor \frac{N}{3} \right\rfloor}}{2}$

Figure 5.2.1 Characterization of electronic topology in AGNRs

The first experimental realization of topological interface states in GNRs came in Rizzo, *et. al* in a collaborative effort between our research group and the Crommie group in Physics at UC Berkeley[49]. Figure 5.2.2a shows the heterojunction between a 7-AGNR with $Z_2 = 0$ and a 9-AGNR with $Z_2 = 1$. This groundbreaking work hinged on the design of a molecular precursor that contains two distinct polymerization sites which cannot reach with each other due to steric effects (Figure 5.2.2b). Consequently, the precursor self-polymerized to form a regioregular 7/9-AGNR superlattice (Figure 5.2.2c), something that was not observed in previous attempts to create AGNR heterojunctions. Electronic structure characterization confirmed the presence of topologically induced bands within the 7-AGNR and 9-AGNR band gap (Figure 5.2.2d). As a direct follow-up to this work, I began working with a modified version of the precursor shown in Figure 5.2.2b to realize a 9/7/9-AGNR double quantum dot (Figure 5.2.3).
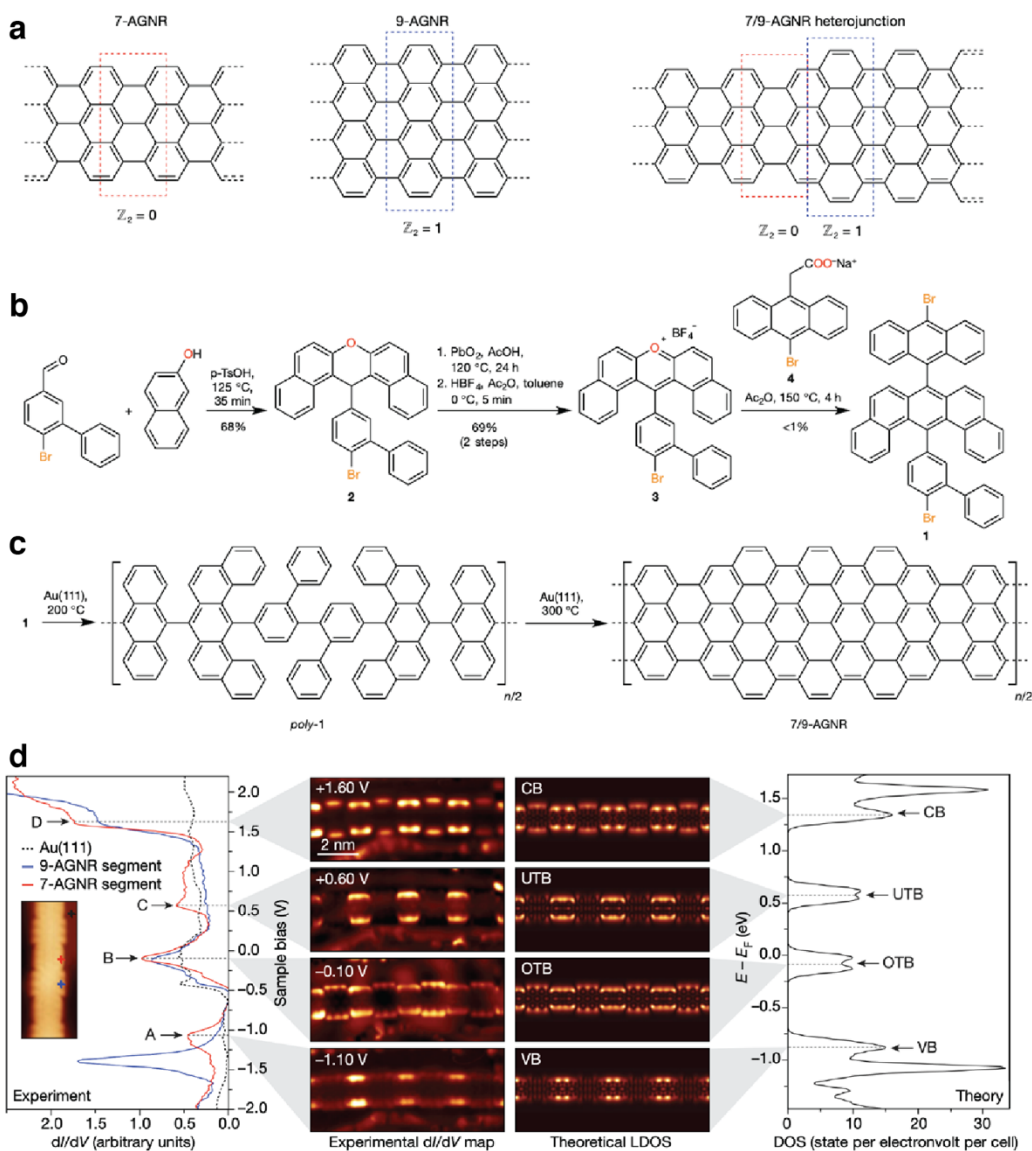
Figure 5.2.2 Characterization of 7/9-AGNR Heterojunctions a, Schematic of 7/9-AGNR Heterojunction States **b,** Synthesis of 7/9-AGNR Precursor **c,** Schematic of 7/9-AGNR Heterojunction **d,** Experimental and Theoretical Electronic Structure Characterization of 7-9/AGNR

5.2.2 9/7/9-AGNR Quantum Dot

One of the most salient features of the 7/9-AGNR superlattice work is the ability to accurate predict the topological bands with a standard two-band tight binding equation,

$$E_\pm(k) = \pm\sqrt{t_1^2 + t_2^2 + 2t_1 t_2 \cos(k)}$$

where t_1 represents the hopping amplitude across a 9-AGNR segment and t_2 serves as the hopping amplitude across a 7-AGNR. The band gap, $E_g = 2||t_1| - |t_2||$, resulting from the topological bands is highly tunable and can be used to induce metallicity in GNRs if t_1 and t_2 are equal. For the 7/9-AGNR superlattice, t_1 is 0.33 eV and t_2 is -0.07 eV as expected due to the differences in bandgap between the 9-AGNR and 7-AGNR. The narrow band gap in the 9-AGNR permits further penetration of the 7/9 interface state into the 9-AGNR segment and the subsequent strong overlap with adjacent interface states given the 9-AGNR segment length. By contrast, the wide band gap in the 7-AGNR segment prevents such strong overlap and allows for the possibility of creating localized states reminiscent of a quantum dot[49]. A modified version of the precursor in Figure 5.2.2b (**5-1**) was designed to create the 9/7/9-AGNR Double Quantum Dot (DQD) in Figure 5.2.3. The 9-AGNR segment in the DQD molecule is capped with a phenyl ring to prevent formation of topological end states that can couple to the 7/9 interface state. Therefore **5-1** can dimerize to form the DQD illustrated in Figure 5.2.3 and **5-1** can be co-deposited with DBBA to increase the length of the 7-AGNR segment and determine the correlation between 7-AGNR segment length and the J-coupling between interface states.
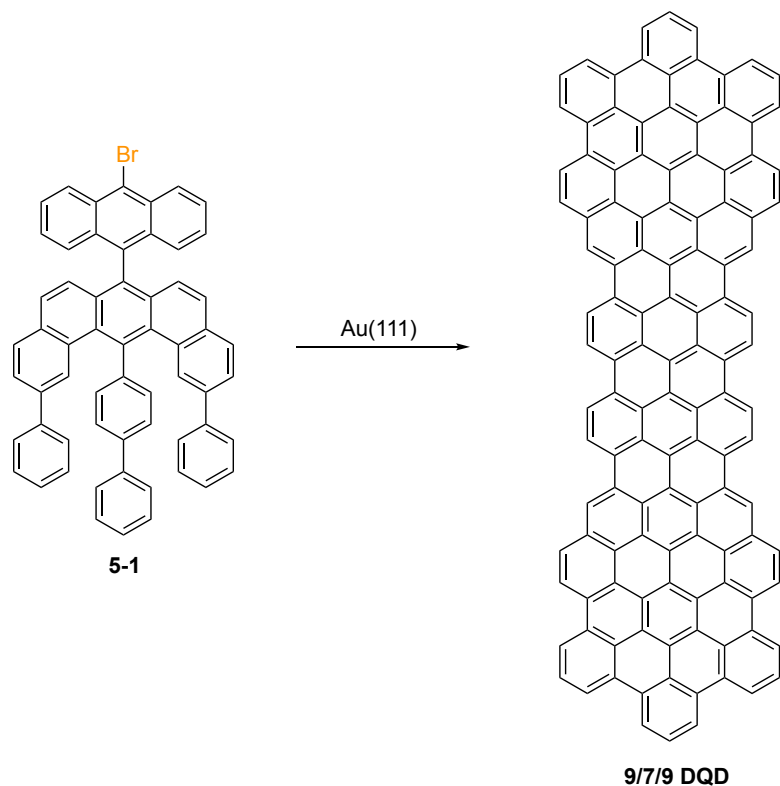
Figure 5.2.3 Schematic of 9/7/9 Double Quantum Dot Synthesis

Initial attempts to synthesize the 9/7/9-DQD molecule were conducted by subliming **5-1** from a Knudsen cell evaporator onto an Au(111) substrate held at 25 °C. STM topographic images of the precursor molecule immediately after deposition are presented in Figure 5.2.4a. While it is possible to find isolated monomers with at least two distinct lobes, the majority of monomers on the surface aggregate into islands in between the Au(111) herringbone reconstruction. Figure 5.2.4b shows the Au(111) after annealing to 300 °C to induce homolytic cleavage of the bromine atom and cyclodehydrogenation. At first glance, there appear to be dimers of the size expected for the 9/7/9-DQD molecule although the surface predominately contains cyclized monomers. Unfortunately, attempts to execute high resolution bond-resolved Scanning Tunneling Microscopy (BRSTM) imaging on suspected dimers were unsuccessful (Figure 5.2.4c) as the "dimer" consistently shifted during BRSTM scans preventing further measurements. Movement in the middle of a scan is entirely unexpected for the dimer structure shown in Figure 5.2.3 and suggests that the two monomers are not covalently linked. To test this hypothesis, BRSTM was carried out on the cyclized monomer to confirm that the monomer cyclized correctly. The BRSTM image unambiguously shows that the planar molecule on the surface is not the desired product. Instead, Figure 5.2.4d makes clear that the anthracene unit and bromine have cleaved prior to dimerization. Even after annealing to lower temperatures (i.e., 200 °C) there is no evidence of anthracene on the surface suggesting that the cleavage occurs during sublimation. The most probable cause for this adverse side reaction is that the temperature required to sublime **5-1** is sufficiently high to induce the cleavage of the anthracene subunit. To circumvent this issue, future experiments on **5-1** should focus on using the Direct Contact Transfer (DCT) method pioneered by Joseph Lyding to put the molecule on the Au(111) substrate[155].
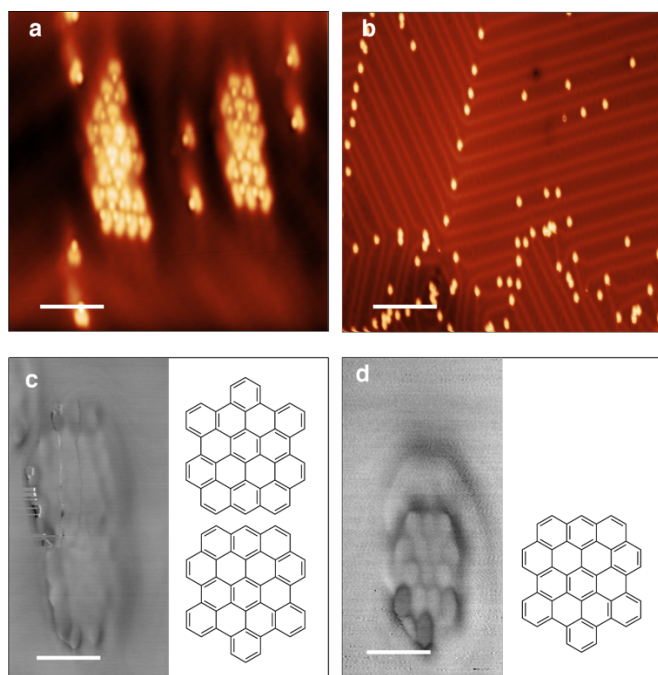
Figure 5.2.4 Bottom-Up Synthesis of 9/7/9 Double Quantum Dot a, STM Topographic Image of **5-1** after deposition at 25 °C (V_s = 50 mV, I_t = 20 pA, scale bar = 5 nm**) b,** STM Topographic Image of panel A after annealing to 300 °C (V_s = 50 mV, I_t = 20 pA, scale bar = 5 nm**) c,** BRSTM Image of suspected dimer (V_s = 10 mV, I_t = 280 pA, V_{ac} = 11 mV scale bar = 1.5 nm**) d,** BRSTM Image of **5-1** (V_s = 10 mV, I_t = 280 pA, V_{ac} = 11 mV scale bar = 1.5 nm)

5.3   Bottom-Up Synthesis of 5/7-AGNR Heterojunctions

5.3.1   Introduction

After the aforementioned successful synthesis of the 7/9-AGNR superlattice, the logical follow-up is to find additional heterojunctions that will produce topologically protected states. While there is a multitude of AGNR heterojunctions that would produce the desired topological interface states, the challenge is finding heterojunctions that can be realized from a single precursor molecule. The most synthetically accessible structure is the 5/7-AGNR superlattice shown below in Figure 5.3.1a which in principle can be synthesized from the precursor in Figure 5.3.1b. In the 5/7-AGNR superlattice, the 7-AGNR segment has a Z_2 invariant of 1 and the 5-AGNR segment has a Z_2 invariant of 0 leading to the expected topological interface state. Additionally, the 5/7-AGNR superlattice represents the narrowest possible topological junction molecule as any AGNRs with a width of less than five carbon atoms is not well-defined. Perhaps more interestingly, the 5-AGNR has a lower band gap than the 9-AGNR used in the previous section. This smaller band gap should lead to a larger hopping parameter and therefore the interface state should extend further into the 5-AGNR segment when compared to the 9-AGNR segment creating the possibility of significant overlap between the adjacent interface states. The larger hopping parameter is confirmed by theoretical calculations (Figure 5.3.1c) that predict a t_1 is 1.03 eV and t_2 is 0.46 eV when fitting the topologically induced bands to the two-orbital tight binding model.
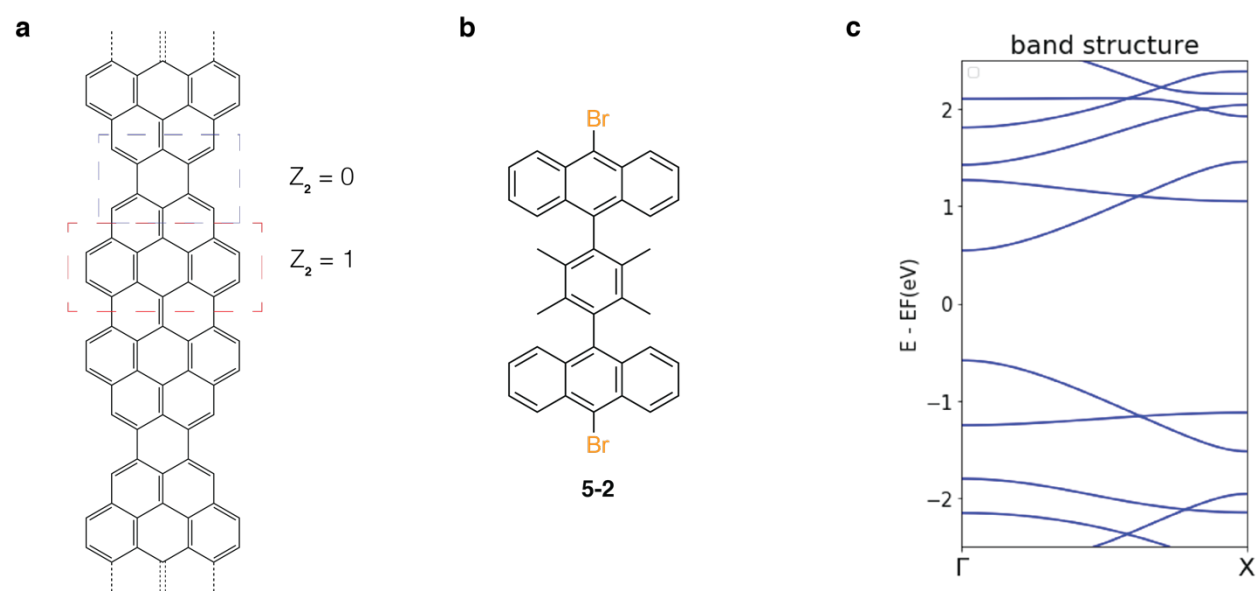
Figure 5.3.1 Schematic of 5/7-AGNR Heterojunction (a) b, 5/7-AGNR Precursor **c,** Theoretical Electronic Structure of 5/7-AGNR

5.3.2   5/7-AGNR Heterojunctions

Once the synthesis of **5-2** was achieved, surface experiments were performed as we embarked upon the study of 5/7-AGNR heterojunctions. **5-2** was sublimed onto an Au(111) substrate that was held at 25 °C from a Knudsen cell evaporator in ultrahigh vacuum. Figure 5.3.2a

contains STM topographic images of **5-2** immediately after deposition and indicates that **5-2** prefers to self-assemble into amorphous islands that appears to contain at least two different orientations. The formation of polymeric structures was confirmed after annealing the substrate to 200 °C (Figure 5.3.2b), and the apparent height of the linear structures (0.45 nm) is consistent with previous results. In a final step, the substrate was annealed to 400 °C so that the Au(111) substrate could catalyze cyclodehydrogenation to form GNRs (Figure 5.3.2c). The result in Figure 5.3.2c appeared promising as it was possible to find extended linear structures that reached upwards of 20 nm and the GNR termini are as expected from 7-AGNR segments. Upon closer inspection however, there was an immediate cause for concern because many of the GNRs significantly deviate from linearity. The connectivity of the resultant GNRs was inspected with BRSTM imaging (Figure 5.3.2d) and revealed the formation of 5-memebered rings along the GNR backbone. Our hypothesis is that the 5-membered ring forms after the cleavage of one of the four methyl groups on the central benzene unit. Frustratingly, the 5-membered ring defect alternates between the left and right pairs of methyl groups (relative to the polymerization axis as drawn in Figure 5.3.1) of the GNR backbone but occurs randomly between the upper and lower methyl groups. The random methyl cleavage suggests that we cannot form a regioregular GNR with **5-2**. In lieu of further deposition attempts with **5-2**, it was suggested to deposit an iodinated version of **5-2**. Owing to the lower bond dissociation energy of iodine compared to bromine, the polymerization should occur at a lower temperature and may circumvent the untimely methyl cleavage.
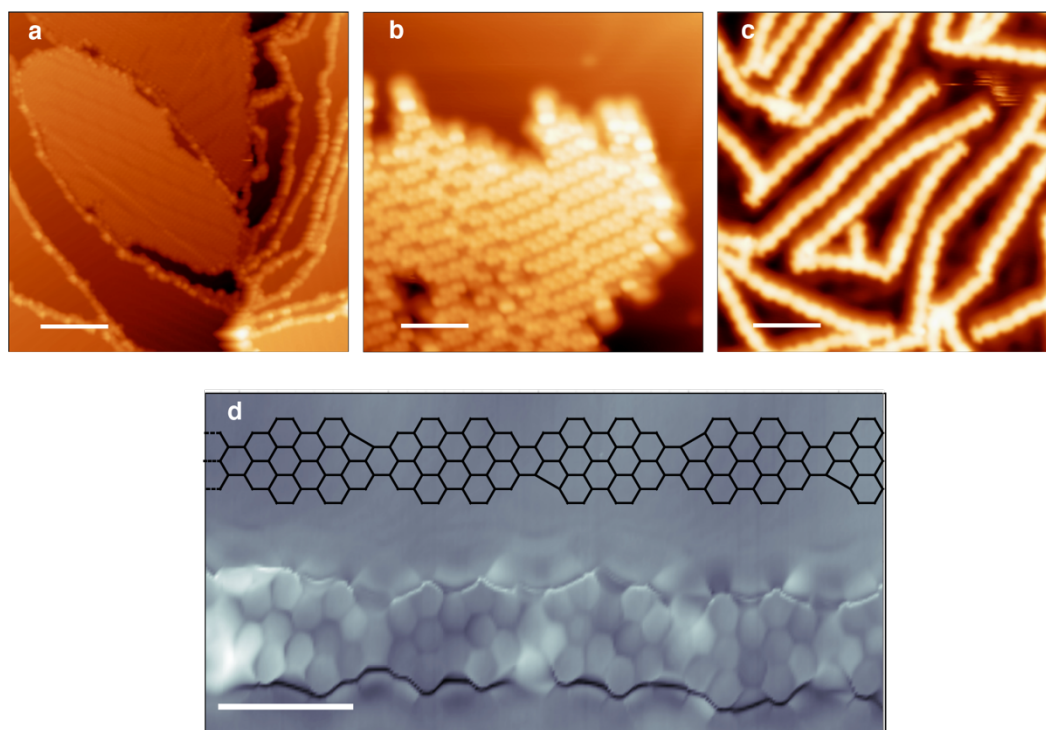
Figure 5.3.2 Bottom-Up Synthesis of 5/7-AGNR a, STM Topographic Image of **5-2** (V_s = 50 mV, I_t = 20 pA, scale bar = 20 nm) **b,** STM Topographic Image of panel A after annealing to 200 °C (V_s = 50 mV, I_t = 20 pA, scale bar = 4 nm) **c,** STM Topographic Image of panel B after annealing to 400 °C (V_s = 50 mV, I_t = 20 pA, scale bar = 5 nm) **d,** BRSTM Image of 5/7-AGNR showing 5-membered ring defect (V_s = 10 mV, I_t = 280 pA, V_{ac} = 11mV scale bar = 1 nm)

With the iodinated version of **5-2** in hand, experiments to synthesize the 5/7-AGNR were restarted. The iodinated **5-2** was sublimed from a Knudsen cell evaporator onto a Au(111) substrate held at 25 °C. After it was confirmed that the precursor molecule adsorbed onto the surface with adequate coverage, the substrate was annealed directly to 400 °C to yield fully cyclized and planar structure. The GNRs obtained have a similar appearance to those in Figure 5.3.2c hinting that the 5-membered ring formation may still be an issue for the iodinated precursor (Figure 5.3.3a). The ensuing BRSTM images (Figure 5.3.3b) affirm that the presence of iodine and lower dehalogenation temperature has no effect on the premature methyl cleavage. Therefore, it is reasonable to hypothesize that the methyl cleavage occurs during after the polymerization stage at some point in the window between 100 °C and 400 °C (cyclodehydrogenation temperature). Another possibility is that methyl cleavage occurs prior to polymerization or independent of the polymerization temperature. To determine the exact cause of the methyl cleavage, the experiments were repeated a third time with an unhalogenated version of **5-2**.
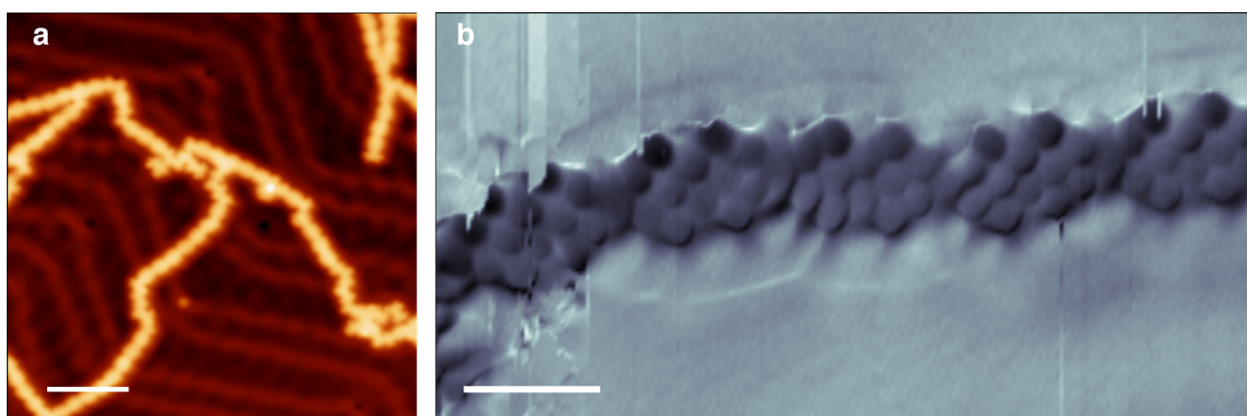
Figure 5.3.3 Bottom-Up Synthesis of 5/7-AGNR via Iodinated Precursor a, STM Topographic Image after annealing to 400 °C (V_s = 50 mV, I_t = 20 pA, scale bar = 6 nm) **b,** BRSTM Image of 5/7-AGNR from panel A (V_s = 10 mV, I_t = 280 pA, V_{ac} = 11 mV scale bar = 1 nm)

The hydrogenated version of **5-2** is especially interesting for two reasons. Firstly, it allows us to determine the root cause of the premature cyclization. Secondly, if it cyclizes correctly on the Au(111) substrate, the resultant structure cannot be depicted with a classical Kekulé structure. To accurately draw this nanographene, known as the Clar goblet (**5-3)**, it is necessary to leave two electrons unpaired forcing the molecule into a magnetically non-trivial ground state. The Clar Goblet was first postulated by Erich Clar in 1972, but isolation of the molecule from solution has proven challenging stemming from its kinetic instability[156]. On the other hand, the Au(111) substrate has the potential to stabilize the Clar goblet and enables access to the exotic physics. Deposition attempts of the hydrogenated **5-2** proceeded in a similar fashion to the iodinated and brominated species. After sublimation onto a Au(111) surface held at 25 °C, the substrate was annealed to 300 °C to induce cyclodehydrogenation. Figure 5.3.4b displays a large-area overview of the Au(111) surface following the anneal and a mixture of products can be observed. In addition to cyclized monomers, there appear to be dimers (Figure 5.3.4c) which is unexpected.
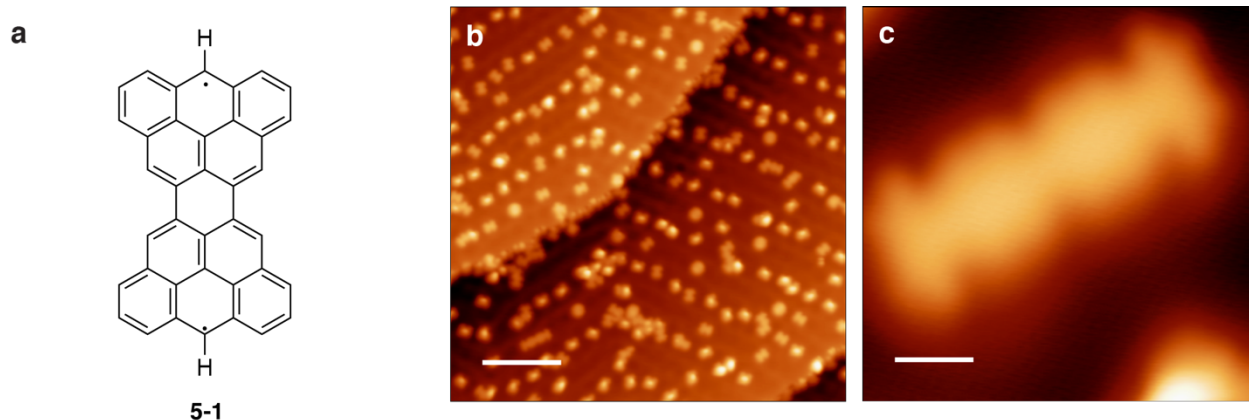
Figure 5.3.4 Bottom-Up Synthesis of Clar Goblet a, Schematic of Clar Goblet **b,** STM Topographic Image of Au(111) substrate after annealing to 300 °C (V_s = 50 mV, I_t = 20 pA, scale bar = 10 nm) **c,** Zoom-In STM topographic Image of dimeric species (V_s = 50 mV, I_t = 20 pA, scale bar = 0.8 nm)

Around this time, Mishra, *et. al* published a paper on magnetism in the Clar Goblet using the same hydrogenated precursor[112]. Although this was disheartening because we could no longer study the Clar goblet, it did confirm that the cyclization occurs as anticipated without polymerization. Using this knowledge, it is evident that further experiments on the 5/7-AGNR superlattice will require a new precursor molecule. Two distinct molecules are shown in Figure 5.3.5. The first precursor uses a similar scaffold to the 5/7-AGNR that was tested here, but instead of a central benzene ring, the central core is pyrene. The idea is that the pyrene can act to both extend the 5-AGNR segment and potentially separate the methyl groups so that the premature cleavage becomes unlikely. The second molecule uses an olympicene scaffold where three-membered sulfur containing ring makes the precursor synthetically accessible. Assuming that the excess hydrogen generated on the surface during cyclodehydrogenation can force the cleavage of the C-S bond, this precursor offers a disparate pathway towards the 5/7-AGNR.
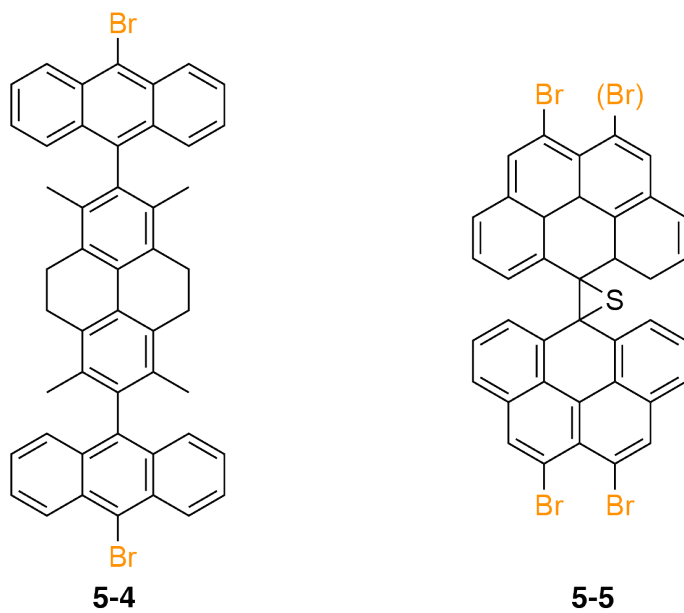
Figure 5.3.5 Alternative 5/7-AGNR Precursor Molecules

5.4 Topological States in Cove-Edged Graphene Nanoribbons

5.4.1 Introduction

The seminal work of Cai, *et. al*[31] marked a critical turning point in the study of GNRs as it served to connect the field of topology with graphene nanoribbons. Nevertheless, the scope of that work was limited to armchair GNRs, which are but a fraction of the GNRs that can be realized with bottom-up synthesis. Building upon this work Lee, *et. al* extended the topological characterization of GNRs to chevron and cove edge structures[147]. Chevron GNRs were extensively discussed in the previous chapter, so this section will focus on the topological classification in cove-edge GNRs. Cove-edge GNRs can be approximated as zigzag GNRs with periodic carbon atom vacancies on both edges. The electronic structure of cove GNRs is inextricably linked to the position and density of these vacancies. The work of Lee, *et. al* focuses on the scenario where one carbon vacancy and one hexagonal vacancy alternatively occur along each edge as this structure is known to be synthetically accessible. Within this framework there are three distinct families where all cove GNRs can be grouped. When the number of zigzag chains forming the parent zigzag GNR (hereafter referred to as N) is odd there is only one possible edge structure (Figure 5.4.1a) and the electronic structure exhibits an inverse relationship with width (Figure 5.4.1d). Conversely, when N is even the carbon vacancies can symmetric where they are directly facing one another (Figure 5.4.1b) or they can be asymmetric where the vacancies are staggered with respect to each other (Figure 5.4.1c). The even cove-GNRs with symmetric vacancies express a similar electronic structure to the odd cove-GNRs and are of minimal interest (Figure 5.4.1d). Instead, the asymmetric, even cove-GNRs that are predicted to be metallic by density functional theory calculations (DFT) within local spin density approximation (LSDA) framework are intriguing. Regioregular metallic graphene nanoribbons have been sought after in our research group from its outset and they could be incorporated into complex devices all-GNR architectures (e.g., Tunneling Field Effect Transitions) and help minimize parasitic resistances.
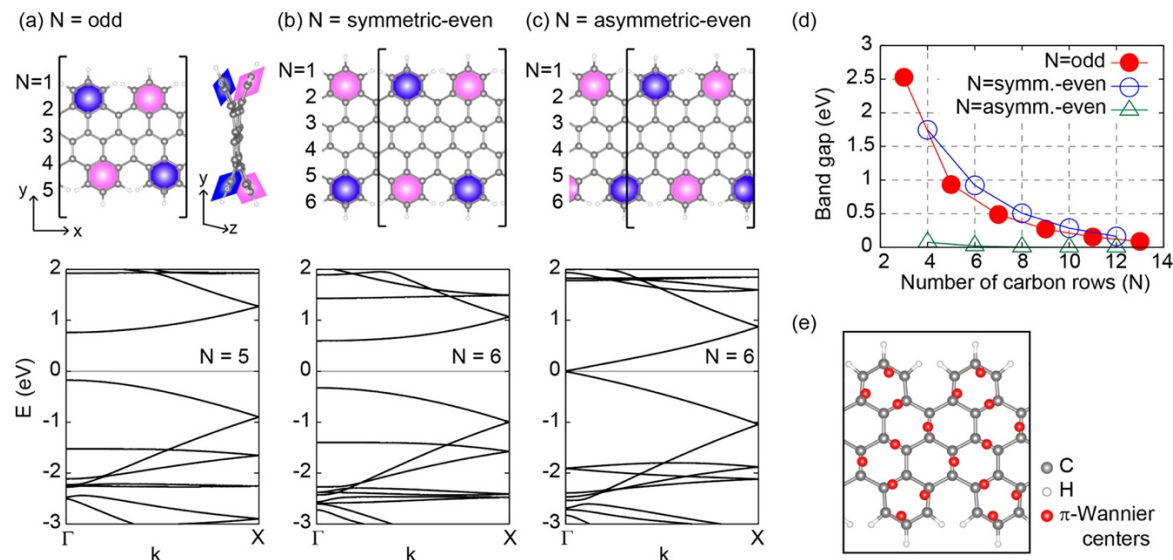
Figure 5.4.1 Schematic structures and band structures of cove-edged GNRs

5.4.2   Synthesis of Asymmetric Cove GNR

The precursor molecule (**5-6**) used in the initial attempts to synthesize the asymmetric cove GNR is presented in Figure 5.4.2a. **5-6** was sublimed in ultrahigh vacuum onto an Au(111) substrate held at 25 °C and it is readily apparent from large-area scans that the molecule prefers to aggregate into islands (Figure 5.4.2b). Careful examination of STM topographic images make clear that the monomer as deposited has four distinct lobes, as expected given the geometry of the precursor. Unfortunately attempts to anneal the sample to higher temperatures and induce polymerization consistently failed. Oligomeric structures were never observed, rather the annealing process only produced pristine Au(111) substrates. Although the natural inclination would be to repeat these experiments with an iodinated precursor and force the polymerization to occur at lower temperatures, it is highly likely that this would have been a waste of time. The naphthalene wings on **5-6** can freely rotate and adopt multiple confirmations on the Au(111) surface. One such confirmation has both Br atoms pointing directly into the surface anchoring the molecule and preventing further diffusion. In this scenario, the molecules would never be able to polymerize because they would immediately desorb when they had enough energy to diffuse. The flexibility of the monomer thus acts in direct opposition to the polymerization. The most straightforward way to bypass this dilemma is to polymerize **5-6** in solution and then transfer the polymer using the Matrix Assisted Deposition (MAD) technique discovered by McCurdy, *et. al*[70]. Once again, the flexibility of the polymer backbone may be an issue, but in this case the polymer can be partially cyclized in solution before using the surface for the final cyclodehydrogenation.

a

5-6
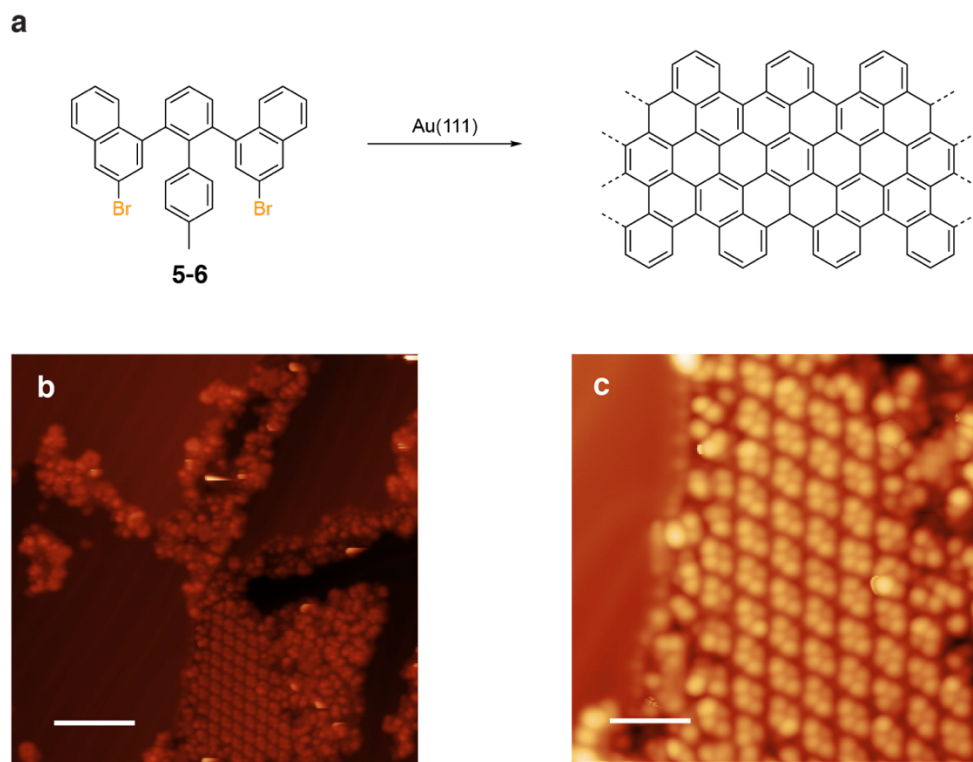
Figure 5.4.2 Bottom-Up Synthesis of Asymmetric Cove GNR a, Schematic of Asymmetric Cove GNR synthesis **b,** STM Topographic Image of **5-6** as deposited (V_s = 50 mV, I_t = 20 pA, scale bar = 10 nm) **c,** Zoom-in STM Topographic Image of panel B (V_s = 50 mV, I_t = 20 pA, scale bar = 3 nm)

5.5 Summary and Outlook

In this chapter the engineering of topological states in graphene nanoribbons with a variety of different edges has been explored. The first two sections are dedicated to armchair edge GNRs and well-defined heterojunctions. Initially the formation of topological interface states at the junctions of 7-AGNR segments and 9-AGNR segments is reviewed. The 9/7/9-Double Quantum Dot structure is explored where the coupling between interface states can easily be measured as function of 7-AGNR segment length. The precursor molecule could not be sublimed intact onto the growth substrate because of the temperature required for sublimation. Fortunately, DCT provides another route as the precursor molecule can be directly applied to the Au(111) substrate. Once the molecule has been transferred, co-deposition with DBBA will give double quantum dot structures with varying 7-AGNR segment length. Even though the 7-AGNR segment length cannot be controlled, the STM can easily characterize all possible lengths.

The second section of this chapter considers the opposite end of the spectrum where the interface states are no longer isolated, but instead strongly interact. To investigate this regime, the 5/7-AGNR heterojunction was analyzed because the 5-AGNR has a narrow band gap, and the precursor could be sublimed onto the surface with relative ease. Attempts to grow the 5/7-AGNR were largely unsuccessful as pernicious methyl cleavage hindered the realization of regioregular structures. Future experiments towards this superlattice should take advantage of the novel precursors depicted in Figure 5.3.5.

The final section is reserved for preliminary exploration into cove edge GNRs. The biggest advantage to cove edge GNRs is the extensive knowledge base to grow long cove GNRs in solution. Consequently, although asymmetric cove GNRs could not be grown on the surface, the polymer can be obtained in solution and transferred via MAD.

Chapter 6: Regioregular Metallic Graphene Nanoribbons

6.1 Introduction

A requisite factor for logic devices based on graphene nanoribbons (GNRs) is locating a suitable material for metallic contacts. State-of-the-art GNR devices that use Pd as the source-drain electrodes are promising as they exhibit a high on-current ($I_{on} > 1\mu A$) and an on-current/off-current ratio of $\sim 10^5$ but the device performance is limited by the Pd contacts due to the Schottky barrier that forms at the Pd-GNR interface[92]. The parasitic current is generated via electrons tunneling across the barrier and transmission through Schottky barrier must minimized to improve device performance. The on-current is not satisfactory for high performance device application and steps must be taken to mitigate the effect of the Schottky barrier. One viable strategy that was considered in Chapter 3 is to lower the band gap of the GNR and bring the Fermi level closer to the Pd contacts. A different strategy that will be examined in-depth in this chapter is to develop metallic GNRs that are compatible with the semiconducting GNRs used for the conducting channels. Logic devices constructed with metallic GNRs have atomically precise junctions and would be capable of exotic quantum transport such as Luttinger liquid behavior, charge density waves, and possibly superconductivity. To access these phenomena and obtain reproducible results, it is essential to synthesize regioregular—where each repeat unit is derived from the same isomer of the precursor—metallic GNRs.

The work in this chapter is dedicated to the realization of regioregular metallic GNRs from two distinct molecular precursors. The first precursor is referred to as the "U-metal" and is based on the U-shaped monomer used for zigzag GNRs and results in a metallic GNR with a wide bandwidth (> 400 meV). The wide bandwidth suggests that the GNR would retain its metallicity even when removed from the Au(111) substrate. By contrast, the second precursor is known as the "cove metal" because the edge structure has cove topology. The metallic GNR that is produced from this precursor has a narrow bandwidth (<50 meV) and could allow the study of Luttinger liquid behavior when the GNR is transferred onto an insulating substrate. I will explore multiple generations of cove precursors and show the design principles that yield GNRs.

6.2 Synthesis of Regioregular Metallic GNRs

6.2.1 Introduction

Recently, our group reported the first intrinsically metallic GNR. In doing this, we developed a general approach to accessing GNR metallicity by embedding a symmetric superlattice of localized zero-mode states along the backbone of a bottom-up, on-surface synthesized GNR[157]. A key aspect of our approach is the design of a novel GNR monomer with an odd number of carbon atoms. The additional odd carbon atom in each monomer contributes a periodic sublattice imbalance site, resulting in a localized zero-mode, to each fused monomer segment within the final GNR. A simple tight-binding electronic structure model applied to a superlattice of zero-modes with regular spacing along the backbone of a GNR predicts that the intracell and intercell electron hopping amplitudes between adjacent zero-modes become equivalent ($t_1 = t_2$). Within this same model, two zero-mode states per GNR unit cell give rise to two zero-mode bands within the GNR and the energy gap between these bands can be simply defined as $\Delta E = 2||t_1| - |t_2||$. Symmetric spacing of the zero-mode states gives $\Delta E = 0$ because $t_1 = t_2$, which means the resulting GNR containing a symmetric zero-mode superlattice should have a metallic electronic structure. We experimentally applied this approach in our previous report of the sawtooth-GNR (sGNR) and 5-sawtooth-GNR (5sGNR). We confirmed the presence of an intrinsically metallic zero-mode band in the 5sGNR with scanning tunneling spectroscopy (STS) and theoretically corroborated it with DFT-LDA calculations (Figure 6.1.1). The width of the metallic zero-mode band, W, is equal to $4t_1$ and Figure 6.1.1c-d shows the difference between the sGNR and 5sGNR is greater than order of magnitude (~20X). The sGNR has a very narrow bandwidth and is not expected to retain its metallicity when removed from the Au(111) substrate. By comparison, the 5sGNR has a more robust metallicity (W = 480 meV) that will survive when the GNR is transferred onto an insulating substrate[157]. This significant difference in bandwidth can be attributed to the sublattice polarization in the graphene. For the sGNR, all the zero-modes lie on the same sublattice, and the hopping parameter is dominated by second-nearest neighbor hopping whereas the 5-membered ring formed in the 5sGNR disrupts this sublattice polarization and the hopping parameter is proportional to the nearest neighbor hopping. Therefore, engineering the zero-mode states so that they lie on opposite sublattices can lead to enduring metallicity.

The major shortcomings of the sGNR and 5sGNR are (i) the sGNR is not intrinsically metallic due to sublattice polarization of zero-mode states and (ii) that both rely on a directional head-to-tail (AB–AB) on-surface polymerization to ensure regular spacing between zero-mode states in the final GNR (Figure 6.1.2). Asymmetry of the monomer imposed by the necessary odd-carbon in the sawtooth monomer and the lack of selectivity offered by on-surface step-growth polymerizations results in just a 50% probability of achieving the desired directionality at each monomer incorporation event during polymerization. If just one monomer attaches in the undesirable head-to-head (AB–BA) or tail-to-tail (BA–AB) configuration then the metallic zero-mode band is disrupted. The applicability of the sawtooth is severely limited by the near zero probability of obtaining extended metallic GNRs at the length scales necessary to explore applications as 1D metallic interconnects or to examine exotic 1D physics. While the sawtooth served as a successful proof-of-concept for our general approach to achieving metallicity in GNRs, improvements in the synthesis to ensure regioregularity and sublattice mixing of zero-mode states

are needed to obtain homogeneous samples of extended GNRs with persistent, intrinsically metallic zero-mode bands.
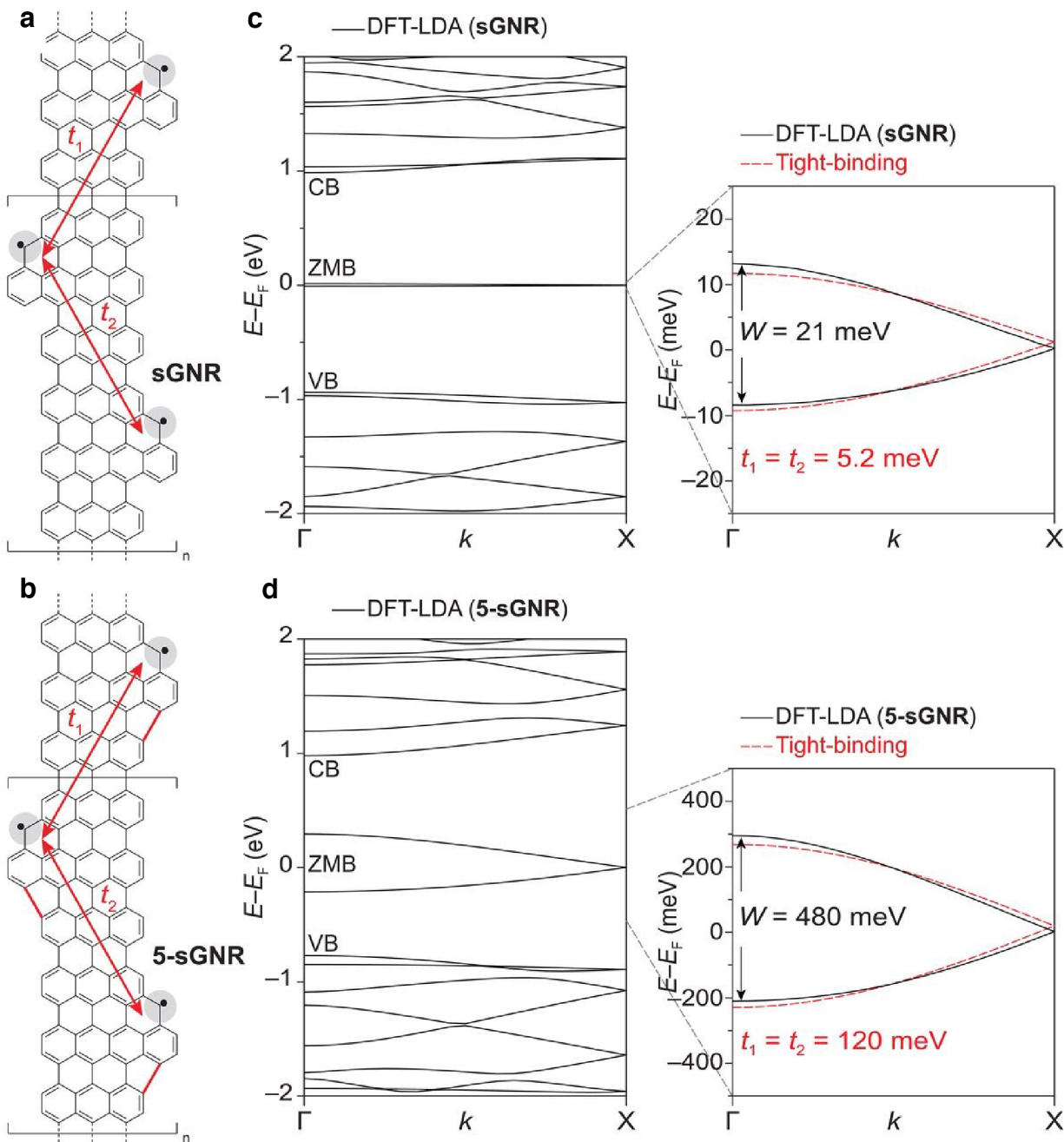
Figure 6.2.1 Zero-mode Band structure Schematic representation of inter- and intracell hopping between localized zero-modes embedded in **(a)** sGNRs and **(b)** 5-sGNRs. **(c)** Left panel: DFT-LDA calculated band structure for sGNRs. Frontier bands are labelled VB, ZMB, and CB. Right panel: tight-binding fit (red) to DFT-LDA band structure yields hopping parameter $t_1 = t_2 = 5.2$ meV. **(d)** The same as **(c)** but for 5-sGNRs. Hopping parameter for 5-sGNR (and corresponding bandwidth) is 23 times larger than for sGNR.

6.2.2 Bottom-Up Synthesis of Regioregular Olympicene GNRs

Our first strategy to synthesize regioregular metallic GNRs builds off the "U-shaped" precursor used for ZGNRs to ultimately yield a novel monomer scaffold resulting in olympicene GNRs (oGNRs). The U-metal precursors **6-1a/6-1b** are designed with an encoded sublattice imbalance site about the C_s symmetry plane to ensure regular placement of zero-mode states in the final GNR via regioregular polymerization. Figure 6.1.2 outlines the polymerization and directly compares the oGNR to the 5sGNR discussed in the introduction. The regioregular nature of the oGNR polymerization is immediately obvious compared to the random polymerization for the 5sGNR. In monomer **6-1a** the methyl group encodes for the sublattice imbalance site while in monomer **6-1b** the sublattice imbalance site is encoded by a methylene group. Each oGNR unit cell contains two fused monomer units where the zero-mode sublattice site alternates between monomer units such that there is no sublattice polarization in the unit cell. Sublattice mixing of zero-mode states in the unit cell is preprogrammed to achieve a robust, metallic zero-mode band in the oGNR. In the oGNR, the sublattice imbalance sites alternate in each consecutive monomer unit such that both sublattices exhibit zero-mode state density.

Figure 6.2.2 Schematic of oGNR Synthesis

On-surface synthesis of oGNRs was initiated by depositing monomer **6-1b** onto an Au (111) surface via sublimation from a Knudsen cell evaporator in UHV. Self-assembled islands of the monomer on Au (111) are depicted in Figure 6.2.3b. The Au (111) substrate was then annealed to 400 °C yielding densely packed oGNRs (Figure 6.2.3c) resulting from polymerization of monomer
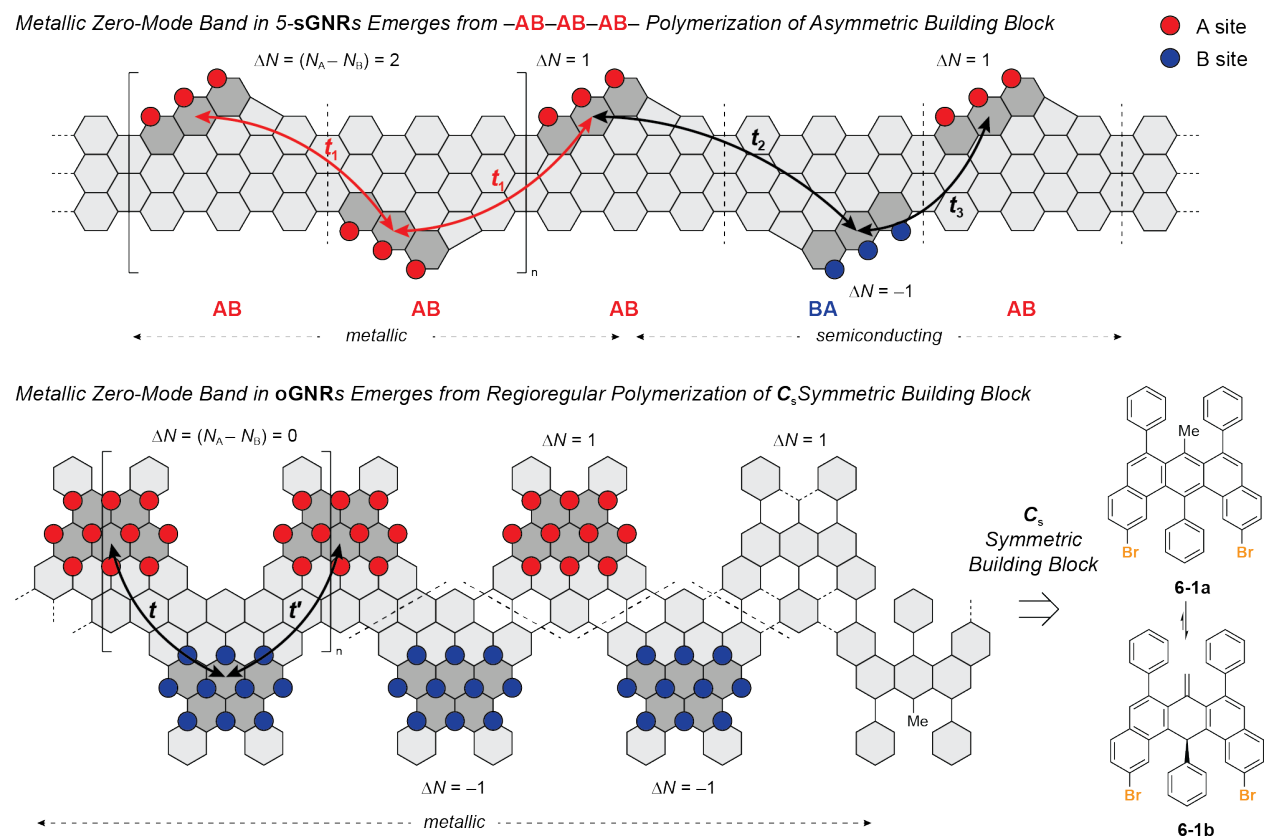
6-1b immediately followed by cyclodehydrogenation. The ability of this new monomer scaffold to polymerize efficiently is highlighted by the extended oGNR structures depicted in Figure 6.2.3c, some reaching close to 50 nm in length. Higher resolution STM topographic scans reveal mixed edge structures (Figure 6.2.4) corresponding to a random combination of the non-planar cove edge structure of oGNRs shown in Figure 6.1.1 and the planar pentagon-fused cove edge structure of 5-oGNRs shown in Figure 6.3.3a. The non-planarity of the oGNR structure imposed by the edge cove regions makes it experimentally difficult to obtain bond-resolved atomic characterization data as well as constant-height STS data on the zero-mode band. For this reason, a low coverage sample of the 5-oGNR depicted in Figure 6.3.3d was synthesized. Extending the annealing time at the graphitization temperature results in a near quantitative fusion of the cove edge to the pentagon-bearing flat edge. At this stage, it became possible to acquire bond-resolved STM (BRSTM) topographic images. The BRSTM images displayed in Figure 6.3.3e unambiguously confirm the formation of the 5-oGNR, but there is significant drift and low bias BRSTM imaging is hindered by the metallic states around zero bias. Further characterization is needed via non-contact Atomic Force Microscopy (nc-AFM).
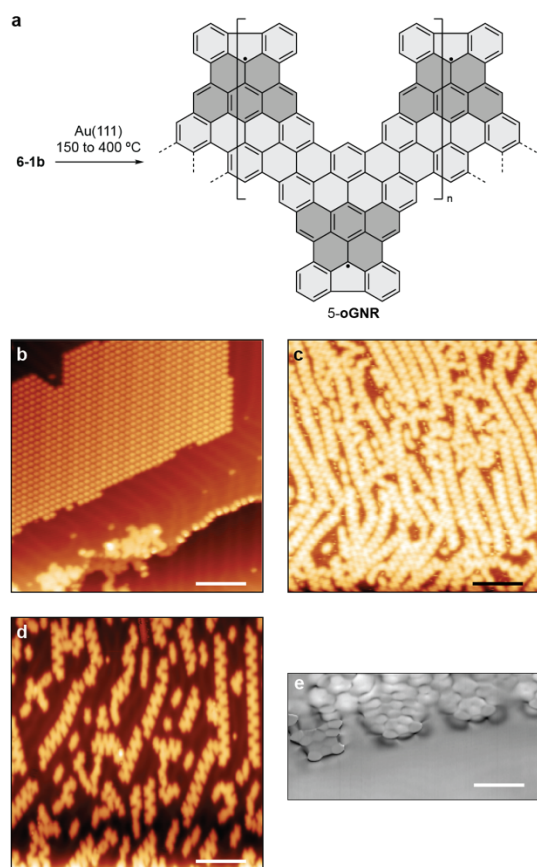
Figure 6.2.3 Bottom-Up Synthesis of oGNRs a, Schematic for the formation of 5-oGNRs **b,** STM Topographic Image of **6-1b** after deposition at 25 °C (V_s = 50 mV, I_t = 20 pA, scale bar = 10 nm) **c,** STM Topographic Image of high coverage deposition after annealing to 350 °C (V_s = 50 mV, I_t = 20 pA, scale bar = 10 nm) **d,** STM Topographic Image of medium coverage deposition after annealing to 350 °C (V_s = 50 mV, I_t = 20 pA, scale bar = 10 nm) **e,** BRSTM Topographic Image of 5-oGNR after annealing to 400 °C (V_s = 10 mV, I_t = 280 pA, V_{ac} = 11 mV, scale bar = 1 nm)
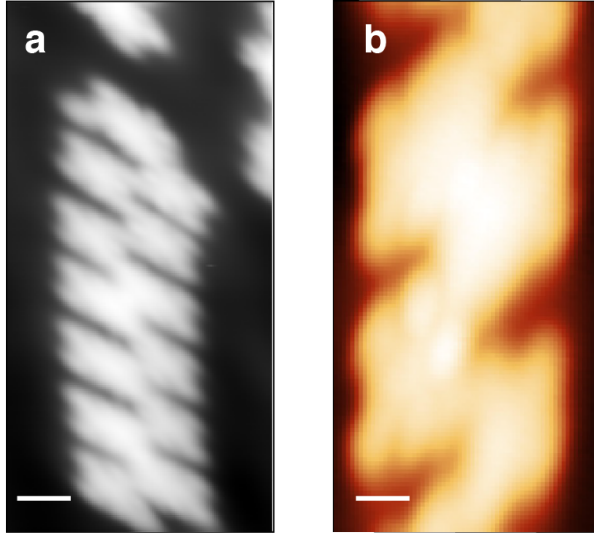
Figure 6.2.4 oGNR Mixed Edge Structure a, STM Topographic Image after annealing to 350 °C showing oGNR (V_s = 50 mV, I_t = 20 pA, scale bar = 1 nm**) b,** STM Topographic Image after annealing to 400 °C showing 5-oGNR (V_s = 50 mV, I_t = 20 pA, scale bar = 0.5 nm)

Additionally, the lower coverage sample allowed ample Au (111) background to obtain further electronic characterization by STS. Fusion of the cove edge to the 5-oGNR does not significantly alter the underlying physics of the metallic GNR and the electronic structure remains nearly identical (Figure 6.2.6). After completing 5-oGNR growth and structural characterization we moved to uncover the frontier electronic structure of these GNRs in hopes of experimentally measuring the robust zero-mode metallic band that the 5-oGNR is designed to host. In Figure 6.2.5a, energy dependent local density of states (LDOS) is shown. These are recorded by measuring the differential conductance (dI/dV) of the STM tunnel junction between the tip and sample above the 5-oGNR edge. The conduction band (CB) onset is recorded at 1.6 V and the presence of the metallic zero-mode band (ZMB) is detected at -0.07 V. dI/dV mapping was performed at the voltages corresponding to the CB onset and ZMB to determine the positional dependence of the LDOS. The images are displayed in Figure 6.2.5b and C. As expected, the LDOS for the CB onset is concentrated along the geometric edges of the 5-oGNR. The ZMB contains significant density along the interior of the 5-oGNR and evidence of the ZMB exist up to 500 meV above the Fermi level. Precise measurement of the VB has proven challenging likely due to overlap with the Au(111) Shockley surface state. Further experiments are necessary to accurately determine the valence band onset.

The experimentally observed resonances in the dI/dV point spectra and in the dI/dV mapping are reproduced by *ab initio* DFT-LDA electronic structure calculations. Figure 6.2.5d shows the 5-oGNR DFT calculated density of states (DOS). One puzzling fact is that the DFT-calculated DOS predicts a U-shaped DOS around zero bias, but this feature has not been observed in the STS point spectra. Figure 6.2.6 shows the DFT-LDA calculated band structure of the oGNR and the 5-oGNR. A large nearest neighbor electron hopping of $t = t' = 115$ meV and $t = t' = 120$ meV between adjacent zero-modes in the 5-oGNR and oGNR respectively results in a large metallic ZMB bandwidth of ~400 meV. Contrary to the scenario involving the sGNR and 5-sGNR, the bandwidth is not affected by the additional planarization caused by the 5-membered closure. This is anticipated because sublattice mixing is already built into the oGNR, so the 5-membered

ring does not disrupt the bipartite lattice. Supplemental calculations will be performed once all experimental spectroscopy has been completed.
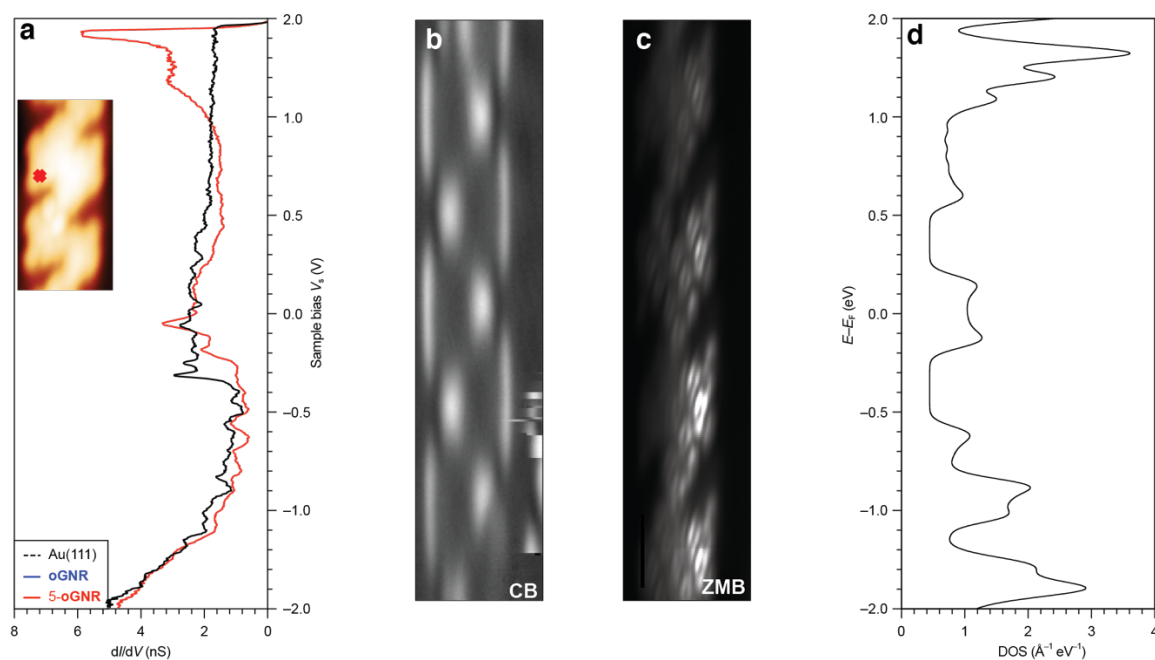
Figure 6.2.5 Electronic Structure Characterization of 5-oGNRa, dI/dV Point Spectroscopy of 5-oGNR recorded on the edge of a 5-oGNR (V_{ac} = 11 mV, f = 455 Hz) **b,** Constant current dI/dV map (V_s = 1.6 eV, I_t = 300 pA, V_{ac} = 11 mV, f = 455 Hz) **c,** Constant height zero-bias dI/dV map (I_t = 300 pA, V_{ac} = 11 mV, f = 455 Hz) **d,** DFT-LDA calculated DOS of 5-oGNR
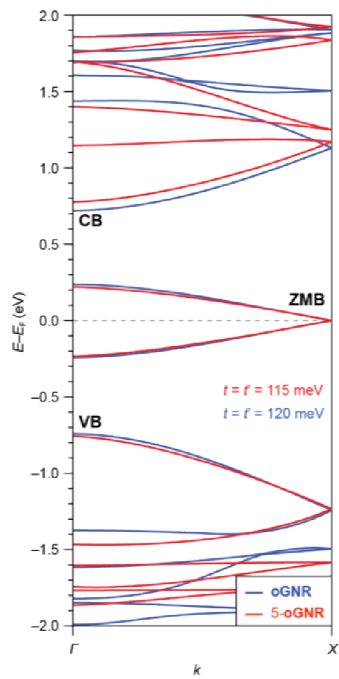
Figure 6.2.6 Calculated DFT Band structure for oGNR and 5-oGNR

6.2.3   Bottom-Up Synthesis of Regioregular Cove Metal GNRs

Along with the olympicene GNR, another candidate for regioregular metallic structures is GNRs with cove edge topology. Cove GNRs are of particular interest because they stem from a symmetric precursor that would allow for the formation of long metallic GNRs[158]. For example, **6-2** is expected to yield the GNR shown in Figure 6.2.7a which is predicted to have a wide bandwidth (> 500 meV). This robust metallicity should in turn survive if the GNR is removed from the Au(111) substrate. In **6-2** the methyl group along the center of the molecule induces the sublattice imbalance that is exploited to realize metallicity. Moreover, the sublattice imbalance alternates between the A and B sites creating the sublattice mixing that typically leads to wide bandwidth metals. **6-2** was sublimed onto a Au(111) substrate held at 25 °C from a Knudsen cell evaporator that was heated to roughly 200 °C and the results are presented in Figure 6.2.7b. The precursors tend to self-assemble into island that begin along the Au(111) herringbone before extended outwards. Although it is possible to observe what appears to be individual monomers, it is difficult to discern anything from these structures. After annealing the Au(111) substrate to 200 °C, there appear to be some oligomeric structures that we tentatively assign as polymers of 6-2 (Figure 6.2.7c). Unfortunately, the final annealing step at 300 °C to prompt cyclodehydrogenation did not produce the cove GNR. The surface was predominately covered in small molecules with no real shape (Figure 6.2.7d). Attempts to lower the deposition coverage only yielded nanostructures that seem to be cyclized monomer.
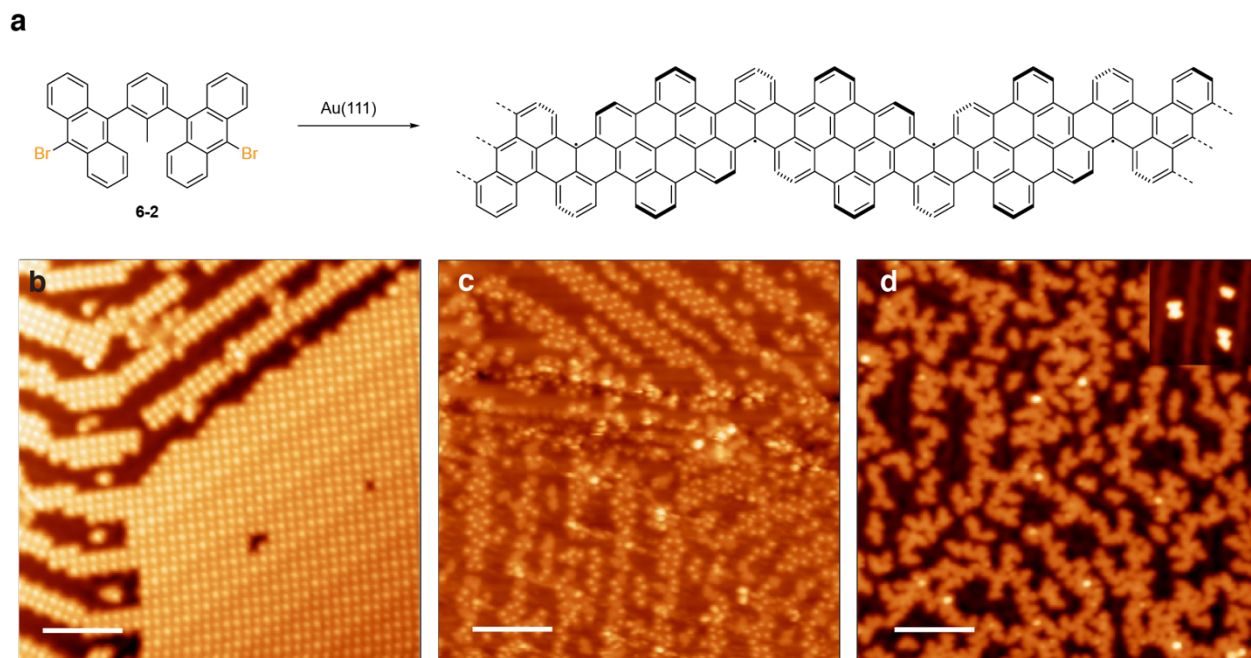
Figure 6.2.7 Bottom-Up Synthesis of Metallic Cove GNR a, Schematic of Metallic Cove GNR Synthesis **b,** STM Topographic Image of **6-2** as deposited (V_s = 50 mV, I_t = 20 pA, scale bar = 10 nm) **c,** STM Topographic Image of panel B after annealing to 200 °C (V_s = 50 mV, I_t = 20 pA, scale bar = 10 nm) **d,** STM Topographic Image of panel C after annealing to 375 °C, inset: STM Topographic image of low coverage sample of **6-2** (V_s = 50 mV, I_t = 20 pA, scale bar = 10 nm)

The working hypothesis is that the polymerization cannot occur because the monomer units are too flat on the Au(111) substrate and the radicals are not at the heights necessary to polymerize[159]. This theory was validated in part by work from the Fasel group at EMPA where they observed that the anthracene units on their precursor hampered the growth of extended structures. To bypass this problem, **6-3** was designed with an additional anthracene unit on each side. The additional anthracene will force the radical to adopt a cruciform geometry that is advantageous to polymerization. Furthermore, calculations on the "extended cove" indicate that this GNR would be a narrow bandwidth metal where the metallicity is less robust and metal-insulator transitions can be explored. **6-3** could not be sublimed onto the surface before decomposition and must be applied to the surface via Direct Contact Transfer (DCT) for future studies.
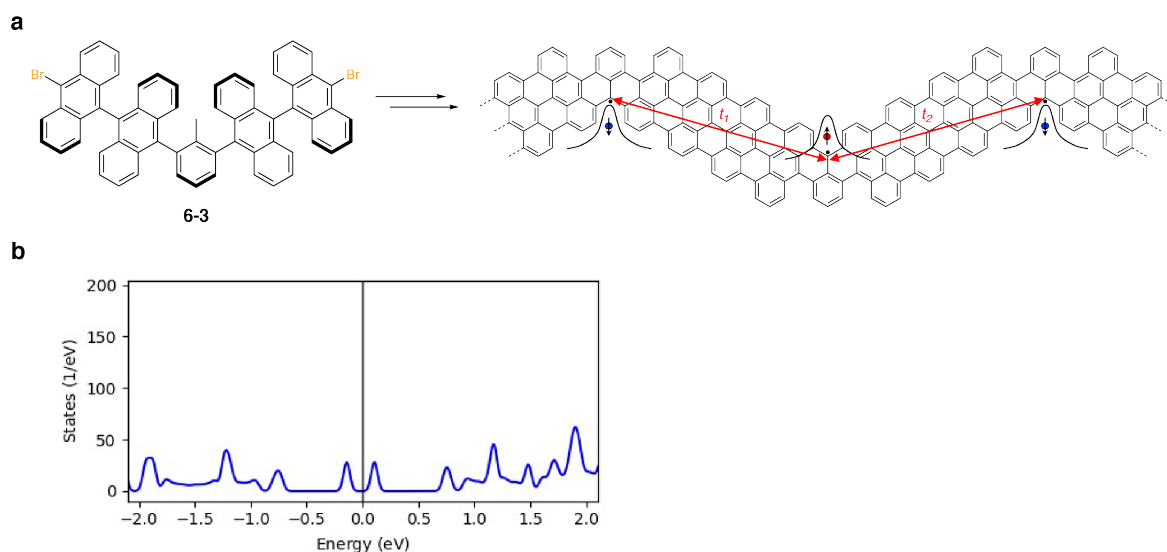
Figure 6.2.8 Schematic of Extended Cove GNR Synthesis (a) b, Calculated DFT-LDA DOS of Extended Cove GNR

6.3 Summary and Future Outlook

In this chapter the progress towards regioregular metallic GNRs that can be used in future device applications has been discussed. The first half of this chapter is focused on the olympicene GNRs based on the U-shaped monomer used for ZGNRs. The olympicene GNRs are notable because they tend to grow quite long and are compatible with ZGNRs opening the door for spintronic device applications. Future work on this scaffold needs to be done in order to parse out the valence band (VB) onset. Once the experimental electronic structure data has been solidified, it is imperative that that data is backed up with sufficient theoretical calculations.

The second half of this chapter is concerned with the cove family of metallic GNRs. Initial trials at synthesizing a metallic cove GNR were unsuccessful because of the geometry of the precursor molecule on the Au(111) substrate. The second-generation cove precursor is designed to force the adoption of a cruciform geometry that is expected to readily polymerize. Experiments on the extended cove GNR will require the use of DCT and if successful could lead to further studies of exotic 1D quantum transport phenomena.

Bibliography

1. Wallace, P. R. The Band Theory of Graphite. *Phys. Rev.* **71**, 622–634 (1947).

2. Haldane, F. D. M. Model for a quantum hall effect without landau levels: Condensed-matter realization of the 'parity anomaly'. *Phys. Rev. Lett.* **61**, 2015–2018 (1988).

3. Semenoff, G. W. Condensed-Matter simulation of a three-Dimensional anomaly. *Phys. Rev. Lett.* **53**, 2449–2452 (1984).

4. Fradkin, E. Critical behavior of disordered degenerate semiconductors. II. Spectrum and transport properties in mean-field theory. *Phys. Rev. B* **33**, 3263–3268 (1986).

5. K. S. Novoselov, A. K. Geim, S. V. Morozov, D. Jiang, Y. Zhang, S. V. Dubonos, I. V. G. and A. A. F. Electric Field Effect in Atomically Thin Carbon Films. **306**, 666–669 (2004).

6. Novoselov, K. S. *et al.* Two-dimensional gas of massless Dirac fermions in graphene. *Nature* **438**, 197–200 (2005).

7. Zhang, Y., Tan, Y. W., Stormer, H. L. & Kim, P. Experimental observation of the quantum Hall effect and Berry's phase in graphene. *Nature* **438**, 201–204 (2005).

8. Schedin, F. *et al.* Detection of individual gas molecules adsorbed on graphene. *Nat. Mater.* **6**, 652–655 (2007).

9. Novoselov, K. S. *et al.* Room-temperature quantum hall effect in graphene. *Science (80-.).* **315**, 1379 (2007).

10. Bolotin, K. I. *et al.* Ultrahigh electron mobility in suspended graphene. *Solid State Commun.* **146**, 351–355 (2008).

11. Das Sarma, S., Adam, S., Hwang, E. H. & Rossi, E. Electronic transport in two dimensional graphene. *Rev. Mod. Phys.* **83**, 408–459 (2011).

12. SHOCKLEY, W. A Unipolar "Field-effect" Transistor. *Proc. I.R.E.* **40**, 1365–1376 (1969).

13. Pereira, V. M., Castro Neto, A. H. & Peres, N. M. R. Tight-binding approach to uniaxial strain in graphene. *Phys. Rev. B - Condens. Matter Mater. Phys.* **80**, 1–8 (2009).

14. Zhang, Y. *et al.* Direct observation of a widely tunable bandgap in bilayer graphene. *Nature* **459**, 820–823 (2009).

15. Castro, E. V. *et al.* Biased bilayer graphene: Semiconductor with a gap tunable by the electric field effect. *Phys. Rev. Lett.* **99**, 8–11 (2007).

16. Ohta, T., Bostwick, A., Seyller, T., Horn, K. & Rotenberg, E. Controlling the electronic structure of bilayer graphene. *Science (80-.).* **313**, 951–954 (2006).

17. Gava, P., Lazzeri, M., Saitta, A. M. & Mauri, F. Ab initio study of gap opening and screening effects in gated bilayer graphene. *Phys. Rev. B - Condens. Matter Mater. Phys.* **79**, 1–13 (2009).

18. Han, M. Y., Özyilmaz, B., Zhang, Y. & Kim, P. Energy band-gap engineering of graphene nanoribbons. *Phys. Rev. Lett.* **98**, 1–4 (2007).

19. Li, X., Wang, X., Zhang, L., Lee, S. & Dai, H. Chemically derived, ultrasmooth graphene nanoribbon semiconductors. *Science (80-.).* **319**, 1229–1232 (2008).

20. Nakada, K., Fujita, M., Dresselhaus, G. & Dresselhaus, M. S. Edge state in graphene ribbons: Nanometer size effect and edge shape dependence. *Phys. Rev. B* **54**, 17954–17961

(1996).

21.   Fujita, M., Wakabayahi, K., Nakada, K. & Kusakabe, K. Pecuilar Localized State at Zigzag Graphite Edge. *J. Phys. Soc.* **65**, 1920–1923 (1996).

22.   Son, Y. W., Cohen, M. L. & Louie, S. G. Energy gaps in graphene nanoribbons. *Phys. Rev. Lett.* **97**, 1–4 (2006).

23.   Yang, L., Park, C. H., Son, Y. W., Cohen, M. L. & Louie, S. G. Quasiparticle energies and band gaps in graphene nanoribbons. *Phys. Rev. Lett.* **99**, 6–9 (2007).

24.   Hybertsen, M. S. & Louie, S. G. Electron correlation in semiconductors and insulators: Band gaps and quasiparticle energies. *Phys. Rev. B* **34**, 5390–5413 (1986).

25.   Kimouche, A. *et al.* Ultra-narrow metallic armchair graphene nanoribbons. *Nat. Commun.* **6**, 1–6 (2015).

26.   Talirz, L. *et al.* On-Surface Synthesis and Characterization of 9-Atom Wide Armchair Graphene Nanoribbons. *ACS Nano* **11**, 1380–1388 (2017).

27.   Chen, Y. C. *et al.* Tuning the band gap of graphene nanoribbons synthesized from molecular precursors. *ACS Nano* **7**, 6123–6128 (2013).

28.   Sun, K. *et al.* On-Surface Synthesis of 8- and 10-Armchair Graphene Nanoribbons. *Small* **15**, 3–9 (2019).

29.   Yamaguchi, J. *et al.* Small bandgap in atomically precise 17-atom-wide armchair-edged graphene nanoribbons. *Commun. Mater.* **1**, 1–9 (2020).

30.   Liu, J. *et al.* Toward Cove-Edged Low Band Gap Graphene Nanoribbons. *J. Am. Chem.*

Soc. **137**, 6097–6103 (2015).

31.   Cai, J. *et al.* Atomically precise bottom-up fabrication of graphene nanoribbons. *Nature* **466**, 470–3 (2010).

32.   Beyer, D. *et al.* Graphene Nanoribbons Derived from Zigzag Edge-Encased Poly(para-2,9-dibenzo[bc, kl]coronenylene) Polymer Chains. *J. Am. Chem. Soc.* 8–11 (2019). doi:10.1021/jacs.8b10407

33.   Ruffieux, P. *et al.* On-surface synthesis of graphene nanoribbons with zigzag edge topology. *Nature* **531**, 489–492 (2016).

34.   Schulz, F. *et al.* Precursor Geometry Determines the Growth Mechanism in Graphene Nanoribbons. *J. Phys. Chem. C* **121**, 2896–2904 (2017).

35.   Zhang, H. *et al.* On-surface synthesis of rylene-type graphene nanoribbons. *J. Am. Chem. Soc.* **137**, 4022–4025 (2015).

36.   Sánchez-Sánchez, C. *et al.* On-Surface Synthesis and Characterization of Acene-Based Nanoribbons Incorporating Four-Membered Rings. *Chem. - A Eur. J.* **25**, 12074–12082 (2019).

37.   Sánchez-Sánchez, C. *et al.* Purely Armchair or Partially Chiral: Noncontact Atomic Force Microscopy Characterization of Dibromo-Bianthryl-Based Graphene Nanoribbons Grown on Cu(111). *ACS Nano* **10**, 8006–8011 (2016).

38.   Shinde, P. P. *et al.* Stability of edge magnetism in functionalized zigzag graphene nanoribbons. *Carbon N. Y.* **124**, 123–132 (2017).

39.   Nguyen, G. D. *et al.* Bottom-Up Synthesis of N = 13 Sulfur-Doped Graphene Nanoribbons. *J. Phys. Chem. C* **120**, 2684–2687 (2016).

40.   Cloke, R. R. *et al.* Site-Specific Substitutional Boron Doping of Semiconducting Armchair Graphene Nanoribbons. *J. Am. Chem. Soc.* **137**, 8872–8875 (2015).

41.   Durr, R. A. *et al.* Orbitally Matched Edge-Doping in Graphene Nanoribbons. *J. Am. Chem. Soc.* **140**, (2018).

42.   Li, J. *et al.* Band Depopulation of Graphene Nanoribbons Induced by Chemical Gating with Amino Groups. *ACS Nano* **14**, 1895–1901 (2020).

43.   Zhang, Y. F. *et al.* Sulfur-doped graphene nanoribbons with a sequence of distinct band gaps. *Nano Res.* **10**, 3377–3384 (2017).

44.   Carbonell-Sanromà, E. *et al.* Doping of Graphene Nanoribbons via Functional Group Edge Modification. *ACS Nano* **11**, 7355–7361 (2017).

45.   Zhang, Y. *et al.* Direct visualization of atomically precise nitrogen-doped graphene nanoribbons. *Appl. Phys. Lett.* **105**, (2014).

46.   Kawai, S. *et al.* Multiple heteroatom substitution to graphene nanoribbon. *Sci. Adv.* **4**, 1–8 (2018).

47.   Kawai, S. *et al.* Atomically controlled substitutional boron-doping of graphene nanoribbons. *Nat. Commun.* **6**, 8098 (2015).

48.   Fu, Y. *et al.* On-Surface Synthesis of NBN-Doped Zigzag-Edged Graphene Nanoribbons. *Angew. Chemie* **132**, 8958–8964 (2020).

49. Rizzo, D. J. *et al.* Topological band engineering of graphene nanoribbons. *Nature* **560**, 204–208 (2018).

50. Gröning, O. *et al.* Engineering of robust topological quantum phases in graphene nanoribbons. *Nature* **560**, 209–213 (2018).

51. Chen, Z., Lin, Y. M., Rooks, M. J. & Avouris, P. Graphene nano-ribbon electronics. *Phys. E Low-Dimensional Syst. Nanostructures* **40**, 228–232 (2007).

52. Abbas, A. N. *et al.* Patterning, characterization, and chemical sensing applications of graphene nanoribbon arrays down to 5 nm using helium ion beam lithography. *ACS Nano* **8**, 1538–1546 (2014).

53. Kosynkin, D. V. *et al.* Longitudinal unzipping of carbon nanotubes to form graphene nanoribbons. *Nature* **458**, 872–876 (2009).

54. Jiao, L., Zhang, L., Wang, X., Diankov, G. & Dai, H. Narrow graphene nanoribbons from carbon nanotubes. *Nature* **458**, 877–880 (2009).

55. Grill, L. *et al.* Nano-architectures by covalent assembly of molecular building blocks. *Nat. Nanotechnol.* **2**, 687–691 (2007).

56. Björk, J., Hanke, F. & Stafström, S. Mechanisms of halogen-based covalent self-assembly on metal surfaces. *J. Am. Chem. Soc.* **135**, 5768–5775 (2013).

57. Bennett, P. B. *et al.* Bottom-up graphene nanoribbon field-effect transistors. *Appl. Phys. Lett.* **103**, 1–5 (2013).

58. Talirz, L., Ruffi, P. & Fasel, R. On-Surface Synthesis of Atomically Precise Graphene

Nanoribbons. 6222–6231 (2016). doi:10.1002/adma.201505738

59. Merino-Díez, N. *et al.* Width-Dependent Band Gap in Armchair Graphene Nanoribbons Reveals Fermi Level Pinning on Au(111). *ACS Nano* **11**, 11661–11668 (2017).

60. Huang, H. *et al.* Spatially resolved electronic structures of atomically precise armchair graphene nanoribbons. *Sci. Rep.* **2**, 1–7 (2012).

61. Di Giovannantonio, M. *et al.* On-Surface Growth Dynamics of Graphene Nanoribbons: The Role of Halogen Functionalization. *ACS Nano* **12**, 74–81 (2018).

62. Hanke, F. Mechanisms of Halogen-Based Covalent Self-Assembly on Metal Surfaces. (2013). doi:10.1021/ja400304b

63. Bronner, C. *et al.* Iodine versus Bromine Functionalization for Bottom-Up Graphene Nanoribbon Growth: Role of Diffusion. *J. Phys. Chem. C* **121**, 18490–18495 (2017).

64. Bronner, C. *et al.* Hierarchical On-Surface Synthesis of Graphene Nanoribbon Heterojunctions. *ACS Nano* **12**, 2193–2200 (2018).

65. Marangoni, T., Haberer, D., Rizzo, D. J., Cloke, R. R. & Fischer, F. R. Heterostructures through Divergent Edge Reconstruction in Nitrogen-Doped Segmented Graphene Nanoribbons. *Chem. - A Eur. J.* **94720**, 13037–13040 (2016).

66. Chen, Y.-C. *et al.* Molecular bandgap engineering of bottom-up synthesized graphene nanoribbon heterojunctions. *Nat. Nanotechnol.* **10**, 156–60 (2015).

67. Nguyen, G. D. *et al.* Atomically precise graphene nanoribbon heterojunctions from a single molecular precursor. *Nat. Nanotechnol.* **12**, 1077–1082 (2017).

68. Yoon, K. Y. & Dong, G. Liquid-phase bottom-up synthesis of graphene nanoribbons. *Mater. Chem. Front.* **4**, 29–45 (2020).

69. Talirz, L., Ruffieux, P. & Fasel, R. On-Surface Synthesis of Atomically Precise Graphene Nanoribbons. *Adv. Mater.* **28**, 6222–6231 (2016).

70. McCurdy, R. D. *et al.* Synergetic Bottom-Up Synthesis of Graphene Nanoribbons by Matrix-Assisted Direct Transfer. *J. Am. Chem. Soc.* **143**, 4174–4178 (2021).

71. Binning, G., Rohrer, H., Gerber, C. & Weibel, E. Surface Studies by Scanning Tunneling Microscopy. *Phys. Rev. Lett.* **49**, 57–61 (1982).

72. Binnig, G., Rohrer, H., Gerber, C. & Weibel, E. Tunneling through a controllable vacuum gap. *Appl. Phys. Lett.* **40**, 178–180 (1982).

73. Tersoff, J. & Hamann, D. R. Theory of the scanning tunneling microscope. *Phys. Rev. B* **31**, 805–813 (1985).

74. Bardeen, J. Tunneling from a many-particle point of view. *Phys. Rev.* **131**, 1083–1086 (1963).

75. Binning, G., Quate, C. F. & Gerber, C. Atomic Force Microscope. *Phys. Rev. Lett.* **56**, 930–934 (1985).

76. Giessibl. Advances in atomic force microscopy. **75**, 1–35 (2013).

77. Gross, L., Mohn, F., Moll, N., Liljeroth, P. & Meyer, G. The Chemical Structure of a Molecule Resolved by Atomic Force Microscopy. *Science (80-.).* **325**, 1110–4 (2009).

78. Giessibl, F. J. Subatomic Features on the Observed by Atomic Force Microscopy. **422**,

(2008).

79. Son, Y.-W., Cohen, M. L. & Louie, S. G. Half-metallic graphene nanoribbons. *Nature* **44**, 347–349 (2006).

80. Mandal, B., Sarkar, S., Pramanik, A. & Sarkar, P. Doped defective graphene nanoribbons: A new class of materials with novel spin filtering properties. *RSC Adv.* **4**, 49946–49952 (2014).

81. Luis, F. & Coronado, E. Spinning on the edge of graphene. *Nature* **557**, 645–647 (2018).

82. Guo, G. P. *et al.* Quantum computation with graphene nanoribbon. *New J. Phys.* **11**, (2009).

83. Ahn, E. C., Wong, H. S. P. & Pop, E. Carbon nanomaterials for non-volatile memories. *Nat. Rev. Mater.* **3**, (2018).

84. Dery, H., Dalal, P., Cywiński & Sham, L. J. Spin-based logic in semiconductors for reconfigurable large-scale circuits. *Nature* **447**, 573–576 (2007).

85. Dery, H. *et al.* Nanospintronics based on magnetologic gates. *IEEE Trans. Electron Devices* **59**, 259–262 (2012).

86. Lin, X., Yang, W., Wang, K. L. & Zhao, W. Two-dimensional spintronics for low-power electronics. *Nat. Electron.* **2**, 274–283 (2019).

87. Zhang, D. B. & Wei, S. H. Inhomogeneous strain-induced half-metallicity in bent zigzag graphene nanoribbons. *npj Comput. Mater.* **3**, 1–5 (2017).

88. Lawrence, J. *et al.* Circumventing the Stability Problems of Graphene Nanoribbon Zigzag Edges. (2021).

89.   Lieb, E. H. Two theorems on the Hubbard model. *Phys. Rev. Lett.* **62**, 1201–1204 (1989).

90.   Perdew, J. P. & Zunger, A. Self-interaction correction to density-functional approximations for many-electron systems. *Phys. Rev. B* **23**, 5048–5079 (1981).

91.   Hayes, C. J. & Hadad, C. M. Combustion pathways of the alkylated heteroaromatics: bond dissociation enthalpies and alkyl group fragmentations. *J. Phys. Chem. A* **113**, 12370–12379 (2009).

92.   Llinas, J. P. *et al.* Short-channel field-effect transistors with 9-atom and 13-atom wide graphene nanoribbons. *Nat. Commun.* **8**, 8–13 (2017).

93.   Deniz, O. *et al.* Revealing the Electronic Structure of Silicon Intercalated Armchair Graphene Nanoribbons by Scanning Tunneling Spectroscopy. *Nano Lett.* **17**, 2197–2203 (2017).

94.   Repp, J., Meyer, G., Stojković, S. M., Gourdon, A. & Joachim, C. Molecules on insulating films: Scanning-tunneling microscopy imaging of individual molecular orbitals. *Phys. Rev. Lett.* **94**, 1–4 (2005).

95.   Ezawa, M. Peculiar width dependence of the electronic properties of carbon nanoribbons. *Phys. Rev. B - Condens. Matter Mater. Phys.* **73**, 1–8 (2006).

96.   Barone, V., Hod, O. & Scuseria, G. E. Electronic structure and stability of semiconducting graphene nanoribbons. *Nano Lett.* **6**, 2748–2754 (2006).

97.   Zhang, W. *et al.* Monitoring the On-Surface Synthesis of Graphene Nanoribbons by Mass Spectrometry. (2017). doi:10.1021/acs.analchem.7b01135

98.   Abdurakhmanova, N. *et al.* Synthesis of wide atomically precise graphene nanoribbons from para-oligophenylene based molecular precursor. *Carbon N. Y.* **77**, 1187–1190 (2014).

99.   Ruffieux, P. *et al.* Electronic structure of atomically precise graphene nanoribbons. *ACS Nano* **6**, 6930–6935 (2012).

100.   Bronner, C. *et al.* Aligning the Band Gap of Graphene Nanoribbons by Monomer Doping. *Angew. Chemie* **125**, 4518–4521 (2013).

101.   Kawai, S. *et al.* Atomically controlled substitutional boron-doping of graphene nanoribbons. *Nat. Commun.* **6**, 1–6 (2015).

102.   Cai, J. *et al.* Graphene nanoribbon heterojunctions. *Nat. Nanotechnol.* **9**, 896–900 (2014).

103.   Bennett, P. B. *et al.* Bottom-up graphene nanoribbon field-effect transistors. *Appl. Phys. Lett.* **103**, 1–5 (2013).

104.   Wang, S. *et al.* Quantum Dots in Graphene Nanoribbons. *Nano Lett.* **17**, 4277–4283 (2017).

105.   Narita, A. *et al.* Bottom-up synthesis of liquid-phase-processable graphene nanoribbons with near-infrared absorption. *ACS Nano* **8**, 11622–11630 (2014).

106.   Linden, S. *et al.* Electronic structure of spatially aligned graphene nanoribbons on Au(788). *Phys. Rev. Lett.* **108**, 23–27 (2012).

107.   Vo, T. H. *et al.* Nitrogen-Doping Induced Self-Assembly of Graphene Nanoribbon-Based Two-Dimensional and Three-Dimensional Metamaterials. *Nano Lett.* **15**, 5770–5777 (2015).

108.   Sun, Z., Boneschanscher, M. P., Swart, I., Vanmaekelbergh, D. & Liljeroth, P. Quantitative

atomic force microscopy with carbon monoxide terminated tips. *Phys. Rev. Lett.* **106**, 1–4 (2011).

109. Giannozzi, P. *et al.* QUANTUM ESPRESSO: A modular and open-source software project for quantum simulations of materials. *J. Phys. Condens. Matter* **21**, (2009).

110. Hla, S., Bartels, L., Meyer, G. & Rieder, K. Inducing All Steps of a Chemical Reaction with the Scanning Tunneling Microscope Tip : Towards Single Molecule Engineering. 2777–2780 (2000).

111. Lafferentz, L. *et al.* hierarchical and substrate-directed growth. **4**, 215–220 (2012).

112. Mishra, S. *et al.* Topological frustration induces unconventional magnetism in a nanographene. *Nat. Nanotechnol.* **15**, 22–28 (2020).

113. Pavliček, N. *et al.* Polyyne formation via skeletal rearrangement induced by atomic manipulation. *Nat. Chem.* **10**, 853–858 (2018).

114. Pavliček, N. *et al.* Synthesis and characterization of triangulene. *Nat. Nanotechnol.* **12**, 308–311 (2017).

115. Borca, B. *et al.* Electric-Field-Driven Direct Desulfurization. *ACS Nano* **11**, 4703–4709 (2017).

116. Gao, H. Y. *et al.* Glaser coupling at metal surfaces. *Angew. Chemie - Int. Ed.* **52**, 4024–4028 (2013).

117. Sánchez-Sánchez, C. *et al.* The flexible surface revisited: Adsorbate-induced reconstruction, homocoupling, and sonogashira cross-coupling on the Au(100) surface. *J.*

Phys. Chem. C **118**, 11677–11684 (2014).

118. Sun, Q. *et al.* On-surface formation of one-dimensional polyphenylene through Bergman cyclization. *J. Am. Chem. Soc.* **135**, 8448–8451 (2013).

119. Carbonell-Sanromà, E. *et al.* Electronic Properties of Substitutionally Boron-Doped Graphene Nanoribbons on a Au(111) Surface. *J. Phys. Chem. C* **122**, 16092–16099 (2018).

120. Senkovskiy, B. V. *et al.* Boron-doped graphene nanoribbons: Electronic structure and raman fingerprint. *ACS Nano* **12**, 7571–7582 (2018).

121. Pedramrazi, Z. *et al.* Concentration Dependence of Dopant Electronic Structure in Bottom-up Graphene Nanoribbons. *Nano Lett.* **18**, 3550–3556 (2018).

122. de Oteyza, D. G. *et al.* Direct Imaging of Covalent Bond. *Science (80-.).* **340**, 1434–1437 (2013).

123. Rogers, C. *et al.* Closing the Nanographene Gap: Surface-Assisted Synthesis of Peripentacene from 6,6???-Bipentacene Precursors. *Angew. Chemie - Int. Ed.* **54**, 15143–15146 (2015).

124. Pozo, I. *et al.* Revisiting Kekulene: Synthesis and Single-Molecule Imaging. *J. Am. Chem. Soc.* **141**, 15488–15493 (2019).

125. Zuzak, R. *et al.* Higher Acenes by On-Surface Dehydrogenation: From Heptacene to Undecacene. *Angew. Chemie - Int. Ed.* **57**, 10500–10505 (2018).

126. Majzik, Z. *et al.* Studying an antiaromatic polycyclic hydrocarbon adsorbed on different surfaces. *Nat. Commun.* **9**, 2–7 (2018).

127. Treier, M. *et al.* Surface-assisted cyclodehydrogenation provides a synthetic route towards easily processable and chemically tailored nanographenes ¨. **3**, 61–67 (2011).

128. Clair, S. & De Oteyza, D. G. Controlling a Chemical Coupling Reaction on a Surface: Tools and Strategies for On-Surface Synthesis. *Chem. Rev.* **119**, 4717–4776 (2019).

129. Björk, J., Stafström, S. & Hanke, F. Zipping up: Cooperativity drives the synthesis of graphene nanoribbons. *J. Am. Chem. Soc.* **133**, 14884–14887 (2011).

130. Wang, X. Y., Yao, X., Narita, A. & Müllen, K. Heteroatom-Doped Nanographenes with Structural Precision. *Acc. Chem. Res.* **52**, 2491–2505 (2019).

131. Wang, X. Y. *et al.* Bottom-Up Synthesis of Heteroatom-Doped Chiral Graphene Nanoribbons. *J. Am. Chem. Soc.* **140**, 9104–9107 (2018).

132. Oki, K. *et al.* Synthesis, Structures, and Properties of Core-Expanded Azacoronene Analogue: A Twisted π-System with Two N-Doped Heptagons. *J. Am. Chem. Soc.* **140**, 10430–10434 (2018).

133. Uno, H. *et al.* Oxidation behavior of 1,3-dihydrothieno[3,4-a]HPHAC. *Bull. Chem. Soc. Jpn.* **92**, 973–981 (2019).

134. Sasaki, Y., Takase, M., Okujima, T., Mori, S. & Uno, H. Synthesis and Redox Properties of Pyrrole- and Azulene-Fused Azacoronene. *Org. Lett.* **21**, 1900–1903 (2019).

135. Takase, M. *et al.* Pyrrole-fused azacoronene family: The influence of replacement with dialkoxybenzenes on the optical and electronic properties in neutral and oxidized states. *J. Am. Chem. Soc.* **135**, 8031–8040 (2013).

136. Takase, M., Enkelmann, V., Sebastiani, D., Baumgarten, M. & Müllen, K. Annularly fused hexapyrrolohexaazacoronenes: An extended π system with multiple interior nitrogen atoms displays stable oxidation states. *Angew. Chemie - Int. Ed.* **46**, 5524–5527 (2007).

137. Zyła, M., Gońka, E., Chmielewski, P. J., Cybińska, J. & Stępień, M. Synthesis of a peripherally conjugated 5-6-7 nanographene. *Chem. Sci.* **7**, 286–294 (2016).

138. Żyła-Karwowska, M. *et al.* An Electron-Deficient Azacoronene Obtained by Radial π Extension. *Angew. Chemie - Int. Ed.* **55**, 14658–14662 (2016).

139. Belser, A. *et al.* Visualization of the Borazine Core of B3N3-Doped Nanographene by STM. *ACS Appl. Mater. Interfaces* **12**, 19218–19225 (2020).

140. Ciccullo, F. *et al.* A Quasi-Free-Standing Single Layer of a B3N3-Doped Nanographene Molecule Deposited on Au(111) Single Crystals. *J. Phys. Chem. C* **120**, 17645–17651 (2016).

141. Wang, X. Y. *et al.* Exploration of pyrazine-embedded antiaromatic polycyclic hydrocarbons generated by solution and on-surface azomethine ylide homocoupling. *Nat. Commun.* **8**, 4–10 (2017).

142. Hapala, P. *et al.* Mechanism of high-resolution STM / AFM imaging with functionalized tips. **085421**, 1–9 (2014).

143. Weiss, C. *et al.* Imaging Pauli repulsion in scanning tunneling microscopy. *Phys. Rev. Lett.* **105**, 2–5 (2010).

144. Deslippe, J. *et al.* BerkeleyGW: A massively parallel computer package for the calculation of the quasiparticle and optical properties of materials and nanostructures. *Comput. Phys.*

Commun. **183**, 1269–1289 (2012).

145. Blum, V. *et al.* Ab initio molecular simulations with numeric atom-centered orbitals. *Comput. Phys. Commun.* **180**, 2175–2196 (2009).

146. Lombardi, F. *et al.* Quantum units from the topological engineering of molecular graphenoids. *Science (80-.).* **366**, 1107–1110 (2019).

147. Lee, Y. L., Zhao, F., Cao, T., Ihm, J. & Louie, S. G. Topological Phases in Cove-Edged and Chevron Graphene Nanoribbons: Geometric Structures, Z 2 Invariants, and Junction States. *Nano Lett.* **18**, 7247–7253 (2018).

148. Jackiw, R. & Rebbi, C. Solitons with fermion number. *Phys. Rev. D* **13**, 3398–3409 (1976).

149. den Nijs, M. Quantized Hall conductance in a two dimensional periodic potential. *Phys. A Stat. Mech. its Appl.* **124**, 199–210 (1984).

150. Klitzing, K. V., Dorda, G. & Pepper, M. New method for high-accuracy determination of the fine-structure constant based on quantized hall resistance. *Phys. Rev. Lett.* **45**, 494–497 (1980).

151. Hasan, M. Z. & Kane, C. L. Colloquium: Topological insulators. *Rev. Mod. Phys.* **82**, 3045–3067 (2010).

152. Qi, X. L. & Zhang, S. C. Topological insulators and superconductors. *Rev. Mod. Phys.* **83**, (2011).

153. Fu, L. & Kane, C. L. Topological insulators with inversion symmetry. *Phys. Rev. B - Condens. Matter Mater. Phys.* **76**, 1–17 (2007).

154. Cao, T., Zhao, F. & Louie, S. G. Topological Phases in Graphene Nanoribbons: Junction States, Spin Centers, and Quantum Spin Chains. *Phys. Rev. Lett.* **119**, 1–5 (2017).

155. Teeter, J. D. *et al.* Dense monolayer films of atomically precise graphene nanoribbons on metallic substrates enabled by direct contact transfer of molecular precursors. *Nanoscale* **9**, 18835–18844 (2017).

156. Clar, E. & Mackay, C. C. Cicobiphenyl and the Attempted Synthesis of 1:14, 3:4, 7:8, 10:11-Tetrabenzoperopyrene. *Tetrahedron* **28**, 6041–6047 (1972).

157. Rizzo, D. J. *et al.* Inducing metallicity in graphene nanoribbons via zero-mode superlattices. *Science (80-.).* **369**, 1597–1603 (2020).

158. Schwab, M. G. *et al.* Structurally defined graphene nanoribbons with high lateral extension. *J. Am. Chem. Soc.* **134**, 18169–18172 (2012).

159. Urgel, J. I. *et al.* Overcoming Steric Hindrance in Aryl-Aryl Homocoupling via On-Surface Copolymerization. *ChemPhysChem* **20**, 2360–2366 (2019).